



**UNIVERSIDAD
DE BURGOS**

ANA GARCÍA RODRÍGUEZ

TESIS DOCTORAL

**MODELIZACIÓN MATEMÁTICA DE LA
RADIACIÓN SOLAR
FOTOSINTÉTICAMENTE ACTIVA**

Dirigida por las Doctoras:
MONTSERRAT DÍEZ MEDIAVILLA
CRISTINA ALONSO TRISTÁN

Burgos, Febrero 2022

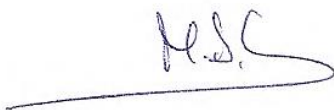
Universidad De Burgos

Escuela De Doctorado

Montserrat Díez Mediavilla y Cristina Alonso Tristán hacen constar:

Que el presente trabajo, titulado “Modelización matemática de la radiación solar fotosintéticamente activa”, que presenta Ana García Rodríguez para la obtención del título de doctor ha sido realizado bajo su supervisión, en el Programa de Doctorado Interuniversitario en Eficiencia Energética y Sostenibilidad en Ingeniería y Arquitectura por la Universidad de Burgos, la Universidad de Vigo y la Universidad del País Vasco/Euskal Herriko Unibertsitatea (5600956; RD 99/2011).

Burgos, 26 de Febrero de 2022



Fdo. Montserrat Díez Mediavilla



Fdo. Cristina Alonso Tristán

Ana García Rodríguez, 2022



A mi familia.

Esta tesis doctoral se presenta como un compendio de publicaciones cumpliendo los requisitos establecidos en el Programa de Doctorado “Eficiencia Energética y Sostenibilidad en Ingeniería y Arquitectura”, programa Interuniversitario de la Universidad de Burgos, la Universidad de Vigo y la Universidad del País Vasco/Euskal Herriko Unibertsitatea (RD 99/2011).

Las publicaciones recogen los resultados obtenidos en los diferentes trabajos de investigación desarrollados para alcanzar los objetivos planteados para la realización de la tesis. Las publicaciones referidas se enumeran en orden de relación con los objetivos de la tesis en la Sección Lista de Artículos y constituyen las Secciones I a IV de esta memoria de tesis. Tres de los cuatro artículos que componen la tesis han sido publicados en revistas indexadas en el Journal of Citation Reports (JCR) y el último ha sido enviado para su publicación y actualmente se encuentra en proceso de revisión. Se incluye también un quinto artículo, ya publicado, derivado de una de las líneas de investigación futuras propuestas en la tesis.

Esta tesis ha sido financiada gracias a los proyectos de investigación siguientes:

1.- Valoración técnica de los niveles de exposición a radiación solar en trabajos de exterior: identificación de grupos de riesgo y medidas de prevención. (INVESTUN/19/BU/004) Junta de Castilla y León. Dirección General de Trabajo y Prevención de riesgos laborales. IP: Montserrat Díez Mediavilla. 01/01/2019-30/09/2021.

2.- Análisis Espectral de la Radiación Solar: Aplicaciones Climáticas, Energéticas y Biológicas (RTI-2018-098900-B-I00). Ministerio de Universidades e Investigación Programa Estatal De I+D+i Orientada a los Retos de la Sociedad. IP: Cristina Alonso Tristán y Montserrat Díez Mediavilla. 1/01/2019-30/09/2022.

3.- Metodología para la rehabilitación energética de edificios de uso público en Castilla y León mediante integración fotovoltaica (BU021G19). Junta de Castilla y León. Programa de Apoyo a los Grupos de Investigación Reconocidos de Universidades públicas de Castilla y León. 01/01/2019-31/12/2021. IP: Montserrat Díez Mediavilla.

Agradecimientos

Lo primero de todo, agradecer enormemente a mis Directoras de Tesis, Montse y Cristina, por confiar en mí, apoyarme y ayudarme en la consecución de este trabajo. Y, sobre todo a nivel personal, por su cercanía y trato, y hacerme ver que las cosas se pueden hacer de otra manera.

No me puedo olvidar en estos agradecimientos al Grupo SWIFT, en especial al “Grupo G”, donde hemos llevado el compañerismo y la expresión “todos a una” a su máxima expresión. Y con quienes las “todo list” interminables y el apagar fuegos, son mucho más llevaderos. Muchas gracias por todo.

No podía faltar en estos agradecimientos mi familia, que me ha apoyado y ayudado en todo momento, calmando mis ánimos cuando más lo necesitaba, y no dejándome caer nunca. Sin vosotros, no habría sido posible.

Por todo ello:

MUCHAS GRACIAS

Resumen

La radiación fotosintéticamente activa (*PAR*) es la componente de la radiación solar que ejerce una mayor influencia en la fotosíntesis y el crecimiento vegetal. La vegetación actúa como sumidero de CO_2 , mitigando los efectos del cambio climático, por lo que conocer la influencia de la *PAR* en el crecimiento vegetal es primordial. La modelización matemática de la *PAR* permite estimar su valor a partir de otras variables, sin necesidad de disponer de instrumentos de medida específicos, ya que no es habitual encontrar, en las estaciones radiométricas, sensores que midan esta componente de la radiación solar.

En este trabajo, se ha modelado matemáticamente la *PAR* en Burgos, España. Para ello, se ha analizado estadísticamente la *PAR* en la localidad, analizando la ratio de esta componente con la irradiancia global horizontal. Se ha realizado una exhaustiva revisión de los modelos existentes y se han calibrado y validado 21 de ellos con datos experimentales procedentes de siete estaciones radiométricas estadounidenses, pertenecientes a la red SURFRAD. La mayor parte de los estudios publicados por otros autores, se centran en resultados para cielos claros, limitando su aplicación al ámbito local y esas condiciones de cielo.

Mediante procedimientos de *machine learning*, aplicados a los datos experimentales obtenidos en Burgos, se ha realizado una selección de variables para modelar la *PAR* mediante regresiones multilineales y redes neuronales. Estos estudios han permitido obtener modelos matemáticos, diferentes para cada tipo de cielo (cubiertos, parciales y claros) clasificados según la norma ISO/CIE y alternativamente, utilizando como parámetro de clasificación el índice de claridad (k_t). El comportamiento de estos últimos modelos, calibrados localmente para

Burgos, ha sido evaluado frente a las medidas de siete estaciones radiométricas de la red SURFRAD, con diferente climatología, obteniendo muy buenos resultados y permitiendo afirmar que estos modelos pueden utilizarse en cualquier localización, independientemente del clima.

Abstract

Photosynthetically active radiation (*PAR*) is the component of solar radiation that most influences photosynthesis and plant growth. Vegetation acts as a CO₂ sink, mitigating the effects of climate change. Therefore, knowledge of the influence of *PAR* on plant growth is of essential importance. Mathematical modelling makes allows estimating *PAR* from different meteorological indices, without the need for specific measuring instruments, since it is not usual to find sensors measuring *PAR* at radiometric stations.

In this thesis, *PAR* has been mathematically modelled in Burgos (Spain). For this purpose, a statistical study has been performed at this location, analysing the ratio of *PAR* with the global horizontal irradiance. An exhaustive review of the existing models has been carried out. Thus, 21 of them have been calibrated and validated with experimental data from the 7 radiometric stations belonging to the SURFRAD network (USA). Most of the studies published by other authors focus on results for clear skies, limiting their application to the local area and to those sky conditions.

Using machine learning procedures, applied to the experimental data obtained in Burgos, a selection of variables has been made to model the *PAR* by means of multilinear regressions and neural networks. These studies have made it possible to obtain different mathematical models for each sky type (overcast, partial and clear) classified according to the

ISO/CIE standard and, alternatively, using the clearness index (k_t) as a classification parameter. The performance of the latter models, locally fitted for Burgos, has been evaluated against the SURFRAD network measurements obtaining very good results. Therefore, it can be stated that these models may be used at any location, regardless of the climate

Listado de Artículos

Artículo I

Ana García-Rodríguez, Sol García-Rodríguez, Montserrat Díez-Mediavilla and Cristina Alonso-Tristán (2020). *Photosynthetic Active Radiation, Solar Irradiance and the CIE Standard Sky Classification*. Applied Sciences 10 (22) ,8007.

DOI: <https://doi.org/10.3390/app10228007>

Journal Citation Reports:

Índice impacto (2020): 2.679. Cuartil: Q2 (38/90).

Categoría JCR: Engineering Multidisciplinary

Scimago Journal Rank:

Índice impacto (2020): 0.435. Cuartil: Q2 (1222/6334)

Categoría SJR: Engineering Miscellaneous

Número de citas:4

Artículo II

Marian de Blas, Ana García-Rodríguez, Ignacio García, José Luis Torres (2022). *Validation and Calibration of Models to Estimate Photosynthetically Active Radiation Considering Different Time Scales and Sky Conditions*. Advances in Space Research. (en revision)

Journal Citation Reports:

Índice impacto (2020): 2.152. Cuartil: Q1 (7/34).

Categoría JCR: Engineering, Aerospace

Scimago Journal Rank:

Índice impacto (2020): 0.682. Cuartil: Q1 (29/314)

Categoría SJR: Engineering, Aerospace.

Artículo III

A. García-Rodríguez, D. Granados-López, S. García-Rodríguez, M. Díez-Mediavilla, C. Alonso-Tristán (2021). *Modelling Photosynthetic Active Radiation (PAR) through meteorological indices under all sky conditions*. Agricultural and Forest Meteorology, 310, 108627.

DOI: <https://doi.org/10.1016/j.agrformet.2021.108627>

Journal Citation Reports

Índice impacto (2020): 5.734. Cuartil: Q1 (12/94).

Categoría JCR: Meteorology and Atmospheric Sciences

Scimago Journal Rank:

Índice impacto (2020): 1.837. Cuartil: Q1 (15/135)

Categoría SJR: Atmospheric Science

Número de citas:1

Artículo IV

Ana García-Rodríguez, Sol García-Rodríguez, Diego Granados-López, Montserrat Díez-Mediavilla and Cristina Alonso-Tristán (2022). *Extension of local all sky conditions PAR models to different climatic zones*. Applied Sciences, 12, 2372.

DOI: <https://doi.org/10.3390/app12052372>.

Journal Citation Reports:

Índice impacto (2020): 2.679. Cuartil: Q2 (38/90).

Categoría JCR: Engineering Multidisciplinary

Scimago Journal Rank:

Índice impacto (2020): 0.435. Cuartil: Q2 (1222/6334)

Categoría SJR: Engineering Miscellaneous

Artículo V

Ribas, J.R; Ribas, J.S; García,A.S; Fariña, E.A; Peña,D.G.; Rodríguez, A.G (2021). *A multicriteria evaluation of sustainable riparian revegetation with local fruit trees around a reservoir of a hydroelectric power plant in Central Brazil*. Sustainability, 13, (14) 7849.

DOI: [https://doi.org/ 10.3390/su13147849](https://doi.org/10.3390/su13147849).

Journal Citation Reports:

Índice impacto (2020): 3.251. Cuartil: Q2 (59/125).

Categoría JCR: Environmental Studies.

Scimago Journal Rank:

Índice impacto (2020): 0.612. Cuartil: Q2 (94/341)

Categoría SJR: Environmental Science (miscellaneous).

INDICE GENERAL DE LA TESIS

Listado de Figuras.....	xx
Listado de Tablas.....	xxii
Nomenclatura.....	xxiv
Capítulo 1	1
Introducción.....	1
Objetivos principal y parciales	14
Resumen de artículos	16
Capítulo 2	19
Resultados por objetivos	19
Capítulo 3	45
Conclusiones.....	45
Líneas de futuro	46
Bibliografía.....	49
Renuncia coautores publicaciones.....	61
Artículos.....	63

Listado de Figuras

Figura 1. Condiciones de cielo estándar CIE. Imágenes de diferentes tipos de cielo grabadas con SONA201D All-Sky Camera en Burgos, España.[47] ...	10
Figura 2. Flujograma con los objetivos y sus publicaciones asociadas.....	15
Figura 3. Ubicación del equipo experimental en la azotea de la Escuela Politécnica Superior edificio de la Universidad de Burgos, España [47].....	21
Figura 4. Vista general de la estación radiométrica situada en la Escuela Politécnica Superior de la Universidad de Burgos	21
Figura 5. Ubicación de las siete estaciones meteorológicas de SURFRAD...22	
Figura 6. Frecuencia de aparición (FOC,%) de tipos de cielo estándar CIE en Burgos, España, entre abril 2019 y enero 2020 [47]	24
Figura 7. Frecuencia de aparición (FOC,%) de la clasificación de nubosidad CIE Burgos, España, entre abril 2019 y enero 2020 [47].	25
Figura 8. Densidad de flujo de fotones fotosintéticos, $Q_p(\mu\text{mol} \cdot \text{m}^{-1} \cdot \text{s}^{-2})$ e irradiancia solar de banda ancha, $RaGH(W \cdot \text{m}^{-2})$ (medida en Burgos, entre abril de 2019 y enero de 2020. [47].	26
Figura 9. Diagrama de cajas y bigotes de la ratio densidad de flujo de fotones fotosintético e irradiancia solar de banda ancha ($Q_p/RaGH$) para cada tipo de cielo standard CIE [47].	27
Figura 10. Resultados estadísticos de los modelos para datos de entrada de 1 minuto.....	31
Figura 11. Frecuencia de aparición ($FOC, \%$) de los tipos de cielo estándar CIE en Burgos, España, entre abril de 2019 y febrero de 2021 [74].....	33
Figura 12. Análisis estadístico de la cobertura de nubes (CC) antes (1) y después (2) de filtrar los datos atípicos [74]	34
Figura 13. El coeficiente de correlación de Pearson ($r(PAR, MI_i)$) calculado para los 10 MI utilizados en este estudio [74]	35
Figura 14. Arquitectura del sistema de red neuronal artificial mediante el algoritmo de retropropagación de Levenberg-Marquardt [74].....	37

Listado de Tablas

Tabla 1. 15 tipos de cielo clasificados según la norma ISO/CIE.....	9
Tabla 2. Marcas y modelos de los sensores instalados en la instalación.....	20
Tabla 3. Modelos evaluados para la estimación de la <i>PAR</i>	29
Tabla 4. Clasificación del cielo según el índice del cielo (SI) propuesto por Igawa.	30
Tabla 5. El coeficiente de correlación de Pearson o Pearson $r(PAR,MI_i)$ teniendo en cuenta las condiciones de cielo definidas por la clasificación del cielo estándar (cubierto, parcial y claro) [74].....	35
Tabla 6. Modelos de regresión multilínea de la <i>PAR</i> (modificado a partir de [74])	36
Tabla 7. Resultados estadísticos de los modelos de regresión multilínea (modificado a partir de [74])	36
Tabla 8. Resultados estadísticos de los modelos de redes neuronales [74]	38
Tabla 9. Índices meteorológicos medidos en Burgos [76].....	40
Tabla 10. Coeficiente de Pearson, $r(PAR,MI_i)$ basado en las condiciones de cielo definidas por la clasificación de cielo de k_t (claro, parcial y cubierto) [76].	41
Tabla 11. Modelos de regresión multilínea de la <i>PAR</i> [76].....	42
Tabla 12. Condiciones climáticas de las siete estaciones americanas (modificado a partir de [76])	43

Nomenclatura

Simbolos

AOD	profundidad óptica de los aerosoles
$cosZ$	coseno del ángulo zenital
CC	cobertura nubosa (%)
e	presión de vapor de agua (hPa)
ε	claridad del cielo de Perez [1]
Δ	brillo del cielo de Perez [1]
G_0	irradiancia extraterrestre ($W \cdot m^{-2}$)
k_b	fracción directa
k_d	fracción difusa de la radiación
k_t	índice de claridad
$k_{t,PAR}$	índice de claridad para el rango de radiación cubierto por la PAR
L_D	longitud del día
m	masa óptica relativa del aire
nm	duración de horas de sol
P	presión de aire (hPa)
Q_p	densidad de flujo de fotones fotosintéticos ($\mu mol \cdot m^{-1} \cdot s^{-2}$)
$Q_p/RaGH$	relación entre Q_p y $RaGH$
R^2	coeficiente de determinación
$RaDH$	irradiancia difusa horizontal ($W \cdot m^{-2}$)
$RaGH$	irradiancia global horizontal ($W \cdot m^{-2}$)
RH	humedad relativa (%)
S	insolación relativa
SI	índice de cielo [2]
T	temperatura del aire ($^{\circ}C$)

T_d	temperatura del punto de rocío ($^{\circ}C$)
TOC	contenido total de la columna de ozono
WV	columna de vapor de agua precipitable (cm)
Z	ángulo solar zenital ($^{\circ}$)
r	coeficiente de correlación de Pearson

Abreviaturas

<i>ANN</i>	red neuronal artificial
<i>CIE</i>	Comisión Internacional de la Iluminación
<i>ECV</i>	Variables Climáticas Esenciales
<i>FAPAR</i>	fracción absorbida de la <i>PAR</i> ($W \cdot m^{-2}$)
<i>FOC</i>	frecuencia de aparición (%)
<i>GCOS</i>	Global Climate Observing System
<i>LMBP</i>	Levenberg-Marquardt Back-Propagation
<i>MI</i>	índice meteorológico
<i>MLR</i>	regresión multilínea
<i>MPE</i>	error de porcentaje medio (%)
<i>ODS</i>	Objetivos de Desarrollo Sostenible
<i>PAR</i>	radiación fotosintéticamente activa ($W \cdot m^{-2}$)
<i>RMSE_r</i>	error cuadrático medio relativo (%)
<i>RSD</i>	desviación relativa estándar (%)
<i>RSME</i>	error cuadrático medio ($W \cdot m^{-2}$)
<i>SURFRAD</i>	Baseline Surface Radiation Network
<i>UNFCCC</i>	United Nations Framework Convention on Climate Change
<i>nMAE</i>	error absoluto medio normalizado (%)
<i>nMBE</i>	error de sesgo medio normalizado (%)
<i>nRMSE</i>	error cuadrático medio normalizado (%)

Capítulo 1: Introducción y Objetivos

1.1. Introducción

El desarrollo sostenible, proporciona un plan compartido para la paz y la prosperidad de las personas y el planeta, ahora y en el futuro. Es una de las actuaciones adoptadas por todos los Estados miembros de las Naciones Unidas en 2015 dentro de la Agenda 2030. En ella se establecen los 17 Objetivos de Desarrollo Sostenible (ODS), que son un llamado urgente a la acción de todos los países, desarrollados y en desarrollo, en una asociación global. Para conseguir poner fin a la pobreza se deben seguir unas estrategias que mejoren la salud y la educación, reduzcan la desigualdad y estimulen el crecimiento económico, todo mientras se aborda el cambio climático y se trabaja para preservar nuestros océanos y bosques. Dentro de estos 17 ODS, los objetivos 7, 13, 14 y 15, están relacionados con la **radiación solar fotosintéticamente activa (PAR)**, debido a su influencia en nuevas fuentes de energía, el cambio climático, la evolución de la vida de los océanos y los ecosistemas terrestres.

La *PAR* es la componente de la radiación global con una longitud de onda comprendida entre 400 y 700 *nm*. Esta franja de longitudes de onda se puede expresar tanto como el flujo de fotones (Q_p en $\mu\text{mol} \cdot \text{s}^{-1} \cdot \text{m}^{-2}$) como de potencia (*PAR*, en $\text{W} \cdot \text{m}^{-2}$) [3]. Normalmente se mide Q_p y se convierte en unidades de potencia a través del factor de conversión de McCree, $4,57 \mu\text{mol} \cdot \text{J}^{-1} \pm 3\%$, dependiendo el margen de error de las condiciones climáticas [4].

Para comprender el cambio climático y sus efectos, es necesaria la observación de la atmósfera y la aplicación de la ciencia atmosférica al conocimiento de los fenómenos meteorológicos. Con el paso de los años se ha comprendido que para entender y predecir el clima es necesaria la observación exhaustiva del sistema climático atmósfera-

Capítulo 1: Introducción y Objetivos

océano-tierra en su conjunto. Esto inspiró el establecimiento del *Global Climate Observing System* (GCOS), que ha definido las Variables Climáticas Esenciales (ECV, por sus siglas en inglés) como "variables que son actualmente viables para su aplicación global y tienen un gran impacto en los requisitos de la *United Nations Framework Convention on Climate Change* (UNFCCC)". La lista de variables se actualiza a medida que surgen nuevos requisitos y se desarrollan nuevas capacidades de observación. El GCOS ha agrupado estas variables en oceánicas, atmosféricas y terrestres y en la actualidad figuran 48 ECVs, tal y como se recoge en la última versión del Plan de Aplicación del GCOS en apoyo de la UNFCCC.

Dentro de estas variables esenciales terrestres se encuentra la *FAPAR* (fracción absorbida de la *PAR*). El GCOS indica que la *PAR* proporciona a la vegetación terrestre la energía necesaria para sintetizar materiales orgánicos a partir de componentes minerales [5].

La *PAR* influye directamente en la fotosíntesis, la producción de energía renovable a partir de biomasa, el crecimiento de la vegetación, de su área foliar y en la evotranspiración, la iluminación natural en los invernaderos, y se utiliza para calcular la profundidad eufótica de los océanos. Cada una de las implicaciones de la *PAR* se han estudiado en los diferentes trabajos que se describen a continuación.

Hao et al. [6] estudiaron las componentes directa y difusa de la radiación descendente de onda corta, y la *PAR* en la superficie de la Tierra. *Deo et al.* [7], concluyeron que la obtención de biocombustibles a partir de algas, se ven afectados por la disponibilidad de la *PAR* en los lugares de cosecha. Por lo tanto, los pronósticos en tiempo real de la *PAR* son un parámetro clave para la producción de biomasa y consideran crucial la *PAR* para cubrir esta demanda de energía sostenible y respetuosa con el medio ambiente.

Capítulo 1: Introducción y Objetivos

La *PAR* tiene también influencia en el crecimiento vegetal y en el área foliar. *Verma et al.* [8] propusieron un tratamiento integrado de aguas residuales mediante algas con la ayuda de la radiación solar y demostraron la rentabilidad económica del método para tratar dichos residuos y producir biomasa en lugares donde la intensidad de la radiación solar es elevada. *Saini y Fricke* [9] estudiaron cómo afecta la *PAR* a la pérdida de agua por transpiración en cultivos de cebada. Se observó que, en este cereal, la transpiración por planta y unidad de superficie foliar, aumentó proporcionalmente a los niveles de *PAR* recibidos, tanto de día como de noche. Concluyeron que las plantas de cebada experimentaban cambios en la pérdida de agua por transpiración de los brotes en respuesta a distintos niveles de *PAR*, ajustando la captación de agua por su raíz. Además, observaron que el crecimiento de las plantas sometidas a bajos niveles de *PAR* reducía el área foliar en casi un 50% en comparación con el área de las plantas que habían sido cultivadas con niveles normales y altos de *PAR*. *Trejo-Tellez et al.* [10] evaluaron los efectos del fosfato, fosfito y de dos tasas de *PAR* media diaria (alta y baja), así como sus interacciones, sobre las concentraciones de flavonoides, nitratos y glucosinolatos, y las características de crecimiento en especies de mostaza cultivadas hidropónicamente. En una de las especies, una mayor *PAR* aumentó la materia seca y, por el contrario, disminuyó el número de hojas. Una *PAR* más baja y el aumento de fosfito disminuyó significativamente la concentración de flavonoides en la otra especie, mientras que el aumento de fosfito con una *PAR* más alta incrementó dicha concentración en esta especie. Este estudio concluyó que mediante el control de la *PAR*, el fosfito y el fosfato se pueden modular las concentraciones de flavonoides, glucosinolatos y nitratos en las especies de mostaza, lo que puede ser una herramienta útil para mejorar la calidad nutracéutica de estas hortalizas de hoja verde si se gestiona adecuadamente.

Capítulo 1: Introducción y Objetivos

También se ha estudiado la influencia de la *PAR* en los océanos. La concentración atmosférica de CO_2 ha aumentado desde que comenzó la industrialización en la década de 1850 [11]. El océano es el principal sumidero de CO_2 atmosférico, y alrededor de un tercio de este CO_2 se incorpora al agua de mar, lo que conduce a la acidificación de los océanos. La *PAR* afecta a la profundidad eufótica (profundidad de la zona de fotosíntesis) en los océanos, el blanqueamiento de los corales y la descomposición vírica marina. *Churilova et al.* [12] estimaron el efecto de la floración de fitoplancton con la disponibilidad de *PAR* en el mar en función de la profundidad, y la capacidad de dicho fitoplancton para absorber la *PAR*. Observaron cómo el aumento de 10 veces de la concentración de clorofila *a* (de $0,4$ a $4,0 \text{ mg} \cdot \text{m}^{-3}$) durante la floración de fitoplancton, conducía a una disminución de la transparencia del agua, lo que provoca un estrechamiento de la zona eufótica. Como consecuencia, la *PAR* media dentro de la capa de hábitat del fitoplancton se reducía casi a la mitad. El aumento de la biomasa de fitoplancton y el cambio en el espectro de irradiación descendente van acompañados de una disminución del coeficiente de absorción específico de los pigmentos del fitoplancton a las mismas profundidades ópticas. Estos autores estimaron por primera vez la eficacia específica de absorción de la luz por parte del fitoplancton y demostraron que dicha eficacia varía dependiendo del espectro luminoso. Concluyeron que sus resultados podrían utilizarse para predecir las consecuencias ecológicas debidas a la influencia de los factores antropogénicos en la intensidad y la frecuencia de las floraciones del fitoplancton. *Jyothibabu et al.* [13] estudiaron cómo afectaron las grandes fluctuaciones de la *PAR*, por la presencia o no de nubosidad, a la respuesta fisiológica del fitoplancton en el norte de la Bahía de Bengala (Océano Índico). En los días nublados, la *PAR* disponible bajo el agua disminuyó drásticamente, siendo la *PAR* del mediodía en la superficie del agua (hasta 2 m de profundidad) de

Capítulo 1: Introducción y Objetivos

$600 \mu\text{mol} \cdot \text{m}^{-2} \cdot \text{s}^{-1}$ en días soleados y disminuía a $50 \mu\text{mol} \cdot \text{m}^{-2} \cdot \text{s}^{-1}$ en días muy días nublados. Se observó que la concentración de clorofila *a* en la columna de agua también estaba relacionada con la presencia de nubes y la atenuación de la luz, ya que aumentó en días nublados, mientras que ocurría lo contrario en días soleados. Estos cambios en la distribución vertical de la clorofila *a* en el norte de la bahía de Bengala se debían a la fotoaclimatación fisiológica del fitoplancton a los grandes cambios en la *PAR* submarina. *Wei et al.* [14] concluyeron que la *PAR* aumenta las tasas de descomposición del virioplancton marino en entornos naturales, afectando más a los virus de baja fluorescencia, ya que son más sensibles al calentamiento y al aumento de la *PAR* que los de alta fluorescencia. *Yu et al.* [15] estudiaron los efectos combinados de la radiación solar y de la concentración de CO_2 elevados. Para ello, expusieron en laboratorio a un alga productora de dimetilsulfoniopropionato (DMSP) a radiaciones combinadas de *PAR* + *UVA* y a *PAR* + *UVA* + *UVB*. El DMSP es precursor del dimetilsulfuro (DMS), un gas activo biogénico volátil, que está relacionado con el clima ya que actúa como núcleo de condensación en la atmósfera, y un aumento de este gas ayudaría a frenar el calentamiento global. Independientemente del nivel de CO_2 existente, el crecimiento de las algas y la concentración de clorofila se incentivó al someter los vegetales a radiación combinada *PAR* + *UVA*, con respecto a la irradiación solo con *PAR*, mientras que el uso de radiación *UVB* produjo el efecto contrario.

Yates et al. [16] estudiaron cómo el aumento de las temperaturas y la radiación solar causa el blanqueamiento de los corales, provocando una gran mortalidad de los mismos. El aumento del CO_2 reduce el pH del agua de mar, retarda el crecimiento del coral y puede causar la pérdida de la estructura del arrecife. Observaron que los corales de manglar prosperaban en condiciones de poca luz (más del 70% de

Capítulo 1: Introducción y Objetivos

atenuación de *PAR* incidente) y a temperaturas más altas que los corales del arrecife cercano. También concluyeron que la materia orgánica disuelta coloreada no contribuía en gran medida a la atenuación de la radiación solar. *Jackson et al.* [17] indicaron que la tasa de fotosíntesis en las zooxantelas asociadas a los corales aumenta linealmente con la *PAR* hasta que los fotosistemas se saturan y se alcanza la tasa máxima. Una vez alcanzado este umbral máximo de luz se produce la fotoinhibición y el exceso de energía lumínica se disipa en forma de calor a través de varios mecanismos fotoprotectores. Si no se disipa toda la energía, se producen daños. Cuando la tasa de fotodeterioro supera a la de reparación fotoprotectora, se acumula el fotodaño y se liberan compuestos oxidativos de oxígeno en los tejidos del coral. Si las condiciones persisten, los corales expulsarán sus zooxantelas y se blanquearán. Una alta concentración de sólidos suspendidos totales puede agravar el fotodaño al reducir aún más la capacidad de absorción de *PAR*. El actual calentamiento de los océanos, la acidificación y la disminución de la calidad del agua están afectando negativamente a los ecosistemas de los arrecifes de coral y pueden provocar un cambio de régimen ecológico, ya que la resistencia de los corales a las perturbaciones sigue disminuyendo. Esto puede llevar a un cambio en la producción de DMS y en el flujo mar-aire de los arrecifes de coral, con posibles impactos en el equilibrio radiativo local. Todos estos trabajos ponen de manifiesto la necesidad de conocer y modelar la *PAR*, debido a su implicación en diferentes aspectos de la vida. La *PAR* es un factor clave para diferentes procesos energéticos, físicos y biológicos importantes en el medio ambiente, y está directamente relacionada con el cambio climático. Es preciso conocer la evolución de esta variable en el tiempo y en función de las condiciones atmosféricas.

Capítulo 1: Introducción y Objetivos

Pese a su importancia, la mayor parte de las estaciones meteorológicas terrestres no disponen de sensores para la medida de la *PAR*, por lo que, en general, es necesario abordar su cálculo a través de la determinación de la relación de la *PAR* con otras variables más habitualmente medidas. Distintos estudios publicados [18–20] en diferentes partes del mundo analizan la relación entre el flujo de fotones (Q_p), y la irradiancia global horizontal (*RaGH*), $Q_p/RaGH$. Los resultados ponen de manifiesto que la relación no es constante pero que, a efectos prácticos, la *PAR* supone entre un 45 – 50% de la *RaGH*. Diferentes autores han establecido modelos matemáticos para obtener la ratio $Q_p/RaGH$ a través de otros parámetros climáticos. De los resultados obtenidos concluyeron que apenas hay dependencias significativas de la relación $Q_p/RaGH$ con factores como la localización, estacionalidad o los efectos diurnos [21]. El estudio de dependencia de la *PAR* con las condiciones de nubosidad del cielo ha sido abordado en numerosas ocasiones, obteniendo que la ratio $Q_p/RaGH$, presenta valores más elevados en condiciones de cielo cubierto y disminuye en condiciones de cielo claro [22,23]. Este hecho es atribuible a los fenómenos de absorción y dispersión de la radiación solar a través de diferentes regiones del espectro.

Además de la modelización de la *PAR* a través de su relación directa con la *RaGH*, se han desarrollado modelos que incluyen otros parámetros y variables meteorológicas. Matemáticamente, muchos de estos modelos, están basados en regresiones lineales a partir de medidas de *RaGH* [24–26], o valores de masa óptica relativa del aire (m) [27], como variables únicas. Otros autores han modelado la *PAR* considerando la influencia simultánea de diversas variables. *Zempila et al.* [28] desarrollaron un modelo a partir de la *RaGH*, del ángulo solar zenital (Z), de la columna de vapor de agua precipitable (WV) y de la profundidad óptica de los aerosoles (AOD). *Wang et al.* [29] estimaron

Capítulo 1: Introducción y Objetivos

la *PAR* a partir del índice de claridad (k_t), la longitud del día (L_D) y el ángulo zenital (Z). *Ferrera-Cobos et al.* [30] utilizaron como variables de entrada para sus modelos la *RaGH*, la irradiancia extraterrestre (G_0), la temperatura (T) y la humedad relativa (RH).

En la mayoría de los trabajos se han analizado estas relaciones en función de las condiciones de cielo. Para cielos claros, *Mottus et al.* [31] encontraron que Z es la variable más importante y el índice de claridad (k_t) permite usar el modelo en presencia de nubes. Distintos estudios [30,32–34] destacan que la *PAR* es una variable de carácter fuertemente local de modo que los modelos desarrollados dependen de la localización geográfica donde se obtienen los datos experimentales. Como toda componente espectral de la radiación solar, la *PAR* está relacionada con las condiciones atmosféricas, representadas por los tipos de cielo. La clasificación de cielos (cubiertos, parcialmente cubiertos y claros) es un problema complejo debido a la utilización de un concepto abstracto como es la consideración de cubierto, claro o todo el rango de cielos parciales. Tradicionalmente, se han clasificado los cielos en función de la nubosidad atendiendo a distintos índices meteorológicos o combinaciones de ellos, como el índice de claridad (k_t) [32,35,36], la insolación relativa (S) [37,38], la claridad del cielo (ϵ), o el brillo del cielo (Δ) [39–42]. Es necesario tener en cuenta la capacidad limitada para clasificar cielos a partir de índices meteorológicos [43], demostrada en diferentes trabajos.

En este sentido, *Kittler et al.* [44,45] propusieron un conjunto de tipos de cielo estándar que describían distintas distribuciones angulares de luminancia en la bóveda celeste. Esta propuesta se consolidó en 2004 con el *CIE Standard General Sky* recogido en la norma ISO 15469:2004(E)/CIE S 011/E:2003 [46]. La norma ISO/CIE establece los 15 tipos de cielo que se muestran en la Tabla 1. De ellos, los cinco primeros pertenecen al grupo de cielos cubiertos, los cinco siguientes

Capítulo 1: Introducción y Objetivos

al de cielos intermedios y los últimos cinco al de claros. La Figura 1 muestra las principales características de cada tipo de cielo estándar según la norma ISO/CIE.

Tabla 1. 15 tipos de cielo clasificados según la norma ISO / CIE.

Tipo de cielo	Descripción de la distribución de luminancia
1	Cielo cubierto estándar CIE, gradación acusada y uniformidad acimutal.
2	Cubierto, con gradación pronunciada y un ligero brillo hacia el sol.
3	Cubierto, moderadamente gradado, con uniformidad azimutal.
4	Cubierto, moderadamente graduado, con un ligero brillo hacia el sol.
5	Cubierto, brumoso o nublado, con uniformidad general.
6	Parcialmente nublado, con gradación uniforme y un ligero brillo hacia el sol.
7	Parcialmente nublado, con un efecto circunsolar brillante y gradación uniforme.
8	Parcialmente nublado, bastante uniforme, con una clara corona solar.
9	Parcialmente nublado, con sol oscurecido.
10	Parcialmente nublado, con región circunsolar más brillante.
11	Cielo blanco-azulado con una clara corona solar.
12	Cielo claro estándar CIE, turbidez de baja iluminancia.
13	Cielo claro estándar CIE, atmósfera contaminada.
14	Cielo turbio sin nubes con amplia corona solar.
15	Cielo turbio blanco-azulado con amplia corona solar.

Capítulo 1: Introducción y Objetivos

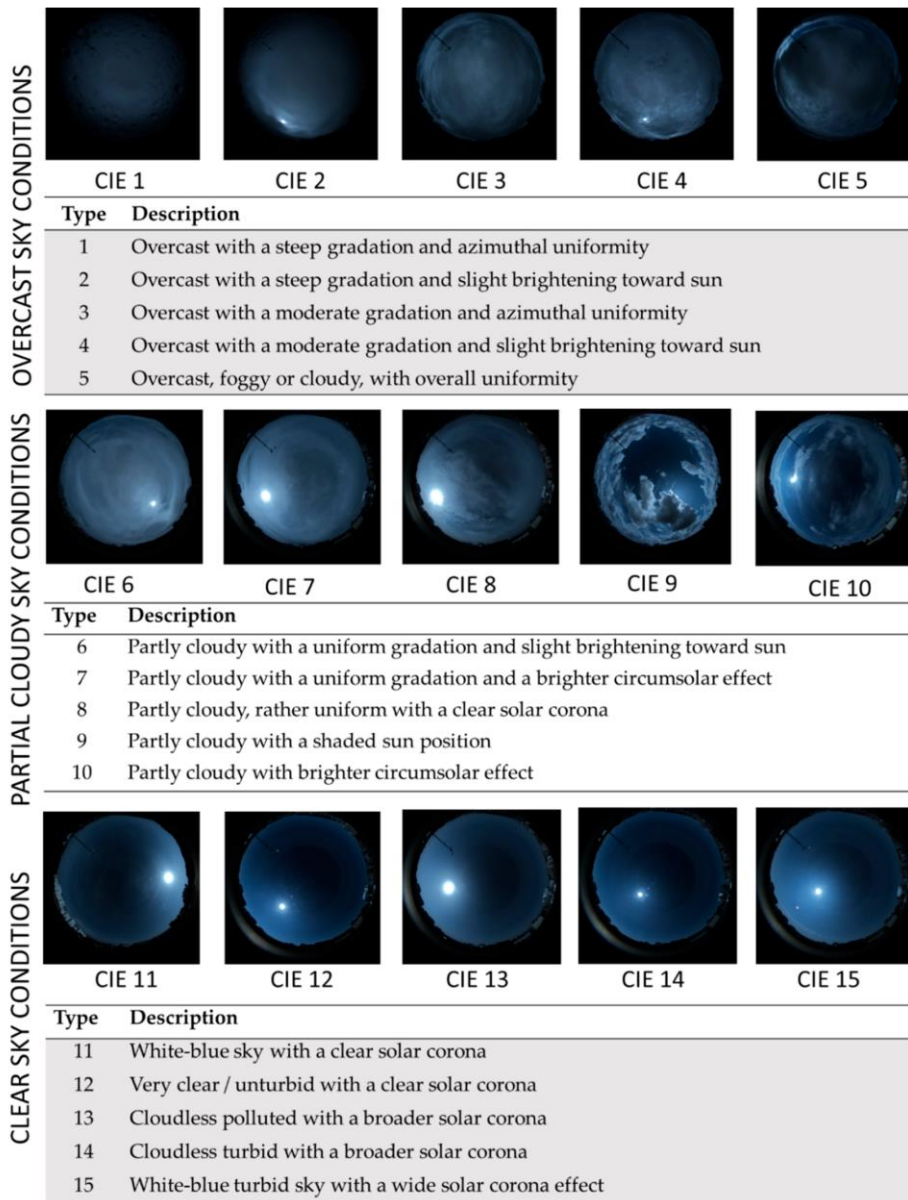


Figura 1. Condiciones de cielo estándar CIE. Imágenes de diferentes tipos de cielo grabadas con un SONA201D SONA201D All-Sky Camera—Day en Burgos, España [47].

En relación con la temporalidad de las medidas, *Frouin y Pinker* [48] observaron que, en las regiones tropicales y árticas, la proporción de *PAR* e insolación permanecía bastante constante en diferentes escalas de tiempo tanto diarias como más largas, independientemente de la

Capítulo 1: Introducción y Objetivos

nubosidad, la composición atmosférica, el tipo de superficie, la estación o la duración del día.

La inteligencia artificial se ha utilizado también para modelar la *PAR*, utilizando algoritmos supervisados, como por ejemplo, las redes neuronales artificiales (*ANN*). La principal ventaja de estos sistemas radica en que no es necesario, *a priori*, conocer las relaciones existentes entre las variables de entrada y salida, permitiendo, con el entrenamiento adecuado del sistema, generar un modelo lo suficientemente preciso para ser utilizado con datos de entrada diferentes a los del entrenamiento. *Ferrera-Cobos et al.* [30] modelaron la *PAR* en climas oceánicos y mediterráneos a través del test de 22 modelos, 11 de regresión multilínea (*MLR*) y 11 modelos basados en *ANN*, utilizando como variables de entrada la *RaGH*, la G_0 , la *T* y la *RH*. Concluyeron que zonas con diferentes condiciones climáticas necesitan diferentes modelos, ajustándose mejor los modelos para climas mediterráneos, que los modelos para climas oceánicos. Estos últimos necesitan una corrección dependiente de su localización geográfica, ya que el mayor porcentaje de humedad que existe en un clima oceánico por la presencia de agua en la atmósfera absorbe más radiación en el espectro infrarrojo aumentando la relación entre la *PAR* y *RaGH*.

Aunque el uso combinado de satélites geoestacionarios y de órbita polar es una solución óptima para estimar la *PAR*, es necesario disponer de una red terrestre de medida de *PAR* para validar los modelos [48]. *Sudhakar et al.* [25] obtuvieron un modelo de regresión de potencia para la estimación de la *PAR* en la India en 6 latitudes, entre 9° y 34°, basado en el promedio horario y mensual de la radiación global diaria. El ajuste de dicho modelo tuvo en cuenta los distintos ángulos solares, nubosidad, condiciones climáticas y su relación con la *RaGH*.

Para desarrollar los distintos modelos de *PAR*, varios autores [26,30] han utilizado datos satelitales proporcionados por la *Satellite*

Capítulo 1: Introducción y Objetivos

Application Facility on Climate Monitoring (CM-SAF), aunque para su validación ha sido necesario el uso de datos de campo. Para cubrir esa necesidad, *Vindel et al.* [49] presentaron una metodología para determinar ubicaciones óptimas para instalar estaciones de medición de *PAR*. Esta metodología se basa en un proceso de agrupamiento aplicado a la $k_{t,PAR}$, parámetro que se calcula dividiendo la *PAR* recibida en la superficie de la Tierra por la parte del espectro correspondiente a la banda de la *PAR* en la parte superior de la atmósfera (39,8% del total). *Nyamsi et al.* [50] presentaron y validaron un método de cielo despejado para estimar la *PAR* a partir del contenido total de la columna de ozono (*TOC*), del *WV* y de las propiedades ópticas de los aerosoles proporcionadas por el *Copernicus Atmosphere Monitoring Service*. El método se validó comparando sus resultados con el valor de *PAR* experimental medido cada minuto, en siete estaciones de la red *Surface Radiation* (SURFRAD) de Estados Unidos, ubicadas en localizaciones con diferentes climatologías. En todas las estaciones el coeficiente de determinación (R^2) resultó mayor de 0,97, lo que demuestra que la gran mayoría de la variabilidad temporal se reproduce bien con el método propuesto. Los autores indicaron que el modelo propuesto se puede combinar con otros que tengan en cuenta la atenuación debida a las nubes para proporcionar estimaciones de *PAR* de todo el cielo.

Ferrera-Cobos et al. [30], al comparar modelos de *MLR* y modelos basados en *ANN*, observaron que, para ambos métodos, la variable más determinante para la estimación de la *PAR* era la *RaGH*, independientemente del clima. De hecho, al realizar los modelos con *ANN*, cuando la *RaGH* no estaba incluida en ellos, dichos modelos empeoraban claramente. En este sentido *Jacovides et al.* [51] utilizaron como variables de entrada para la realización de los modelos basados en *ANN* la duración de horas de sol (nM), la *T*, la *RaGH*, la G_0 y la *RH*.

Capítulo 1: Introducción y Objetivos

Obtuvieron que la duración de la luz solar juega un papel importante a la hora de obtener predicciones de modelos aceptables, y que el modelo que mejor predice los valores de *PAR* es el que combina la *nm* y la *RaGH*.

López et al. [52] realizaron un modelo a través de datos de *PAR* obtenidos de estaciones radiométricas mediante una *ANN*, estimando la *PAR* a partir de la *RaGH* horaria como única variable de entrada. Con una segunda *ANN* se desarrolló un modelo basado en mediciones de la duración de la luz solar y se demostró que es una alternativa aceptable para calcular la *PAR*.

Pankaew et al. [53], a partir de un modelo de *ANN* cuyas variables de entrada fueron diferentes parámetros atmosféricos (coseno del ángulo de cénit solar, $\cos Z$, índice de nubosidad, *CC*, *WV*, y *AOD*), estimaron la *PAR* horaria, a partir de datos satelitales. *Qin et al.* [54] propusieron ocho modelos de inteligencia artificial, de los cuales, el obtenido a partir de una red neuronal de retropropagación (*BP*) fue el que presentó la mayor precisión. *Wang et al.* [55] propusieron tres métodos de *ANN* mejorados, (perceptrón multicapa, *MLP*, red neuronal de regresión generalizada, *GRNN*, y red neuronal de base radial, *RBNN*, para la estimación de la *PAR*, a partir de observaciones horarias a largo plazo de *PAR*, *RaGH* y diferentes variables meteorológicas (*T*, *RH*, temperatura de rocío (T_d), presión de vapor de agua (*e*), presión de aire (*P*)). Concluyeron que los diferentes parámetros meteorológicos influyen de manera diferente en la estimación de la *PAR* según los diferentes ecosistemas afectados (tierras agrícolas, tierra, bosque, bahía, pradera, desierto y lago).

1.2. Objetivos principal y parciales

El objetivo principal de este trabajo es caracterizar y **modelar la radiación fotosintéticamente activa (PAR)**. Como se ha puesto de manifiesto en la Sección anterior, la *PAR* es un parámetro clave para la obtención de biomasa, para la fotosíntesis y para la producción vegetal primaria. Los objetivos parciales planteados para obtener el objetivo principal son los siguientes:

- 1.- Análisis y estudio estadístico de la *PAR*.
- 2.- Revisión bibliográfica de modelos de *PAR* y ajuste con valores experimentales en diferentes ubicaciones.
- 3.- Modelado local de la *PAR* con diferentes índices meteorológicos para todo tipo de cielo y con diferentes categorías de cielo.
- 4.- Modelado de la *PAR* para Burgos en función de los tipos de cielo clasificados según el índice de claridad (k_t) y validación de los mismos para otras localizaciones.

Cada uno de estos objetivos parciales que completan el objetivo principal se ha materializado con la publicación de un artículo científico en una revista bajo revisión por pares e indexada en el *Journal Citation Reports*, en los primeros cuartiles de distintas categorías, como se ha indicado en la Sección Listado de Artículos de esta memoria. La interrelación entre los objetivos y los resultados obtenidos se muestra en el flujograma de la Figura 2:

Capítulo 1: Introducción y Objetivos

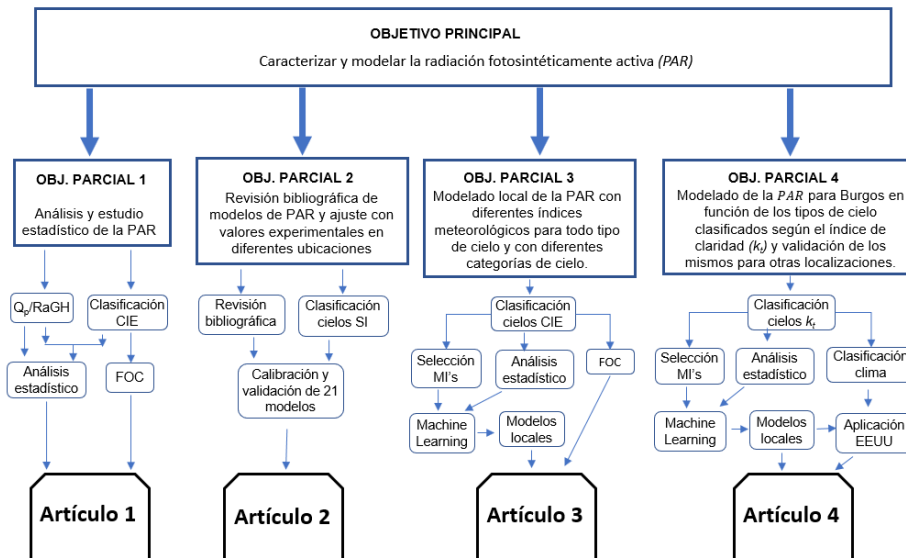


Figura 2. Flujograma con los objetivos y sus publicaciones asociadas

Este documento se estructura de la siguiente forma: en el Capítulo 1, se realiza la introducción del tema fundamental del trabajo, la *PAR*, su importancia e influencia en la fotosíntesis, el cambio climático y la producción vegetal, a través de la revisión del estado del arte. En este mismo capítulo se describe el objetivo principal y los objetivos parciales del trabajo y se incluye un breve resumen de los artículos que constituyen el trabajo. En el Capítulo 2: Resultados por Objetivos, se describe la investigación realizada para caracterizar y modelar la *PAR* de acuerdo con los artículos publicados, con los resultados obtenidos y que van conformando los objetivos parciales. Para finalizar, el Capítulo 3 recoge las conclusiones y las líneas futuras de trabajo.

1.3. Resumen de artículos

Esta tesis, presentada en la modalidad de compendio de artículos, está formada por cuatro artículos que desarrollan cada uno de los objetivos parciales.

En el artículo 1, titulado *Photosynthetic Active Radiation, Solar Irradiance and the CIE Standard Sky Classification* se analiza la relación entre la densidad de flujo de fotones fotosintéticos (Q_p) y la irradiancia global horizontal ($RaGH$) en Burgos, y su dependencia con el tipo de cielo, clasificado según la norma ISO/CIE. Posteriormente, se realiza un estudio estadístico de los datos de la relación $Q_p/RaGH$ obtenidos durante la campaña experimental desarrollada entre abril de 2019 y enero de 2020.

En el artículo 2, titulado *Validation and Calibration of Models to Estimate Photosynthetically Active Radiation Considering Different Time Scales and Sky Conditions*, se realiza, un estudio exhaustivo de la bibliografía existente de modelos matemáticos para estimar la PAR a partir de parámetros meteorológicos. Se calibran y validan 21 modelos analíticos en base minutal y horaria, considerando distintos tipos de cielo clasificados a partir del índice de cielo. Los modelos se evalúan mediante los datos experimentales de siete estaciones meteorológicas pertenecientes a la red estadounidense SURFRAD.

En el artículo 3, titulado *Modelling Photosynthetic Active Radiation (PAR) through meteorological indices under all sky conditions*, se procede al modelado matemático de la PAR en Burgos a partir de diferentes índices meteorológicos ($MI's$), para los distintos tipos de cielo, clasificados según la norma ISO/CIE. Los modelos se formulan mediante dos estrategias: modelos MLR y modelos ANN , para cada tipo de cielo, obteniendo los parámetros estadísticos necesarios para determinar la bondad de ajuste de cada modelo. Previamente se realiza

Capítulo 1: Introducción y Objetivos

una selección de variables para determinar los *MI's* mas influyentes en la *PAR*, y eliminar redundancia en la información.

En el artículo 4, titulado *Extension of local all sky conditions PAR models to different climatic zones*, se modela la *PAR* también a partir de diferentes *MI's*, utilizando el índice de claridad, k_t , para clasificar los datos según los tipos de cielo. Se realizan modelos mediante regresiones multilineales y redes neuronales, para cada tipo de cielo, a partir de datos obtenidos en Burgos, obteniendo los parámetros estadísticos necesarios para determinar la bondad de ajuste de cada modelo. Una vez obtenidos los modelos, se evalúan con los datos de las siete estaciones de la red SURFRAD, comprobando la validez de modelos ajustados localmente en otras localizaciones con diferente clima.

Capítulo 1: Introducción y Objetivos

Capítulo 2

Resultados por objetivos

La *PAR* juega un papel fundamental en la fisiología de las plantas, producción de biomasa y la iluminación de invernaderos, entre otros. La determinación de la incidencia de esta componente solar en estos importantes ámbitos precisa el conocimiento detallado de esta variable en las zonas de interés y su dependencia con las características climatológicas. El problema reside en la escasez de medidas terrestres experimentales de *PAR*. La mayoría de las estaciones meteorológicas no disponen de los sensores necesarios para medir esta componente de la radiación. Entre las estrategias para solventar este problema, la más usual consiste en modelarla a partir de otras variables o (*MI's*). Algunos de estos *MI's* se miden frecuentemente en muchas estaciones, como puede ser la irradiancia solar global, difusa o directa, o la temperatura. Otras variables se obtienen a través de expresiones matemáticas contrastadas en la literatura, y testadas con valores experimentales en varios lugares.

Los datos experimentales que se han utilizado en la tesis doctoral provienen de la instalación meteorológica del grupo de investigación *Solar and Wind Feasibility Technologies* (SWIFT) de la Universidad de Burgos. Esta instalación está situada en la azotea del edificio de la Escuela Politécnica Superior de la Universidad de Burgos (42°21'04"N, 3°41'20"O, 856 m de altura sobre el nivel del mar) (Figura 3). En la instalación, cuya imagen se puede apreciar en la Figura 4, se miden los parámetros climáticos de presión y temperatura ambiental, humedad relativa, precipitación, velocidad y dirección de viento. Adicionalmente, la instalación cuenta con numerosos sensores que permiten

Capítulo 2: Resultados por objetivos

caracterizar la radiación solar. Se incluyen registros de valores de irradiancia (piranómetro) e iluminancia global (luxómetro), densidad de flujo de fotones (photon sensor) y ultravioleta global y en las bandas A, B y E (radiómetros UV). De cada variable controlada se disponen sensores sobre plano horizontal y vertical orientadas hacia los cuatro puntos cardinales, además de medidas de las diferentes componentes de la radiación solar, global difusa y directa. En la instalación se toman medidas con una frecuencia de 30 segundos, y se almacena el valor promedio cada 10 minutos. Todas las variables se analizan y se filtran aplicando los criterios de calidad más exigentes [56]. La Tabla 2 muestra un listado de los sensores (marca y modelo) de cada tipo instalados en la estación.

Tabla 2. Marcas y modelos de los sensores instalados en la instalación.

Tipo	Medida / Orientación	Unidades	Marca	Modelo
Precipitación		<i>mm</i>	Campbell Scientific	52202
Viento		$m \cdot s^{-1}$	Campbell Scientific	03002 Wind Sentry Set
Presión		<i>mbar</i>	VAISALA	PTB110
Temperatura		$^{\circ}C$	Campbell Scientific	CS215
Irradiancia	N, E, S, O	$W \cdot m^{-2}$	K&Z	CM6b
Irradiancia	Glo, Dif, Dir	$W \cdot m^{-2}$	Hukseflux	SR12-T205
Iluminancia	N, E, S, O	<i>lx</i>	EKO	ML-020S
Iluminancia	Glo, Dif, Dir	<i>lx</i>	EKO	ML-020S
PAR	N, E, S, O	$\mu mol \cdot s^{-1} \cdot m^{-2}$	EKO	ML-020P
PAR	Glo, Dif, Dir	$\mu mol \cdot s^{-1} \cdot m^{-2}$	EKO	ML-020P
Difusa vertical	N, E, S, O	$W \cdot m^{-2}$	Hukseflux	SR11

(**N:** norte; **E:** este; **O:** oeste; **S:** sur; **Glo:** global; **Dir:** directa; **Dif:** Difusa)



Figura 3. Ubicación del equipo experimental en la azotea de la Escuela Politécnica Superior edificio de la Universidad de Burgos, España [47].



Figura 4. Vista general de la estación meteorológica y radiométrica situada en la Escuela Politécnica Superior de la Universidad de Burgos

La estación cuenta además con un *sky-scanner* comercial (EKO modelo MS-321LR) que permite obtener la distribución de radiancia y luminancia del cielo y a través de ella, la clasificación estándar CIE del cielo, que se utilizará en el trabajo como parámetro representativo de las características de la atmósfera. El sky scanner realiza un barrido de la cúpula celeste cada 10 minutos, tardando 4 minutos en realizar el barrido completo.

También se han utilizado datos experimentales de las 7 estaciones meteorológicas pertenecientes a la red SURFRAD. La ubicación de estas estaciones se muestra en la Figura 5. Las variables meteorológicas registradas en esta red y que se han empleado en el trabajo son *PAR*, *RaGH*, *RaDH*, temperatura (*T*) y humedad relativa

Capítulo 2: Resultados por objetivos

(RH). Otras variables utilizadas se han calculado a través de expresiones conocidas como la temperatura de rocío (T_d), la presión de vapor de agua (e) y el agua precipitable (WV).

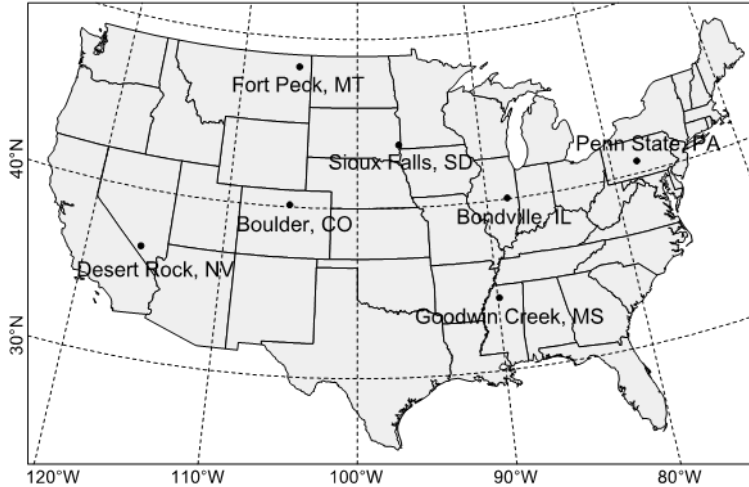


Figura 5. Ubicación de las siete estaciones meteorológicas de SURFRAD.

La red SURFRAD somete los datos de irradiación registrados por sus estaciones al procedimiento de control de calidad propuesto por la Baseline Surface Radiation Network (BSRN) y recogido en *Long y Dutton* [57]. Dicho procedimiento contempla tres niveles de control de las medidas de irradiación, pero ninguno para la *PAR*. En este trabajo, se ha establecido un criterio de control de calidad de *PAR* relativo a sus límites físicos: la *PAR* global sobre el plano horizontal no debe superar el valor de *PAR* extraterrestre sobre el plano horizontal correspondiente a ese mismo momento. *Gueymard* [58] obtuvo un valor de $1361.1 W \cdot m^{-2}$ de constante solar o irradiación solar total pero sin valor estandarizado para la irradiación en el rango espectral de la *PAR*. La curva de irradiación entre 400 y 700 nm del espectro extraterrestre propuesto por *Gueymard et al.* [59] fue integrado, para poder estimar esta constante, resultando un valor de $530.8 W \cdot m^{-2}$.

El objetivo general de la tesis, la caracterización y modelado de la *PAR*, se ha dividido en 4 tareas, que conforman cada una de ellas un objetivo

parcial de la tesis, y que se completan con los cuatro artículos publicados que recogen los resultados de la investigación realizada.

2.1. Objetivo parcial 1: *Análisis y estudio estadístico de la PAR*

El Objetivo Parcial 1, como se observa en el flujograma representado en la Figura 1, radica en conocer la variabilidad temporal y la relación de esta componente de la radiación solar con las condiciones climáticas. Este objetivo parcial se concreta en el artículo *Photosynthetic Active Radiation, Solar Irradiance and the CIE Standard Sky Classification*, publicado en *Applied Sciences*.

Como se ha comentado anteriormente, la escasez de datos experimentales de *PAR* hace necesario modelarla a partir de variables medidas habitualmente, como puede ser la *RaGH*. Muchos trabajos coinciden en que la relación $Q_p/RaGH$ es prácticamente constante y se establece una ratio $Q_p/RaGH$ que oscila entre $1,75-2,3 \mu\text{mol} \cdot \text{J}^{-1}$ [60]. En este trabajo, se evalúa la relación $Q_p/RaGH$ en Burgos y se analiza su dependencia con las características climatológicas definidas a partir de los distintos tipos de cielo y para diferentes intervalos temporales (diezminutales, horarios, diarios, mensuales, estacionales).

La revisión bibliográfica ha comprobado que la mayoría de los autores trabajan para cielos claros [31,50,61,62]. En este estudio se ha utilizado el estándar ISO/CIE para la clasificación de los cielos. Para ello, se ha caracterizado la frecuencia de aparición, *FOC*, (%), de cada tipo de cielo estándar ISO/CIE en Burgos, considerando para su clasificación la ratio de normalización (NR) introducida por *Littlefair* [63,64]. La *FOC* de cada tipo de cielo durante el periodo estudiado, desde abril de 2019 hasta enero de 2020, se muestra en la Figura 6.

Capítulo 2: Resultados por objetivos

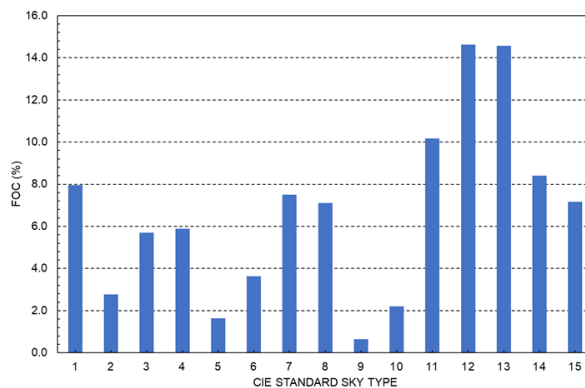


Figura 6. Frecuencia de aparición (FOC, %) de tipos de cielo estándar CIE en Burgos, España, entre abril 2019 y enero 2020 [47].

De la Figura 6 se deduce que, en la ciudad de Burgos aparecen los 15 tipos de cielo clasificados según la norma ISO/CIE. Los tipos de cielo correspondientes a las categorías 11, 12, y 13, que se describen como cielos claros, presentan una frecuencia de aparición alta, entre el 10 y 14,5%, seguidos del tipo de cielo 14, con una frecuencia del 8,4%. Los tipos de cielo 1, 7, 8 y 15 presentan valores de *FOC* en torno al 7%. Los cielos 5, 9 y 10 presentan una frecuencia muy baja, inferior al 3%.

La utilización del estándar ISO/CIE para la clasificación de cielos es poco usual en la literatura científica, puesto que esta clasificación precisa de dispositivos *sky-scanner* para poder obtener la distribución de luminancia y radiancia de la cúpula celeste [45]. Habitualmente, los cielos se clasifican, atendiendo a la nubosidad, en cielos claros, parciales y cubiertos. El estándar ISO/CIE considera cielos cubiertos los tipos de cielo 1 a 5, parciales los tipos 6 a 10 y claros los tipos 11 a 15. Otras clasificaciones que emplean la misma taxonomía (cielos claros, parciales y cubiertos) utilizan como criterio de evaluación, el valor numérico de uno o varios *MI's* combinados, estableciendo intervalos de clasificación [43]. Atendiendo a esta clasificación, la *FOC* de cada una de dichas categorías en Burgos se describe en la Figura 7. Durante la campaña de medidas, los cielos son predominantemente claros, con una *FOC* cercana al 62%; mientras que las categorías de

Capítulo 2: Resultados por objetivos

cielos cubiertos y parcialmente cubiertos tienen una frecuencia considerablemente inferior a la de los cielos claros, entorno al 20%.

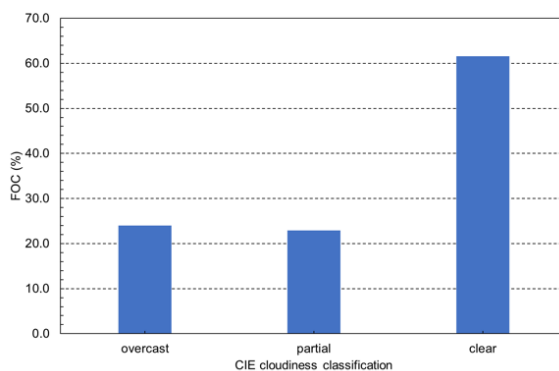


Figura 7. Frecuencia de aparición (FOC, %) de la clasificación de nubosidad CIE Burgos, España, entre abril 2019 y enero 2020 [47].

Los resultados obtenidos revelan que los cielos cubiertos predominan durante los meses de noviembre a enero y los cielos claros de mayo a octubre. Además, los cielos claros predominan en todas las horas del día, aunque las diferencias de *FOC* con respecto a los cielos cubiertos y parciales, decrecen hacia el mediodía.

Una vez conocidas las características de los cielos en la localización de medida, el trabajo ha analizado la dependencia de la ratio $Q_p/RaGH$ en base diezminutal. Se observa (Figura 8) una relación lineal prácticamente perfecta entre la Q_p y la $RaGH$, con un valor de $R^2 = 0,99$. La pendiente de la curva es $1,893 \pm 0,001 \mu mol \cdot J^{-1}$, valor que se ajusta a los datos obtenidos por otros autores [65].

Los valores $Q_p/RaGH$ se han promediado en base diezminutal, media horaria y mensual y se han analizado estadísticamente para detectar valores anómalos. Se han obtenido las gráficas de cajas y bigotes $Q_p/RaGH$ para cada una de las bases temporales analizadas.

Capítulo 2: Resultados por objetivos

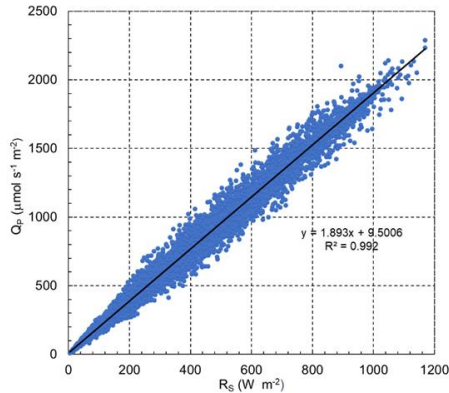


Figura 8. Densidad de flujo de fotones fotosintéticos, Q_p ($\mu\text{mol} \cdot \text{s}^{-1} \cdot \text{m}^{-2}$) e irradiancia solar de banda ancha, $RaGH$ ($W \cdot \text{m}^{-2}$) medida en Burgos, entre abril de 2019 y enero de 2020 [47].

Con respecto a la variación diaria, se observa que la relación entre ambas magnitudes va aumentando en las primeras horas del día, se estabiliza en las horas centrales y tiende a disminuir a medida que se alcanza la puesta de sol. La dispersión de los valores es mayor en las primeras y últimas horas del día frente a las centrales. Los datos mensuales son prácticamente constantes durante los meses centrales del año, de mayo a octubre, oscilando la desviación estándar entre $0,11$ y $0,16 \mu\text{mol} \cdot J^{-1}$ y el rango intercuartílico varía entre $0,10$ y $0,15 \mu\text{mol} \cdot J^{-1}$. Es de destacar que noviembre es el mes con mayor dispersión con un rango intercuartílico de $0,24 \mu\text{mol} \cdot J^{-1}$, y una desviación estándar de $0,20 \mu\text{mol} \cdot J^{-1}$. El valor máximo se obtiene en abril ($1,98 \pm 0,15 \mu\text{mol} \cdot J^{-1}$), mientras que el mínimo se alcanza en diciembre ($1,91 \pm 0,17 \mu\text{mol} \cdot J^{-1}$). La media mensual de $Q_p/RaGH$ es de $1,93 \pm 0,025 \mu\text{mol} \cdot J^{-1}$.

El siguiente estudio estadístico se realiza considerando el cociente $Q_p/RaGH$ con datos diezminutales para cada tipo de cielo clasificado según la norma ISO/CIE como se puede observar en la Figura 9. En esta gráfica se deduce que los tipos de cielo claro 12, 13, 14 y 15 muestran desviaciones estándar muy pequeñas ($0,06$ a $0,11 \mu\text{mol} \cdot J^{-1}$) y un menor rango intercuartílico. Los valores

Capítulo 2: Resultados por objetivos

más altos de $Q_p/RaGH$ se obtienen en los tipos de cielo CIE 1, 2, 3 y 4 que se corresponden con las condiciones de cielo cubierto. Los tipos de cielo 5 y 9 presentan un comportamiento anómalo. La norma ISO/CIE define estos dos tipos de cielo como cubierto y parcialmente cubierto, pero en este caso para Burgos presentan valores medios de $Q_p/RaGH$ más próximos a los valores de las categorías de cielo claro.

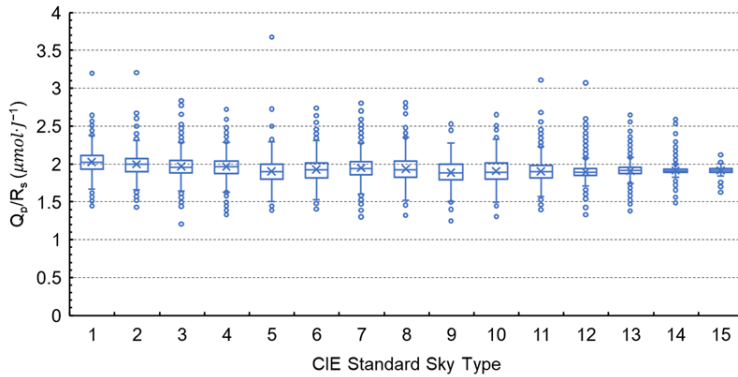


Figura 9. Diagrama de cajas y bigotes de la ratio densidad de flujo de fotones fotosintético e irradiancia solar de banda ancha ($Q_p/RaGH$) para cada tipo de cielo estandar CIE [47].

Del estudio de esta clasificación se desprende que el promedio de la relación $Q_p/RaGH$ para cielos claros y para cielos cubiertos es de $1,90 \pm 0,11 \mu\text{mol} \cdot \text{J}^{-1}$ y $1,98 \pm 0,16 \mu\text{mol} \cdot \text{J}^{-1}$, respectivamente. Los cielos parcialmente cubiertos muestran la mayor dispersión de los datos con valores de desviación estándar de 0,17 y un rango intercuartílico de $0,19 \mu\text{mol} \cdot \text{J}^{-1}$, siendo el valor medio $1,93 \mu\text{mol} \cdot \text{J}^{-1}$. Sin embargo, el conjunto de datos de cielos claros presenta el mayor número de valores atípicos.

Para concluir el análisis estadístico, se realiza el cálculo del coeficiente de correlación de Spearman, que determina la fuerza y la dirección de la correlación entre 2 variables. También en este caso se analiza la relación $Q_p/RaGH$ con la clasificación CIE, y se obtiene una correlación moderada de $-0,23$ y un p – valor $< 0,001$. Como el p – valor es inferior a 0,05 en todas las pruebas y este parámetro es el que

Capítulo 2: Resultados por objetivos

determina la significancia de los resultados con la hipótesis nula (es decir, los resultados son debidos al azar), podemos concluir que hay una diferencia estadísticamente significativa entre los promedios de la relación para cada tipo de cielo CIE, con un nivel de significancia del 5%. Cuando se analiza la correlación Spearman para la clasificación en tres tipos de cielo se obtiene un valor de 0,52 lo que califica como débil la relación entre el valor de la relación $Q_p/RaGH$ y la clasificación del cielo estándar ISO/CIE en tres categorías. Dado que los valores de la relación son más altos en condiciones de cielo cubierto y menores para cielo claro, se concluye la importancia de la presencia o ausencia de nubes en el valor del ratio $Q_p/RaGH$.

Analizada la *PAR*, su variación y su relación con la irradiancia global horizontal y el tipo de cielo, se ha conseguido cumplir el primer objetivo parcial de la tesis doctoral: ***Análisis y estudio estadístico de la PAR.***

2.2. OBJETIVO PARCIAL 2: Revisión bibliográfica de modelos de PAR y ajuste con valores experimentales en diferentes ubicaciones.

El Objetivo Parcial 2 consiste en determinar los diferentes modelos de *PAR* desarrollados hasta el momento, a través de una rigurosa revisión bibliográfica. Este objetivo se completa con un análisis pormenorizado de la bondad estos modelos mediante su aplicación a los datos experimentales obtenidos de 7 estaciones pertenecientes a la red SURFRAD, que incluye estaciones situadas en localizaciones con diferentes condiciones climáticas según la clasificación Köppen [66]. Este objetivo parcial se concreta en el artículo *Validation and Calibration of Models to Estimate Photosynthetically Active Radiation Considering Different Time Scales and Sky Conditions*, trabajo actualmente en proceso de revisión en la revista *Advances in Space Research*.

Capítulo 2: Resultados por objetivos

La revisión bibliográfica realizada ha permitido seleccionar 21 modelos de *PAR* desarrollados en distintas ubicaciones, con diferentes escalas temporales. La selección de los modelos se ha realizado atendiendo a las variables disponibles en las estaciones meteorológicas seleccionadas. Estos modelos se describen en la Tabla 3, donde se muestra la expresión matemática del modelo y la referencia bibliográfica de la que se ha obtenido.

Distintos autores manifiestan que la validez de los modelos depende de las características meteorológicas estacionales y geográficas del lugar para el que se desarrolla el modelo [30,32–34].

Los modelos seleccionados se desarrollaron originalmente para datos con diferente resolución temporal, en concreto, para valores diezminutales y mensuales.

Tabla 3. Modelos evaluados para la estimación de la *PAR*.

Modelo	EXPRESIÓN	REF.
M1	$PAR = G(a_1 \ln \epsilon + b_1 \ln \Delta + c_1 T_d + d_1 \cos^2 \theta_z + f_1)$	[42]
M2	$PAR = G(a_2 \ln \epsilon + b_2 \ln \Delta + c_2 \cos^2 \theta_z + d_2)$	[42]
M3	$PAR = G(a_3 \ln k_T + b_3 T_d + c_3 \cos \theta_z + d_3)$	[42]
M4	$PAR = G(a_4 \ln k_T b_4 \cos \theta_z + c_4)$	[42]
M5	$PAR = G(a_5 \ln k_T + b_5)$	[50]
M6	$PAR = G[a_6 (\ln k_T)^2 + b_6 \ln k_T + c_6]$	[67]
M7	$PAR = G(a_7 \ln k_d + b_7 \ln \Delta + c_7)$	[67]
M8	$PAR = G[a_8 (\ln k_T)^2 + b_8 \ln k_T + c_8 T_d + d_8]$	[67]
M9	$PAR = G[a_9 (\ln k_T)^2 + b_9 \ln k_T + c_9 \cos \theta_z + d_9]$	[67]
M10	$PAR = G[a_{10} (\ln k_T)^2 + b_{10} \ln k_T + c_{10} T_d + d_{10} \cos \theta_z + f_{10}]$	[67]
M11	$PAR = G(a_{11} \ln \epsilon + b_{11} \ln \Delta + c_{11} \ln w + d_{11} \cos \theta_z + f_{11})$	[68]
M12	$PAR = G(a_{12} \ln \epsilon + b_{12} \ln \Delta + c_{12} \cos \theta_z + d_{12})$	[68]
M13	$PAR = G(a_{13} \ln k_T + b_{13} w + c_{13} \cos \theta_z + d_{13})$	[68]
M14	$PAR = (a_{14} k_T + b_{14} k_T^2 + c_{14} k_T^3 + d_{14}) (\cos \theta_z)^{f_{14}}$	[29]
M15	$PAR = a_{15} k_T \cos \theta_z$	[65]
M16	$PAR = a_{16} G + b_{16}$	[69]
M17	$PAR = a_{17} G + b_{17} k_T + c_{17}$	[69]
M18	$PAR = a_{18} G + b_{18} k_T + c_{18} \cdot e + d_{18}$	[69]
M19	$PAR = G(a_{19} \ln k_T + b_{19} \ln m + c_{19} \cdot e + d_{19})$	[70]
M20	$PAR = a_{20} \cdot G + b_{20} G \cos \theta_z + c_{20} G k_T + d_{20}$	[71]
M21	$PAR = a_{23} k_T \cos \theta_z + b_{23}$	Variación M15

Las primeras mediciones de radiación de la red SURFRAD se tomaron en 1995 y las últimas, en 2003. Con el objetivo de comparar series temporales paralelas, en este trabajo se ha considerado la serie de registros comprendida entre 2004 y 2018.

Capítulo 2: Resultados por objetivos

Los datos de las estaciones radiométricas se registran minutalmente y se clasifican según el tipo de cielo utilizando para la clasificación el índice de cielo propuesto por Igawa [2]. Este índice considera 5 tipos de cielo atendiendo a los intervalos mostrados en la Tabla 4.

Tabla 4. Clasificación del cielo según el índice del cielo (SI) propuesto por Igawa

Clasificación de cielos	Índice de Cielo (SI)
Cielo Claro (Claro)	< 0.15
Cielo Intermedio-Claro (I-Claro)	$0.15 \leq SI < 0.3$
Cielo Intermedio (Intermedio)	$0.3 \leq SI < 0.9$
Cielo Intermedio-Cubierto (I-Cubierto)	$0.9 \leq SI < 1.15$
Cielo Cubierto (Cubierto)	$SI \geq 1.15$

Para conseguir homogeneidad, todos los modelos se ajustan para valores de PAR , medidos en $W \cdot m^{-2}$, adaptando los modelos originales que en algunos casos proponen el cálculo de la relación $PAR/RaGH$. El estudio se realiza tanto en base minutal como en base horaria.

Los modelos se ajustan de forma global con los datos de todas las estaciones, empleando el 50% de los datos experimentales para calibrar el modelo y determinar los coeficientes propios del modelo en cada localización y el 50% de datos restante para la comprobación de la bondad del modelo. La distribución del conjunto de datos experimentales entre el conjunto de calibración y el de prueba se realiza arbitrariamente. Los indicadores estadísticos tradicionales, coeficiente de determinación (R^2), error cuadrático medio ($RSME$), el error cuadrático medio relativo ($RMSEr$), la desviación relativa estándar (RSD) y error de porcentaje medio (MPE) se emplean como indicadores de la calidad del ajuste.

La Figura 10 muestra todos los parámetros estadísticos obtenidos para los 21 modelos para el caso del ajuste en base minutal. En la figura se observa que, en general, todos los modelos presentan muy buen ajuste, con valores de R^2 mayores del 0,99 y con unas desviaciones relativas estándar siempre inferiores al 12%. Los valores de $RMSEr$, son bajos, comprendidos entre 3,9 y 5 %. Los modelos $M15$ y $M21$ presentan los

Capítulo 2: Resultados por objetivos

mayores valores de $RMSEr$, por encima del 4%, y el valor mayor de desviación, próximo al 12%, se obtiene para el modelo $M15$.

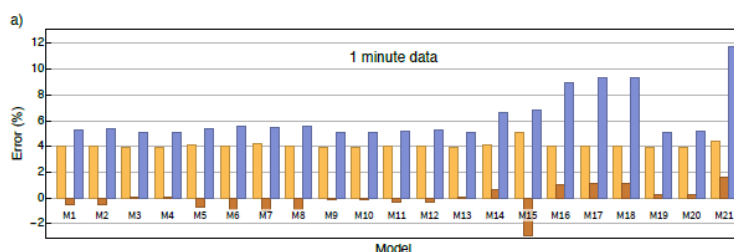


Figura 10. Resultados estadísticos de los modelos para datos de entrada de 1 minuto.

A continuación, se evalúa el comportamiento de los modelos calibrados a partir de los registros minutales, al utilizarlos con datos horarios. Los valores obtenidos del $RMSEr$ están comprendidos entre 3,6 y 4,7% y como ocurre con los datos minutales, solo los modelos $M15$ y $M21$ presentan valores ligeramente superiores.

Por último, se ha analizado la bondad de los distintos modelos cuando se tienen en cuenta las características de cielo. En este trabajo, la clasificación del cielo distingue las 5 categorías mostradas en la Tabla 4.

El ajuste de los diferentes modelos mejora cuando los datos están previamente clasificados, especialmente en el caso de cielos claros, intermedios-claros e intermedios, en el que los estadísticos de error presentan valores ligeramente inferiores. Es significativo que, en el caso de cielos intermedios-claros, los modelos $M15$ y $M21$ muestran un peor comportamiento, siendo los valores de RSD próximos al 8%, y particularmente el modelo $M21$ alcanza un valor cercano al 12% para cielos intermedios.

Para cielos intermedios-cubiertos y cubiertos, los modelos obtienen valores de RSD y de MPE superiores al resto de tipos de cielo. Para cielos intermedios-cubiertos los valores de RSD que se obtienen para la desviación de los modelos $M14$, $M16$, $M17$, $M18$ y $M21$ son relativamente altos, comprendidos entre el 15 y 30%. En el caso de

Capítulo 2: Resultados por objetivos

cielos cubiertos, cuando no se tiene en cuenta la irradiancia global o está integrada en la ecuación lineal como ocurre en los modelos *M15*, *M16*, *M17*, *M18* y *M21*, los errores estadísticos presentan gran variación, con valores de *RMSE_r* entre 7 y 10% y valores de *RSD* entre el 10 y 30%. Es destacable el comportamiento del modelo *M21* con un *MPE* próximo al 15%.

En resumen, se puede concluir que, en general, todos los modelos predicen con precisión el valor de *PAR* en condiciones de cielo claro y empeoran la predicción a medida que aumenta la presencia de nubes. En definitiva, la selección de un modelo de *PAR* u otro debe realizarse fundamentalmente en base a las variables disponibles para el cálculo y atendiendo a la predominancia o no de cielos claros en la localización. Con este trabajo se ha completado el segundo objetivo de la tesis doctoral: ***Revisión bibliográfica de modelos de PAR y ajuste con valores experimentales en diferentes ubicaciones.***

2.3. OBJETIVO PARCIAL 3: *Modelado local de la PAR con diferentes índices meteorológicos para todo tipo de cielo y con diferentes categorías de cielo.*

El siguiente objetivo parcial trata de modelar la *PAR* en Burgos a partir de los datos experimentales disponibles utilizando diferentes estrategias y atendiendo a las características climáticas. Este objetivo se concreta en el artículo *Modelling Photosynthetic Active Radiation (PAR) through meteorological indices under all sky conditions* publicado en *Agricultural and Forest Meteorology*.

Muchos de estos modelos, desarrollados y validados para diferentes puntos geográficos, emplean regresiones lineales y multilineales para estimar la *PAR*, utilizando como variables meteorológicas la turbidez, nubosidad, contenido de agua atmosférica y aerosoles, claridad y brillo del cielo, fracción difusa, la temperatura del punto de rocío y el ángulo

Capítulo 2: Resultados por objetivos

zenital solar, entre otras [32,42,55,67]. La mayor parte de los trabajos revisados, destacan una gran dependencia local en la respuesta de los modelos, lo que requiere una recalibración local para su empleo en ubicaciones diferentes a la del trabajo original [30,32–34].

Los $MI's$ disponibles para el modelado de la PAR que se incluyen en este estudio son: índice de claridad (k_t), fracción difusa (k_d), fracción directa (k_b), claridad del cielo (ε), brillo del cielo (Δ), nubosidad (CC), temperatura del aire (T), presión (P), coseno azimutal solar ($\cos Z$) e irradiación global horizontal ($RaGH$). A partir de estas variables se obtienen el resto de $MI's$ a utilizar en los modelos propuestos. Además de las variables meteorológicas y radiativas, se realiza la determinación del tipo de cielo CIE cada 10 minutos, siguiendo el procedimiento descrito en trabajos anteriores [43,72,73].

La campaña experimental abarca desde abril de 2019 hasta enero de 2021. Los datos de Q_p ($\mu mol \cdot m^{-1} \cdot s^{-1}$) se han transformado a valores de PAR ($W \cdot m^{-2}$) a través del factor de conversión de McCree [3].

La FOC de cada tipo de cielo CIE en Burgos durante la campaña experimental, se muestra en la Figura 11. Como se ha demostrado en trabajos anteriores [47], los tipos de cielo predominantes son los pertenecientes a la categoría de cielos claros, cielos del 11 al 14.

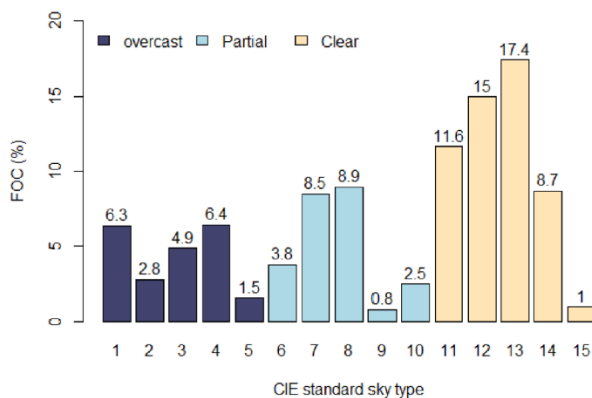


Figura 11. Frecuencia de aparición (FOC , %) de los tipos de cielo estándar CIE en Burgos, España, entre abril de 2019 y febrero de 2021 [74].

Capítulo 2: Resultados por objetivos

Los datos anómalos en el conjunto de datos experimentales se determinan a través de un diagrama de bigotes y cajas de los diferentes $MI's$ utilizados en función de los tipos de cielo. Este proceso elimina el 10% de los datos iniciales. En estas gráficas, se observa que T, P y $\cos Z$ no están influenciados por el tipo de cielo, mientras que $CC, k_t, k_d, k_b, \varepsilon$ y Δ son muy dependientes de las condiciones del cielo. En la Figura 12, en la que se muestra el diagrama de cajas y bigotes de CC , con los datos antes de eliminar los valores atípicos (izquierda) y una vez eliminados dichos datos atípicos (derecha), se puede apreciar que la eliminación de los valores “no válidos” es importante ya que modifican los valores estadísticos y tiene su repercusión en los resultados que se obtienen al comparar los datos modelados y los experimentales.

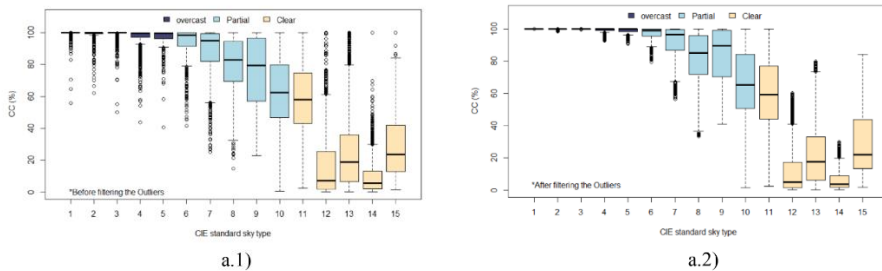


Figura 12. Análisis estadístico de la cobertura de nubes (CC) frente al tipo de cielo estandar CIE: antes (1.) y después (2) de filtrar los valores atípicos [74].

La selección de los $MI's$ con mayor relevancia en la estimación de la PAR , independientemente de las condiciones de cielo se lleva a cabo a través del coeficiente de correlación de Pearson (r). En la Figura 13 se puede observar cómo la $RaGH$ es la variable que más influye en la PAR con una correlación muy fuerte, mientras que se establece una correlación simplemente fuerte entre PAR y los siguientes $MI's$: ε, k_t y $\cos Z$, con valores de $r > 0,7$. El resto de los índices presenta una relación moderada, débil o insignificante, por lo que estos se descartan como variables para modelar la PAR . Este mismo análisis se repite considerando, en lugar de los 15 tipos de cielo CIE, la

Capítulo 2: Resultados por objetivos

agrupación de los mismos en tres categorías, cielos claros, parciales y cubiertos. Los resultados se recogen en la Tabla 5.

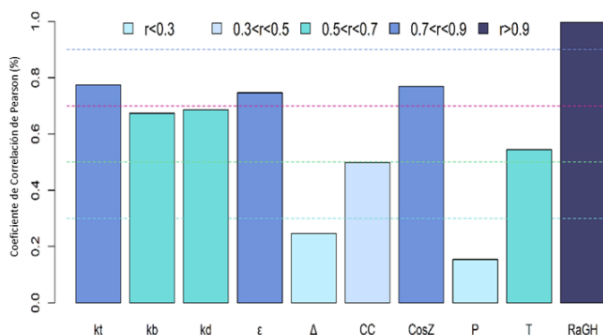


Figura 13. El coeficiente de correlación de Pearson ($r(PAR, MI_i)$) calculado para los 10 MI's utilizados en este estudio [74].

Tabla 5. El coeficientes de correlación de Pearson o Pearson $r(PAR, MI)$ teniendo en cuenta las condiciones de cielo definidas por la clasificación del cielo estándar (cubierto, parcial y claro) [74].

Tipo de cielo CIE	$ r(PAR, MI_i) $				
	[1-0.9]	(0.9-0.7]	(0.7-0.5]	(0.5-0.3]	(0.3,0]
Cubierto	RaGH	k_t, Δ	cosZ	k_b, ε	P, T,
Parcial	RaGH,	cosZ	k_t, ε	k_b, T	CC, P,
Claro	RaGH, cosZ	ε	$k_t,$	k_b, T	

Como se puede observar en la Tabla 5, nuevamente la RaGH es la variable que más influye en el modelado de la PAR, independientemente de las condiciones de cielo, con una correlación muy fuerte, mientras que cosZ muestra una correlación muy fuerte con la PAR solo para cielos claros. Los índices que tienen una correlación fuerte son ε para cielos claros, cosZ para cielos parciales, y k_t y Δ en condiciones de cielo cubierto. El factor de brillo Δ , que presenta correlaciones débiles con PAR cuando los datos no están agrupados, en este caso destaca su fuerte correlación en cielos cubiertos. Una vez determinados qué índices son los más relevantes según la categoría de cielo, con un $r > 0,7$, se procede al modelado de la PAR mediante MLRs.

Capítulo 2: Resultados por objetivos

Para obtener los modelos mediante *MLR*, se dividen los datos experimentales en 2 grupos, uno con el 85% para ajustar los modelos y el 15% restante, para validarlos. La comparación entre los valores de *PAR* obtenidos por el modelo y los experimentales se hace a través de tres parámetros estadísticos: el coeficiente de determinación (R^2), error de sesgo medio normalizado (*nMBE*), el error cuadrático medio normalizado (*nRMSE*) y error absoluto medio normalizado (*nMAE*). En la Tabla 6 se muestran los modelos *MLR* y en la Tabla 7 los valores de los parámetros estadísticos obtenidos para cada tipo de cielo

Tabla 6. Modelos de regresión multilínea de la *PAR* (modificado a partir de [74]).

Condiciones del cielo	Modelos de regresión multilínea
MLR1 (claros)	$PAR = 0.3806 \cdot RaGH + 0.524 \cdot \varepsilon + 33.247 \cdot \cos Z - 2.646$
MLR 2 (parciales)	$PAR = 0.3958 \cdot RaGH + 18.282 \cdot \cos Z - 2.508$
MLR 3 (cubiertos)	$PAR = 0.4335 \cdot RaGH - 7.726 \cdot kt - 9.078 \cdot \Delta + 4.065$

Tabla 7. Resultados estadísticos de los modelos de regresión multilínea (modificado a partir de [74]).

Condiciones de cielo	R^2	<i>nRMSE</i> (%)	<i>nMAE</i> (%)	<i>nMBE</i> (%)
MLR 1 (claros)	0,991	3,93	2,72	$-2,10 \cdot 10^{-6}$
MLR 2 (parciales)	0,976	7,81	5,04	$-2,10 \cdot 10^{-6}$
MLR 3 (cubiertos)	0,985	6,62	4,44	$-5,10 \cdot 10^{-6}$

Otra estrategia utilizada en el trabajo para modelar la *PAR* a través de *MI's* es la utilización de *ANN*. Nuevamente, se realiza una clasificación previa de los datos en función de las características del cielo distribuidos en tres categorías según el estándar ISO/CIE (claros, parciales y cubiertos) y se utilizan como variables de entrada a la *ANN* los *MI's* seleccionados previamente a través del coeficiente de Pearson. Se programa una *ANN* entrenada con el algoritmo Levenberg-Marquardt Back-Propagation (*LMBP*) [75] compuesta por 3 capas:

Capítulo 2: Resultados por objetivos

capa de entrada, capa oculta y capa de salida. En la Figura 14 se muestra la estructura de una red neuronal.

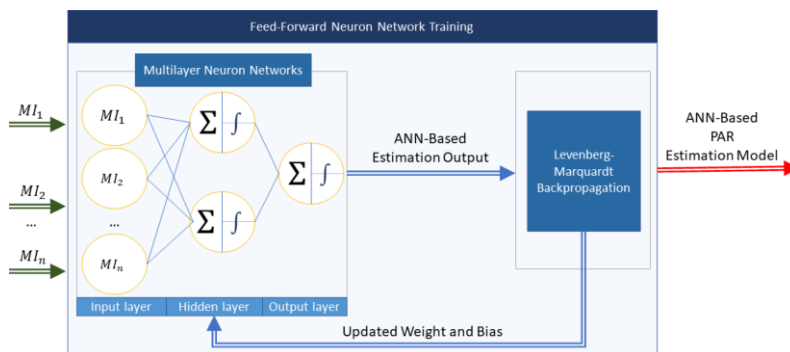


Figura 14. Arquitectura del sistema de red neuronal artificial mediante el algoritmo de retropropagación de Levenberg-Marquardt [74].

El conjunto de datos de entrada de una ANN se divide en tres grupos: un grupo de entrenamiento (con el 70% de los datos), un conjunto de datos de validación (15% de los datos) y un conjunto de datos de prueba (15% de los datos). El entrenamiento y los grupos de validación se han establecido dividiendo el conjunto de datos de ajuste utilizado en el modelo *MLR*. El grupo de entrenamiento se utiliza para determinar, en un proceso iterativo, la matriz ponderada y el sesgo. En este caso el entrenamiento termina cuando los resultados del rendimiento del modelo resultante, calculado utilizando el conjunto de validación, alcanza la calidad deseada. El grupo de datos de prueba se utiliza para calcular la bondad del modelo. Dicho conjunto de datos coincide con el utilizado para la validación de los modelos *MLRs*.

Obtenidos y validados los diferentes modelos para cada tipo de cielo se procede al test de los mismos utilizando el mismo grupo de datos experimentales que se empleó en el test de los modelos de regresión. En la Tabla 8 se recogen los valores de los parámetros estadísticos obtenidos. Se puede ver que todos los valores de $R^2 > 0,97$ y los valores de $nRMSE$ están todos por debajo del 8%. Se puede destacar que, para cielos claros, se obtienen los valores menores de $nRMSE$. Los

Capítulo 2: Resultados por objetivos

valores de $nMBE$ son prácticamente insignificantes en todos los casos, aunque su valor negativo muestra que todos los modelos tienden a subestimar los valores de PAR .

Tabla 8. Resultados estadísticos de los modelos de redes neuronales [74].

Condiciones del cielo	R^2	nRMSE (%)	nMAE (%)	nMBE (%)
ANN1 (claros)	0.992	3.846	2.59	$-2.10 \cdot 10^{-6}$
ANN2 (parciales)	0.976	7.795	5.00	$-3.10 \cdot 10^{-6}$
ANN3 (cubiertos)	0.987	6.466	4.34	$-5.10 \cdot 10^{-6}$

Se puede concluir que ambos procedimientos para estimar la PAR , mediante MLR y mediante ANN , se ajustan muy bien para las 3 categorías de cielo establecidas: claro, parcial y cubierto. Es de destacar que la categoría de cielos para la que mejor se ajustan los modelos, tanto las $MLRs$ como las ANN , es la de cielos claros con valores de R^2 mayores del 0.99 y de $nRSME$ menores del 4% en ambos casos.

Una vez obtenidos diferentes modelos para diferentes tipos de cielo que nos permiten obtener valores de PAR con un buen ajuste para Burgos, se ha conseguido el tercer objetivo parcial de la tesis: ***Modelado local de la PAR con diferentes índices meteorológicos para todo tipo de cielo y con diferentes categorías de cielo.***

2.4. Objetivo parcial 4: Modelado de la PAR para Burgos en función de los tipos de cielo clasificados según el índice de claridad (k_t) y validación de los mismos para otras localizaciones.

El último Objetivo Parcial de la tesis incide en el estudio del carácter local de los modelos de PAR . Este objetivo se concreta en el artículo *Extension of local all sky conditions PAR models to different climatic zones*, publicado en *Applied Sciences*. Se desarrollan nuevos modelos de PAR basados en MI 's a través de $ANNs$ y $MLRs$, que se calibran y

Capítulo 2: Resultados por objetivos

validan en Burgos gracias a los datos experimentales disponibles. Los modelos desarrollados tienen en cuenta las condiciones del cielo utilizando como parámetro para su clasificación el índice de claridad, k_t , parámetro tradicionalmente empleado para esta caracterización [43]. La ventaja de usar el índice de claridad es que se puede obtener en la mayoría de las estaciones meteorológicas y se permite la clasificación de los cielos en tres categorías.

Los modelos se desarrollan utilizando tanto *MLRs* como *ANNs*, siguiendo los procedimientos ya descritos en la Sección 2.3. La diferencia radica en los *MI's* seleccionados como entradas a los modelos. Los modelos desarrollados para Burgos, se aplican utilizando los datos experimentales obtenidos de las estaciones de la red SURFRAD, red que se ha utilizado también en la Sección 2.2. En este trabajo, se van a utilizar los *MI's* disponibles en esta red que coinciden con los que se registran o se pueden calcular en Burgos, y que se resumen en la Tabla 9. Todas las variables y datos meteorológicos se utilizan en base diezminutal. Los datos de la estación de Burgos se obtienen directamente en esta base temporal, mientras que los datos de las estaciones de la red SURFRAD, registrados minutalmente, se promedian cada diez minutos para realizar la transformación de la base temporal.

Capítulo 2: Resultados por objetivos

Tabla 9. Índices meteorológicos medidos en Burgos [76].

<i>MI</i>	<i>MI</i>	Expresión
<i>RaGH</i>	Radiación global horizontal	Medida directamente
k_d	Fracción horizontal difusa	$k_d = \frac{RaDH}{RaGH}$
Q_p	Densidad de flujo de fotones fotosintéticos	Medida directamente
<i>PAR</i>	Radiación fotosintéticamente activa	$PAR = Q_p/4.57\mu\text{mol} \cdot \text{J}^{-1}$
k_t	Índice de claridad	$k_t = \frac{RaGH}{B_{sc} \cdot \varepsilon_0 \cdot \cos Z_s}$
<i>T</i>	Temperatura del aire	Medida directamente
<i>P</i>	Presión	Medida directamente
T_d	Temperatura del punto de rocío	$T_d = \frac{35.859 \cdot \log P_v - 21.48496}{\log P_v - 10.2858}$
<i>cosZ</i>	Coseno azimuth solar	$\cos Z = \sin \delta \cdot \sin \phi + \cos \delta \cdot \cos \phi \cdot \cos \omega$
ε	Índice de claridad	$\varepsilon = \frac{\frac{RaDH + RaB}{RaDH} + 1.04 \cdot Z_s^3}{1 + 1.04 \cdot Z_s^3}$
Δ	Factor de brillo	$\Delta = \frac{m \cdot RaDH}{B_{sc} \cdot \varepsilon_0 \cdot \cos Z_s}$

La selección de variables a través del coeficiente de correlación de Pearson, con mayor relación con la *PAR*, se realiza con los datos experimentales de Burgos incluyendo todos los tipos de cielo. Un segundo análisis se realiza clasificando previamente los datos en función de los tipos de cielo atendiendo al valor del k_t . Los resultados del análisis se muestran en la Tabla 10.

Capítulo 2: Resultados por objetivos

Tabla 10. Coeficiente de Pearson, $r (PAR, MI_i)$ basado en las condiciones de cielo definidas por la clasificación de cielo de k_t (claro, parcial y cubierto) [76].

Intervalos (k_t)	$ r (PAR, MI_i) $				
	[1-0.9]	(0.9-0.7]	(0.7-0.5]	(0.5-0.3]	(0.3,0]
Todo tipo de cielo	$RaGH$	$cosZ, k_t$	k_d, ε	T	Δ, P, T_d
Claro	$RaGH, cosZ$		k_t, ε	T	k_d, Δ, P, T_d
Parcial	$RaGH, cosZ$			T	$k_t, k_d, \Delta, \varepsilon, P, T_d$
Cubierto	$RaGH$	$cosZ$	k_t, Δ		$k_d, \varepsilon, P, T, T_d$

Como es previsible, se observa que la $RaGH$ es el parámetro que más influye, independientemente del tipo de cielo. $cosZ$ tiene una muy fuerte relación para cielos claros y parciales y fuerte para todo tipo de cielo y para cielos cubiertos. Los índices k_t , k_d , ε y Δ , presentan una relación más débil en general, salvo para los cielos parciales en los que no hay ningún efecto sobre el valor de PAR .

A partir de los valores experimentales recogidos en la estación de Burgos se han desarrollado modelos de medida de la PAR mediante $MLRs$ y ANN . Para calibrar los modelos basados en regresiones multilineales, se utilizan el 85% de los datos lo que permite calcular los coeficientes de cada modelo. Para comprobar la bondad de los modelos se utiliza el 15% restantes de los valores experimentales. La bondad de los modelos se determina a través de los siguientes parámetros estadísticos: R^2 , $nMBE$ y $nRMSE$.

Los resultados del modelo, aplicados al conjunto de datos experimentales de test disponibles, se muestran en la Tabla 11. Todos los modelos presentan valores de R^2 entre 0,97 y 0,99. Los valores de $nRMSE$ en todas las categorías de cielo están por debajo del 7,5%.

Capítulo 2: Resultados por objetivos

Tabla 11. Modelos de regresión multilineal de la PAR [76].

Condiciones del cielo	R^2	nRMSE (%)	nMBE (%)
MLR1 (Todos los tipos)	0.994	4.37	$-2.74 \cdot 10^{-13}$
MLR2 (Cielos claros)	0.990	3.27	$-1.45 \cdot 10^{-14}$
MLR3 (Cielos parciales)	0.977	6.80	$-5.32 \cdot 10^{-13}$
MLR4 (Cielos cubiertos)	0.978	7.33	$1.87 \cdot 10^{-13}$

Los modelos basados en *ANN* se han entrenado mediante el algoritmo Levenberg-Marquardt Back-Propagation (*LMBP*) [75] para cada categoría: todo tipo de cielos, claros, parciales y cubiertos, usando los índices que más influencia han demostrado en la *PAR* a través del coeficiente de Pearson (Tabla 10). En este caso, se divide en dos grupos el 85% de los datos experimentales que conformaban en conjunto de calibración para los modelos *MLR*. Uno de estos grupos, que comprende el 70% de los datos, se usa para el entrenamiento de la *ANN*, mientras que el 15% restante se emplea para la validación del modelo. El mismo conjunto de datos empleado anteriormente para la determinación de la bondad del modelo, se emplea para testar la fiabilidad del modelo *ANN*. Los resultados de estas pruebas, arrojan valores de R^2 superiores al 0,97 y valores de *nRMSE* inferiores al 8%.

Una vez obtenidos los modelos en Burgos, cuya climatología corresponde con un tipo *Csb* (clima Mediterraneo oceánico), según la clasificación climática Köppen [66], se evalúan con los datos de las siete estaciones meteorológicas de la red SURFRAD. En la Tabla 12 se muestra la clasificación Köppen de cada una de las localizaciones analizadas.

Capítulo 2: Resultados por objetivos

Tabla 12. Condiciones climáticas de las siete estaciones americanas (modificado a partir de [76]).

Estaciones	Clima
Bondville, Illinois	Dfa
Table Mountain, Boulder, Colorado	Bsk
Desert Rock, Nevada	Bwh
Fort Peck, Montana	Bsk
Goodwin Creek, Mississippi	Cfa
Penn State, Univ. Pennsylvania	Dfb
Sioux Falls, South Dakota	Dfa

(**Dfa**: continental húmedo de verano cálido; **Bsk**: semiárido frío; **Bwh**: árido desértico; **Cfa**: subtropical húmedo; **Dfb**: continental húmedo de verano moderado)

Los resultados obtenidos por los modelos, tanto *MLR* como *ANN* en las estaciones meteorológicas de la red SURFRAD, presentan valores de $R^2 > 0,99$ y valores de *nRMSE* inferiores al 7%. Se observa que, para cielos claros, para ambos procedimientos se obtienen valores de $R^2 > 0,98$ y *nRMSEs* aún más bajos, ya que en ninguna estación se obtienen valores de *nRMSE* $> 6\%$. Cuando se analizan los cielos parciales, el valor de R^2 está también por encima del 0,99 y los errores (*nRMSE* y *nMBE*) son menores del 9,5%. Por último, con los cielos cubiertos siguen ajustándose muy bien los modelos con valores de $R^2 > 0,98$. Sin embargo, hay que destacar que los *nRMSEs* obtenidos con los modelos *MLR* son menores del 8%, pero con los modelos *ANN* en la estación Desert Rock, de clima árido, se alcanza un *nRMSE* de 11,07%, relativamente grande frente al resto.

Al analizar los resultados según zonas climáticas, apenas se observa diferencias en los valores de R^2 , encontrándose todos por encima de 0,980. El mayor error *nRMSE* se obtiene para cielos cubiertos y se corresponde con la zona desértica (Bwh), zona climática muy diferente a la de Burgos, mientras que el menor *nRSME* se da en zonas continentales (Dfb y Dfa) con cielos claros. En resumen, las

Capítulo 2: Resultados por objetivos

características locales de la *PAR*, se atenúan cuando los modelos desarrollados incluyen las variables adecuadas.

Con este trabajo, se se ha conseguido el cuarto objetivo parcial de la tesis: ***Análisis de la localidad de los modelos de PAR.***

Capítulo 3: Conclusiones y líneas de futuro

3.1. Conclusiones

El objetivo general de esta Tesis es **modelar la radiación fotosintéticamente activa (PAR)**. Este objetivo se ha conseguido a través de cuatro objetivos parciales materializados en 4 artículos publicados en revistas científicas indexadas en JCR.

Como primera conclusión, se ha demostrado una dependencia representativa entre la relación $Q_p/RaGH$ y las condiciones de tipo de cielo clasificadas según la propuesta de la norma ISO/CIE. Los valores más altos de esta relación corresponden a cielos cubiertos, mientras que los valores más bajos y dispersos corresponden a cielos claros.

La *PAR* no presenta ninguna tendencia diaria o estacional característica, siendo las condiciones de cielo y la presencia de nubes el parámetro que más influye en su ratio con respecto a la irradiancia global horizontal.

Se ha realizado una exhaustiva revisión de los modelos de *PAR* global existentes. Todos los autores indican un fuerte carácter local de esta componente de la radiación solar.

Todos los modelos, existentes y los desarrollados en este trabajo, presentan los mejores resultados para predecir el valor de la *PAR* a través de otras magnitudes, cuando la irradiancia global horizontal es variable de entrada en el modelo, y esto para todos los tipos de cielo independientemente de la metodología de clasificación de cielos utilizada.

La base temporal de los datos experimentales utilizada para la obtención de los modelos no tiene excesiva influencia en la bondad de los mismos, aunque cuanto mayor es la resolución temporal de los

Capítulo 3: Conclusiones y líneas de futuro

datos, los modelos presentan, en general, valores inferiores de los parámetros estadísticos característicos, obteniendo mejores ajustes.

Cuando los modelos se calibran utilizando datos agregados de diferentes localizaciones, estos arrojan resultados satisfactorios en localizaciones de diferentes características climáticas de la clasificación de Köppen.

Generalmente, los modelos calculados para diferentes tipos de cielo presentan mejor ajuste en el caso de cielos claros y errores más elevados en el caso de cielos cubiertos. Y esto independientemente del procedimiento de clasificación de cielos utilizado. Este hecho se puede explicar por las diferencias en el espesor y las características de las nubes y la presencia de aerosoles, que dan lugar a distintos efectos de dispersión y absorción de la radiación en las distintas bandas del espectro.

Las redes neuronales artificiales y los métodos tradicionales basados en regresiones multilineales son procedimientos equivalentes para modelar la radiación fotosintéticamente activa cuando se realiza una selección de variables de entrada previa adecuada que incluye, al menos la irradiancia global horizontal como índice meteorológico con mayor influencia.

A partir de datos experimentales medidos en Burgos (España) y clasificados según los tipos de cielo propuestos por la norma ISO/CIE, se ha modelizado matemáticamente la *PAR* mediante regresión multilineal y redes neuronales, obteniendo muy buenos ajustes con ambos procedimientos para las 3 categorías de cielo (claro, parcial y cubierto). Todos los valores de R^2 son mayores de 0,97 y los errores ($nRMSE$) menores del 8%; destacando que para cielos claros, es la categoría de cielo donde se obtiene menores $nRMSE$.

La modelización de datos de *PAR* con datos experimentales de Burgos, clasificados según tipos de cielo a partir del índice de claridad (k_t),

Capítulo 3: Conclusiones y líneas de futuro

mediante regresiones multilineales y redes neuronales, permite obtener modelos con muy buenos ajustes para las 3 categorías de cielo. Además, dichos modelos se pueden aplicar a diferentes localizaciones con distinto clima según la clasificación de Köppen con un error razonablemente bajo. Los modelos presentan los errores cuadráticos mayores para cada tipo de cielo cuando se aplican a localizaciones con clima desértico cálido.

En definitiva, el trabajo ha conseguido obtener un conocimiento representativo de la radiación fotosintéticamente activa en su componente global relacionándola con índices meteorológicos habitualmente registrados en estaciones meteorológicas lo que permite su modelado a través de estos índices y para diferentes condiciones de cielo y localizaciones geográficas con distintos climas característicos.

3.2 Líneas de futuro

Una vez modelada la *PAR*, se pueden abrir nuevos ámbitos de investigación en los que poner en práctica estos modelos, ya que puede resultar de gran utilidad.

De cara a mejorar la productividad agrícola de diferentes cultivos y a obtener nuevos modelos en los que pueden influir otros parámetros o variables meteorológicas, propiedades físicoquímicas del suelo, etc, se pueden establecer las siguientes líneas futuras de investigación:

- Estudio de la calidad del aire con ayuda de las estaciones meteorológicas situadas en Burgos, considerando la influencia de los aerosoles en la estimación de la *PAR*, para poder obtener modelos que se ajusten a diferentes concentraciones de aerosoles presentes.
- Estudio de la influencia de la inclinación y orientación del terreno sobre la fracción absorbida de la *PAR* en cultivos a ras de suelo y todo tipo de vegetación.

Capítulo 3: Conclusiones y líneas de futuro

- Aplicación de los modelos en ecosistemas acuáticos, para estimar el crecimiento de fitoplancton dependiendo de la *PAR* recibida. Así, se podría controlar y tratar de minimizar la eutrofización en zonas de grandes floraciones de fitoplancton.
- Evaluación de las especies más adecuadas para reforestar los márgenes de las tierras inundadas tras la construcción de un embalse, a partir de datos de índice de área foliar (*LAI*, por sus siglas en inglés) y de las características de la zona. Los resultados se han recogido en el artículo: “*A Multicriteria Evaluation of Sustainable Riparian Revegetation with Local Fruit Trees around a Reservoir of a Hydroelectric Power Plant in Central Brazil*”, *Sustainability* 2021, 13(14), incluido en el conjunto de artículos derivados de la tesis
- Estimación de la distribución angular de la *PAR* en el cielo a partir de las imágenes hemisféricas de la bóveda celeste obtenidas mediante una cámara de cielo calibrada.
- Estudio de la *IPAR* según los distintos tipos de cielo con ayuda de mapas y equipos de medida, como el LAI-2200C.
- Utilización de los modelos experimentales obtenidos para validar los datos obtenidos por satélite y así tener otra fuente fiable de datos con los que estimar la *PAR* en localizaciones que cuenten con escasas estaciones de medida que midan esta componente de la radiación solar.

Bibliografía

- [1] R. Perez, P. Ineichen, R. Seals, J. Michalsky, R. Stewart, Modeling daylight availability and irradiance components from direct and global irradiance, *Sol. Energy*. 44 (1990) 271–289. [https://doi.org/10.1016/0038-092X\(90\)90055-H](https://doi.org/10.1016/0038-092X(90)90055-H).
- [2] N. Igawa, Improving the All Sky Model for the luminance and radiance distributions of the sky, *Sol. Energy*. 105 (2014) 354–372. <https://doi.org/10.1016/j.solener.2014.03.020>.
- [3] K.J. McCree, The measurement of photosynthetically active radiation, *Sol. Energy*. 15 (1973) 83–87. [https://doi.org/10.1016/0038-092X\(73\)90010-8](https://doi.org/10.1016/0038-092X(73)90010-8).
- [4] T. Akitsu, A. Kume, Y. Hirose, O. Ijima, K. Nasahara, On the stability of radiometric ratios of photosynthetically active radiation to global solar radiation in Tsukuba, Japan, *Agric. For. Meteorol.* 209–210 (2015) 59–68. <https://doi.org/10.1016/j.agrformet.2015.04.026>.
- [5] GCOS, (n.d.). <https://gcos.wmo.int/en/home>.
- [6] D. Hao, G.R. Asrar, Y. Zeng, Q. Zhu, J. Wen, Q. Xiao, M. Chen, Estimating hourly land surface downward shortwave and photosynthetically active radiation from DSCOVR/EPIC observations, *Remote Sens. Environ.* 232 (2019) 111320. <https://doi.org/10.1016/j.rse.2019.111320>.
- [7] R.C. Deo, N.J. Downs, J.F. Adamowski, A. V. Parisi, Adaptive Neuro-Fuzzy Inference System integrated with solar zenith angle for forecasting sub-tropical Photosynthetically Active Radiation, *Food Energy Secur.* 8 (2019). <https://doi.org/10.1002/fes3.151>.
- [8] S. Verma, R. Chowdhury, S.K. Das, M.J. Franchetti, G. Liu, Sunlight Intensity, Photosynthetically Active Radiation Modelling

Bibliografía

- and Its Application in Algae-Based Wastewater Treatment and Its Cost Estimation, *Sustainability*. 13 (2021) 11937. <https://doi.org/10.3390/su132111937>.
- [9] G. Saini, W. Fricke, Photosynthetically active radiation impacts significantly on root and cell hydraulics in barley (*Hordeum vulgare* L.), *Physiol. Plant.* 170 (2020) 357–372. <https://doi.org/10.1111/ppl.13164>.
- [10] L.I. Trejo-Téllez, E. Estrada-Ortiz, F.C. Gómez-Merino, C. Becker, A. Krumbein, D. Schwarz, Flavonoid, nitrate and glucosinolate concentrations in Brassica species are differentially affected by photosynthetically active radiation, phosphate and phosphite, *Front. Plant Sci.* 10 (2019). <https://doi.org/10.3389/fpls.2019.00371>.
- [11] X. Zhang, X. Li, D. Chen, H. Cui, Q. Ge, Overestimated climate warming and climate variability due to spatially homogeneous CO₂ in climate modeling over the Northern Hemisphere since the mid-19th century, *Sci. Rep.* 9 (2019) 1–9. <https://doi.org/10.1038/s41598-019-53513-7>.
- [12] T.Y. Churilova, V. V. Suslin, N.A. Moiseeva, T. V. Efimova, Phytoplankton Bloom and Photosynthetically Active Radiation in Coastal Waters, *J. Appl. Spectrosc.* 86 (2020) 1084–1091. <https://doi.org/10.1007/s10812-020-00944-0>.
- [13] R. Jyothibabu, N. Arunpandi, L. Jagadeesan, C. Karnan, K.R. Lallu, P.N. Vinayachandran, Response of phytoplankton to heavy cloud cover and turbidity in the northern Bay of Bengal, *Sci. Rep.* 8 (2018) 1–15. <https://doi.org/10.1038/s41598-018-29586-1>.
- [14] W. Wei, R. Zhang, L. Peng, Y. Liang, N. Jiao, Effects of temperature and photosynthetically active radiation on virioplankton decay in the western Pacific Ocean, *Sci. Rep.* 8 (2018). <https://doi.org/10.1038/s41598-018-19678-3>.

Bibliografía

- [15] J. Yu, J.Y. Tian, G. Gao, R. Xu, J.G. Lai, G.P. Yang, Growth, DMS and DMSP production in *Emiliana huxleyi* under elevated CO₂ and UV radiation, *Environ. Pollut.* 294 (2022) 118643. <https://doi.org/10.1016/j.envpol.2021.118643>.
- [16] K.K. Yates, C.S. Rogers, J.J. Herlan, G.R. Brooks, N.A. Smiley, R.A. Larson, Diverse coral communities in mangrove habitats suggest a novel refuge from climate change, *Biogeosciences*. 11 (2014) 4321–4337. <https://doi.org/10.5194/bg-11-4321-2014>.
- [17] R.L. Jackson, A.J. Gabric, P.A. Matrai, M.T. Woodhouse, R. Cropp, G.B. Jones, E.S.M. Deschaseaux, Y. Omori, E.L. McParland, H.B. Swan, H. Tanimoto, Parameterizing the Impact of Seawater Temperature and Irradiance on Dimethylsulfide (DMS) in the Great Barrier Reef and the Contribution of Coral Reefs to the Global Sulfur Cycle, *J. Geophys. Res. Ocean.* 126 (2021) 1–17. <https://doi.org/10.1029/2020JC016783>.
- [18] M. Tsubo, S. Walker, Relationships between photosynthetically active radiation and clearness index at Bloemfontein, South Africa, *Theor. Appl. Climatol.* 80 (2005) 17–25. <https://doi.org/10.1007/s00704-004-0080-5>.
- [19] P. Moon, Proposed standard solar-radiation curves for engineering use, *J. Franklin Inst.* 230 (1940) 583–617. [https://doi.org/10.1016/S0016-0032\(40\)90364-7](https://doi.org/10.1016/S0016-0032(40)90364-7).
- [20] J.L. Monteith, W.E. Reifsnyder, Principles of Environmental Physics, *Phys. Today.* 27 (1974) 51–52. <https://doi.org/10.1063/1.3128494>.
- [21] D.W. Meek, J.L. Hatfield, T.A. Howell, S.B. Idso, R.J. Reginato, Generalized relationship between photosynthetically active radiation and solar radiation., *Agron. J.* 76 (1984) 939–945. <https://doi.org/10.2134/agronj1984.00021962007600060018x>.
- [22] C.J. Stigter, V.M.M. Musabilha, The Conservative Ratio of

Bibliografía

- Photosynthetically Active to Total Radiation in the Tropics, *J. Appl. Ecol.* 19 (1982) 853–858. <https://doi.org/10.2307/2403287>.
- [23] W.J. Blackburn, J.T.A. Proctor, Estimating photosynthetically active radiation from measured solar irradiance, *Sol. Energy.* 31 (1983) 233–234. [https://doi.org/10.1016/0038-092X\(83\)90087-7](https://doi.org/10.1016/0038-092X(83)90087-7).
- [24] A. Majnooni-heris, Estimating photosynthetically active radiation (PAR) using air temperature and sunshine durations, 5 (2014) 371–377.
- [25] K. Sudhakar, T. Srivastava, G. Satpathy, M. Premalatha, Modelling and estimation of photosynthetically active incident radiation based on global irradiance in Indian latitudes, *Int. J. Energy Environ. Eng.* 4 (2013) 1–8. <https://doi.org/10.1186/2251-6832-4-21>.
- [26] J.M. Vindel, R.X. Valenzuela, A.A. Navarro, L.F. Zarzalejo, A. Paz-Gallardo, J.A. Souto, R. Méndez-Gómez, D. Cartelle, J.J. Casares, Modeling photosynthetically active radiation from satellite-derived estimations over mainland Spain, *Remote Sens.* 10 (2018) 1–13. <https://doi.org/10.3390/rs10060849>.
- [27] B. Hu, Y. Yu, Z. Liu, Y. Wang, Analysis of photosynthetically active radiation and applied parameterization model for estimating of PAR in the North China Plain, *J. Atmos. Chem.* 73 (2016) 345–362. <https://doi.org/10.1007/s10874-016-9330-z>.
- [28] M.-M. Zempila, M. Taylor, A. Bais, S. Kazadzis, Modeling the relationship between photosynthetically active radiation and global horizontal irradiance using singular spectrum analysis, *J. Quant. Spectrosc. Radiat. Transf.* 182 (2016) 240–263. <https://doi.org/10.1016/j.jqsrt.2016.06.003>.
- [29] L. Wang, W. Gong, C. Li, A. Lin, B. Hu, Y. Ma, Measurement and estimation of photosynthetically active radiation from 1961 to 2011 in Central China, *Appl. Energy.* 111 (2013) 1010–1017.

Bibliografía

- <https://doi.org/10.1016/j.apenergy.2013.07.001>.
- [30] F. Ferrera-Cobos, J.M. Vindel, R.X. Valenzuela, J.A. González, Models for estimating daily photosynthetically active radiation in oceanic and mediterranean climates and their improvement by site adaptation techniques, *Adv. Sp. Res.* 65 (2020) 1894–1909. <https://doi.org/10.1016/j.asr.2020.01.018>.
- [31] M. Möttus, J. Ross, M. Sulev, Experimental study of ratio of PAR to direct integral solar radiation under cloudless conditions, *Agric. For. Meteorol.* 109 (2001) 161–170. [https://doi.org/10.1016/S0168-1923\(01\)00269-6](https://doi.org/10.1016/S0168-1923(01)00269-6).
- [32] A.A. Al-Shooshan, Estimation of photosynthetically active radiation under an arid climate, *J. Agric. Eng. Res.* 66 (1997) 9–13. <https://doi.org/10.1006/jaer.1996.0112>.
- [33] I. Alados, L. Alados-Arboledas, Validation of an empirical model for photosynthetically active radiation, *Int. J. Climatol.* 19 (1999) 1145–1152. [https://doi.org/10.1002/\(SICI\)1097-0088\(199908\)19:10<1145::AID-JOC428>3.0.CO;2-3](https://doi.org/10.1002/(SICI)1097-0088(199908)19:10<1145::AID-JOC428>3.0.CO;2-3).
- [34] S. Nwokolo, S.O. Amadi, A Global Review of Empirical Models for Estimating Photosynthetically Active Radiation, *Trends Renew. Energy.* 4 (2018) 236–327. <https://doi.org/10.17737/tre.2018.4.2.0079>.
- [35] C.P. Jacovides, F.S. Tymvios, V.D. Assimakopoulos, N.A. Kaltsounides, The dependence of global and diffuse PAR radiation components on sky conditions at Athens, Greece, *Agric. For. Meteorol.* (2007). <https://doi.org/10.1016/j.agrformet.2007.01.004>.
- [36] D.A. Finch, W.G. Bailey, L.J.B. McArthur, M. Nasitwitwi, Photosynthetically active radiation regimes in a southern African savanna environment, *Agric. For. Meteorol.* 122 (2004) 229–238. <https://doi.org/10.1016/j.agrformet.2003.09.015>.

Bibliografía

- [37] J.F. Escobedo, E.N. Gomes, A.P. Oliveira, J. Soares, Modeling hourly and daily fractions of UV, PAR and NIR to global solar radiation under various sky conditions at Botucatu, Brazil, *Appl. Energy*. 86 (2009) 299–309. <https://doi.org/10.1016/j.apenergy.2008.04.013>.
- [38] L. Wang, W. Gong, A. Lin, B. Hu, Analysis of photosynthetically active radiation under various sky conditions in Wuhan, Central China, *Int. J. Biometeorol.* 58 (2014) 1711–1720. <https://doi.org/10.1007/s00484-013-0775-3>.
- [39] S.O. Udo, T.O. Aro, Global PAR related to global solar radiation for central Nigeria, *Agric. For. Meteorol.* 97 (1999) 21–31. [https://doi.org/10.1016/S0168-1923\(99\)00055-6](https://doi.org/10.1016/S0168-1923(99)00055-6).
- [40] P.P. Kastendeuch, P. Lacarrere, G. Najjar, J. Noilhan, F. Gassmann, P. Paul, New empirical relationships for determining global par from measurements of global solar radiation, infrared radiation of sunshine duration, *Int. J. Climatol.* 20 (2000) 1265–1274. [https://doi.org/10.1002/1097-0088\(200008\)20:10<1265::AID-JOC530>3.0.CO;2-C](https://doi.org/10.1002/1097-0088(200008)20:10<1265::AID-JOC530>3.0.CO;2-C).
- [41] C.P. Jacovides, F.S. Timvios, G. Papaioannou, D.N. Asimakopoulos, C.M. Theofilou, Ratio of PAR to broadband solar radiation measured in Cyprus, *Agric. For. Meteorol.* 121 (2004) 135–140. <https://doi.org/10.1016/j.agrformet.2003.10.001>.
- [42] I. Alados, I. Foyo-Moreno, L. Alados-Arboledas, Photosynthetically active radiation: measurements and modelling, *Agric. For. Meteorol.* 78 (1996) 121–131. [https://doi.org/10.1016/0168-1923\(95\)02245-7](https://doi.org/10.1016/0168-1923(95)02245-7).
- [43] A. Suárez-García, M. Díez-Mediavilla, D. Granados-López, D. González-Peña, C. Alonso-Tristán, Benchmarking of meteorological indices for sky cloudiness classification, *Sol. Energy*. 195 (2020) 499–513.

Bibliografía

- <https://doi.org/10.1016/j.solener.2019.11.060>.
- [44] S. Kittler, R.; Perez, R.; Darula, A new generation of sky standards., in: Proc. Eighth Eur. Light. Conf., Amsterdam, The Netherlands, 1997: pp. 359–373.
- [45] R. Kittler, R. Perez, S. Darula, A set of standard skies. Characterizing daylight conditions for computer and energy conscious design., 1998. <https://doi.org/10.13140/RG.2.1.4798.7048>.
- [46] ISO 15469:2004(E)/CIE S 011/E:2003, 2004. Spatial Distribution of Daylight – CIE Standard General Sky. Geneva: ISO, Vienna: CIE., n.d.
- [47] A. García-Rodríguez, S. García-Rodríguez, M. Díez-Mediavilla, C. Alonso-Tristán, Photosynthetic active radiation, solar irradiance and the cie standard sky classification, Appl. Sci. 10 (2020) 1–14. <https://doi.org/10.3390/app10228007>.
- [48] R. Frouin, R.T. Pinker, Estimating Photosynthetically Active Radiation (PAR) at the earth's surface from satellite observations, Remote Sens. Environ. 51 (1995) 98–107. [https://doi.org/10.1016/0034-4257\(94\)00068-X](https://doi.org/10.1016/0034-4257(94)00068-X).
- [49] J.M. Vindel, R.X. Valenzuela, A.A. Navarro, L.F. Zarzalejo, Methodology for optimizing a photosynthetically active radiation monitoring network from satellite-derived estimations: A case study over mainland Spain, Atmos. Res. 212 (2018) 227–239. <https://doi.org/10.1016/j.atmosres.2018.05.010>.
- [50] W.W. Nyamsi, P. Blanc, J.A. Augustine, A. Arola, L. Wald, A new clear-sky method for assessing photosynthetically active radiation at the surface level, Atmosphere (Basel). 10 (2019). <https://doi.org/10.3390/ATMOS10040219>.
- [51] C.P. Jacovides, F.S. Tymvios, J. Boland, M. Tsitouri, Artificial Neural Network models for estimating daily solar global UV, PAR

Bibliografía

- and broadband radiant fluxes in an eastern Mediterranean site, *Atmos. Res.* 152 (2015) 138–145. <https://doi.org/10.1016/j.atmosres.2013.11.004>.
- [52] G. López, M. Rubio, M. Martínez, F. Batlles, Estimation of hourly global photosynthetically active radiation using artificial neural network models, *Agric. For. Meteorol.* 107 (2001) 279–291. [https://doi.org/10.1016/S0168-1923\(01\)00217-9](https://doi.org/10.1016/S0168-1923(01)00217-9).
- [53] P. Pankaew, S. Pattarapanitchai, S. Buntoung, R. Wattan, I. Masiri, A. Sripradit, S. Janjai, Estimating photosynthetically active radiation using an artificial neural network, in: *Proc. 2014 Int. Conf. Util. Exhib. Green Energy Sustain. Dev. ICUE 2014*, IEEE Computer Society, 2014.
- [54] W. Qin, L. Wang, M. Zhang, Z. Niu, M. Luo, A. Lin, B. Hu, First effort at constructing a high-density photosynthetically active radiation dataset during 1961–2014 in China, *J. Clim.* 32 (2019) 2761–2780. <https://doi.org/10.1175/JCLI-D-18-0590.1>.
- [55] L. Wang, O. Kisi, M. Zounemat-Kermani, B. Hu, W. Gong, Modeling and comparison of hourly photosynthetically active radiation in different ecosystems, *Renew. Sustain. Energy Rev.* 56 (2016) 436–453. <https://doi.org/10.1016/j.rser.2015.11.068>.
- [56] C.A. Gueymard, J.A. Ruiz-Arias, Extensive worldwide validation and climate sensitivity analysis of direct irradiance predictions from 1-min global irradiance, *Sol. Energy.* (2016). <https://doi.org/10.1016/j.solener.2015.10.010>.
- [57] E. Long, C., Dutton, *BSRN Global Network Recommended QC Tests*, 2002.
- [58] C.A. Gueymard, A reevaluation of the solar constant based on a 42-year total solar irradiance time series and a reconciliation of spaceborne observations, *Sol. Energy.* 168 (2018) 2–9. <https://doi.org/10.1016/j.solener.2018.04.001>.

Bibliografía

- [59] C.A. Gueymard, D. Myers, K. Emery, Proposed reference irradiance spectra for solar energy systems testing, *Sol. Energy.* 73 (2002) 443–467. [https://doi.org/10.1016/S0038-092X\(03\)00005-7](https://doi.org/10.1016/S0038-092X(03)00005-7).
- [60] B. Hu, Y. Wang, G. Liu, Spatiotemporal characteristics of photosynthetically active radiation in China, *J. Geophys. Res. Atmos.* 112 (2007) 1–12. <https://doi.org/10.1029/2006JD007965>.
- [61] C. Gueymard, A two-band model for the calculation of clear sky solar irradiance, illuminance, and photosynthetically active radiation at the earth's surface, *Sol. Energy.* 43 (1989) 253–265. [https://doi.org/10.1016/0038-092X\(89\)90113-8](https://doi.org/10.1016/0038-092X(89)90113-8).
- [62] W. Wandji Nyamsi, B. Espinar, P. Blanc, L. Wald, Estimating the photosynthetically active radiation under clear skies by means of a new approach, *Adv. Sci. Res.* 12 (2015) 5–10. <https://doi.org/10.5194/asr-12-5-2015>.
- [63] P.J. Littlefair, A comparison of sky luminance models with measured data from Garston, United Kingdom, *Sol. Energy.* 53 (1994) 315–322. [https://doi.org/10.1016/0038-092X\(94\)90034-5](https://doi.org/10.1016/0038-092X(94)90034-5).
- [64] P.J. Littlefair, The luminance distributions of clear and quasi-clear skies, in: *Proc. CIBSE Natl. Light. Conf.*, Cambridge, UK, 1994: pp. 267–283.
- [65] I. Foyo-Moreno, I. Alados, L. Alados-Arboledas, A new conventional regression model to estimate hourly photosynthetic photon flux density under all sky conditions, *Int. J. Climatol.* 37 (2017) 1067–1075. <https://doi.org/10.1002/joc.5063>.
- [66] M.. Peel, B.. Finlayson, T.. McMahon, Updated world map of the Köppen-Geiger climate classification, *Hydrol. Earth Syst. Sci.* 11 (2007) 1633–1644.
- [67] X. Yu, Z. Wu, W. Jiang, X. Guo, Predicting daily photosynthetically active radiation from global solar radiation in

Bibliografía

- the Contiguous United States, *Energy Convers. Manag.* 89 (2015) 71–82. <https://doi.org/10.1016/j.enconman.2014.09.038>.
- [68] B. Hu, Y. Wang, G. Liu, Measurements and estimations of photosynthetically active radiation in Beijing, *Atmos. Res.* 85 (2007) 361–371. <https://doi.org/10.1016/j.atmosres.2007.02.005>.
- [69] L.J.G. Aguiar, G.R. Fischer, R.J. Ladle, A.C.M. Malhado, F.B. Justino, R.G. Aguiar, J.M.N. da Costa, Modeling the photosynthetically active radiation in South West Amazonia under all sky conditions, *Theor. Appl. Climatol.* 108 (2011) 631–640. <https://doi.org/10.1007/s00704-011-0556-z>.
- [70] Y. Mizoguchi, Y. Yasuda, Y. Ohtani, T. Watanabe, Y. Kominami, K. Yamanoi, A practical model to estimate photosynthetically active radiation using general meteorological elements in a temperate humid area and comparison among models, *Theor. Appl. Climatol.* 115 (2014) 583–589. <https://doi.org/10.1007/s00704-013-0912-2>.
- [71] S. Ge, R.G. Smith, C.P. Jacovides, M.G. Kramer, R.I. Carruthers, Dynamics of photosynthetic photon flux density (PPFD) and estimates in coastal northern California, *Theor. Appl. Climatol.* 105 (2011) 107–118. <https://doi.org/10.1007/s00704-010-0368-6>.
- [72] A. Suárez-García, D. Granados-López, D. González-Peña, M. Díez-Mediavilla, C. Alonso-Tristán, Seasonal characterization of CIE standard sky types above Burgos, northwestern Spain, *Sol. Energy.* 169 (2018) 24–33. <https://doi.org/10.1016/j.solener.2018.04.028>.
- [73] D. Granados-López, M. Díez-Mediavilla, M.I. Dieste-Velasco, A. Suárez-García, C. Alonso-Tristán, Evaluation of the vertical sky component without obstructions for daylighting in Burgos, Spain, *Appl. Sci.* 10 (2020) 1–15. <https://doi.org/10.3390/app10093095>.

Bibliografía

- [74] A. García-Rodríguez, D. Granados-López, S. García-Rodríguez, M. Díez-Mediavilla, C. Alonso-Tristán, Modelling Photosynthetic Active Radiation (PAR) through meteorological indices under all sky conditions, *Agric. For. Meteorol.* 310 (2021). <https://doi.org/10.1016/j.agrformet.2021.108627>.
- [75] Y.C. Du, A. Stephanus, Levenberg-marquardt neural network algorithm for degree of arteriovenous fistula stenosis classification using a dual optical photoplethysmography sensor, *Sensors.* 18 (2018). <https://doi.org/10.3390/s18072322>.
- [76] A.. García-Rodríguez, S.. García-Rodríguez, D.. Granados-López, M.. Díez-Mediavilla, C. Alonso-Tristán, Extension of PAR Models under Local All Sky Conditions to Different Climatic Zones, *Appl. Siences.* 12 (2022) 1–15. <https://doi.org/https://doi.org/10.3390/app12052372>.

Bibliografía



Los Investigadores **SOL GARCÍA RODRÍGUEZ**, con DNI 71278921N y **DIEGO GRANADOS LÓPEZ**, con DNI 71292836N como coautores de los siguientes trabajos:

- García-Rodríguez, S. García-Rodríguez, M. Díez-Mediavilla and C. Alonso-Tristán (2020). Photosynthetic Active Radiation, Solar Irradiance and the CIE Standard Sky Classification. Applied Sciences 10 (22) ,8007. DOI: <https://doi.org/10.3390/app10228007>
- García-Rodríguez, D. Granados-López, S. García-Rodríguez, M. Díez-Mediavilla, C. Alonso-Tristán (2021). Modelling Photosynthetic Active Radiation (PAR) through meteorological indices under all sky conditions. Agricultural and Forest Meteorology, 310, 108627. DOI: <https://doi.org/10.1016/j.agrformet.2021.108627>
- García-Rodríguez, S. García-Rodríguez, D. Granados-López, M. Díez-Mediavilla and C. Alonso-Tristán (2022). Extension of local all sky conditions PAR models to different climatic zones. Applied Sciences, 12, 2372. DOI: <https://doi.org/10.3390/app12052372>.

expresamos mediante el presente escrito nuestra renuncia a la utilización de las anteriores publicaciones para la presentación de una tesis por compendio de artículos.

En Burgos, a 26 de febrero de 2022


Fdo. Diego Granados López

Fdo. Sol García Rodríguez

Artículos

Article

Photosynthetic Active Radiation, Solar Irradiance and the CIE Standard Sky Classification

Ana García-Rodríguez, Sol García-Rodríguez, Montserrat Díez-Mediavilla and Cristina Alonso-Tristán * 

Research Group Solar and Wind Feasibility Technologies (SWIFT), Electromechanical Engineering Department, Universidad de Burgos, 09006 Burgos, Spain; agrodriguez@ubu.es (A.G.-R.); solgr@ubu.es (S.G.-R.); mdmr@ubu.es (M.D.-M.)

* Correspondence: catristan@ubu.es or cristinaalonso.tristan@gmail.com

Received: 1 October 2020; Accepted: 9 November 2020; Published: 12 November 2020



Abstract: Plant growth is directly related to levels of photosynthetic photon flux density, Q_p . The improvement of plant-growth models therefore requires accurate estimations of the Q_p parameter that is often indirectly calculated on the basis of its relationship with solar irradiance, R_s , due to the scarcity of ground measurements of photosynthetic photon flux density. In this experimental campaign in Burgos, Spain, between April 2019 and January 2020, an average value of the Q_p/R_s ratio is determined on the basis of measurements at ten-minute intervals. The most influential factor in the Q_p/R_s ratio, over and above any daily or seasonal pattern, is the existence of overcast sky conditions. The CIE standard sky classification can be used to establish an unequivocal characterization of the cloudiness conditions of homogeneous skies. In this study, the relation between the CIE standard sky type and Q_p/R_s is investigated. Its conclusions were that the Q_p/R_s values, the average of which was $1.93 \pm 0.15 \mu\text{mol}\cdot\text{J}^{-1}$, presented statistically significant differences for each CIE standard sky type. The overcast sky types presented the highest values of the ratio, while the clear sky categories presented the lowest and most dispersed values. During the experimental campaign, only two exceptions were noted for covered and partial covered sky-type categories, respectively, sky types 5 and 9. Their values were closer to those of categories classified as clear sky according to the CIE standard. Both categories presented high uniformity in terms of illumination.

Keywords: photosynthetic active radiation; CIE standard skies; solar irradiance

1. Introduction

The portion of the solar spectrum that plant biochemical processes use in photosynthesis for converting light energy into biomass is a composite of wavelengths between 400 and 700 nm that are diffused within the visible light spectrum band (380–780 nm). These wavelength limits define the so-called photo-synthetically active radiation that covers both photon (Photosynthetic Photon Flux Density, Q_p ($\mu\text{mol}\cdot\text{s}^{-1}\cdot\text{m}^{-2}$)) and energy (PAR, Photo-synthetically Active Radiation, $\text{W}\cdot\text{m}^{-2}$) terms [1]. Usually, Q_p is recorded, and converted into energy units according to the McCree conversion factor of $4.57 \mu\text{mol}\cdot\text{J}^{-1} \pm 3\%$ depending on climatic factors [2]. Accurate PAR estimations are needed for modelling plant productivity and biomass production [3], natural illumination in greenhouses [4], plant physiology studies and leaf photosynthesis [5], to measure the productivity of forests [6], and to calculate the euphotic depth of the oceans [7]. Moreover, accurate PAR measurements have become central to the determination of deforestation and climate-change impacts on agriculture [8].

A global routine network for measuring PAR has yet to be established. This parameter is often indirectly calculated, due to the scarcity of PAR data, based on its relationship with global horizontal solar irradiance, R_s . The conventional PAR/ R_s ratio falls between 0.45 and 0.50 [9]. Moon [10]

estimated the PAR/ R_s ratio at between 44% and 45% at sea level with a solar zenith angle of 30° over the horizon. Monteith [11] suggested that a constant ratio of 50% can be a good approximation for practical applications regardless of atmospheric aerosol and water vapor concentrations [12]. In terms of $\mu\text{mol}\cdot\text{J}^{-1}$, empirical relations [13] established Q_p/R_s ratios of between 2.1 and 2.9 $\mu\text{mol}\cdot\text{J}^{-1}$, depending on the location. The monthly Q_p/R_s average was calculated on a daily basis from experimental data [14] collected in an arid climate at between 2.02 and 2.19 $\mu\text{mol}\cdot\text{J}^{-1}$ and the mean daily value was 2.16 $\mu\text{mol}\cdot\text{J}^{-1}$. In Spain, Foyo-Moreno et al. [15] estimated a mean value of 1.95 $\mu\text{mol}\cdot\text{J}^{-1}$ a value close to other values from different locations [3,16]. Hu et al. [17] evaluated the Q_p/R_s ratio at many locations within China at between 1.75 $\mu\text{mol}\cdot\text{J}^{-1}$ and 2.30 $\mu\text{mol}\cdot\text{J}^{-1}$.

Several studies have been conducted to determine the relation between PAR/ R_s and different parameters. In some cases, significant relationships were found, but any dependencies on site geography, climatic and weather factors, seasonal trends, and both day length and diurnal effects were very slight and negligible for practical purposes [18]. Solar elevation has no significant effect on PAR/ R_s when greater than 10° [18,19].

The variations of this ratio with sky conditions have been studied to develop weather-dependent functions. Most studies have concluded that the PAR/ R_s ratio presents its highest values for cloud-covered skies [20,21]. This fact is attributable to cloud-related absorption and diffusion of solar radiation across different regions of the spectrum. The observed seasonal dependence of broad-band solar radiation is essentially caused by changes to turbidity, precipitable water, ozone, and clouds within the air masses at the location throughout the year [22]. The presence of water vapor increases the absorption effects within the infrared region of the spectrum, decreasing broadband solar irradiance levels to a greater extent than PAR. A secondary effect of the atmospheric water content is the enhancement of aerosol-related diffusion, which affects PAR more than broadband solar irradiance, R_s [4,23]. Some studies have proposed experimental models of PAR that include different parameters to take into account the atmospheric water vapor content, such as vapor pressure [16,24] and/or dewpoint temperature [4].

The definition of sky types (clear, overcast, and partly-cloudy) for this task take into account different combinations of meteorological variables, mainly the clearness index, k_t (ratio of global solar radiation to extraterrestrial solar radiation) [14,25–28]; k_t and relative sunshine, S , [29,30]; Perez's clearness index, ε , and sky brightness, Δ , [4,31], and types and extent of cloud cover [32]. However, the conclusions of a previous work [33] suggested that the use of meteorological variables or meteorological indices, showed limited results for sky classification. The use of meteorological indices for sky classification depends more on their availability than on their accuracy and various authors have used such indices (or combinations thereof) in different ways.

Sky classification is a complex problem, due in part to such abstract conceptual definitions as clear, partial cloudy, and overcast, as well as other intermediate ranges. The study of the dependence of any magnitude with respect to the type of sky firstly requires a standardized classification of the skies, to specify the atmospheric characteristics and illumination levels of each of the established types. In 2003, the International Commission on Illumination (Commission Internationale de L'Éclairage or CIE) defined 15 standard sky types, five categorized as clear, five as partial cloudy, and five as overcast skies. In several works, it was concluded that the CIE standard sky classification adequately represented empirical sky conditions [34–40]. Sky types of the same category have the same well-defined sky luminance patterns that easily yield the solar irradiance and daylight illuminance on the surfaces of interest through simple mathematical expressions [41]. Therefore, the CIE standard classification characterizes each type of sky in terms of energy and daylight. Figure 1 shows the main characteristics of each CIE standard sky type. Taking into account that illuminance (400–780 nm) and PAR (400–700 nm) share part of the spectrum of visible radiation, the use of the CIE Standard Classification is proposed in this work as the main parameter for characterizing the dependency of the Q_p/R_s ratio on atmospheric conditions.

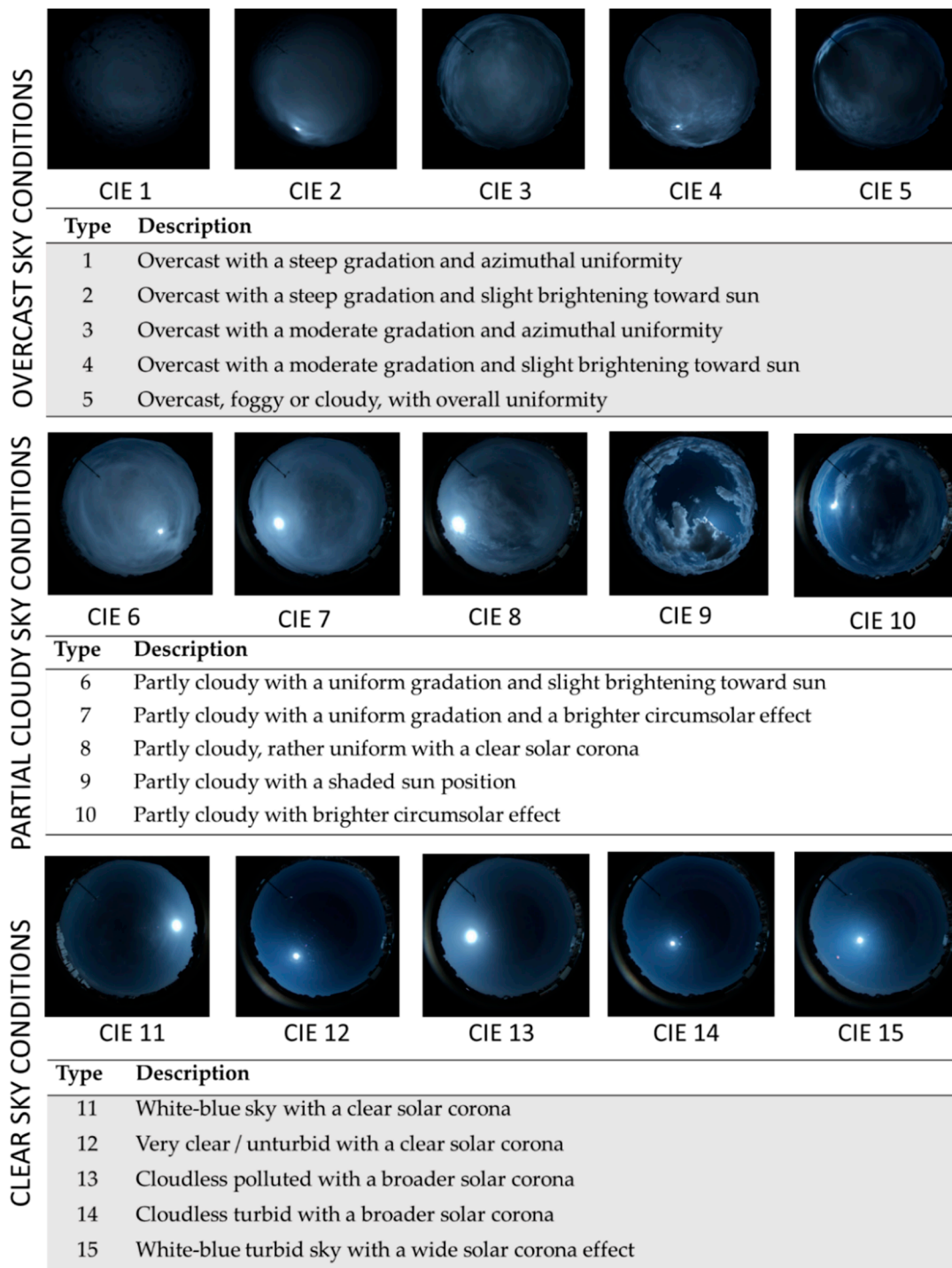


Figure 1. CIE Standard sky conditions. Images of different sky types recorded with a SONA201D All-Sky Camera—Day in Burgos, Spain.

The study is focused on the determination of the Q_p/R_s ratio in Burgos, Spain and its dependency on sky conditions. Experimental data on horizontal solar global irradiation, R_s ; photon photosynthetic flux density, Q_p ; and, the CIE standard classification for homogeneous skies; collected through experimental sky scanner measurements, were available for this work. A complete statistical analysis of the results over different temporal (ten-minute, hourly, daily, and monthly) phases was completed. The results collected under different sky conditions were tested in a 10-month experimental test campaign.

The paper will be structured as follows. The experimental facility and the measurement campaign as well the quality filters applied to the experimental data will be described in Section 2. The CIE Standard sky classification in Burgos during the experimental campaign will be introduced in Section 3. Temporal variability of the Q_p/R_s ratio over the different temporal intervals will be explained in Section 4. A variability analysis of the Q_p/R_s ratio in accordance with the CIE Standard Sky types will be analyzed in detail in Section 5. Finally, the main results and the conclusions of the study will be summarized in Section 6.

2. Experimental Data

The meteorological and radiometric weather station that recorded the experimental data for this study is located on the roof of the Higher Polytechnic School building (EPS) of Burgos University ($42^{\circ}21'04''$ N, $3^{\circ}41'20''$ W, 856 m above mean sea level). Figure 2 shows the location of the meteorological station on the flat roof of the EPS building, where the climatic parameters are measured: ambient temperature, relative humidity, atmospheric pressure, wind speed and direction, and rainfall. A complete description of the experimental facility and its location can be found in previous papers [33,42].

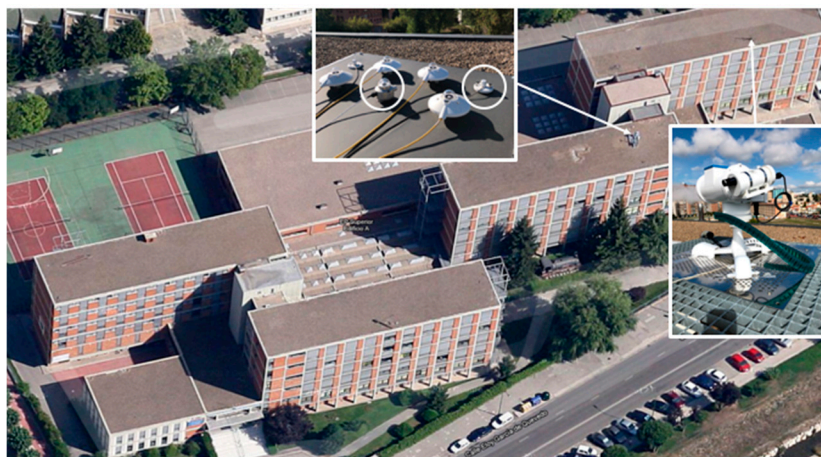


Figure 2. Location of the experimental equipment on the roof of the Higher Polytechnic School building at the University of Burgos, Spain.

Global horizontal irradiation, R_s data were measured by a pyranometer (model SR11, Hukseflux, Delft, The Netherlands,). An ML-020P photon meter was used to measure Q_p . The sky luminance and irradiance distribution were determined by a commercial MS-321LR sky scanner. Both instruments were manufactured by EKO Instruments (EKO Instruments Europe B.V., Den Haag, The Netherlands). The technical specifications of the various measurement instruments are shown in Tables 1–3.

Table 1. Sky scanner technical specifications.

Model	MS-321LR Sky Scanner
Dimensions (W × D × H)	430 mm × 380 mm × 440 mm
Mass	12.5 kg
FOV	11°
Luminance	0 to 50 kcd/m ²
Radiance	0 to 300 W/m ²
A/D Convertor	16 bits
Calibration Error	2%

Table 2. Pyranometer technical specifications.

Model	SR11
ISO classification	first class
Spectral range	300 to 2800 nm
Irradiance range	0 to 2000 W/m ²
Sensitivity	15 × 10 ⁻⁶ V/(Wm ⁻²)
Calibration uncertainty	<1.8%

Table 3. Photon-meter technical specifications.

Model	ML-020P
Measurement Range	0–3000 μmol·s ⁻¹ ·m ⁻²
Spectral range	400 to 700 nm
Operating temperature	−10 °C to 50 °C
Temperature response	±1%
Sensitivity	0.15 × 10 ⁻⁶ V/μmol·s ⁻¹ ·m ⁻²

Broadband solar irradiance, R_s , and photosynthetic photon flux density data, Q_p , were recorded every 10 min (recorded scans of 30 s on average). Experimental data were analyzed and then filtered using conventional quality criteria [43]. The sky scanner was adjusted on a monthly basis for taking measurements from sunrise to the sunset. It completed a full scan in four minutes and started a new scan every 10 min. The first and last measurements of the day ($\alpha_s \leq 7.5^\circ$) were discarded, as well as measurements higher than 50 kcd·m⁻² and lower than 0.1 kcd·m⁻², following the specifications of the equipment. If a data set (R_s , Q_p , or sky scanner measurement) failed to pass the quality criteria, then all the simultaneous data sets were rejected.

The experimental campaign ran between 1 April 2019 to 31 January 2020, during which time 20,631 data sets were collected, 18% of which were rejected after failing the quality criteria test. Therefore, the total data set comprised 16,937 ten-minute samples of R_s , Q_p , and the CIE Standard sky classification data sets.

3. CIE Standard Sky Classification in Burgos between 1 April 2019 and 21 January 2020

The Normalization Ratio (NR) introduced by Littlefair [44,45] in the original Standard Sky Luminance Distribution (SSLD) method [46], detailed and described in a previous paper [42], was used to determine the CIE standard sky types over Burgos between April 2019 and January 2020. The Frequency of Occurrence (FOC, %) of each sky type during the period under study is shown in Figure 3. As can be seen, all types of CIE standard skies can be found in Burgos. Sky types 11, 12, and 13, corresponding to CIE standard clear sky categories, had FOCs of around 10% (sky type 11) and 14.5% (sky types 12 and 13), followed by sky type 14 (FOC 8.4%). FOCs of around 7% were accounted for by sky types 1, 7, 8, and 15. The appearances of sky types 5, 9, and 10 were anecdotal in Burgos in the period under study, with FOCs of less than 3%. When only three sky categories were considered, the sky conditions in Burgos were predominantly clear, with FOCs of almost 62%, while the FOCs of overcast and partial cloudy conditions were 23.96% and 22.92%, respectively, as shown in Figure 4.

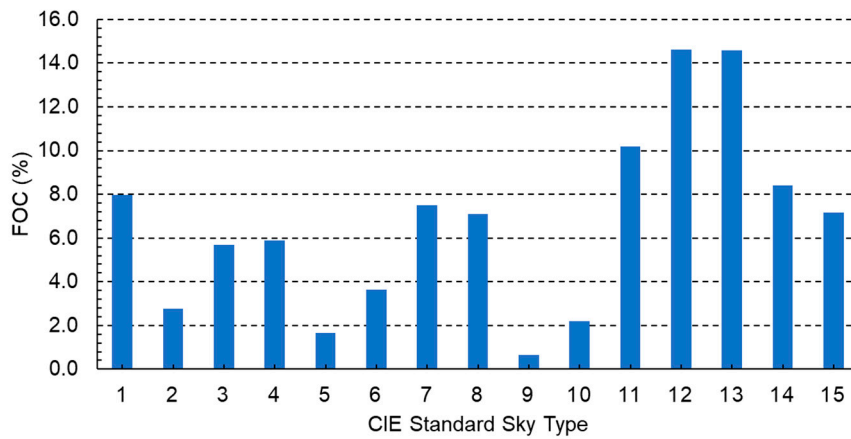


Figure 3. Frequency of occurrence (FOC, %) of CIE standard sky types in Burgos, Spain, between April 2019 and January 2020.

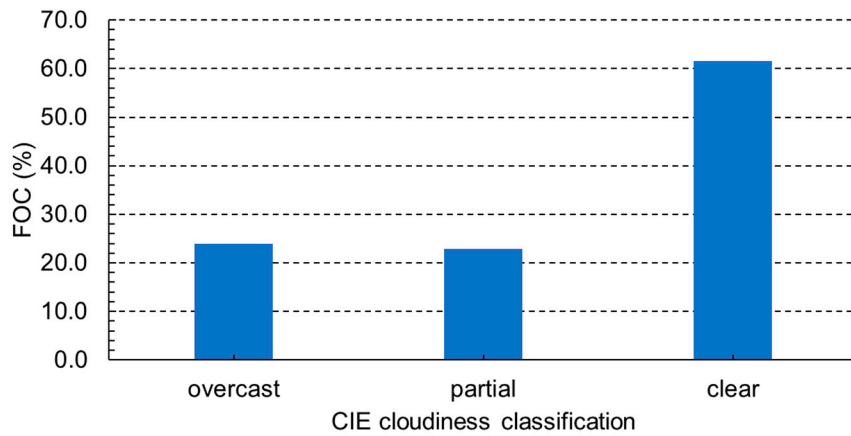


Figure 4. Frequency of occurrence (FOC, %) of CIE Cloudiness classification in Burgos, Spain, between April 2019 and January 2020.

Figure 5 shows that overcast sky conditions predominated in November and January and clear skies predominated from May to October in Burgos during the experimental campaign. Figure 6 reflects the predominance of clear skies in all hourly intervals of the day, from sunrise to sunset, at which point the standard CIE tends to classify the skies as partially overcast.

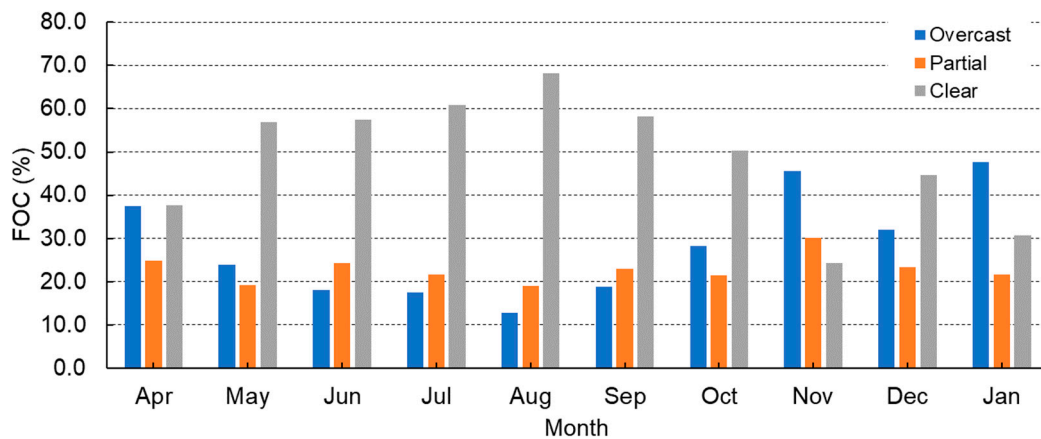


Figure 5. Monthly frequency of occurrence of clear, partial, and overcast sky conditions in Burgos between April 2019 and January 2020.

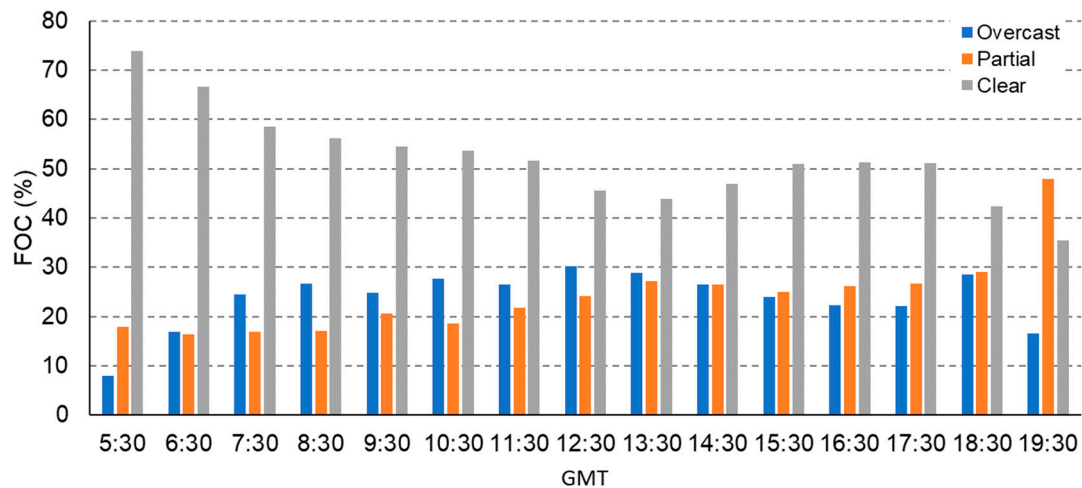


Figure 6. Daily frequency of occurrence of clear, partial, and overcast sky conditions in Burgos between April 2019 and January 2020.

4. Temporal Variability of the Q_p/R_s Ratio

The seasonal characteristics of the Q_p/R_s ratio were studied at differing intervals: ten-minute, hourly, daily and monthly. Figure 7 shows the high positive correlation between Q_p and R_s at ten-minute intervals ($R^2 = 0.992$) with a slope of $1.893 \pm 0.001 \mu\text{mol}\cdot\text{J}^{-1}$. This value is close to the mean value $1.93 \pm 0.15 \mu\text{mol}\cdot\text{J}^{-1}$, with a standard deviation of $\pm 0.15 \mu\text{mol}\cdot\text{J}^{-1}$. The Q_p/R_s ratio had similar values to those reported by other researchers [15], ranging between 1.21 and $2.84 \mu\text{mol}\cdot\text{J}^{-1}$.

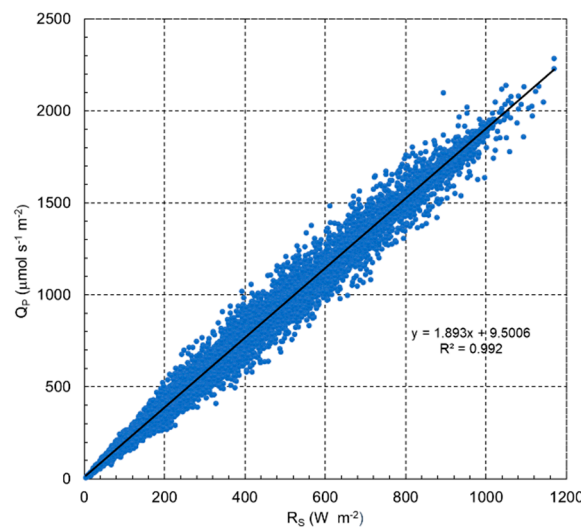


Figure 7. Photosynthetic photon flux density, Q_p ($\mu\text{mol}\cdot\text{s}^{-1}\cdot\text{m}^{-2}$), and broadband solar irradiance, R_s ($\text{W}\cdot\text{m}^{-2}$), measured in Burgos, between April 2019 and January 2020.

Figure 8 shows the box-plot of the mean hourly values of the Q_p/R_s ratio, calculated from the average of the ten-minute data, from sunrise to sunset, using the whole data base. The graph represents the mean value, the median, the three quartiles and both the maximum and the minimum values of the data, as well as the outlier values. Rising in the early hours of the day, Q_p/R_s stabilized in the central hours and tended to decrease at sun set. Higher dispersion of the values in the first and last hours than in the central hours of the day may be observed, as the interquartile range shows. The standard deviation ranged from $0.11 \mu\text{mol}\cdot\text{J}^{-1}$ within the hourly interval starting at 7:00 to $0.17 \mu\text{mol}\cdot\text{J}^{-1}$, within the hourly interval starting at 14:00. The average values were higher than the median values in all hours of the day except for the hourly interval starting at 06:00. The hourly average of the

ratio was $1.910 \pm 0.016 \mu\text{mol}\cdot\text{J}^{-1}$, with maximum and minimum values of $1.98 \pm 0.11 \mu\text{mol}\cdot\text{J}^{-1}$ and $1.75 \pm 0.16 \mu\text{mol}\cdot\text{J}^{-1}$, respectively, at 07:00 and at 19:00 h.

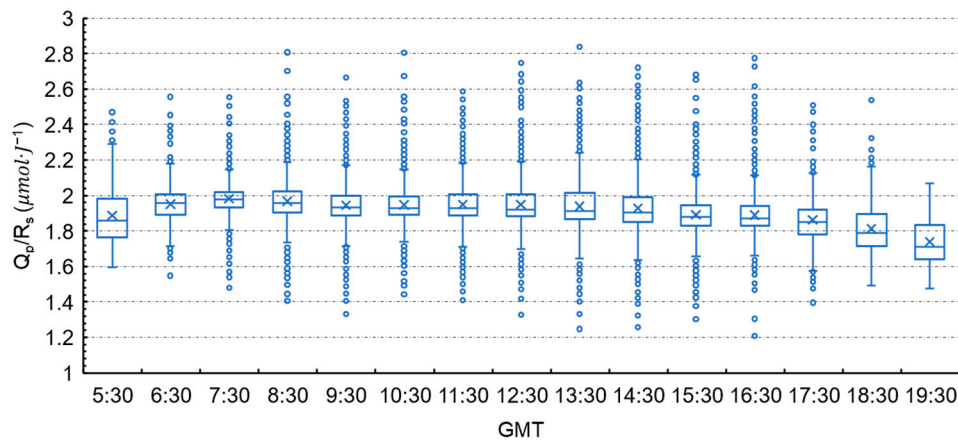


Figure 8. Box-plot of the hourly average of the ratio of photosynthetic photon flux density to broadband solar irradiance, Q_p/R_s . Blue crosses indicate the mean and blue lines inside the box, the median. The limits of the boxes give the 1st, 2nd, and 3rd quartiles, while the extreme whiskers are the minimum and the maximum points. Blue circles represent outliers.

Figure 9 presents the monthly values of the Q_p/R_s ratio calculated with the average of the ten-minute data, using the whole data base. Figure 8 shows that the monthly data were almost constant throughout the central months of the year, from May to October, with a standard deviation between 0.11 and $0.16 \mu\text{mol}\cdot\text{J}^{-1}$, and an interquartile range between 0.10 and $0.15 \mu\text{mol}\cdot\text{J}^{-1}$. November was the measurement campaign month with the highest data dispersion: the interquartile range was $0.24 \mu\text{mol}\cdot\text{J}^{-1}$, with a standard deviation of $0.20 \mu\text{mol}\cdot\text{J}^{-1}$. The maximum value was recorded in April ($1.98 \pm 0.15 \mu\text{mol}\cdot\text{J}^{-1}$), while the minimum was reached in December ($1.91 \pm 0.17 \mu\text{mol}\cdot\text{J}^{-1}$). The monthly average of Q_p/R_s was $1.930 \pm 0.025 \mu\text{mol}\cdot\text{J}^{-1}$. Based on the results of the monthly average of Q_p/R_s , some authors have suggested the existence of a seasonal dependence of this term. Alados et al. [4] recorded higher values in the summer months and lower values from November to January, in Granada, Spain. However, in Greece, Proutsos et al. [47] recorded the highest values for autumn (September) while the lowest averages (March) were recorded in spring, with intermediate values for summer and winter. In Midwestern US [48], the lower values with smaller deviations were recorded in the summer months while the winter months showed higher values of the ratio with larger deviations. In Lhasa (Tibetan Plateau), the ratio of photosynthetically-active to broadband solar radiation increased almost linearly from January to June and decreased until the end of the year in the same way [49]. In this study, slightly higher values were recorded in spring and autumn. The monthly average of the Q_p/R_s ratio was always above the median and the number of outliers above the maximum value was greater and had a higher absolute value than those below the minimum value.

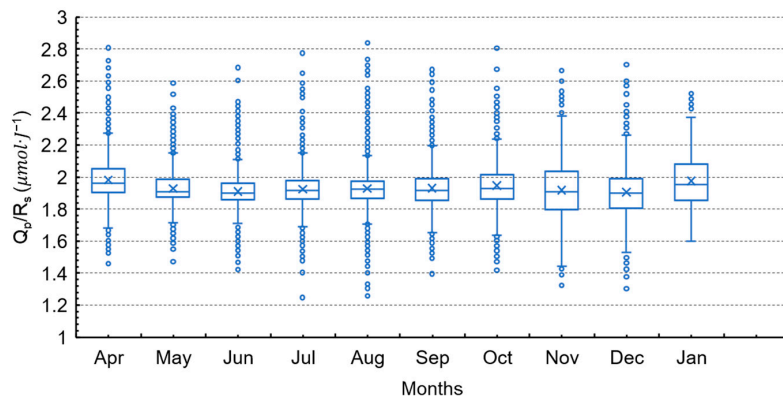
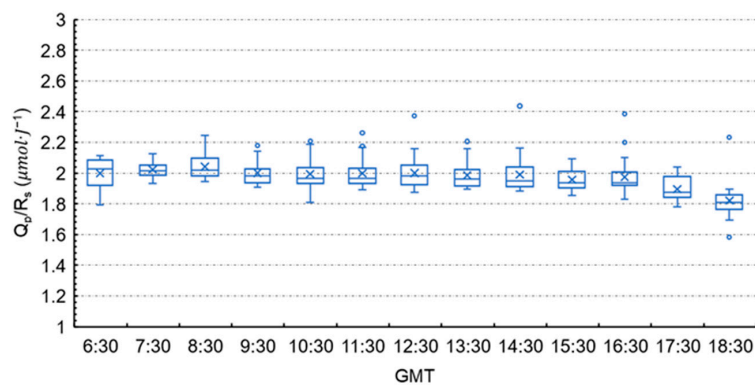
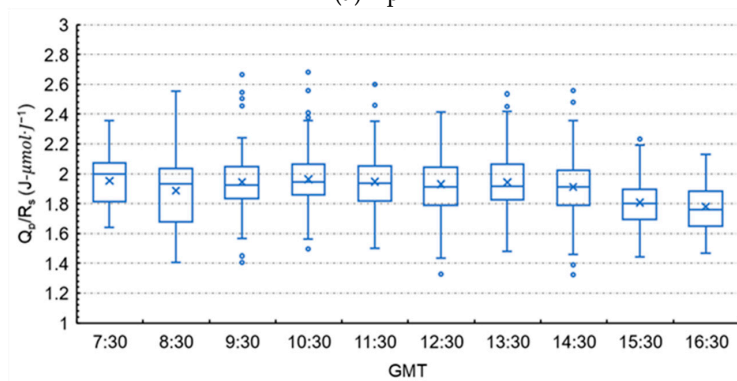


Figure 9. Box-plot of the monthly average of the photosynthetic photon flux density to broadband solar irradiance, Q_p/R_s , ratio.

A deeper analysis was conducted with the hourly values for the two months and the extreme values of the monthly averages of Q_p/R_s . Figure 10 shows the daily pattern of the hourly averages of the Q_p/R_s ratio, for April and November, including information on mean, median and variability through the quartile range. April presented higher and constant values throughout the day, decreasing in the last hours of the day, while November showed lower values of the ratio and more variability throughout the day. Both months presented similar patterns, with constant values of the Q_p/R_s ratio around noon, in a trend that decreased over the last few hours of the day. Apart from the differences in daily means, shown previously, there is also evidence of greater variability during November, mainly in the first hours of the day.



(a) April



(b) November

Figure 10. Daily pattern of the ratio photosynthetically-active photon flux density to broadband solar irradiance.

5. Variability of the Q_p/R_s Ratio with the CIE Standard Sky Types

Figure 11 shows the average photosynthetic photon flux density to broadband solar irradiance, Q_p/R_s , ratio, calculated on a ten minutes basis, for each CIE standard sky type. Clear sky types 12, 13, 14, and 15 showed smaller standard deviations (from 0.06 to 0.11 $\mu\text{mol}\cdot\text{J}^{-1}$) and a smaller interquartile range (from 0.05 to 0.09 $\mu\text{mol}\cdot\text{J}^{-1}$). However, the numbers of outliers were important for all these categories. The dispersion of the data within the categories corresponding to overcast and partial overcast skies was similar, with standard deviations between 0.15 $\mu\text{mol}\cdot\text{J}^{-1}$ (sky type 4) and 0.21 $\mu\text{mol}\cdot\text{J}^{-1}$ (sky type 9) and an interquartile range between 0.16 $\mu\text{mol}\cdot\text{J}^{-1}$ (sky types 3 and 4) and 0.21 $\mu\text{mol}\cdot\text{J}^{-1}$ (sky types 8 and 9). The highest values of the Q_p/R_s ratio were under CIE standard sky types 1, 2, 3, and 4; all categories of overcast sky conditions.

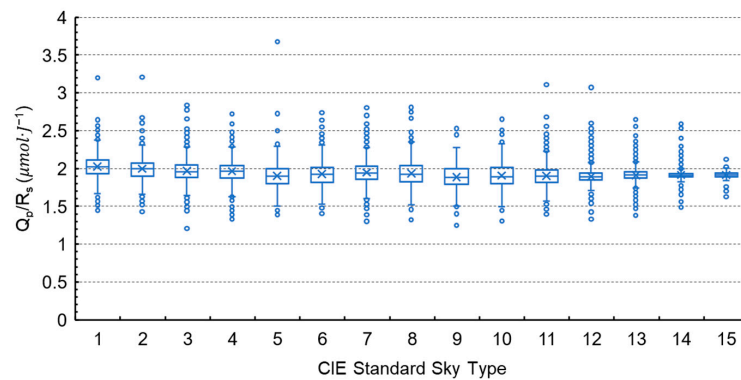


Figure 11. Box-plot ratio of photosynthetic photon flux density to broadband solar irradiance, Q_p/R_s , for each CIE standard sky type.

The categories of clear skies (CIE standard sky types from 11 to 15) showed the smallest values of the ratio. Sky types 5 and 9 presented an anomalous behavior. They are categorized as overcast and partial overcast categories, but the average values of the Q_p/R_s ratios for both sky types were closer to the values of clear sky categories. Furthermore, sky type 9 showed the smallest average value: $1.89 \pm 0.21 \mu\text{mol}\cdot\text{J}^{-1}$. The FOCs of both sky types, 5 and 9, were very scarce in the measurement campaign: 1.65% and 0.64%, respectively. CIE standard sky type 5, described as “overcast, foggy or cloudy, with overall uniformity”, presented high uniformity in terms of illuminance and broadband solar irradiance, as well sky type 9, described as “partly cloudy with a shaded sun position”.

When the 15 CIE standard sky types were reduced to three, (overcast, from sky types 1 to 5, partial, from sky type 6 to 10, and clear sky, from sky types 11 to 15), the average photosynthetic photon flux density to broadband solar irradiance ratio, Q_p/R_s , increased when sky cloudiness increased, as shown in Figure 12.

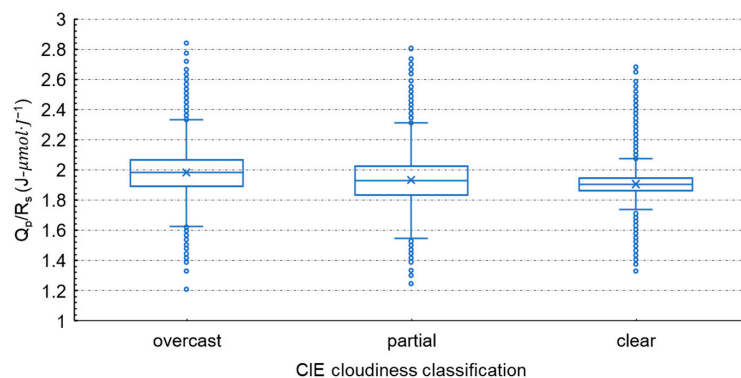


Figure 12. Box-plot of the ratio of photosynthetic photon flux density to broadband solar irradiance, Q_p/R_s , by CIE cloudiness sky classifications.

The average Q_p/R_s ratio for clear skies and for overcast skies was $1.90 \pm 0.11 \mu\text{mol}\cdot\text{J}^{-1}$ and $1.98 \pm 0.16 \mu\text{mol}\cdot\text{J}^{-1}$, respectively. Partial cloudy skies showed the highest dispersion of the data, with standard deviation and interquartile range values of 0.17 and $0.19 \mu\text{mol}\cdot\text{J}^{-1}$, respectively. However, the clear skies dataset had the largest number of outliers.

The Spearman correlation coefficient is a non-parametric measure of rank correlation, to determine the strength and direction of the relationship between two variables. If two datasets X and X' are strongly correlated, then the Spearman coefficient will be 1 (direct correlation) or if otherwise -1 (inverse correlation). Although $r(Q_p, CIE) = 0.56$ (p -value < 0.001) and $r(R_s, CIE) = 0.57$ (p -value < 0.001) both imply a moderate correlation, $(Q_p/R_s, CIE) = -0.23$ (p -value < 0.001). The p -value determine the significance of the results in relation to the null hypothesis (the results are due to random chance). The lower the p -value, the greater the statistical significance of the test and greater the confirmation of the hypothesis [50]. As the p -value was lower than 0.05 in all the tests, there was a statistically significant difference between the average Q_p/R_s ratios for each type of CIE sky, at a significance level of 5%.

When only three CIE categories were considered (clear = 3, partial = 2, and overcast = 1), $r(Q_p, CIE_{cloudiness}) = 0.52$ (p -value < 0.001) and $r(R_s, CIE_{cloudiness}) = 0.52$ (p -value < 0.001), and $(Q_p/R_s, CIE_{cloudiness}) = -0.22$ (p -value < 0.001). From these results, a weak relationship can be established between the value of the Q_p/R_s ratio and the CIE standard sky classification. However, previous results were confirmed in this research, in so far as the ratio of photosynthetic photon flux density to broadband solar irradiance, Q_p/R_s , presented its highest values over cloudy conditions and decreased with clear sky conditions, following the CIE Standard Sky classification as a reference for defining the sky conditions.

6. Conclusions

The analysis of photosynthetic photon flux density to broadband solar radiation ratios registered between April 2019 and January 2020 in Burgos, Spain, at ten-minute intervals, has shown a representative dependency on the sky type conditions classified by CIE taxonomy. The higher values of the Q_p/R_s ratio were for overcast sky types, while the values were lower and more dispersed under clear sky conditions.

Statistically significant differences have been found in the Q_p/R_s ratios for each CIE standard sky type. The overcast sky types presented the highest values of the ratio, with the clear sky categories presenting the lowest and most dispersed values. During the experimental campaign, there were only two exceptions to the expected behavior: sky types 5 and 9. They belonged to covered and partial covered sky type categories, respectively, presenting values closer to the clear sky categories according to the CIE standard. The main characteristic of both categories was a high uniformity in terms of illumination.

The higher dispersion of data corresponding to clear skies categories could be explained by the presence of aerosols or atmospheric turbidity, characteristics of clear sky types 13, 14 and 15, with FOC's 15%, 8% and 7% (Figure 3).

No seasonal dependency of Q_p/R_s can be established, as highlighted in this and the other studies that were reviewed, due mainly to the different sky conditions recorded during the experimental campaigns. As shown in Figure 5, between April 2019 to January 2020 in Burgos, Spain, clear skies predominated in summer, while in winter the overcast conditions presented the highest frequency of occurrence.

The analysis of the hourly values also revealed a daily pattern with higher and more stable values of Q_p/R_s in the first hours of the day that tended to stabilize around noon and to decrease around sunset. The study of the daily pattern of the sky types (clear, overcast and partial) show that, although clear skies are predominant at all hours of the day, the differences of the frequency of occurrence with respect to overcast and partially overcast skies decreases towards noon, as Figure 6 showed.

As has been demonstrated in this study and in others, the most influential factor in the Q_p/R_s value was the presence of overcast sky conditions. Although other authors used different climatological parameters for sky classification, the CIE Standard sky classification has proven itself to offer a good overall framework that can represent the sky conditions, covering the complete spectrum of sky categories.

Author Contributions: Conceptualization, M.D.-M. and C.A.-T.; methodology, A.G.-R. and S.G.-R.; software, A.G.-R.; validation, A.G.-R., M.D.-M.; formal analysis, A.G.-R. and S.G.-R.; investigation, A.G.-R. and S.G.-R.; original draft preparation, M.D.-M.; writing—review and editing, C.A.-T.; visualization, A.G.-R. and S.G.-R.; supervision, M.D.-M. and C.A.-T.; project administration, M.D.-M.; funding acquisition, C.A.-T. All authors have read and agreed to the published version of the manuscript.

Funding: This research was funded by Spanish Ministry of Science and Innovation, grant number RTI2018-098900-B-I00 and Consejería de Educación, Junta de Castilla y León, grant number BU021G19.

Conflicts of Interest: The authors declare no conflict of interest.

References

1. McCree, K.J. The measurement of photosynthetically active radiation. *Sol. Energy* **1973**, *15*, 83–87. [\[CrossRef\]](#)
2. Akitsu, T.; Kume, A.; Hirose, Y.; Ijima, O.; Nasahara, K.N. On the stability of radiometric ratios of photosynthetically active radiation to global solar radiation in Tsukuba, Japan. *Agric. For. Meteorol.* **2015**, *209–210*, 59–68. [\[CrossRef\]](#)
3. Aguiar, L.J.G.; Fischer, G.R.; Ladle, R.J.; Malhado, A.C.M.; Justino, F.B.; Aguiar, R.G.; da Costa, J.M.N. Modeling the photosynthetically active radiation in South West Amazonia under all sky conditions. *Theor. Appl. Climatol.* **2012**, *108*, 631–640. [\[CrossRef\]](#)
4. Alados, I.; Foyo-Moreno, I.; Alados-Arboledas, L. Photosynthetically active radiation: Measurements and modelling. *Agric. For. Meteorol.* **1996**, *78*, 121–131. [\[CrossRef\]](#)
5. McCree, K.J. Test of current definitions of photosynthetically active radiation against leaf photosynthesis data. *Agric. Meteorol.* **1972**, *10*, 443–453. [\[CrossRef\]](#)
6. Landsberg, J.J.; Waring, R.H. A generalised model of forest productivity using simplified concepts of radiation-use efficiency, carbon balance and partitioning. *For. Ecol. Manag.* **1997**, *95*, 209–228. [\[CrossRef\]](#)
7. Kirk, J. Spectral Distribution of Photosynthetically Active Radiation in some South-eastern Australian Waters. *Mar. Freshw. Res.* **1979**, *30*, 81–91. [\[CrossRef\]](#)
8. Pei, F.; Li, X.; Liu, X.; Lao, C. Assessing the impacts of droughts on net primary productivity in China. *J. Environ. Manag.* **2013**, *114*, 362–371. [\[CrossRef\]](#)
9. Tsubo, M.; Walker, S. Relationships between photosynthetically active radiation and clearness index at Bloemfontein, South Africa. *Theor. Appl. Climatol.* **2005**, *80*, 17–25. [\[CrossRef\]](#)
10. Moon, P. Proposed standard solar-radiation curves for engineering use. *J. Frankl. Inst.* **1940**, *230*, 583–617. [\[CrossRef\]](#)
11. Monteith, J.L.; Reifsnnyder, W.E. Principles of Environmental Physics. *Phys. Today* **1973**, *27*, 51–52. [\[CrossRef\]](#)
12. Szeicz, G. Solar radiation for plant growth. *J. Appl. Ecol.* **1974**, *11*, 617–636. [\[CrossRef\]](#)
13. McCartney, H.A. Spectral distribution of solar radiation. II: Global and diffuse. *Q. J. R. Meteorol. Soc.* **1978**, *104*, 911–926. [\[CrossRef\]](#)
14. Al-Shooshan, A.A. Estimation of photosynthetically active radiation under an arid climate. *J. Agric. Eng. Res.* **1997**, *66*, 9–13. [\[CrossRef\]](#)
15. Foyo-Moreno, I.; Alados, I.; Alados-Arboledas, L. A new conventional regression model to estimate hourly photosynthetic photon flux density under all sky conditions. *Int. J. Climatol.* **2017**, *37*, 1067–1075. [\[CrossRef\]](#)
16. Bai, J. Observations and estimations of PAR and solar visible radiation in North China. *J. Atmos. Chem.* **2012**, *69*, 231–252. [\[CrossRef\]](#)
17. Hu, B.; Wang, Y.; Liu, G. Spatiotemporal characteristics of photosynthetically active radiation in China. *J. Geophys. Res. Atmos.* **2007**, *112*. [\[CrossRef\]](#)
18. Meek, D.W.; Hatfield, J.L.; Howell, T.A.; Idso, S.B.; Reginato, R.J. Generalized relationship between photosynthetically active radiation and solar radiation. *J. Agron.* **1984**, *76*, 939–945. [\[CrossRef\]](#)
19. Stanhill, G.; Fuchs, M. The relative flux density of photosynthetically active radiation. *J. Appl. Ecol.* **1977**, *14*, 317–322. [\[CrossRef\]](#)

20. Blackburn, W.J.; Proctor, J.T.A. Estimating photosynthetically active radiation from measured solar irradiance. *Sol. Energy* **1983**, *31*, 233–234. [[CrossRef](#)]
21. Stigter, C.J.; Musabilha, V.M.M. The conservative ratio of photosynthetically active to total radiation in the tropics (Dar es Salaam). *J. Appl. Ecol.* **1982**, *19*, 853–858. [[CrossRef](#)]
22. Rao, C.R.N. Photosynthetically active components of global solar radiation: Measurements and model computations. *Arch. Meteorol. Geophys. Bioclimatol. Ser. B* **1984**, *34*, 353–364. [[CrossRef](#)]
23. Harmel, T.; Chami, M. Estimation of daily photosynthetically active radiation (PAR) in presence of low to high aerosol loads: Application to OLCI-like satellite data. *Opt. Express* **2016**, *24*, A1390–A1407. [[CrossRef](#)] [[PubMed](#)]
24. Bat-Oyun, T.; Shinoda, M.; Tsubo, M. Effects of cloud, atmospheric water vapour and dust on photosynthetically active radiation and total solar radiation in a Mongolian grassland. *J. Arid Land* **2012**, *4*, 349–356. [[CrossRef](#)]
25. Escobedo, J.F.; Gomes, E.N.; Oliveira, A.P.; Soares, J. Modeling hourly and daily fractions of UV, PAR and NIR to global solar radiation under various sky conditions at Botucatu, Brazil. *Appl. Energy* **2009**, *86*, 299–309. [[CrossRef](#)]
26. Finch, D.A.; Bailey, W.G.; McArthur, L.J.B.; Nasitwitwi, M. Photosynthetically active radiation regimes in a southern African savanna environment. *Agric. For. Meteorol.* **2004**, *122*, 229–238. [[CrossRef](#)]
27. Jacovides, C.P.; Tymvios, F.S.; Assimakopoulos, V.D.; Kaltsounides, N.A. The dependence of global and diffuse PAR radiation components on sky conditions at Athens, Greece. *Agric. For. Meteorol.* **2007**, *143*, 277–287. [[CrossRef](#)]
28. Wang, L.; Gong, W.; Lin, A.; Hu, B. Analysis of photosynthetically active radiation under various sky conditions in Wuhan, Central China. *Int. J. Biometeorol.* **2014**, *58*, 1711–1720. [[CrossRef](#)]
29. Udo, S.O.; Aro, T.O. Global PAR related to global solar radiation for central Nigeria. *Agric. For. Meteorol.* **1999**, *97*, 21–31. [[CrossRef](#)]
30. Udo, S.O.; Aro, T.O. New empirical relationships for determining global PAR from measurements of global solar radiation, infrared radiation or sunshine duration. *Int. J. Climatol.* **2000**, *20*, 1265–1274. [[CrossRef](#)]
31. Jacovides, C.P.; Tymvios, F.S.; Papaioannou, G.; Asimakopoulos, D.N.; Theofilou, C.M. Ratio of PAR to broadband solar radiation measured in Cyprus. *Agric. For. Meteorol.* **2004**, *121*, 135–140. [[CrossRef](#)]
32. Alados, I.; Olmo, F.J.; Foyo-Moreno, I.; Alados-Arboledas, L. Estimation of photosynthetically active radiation under cloudy conditions. *Agric. For. Meteorol.* **2000**, *102*, 39–50. [[CrossRef](#)]
33. Suárez-García, A.; Díez-Mediavilla, M.; Granados-López, D.; González-Peña, D.; Alonso-Tristán, C. Benchmarking of meteorological indices for sky cloudiness classification. *Sol. Energy* **2020**, *195*, 499–513. [[CrossRef](#)]
34. Alshaibani, K. Finding frequency distributions of CIE Standard General Skies from sky illuminance or irradiance. *Light. Res. Technol.* **2011**, *43*, 487–495. [[CrossRef](#)]
35. Li, D.H.W.; Cheung, G.H.W. Average daylight factor for the 15 CIE standard skies. *Light. Res. Technol.* **2006**, *38*, 137–152. [[CrossRef](#)]
36. Li, D.H.W.; Lam, T.N.T.; Cheung, K.L.; Tang, H.L. An analysis of luminous efficacies under the CIE standard skies. *Renew. Energy* **2008**, *33*, 2357–2365. [[CrossRef](#)]
37. Li, D.H.W.; Tang, H.L.; Wong, S.L.; Tsang, E.K.W.; Cheung, G.H.W.; Lam, T.N.T. Skies classification using artificial neural networks (ANN) techniques. In Proceedings of the 6th International Conference on Indoor Air Quality, Ventilation and Energy Conservation in Buildings: Sustainable Built Environment, IAQVEC 2007, Sendai, Japan, 28–31 October 2007; pp. 61–68.
38. Torres, J.L.; de Blas, M.; García, A.; Gracia, A.; de Francisco, A. Sky luminance distribution in Pamplona (Spain) during the summer period. *J. Atmos. Sol. Terr. Phys.* **2010**, *72*, 382–388. [[CrossRef](#)]
39. Torres, J.L.; de Blas, M.; García, A.; Gracia, A.; de Francisco, A. Sky luminance distribution in the North of Iberian Peninsula during winter. *J. Atmos. Sol. Terr. Phys.* **2010**, *72*, 1147–1154. [[CrossRef](#)]
40. Tregenza, P.R. Analysing sky luminance scans to obtain frequency distributions of CIE Standard General Skies. *Light. Res. Technol.* **2004**, *36*, 271–279. [[CrossRef](#)]
41. Li, D.H.W.; Chau, N.T.C.; Wan, K.K.W. Predicting daylight illuminance and solar irradiance on vertical surfaces based on classified standard skies. *Energy* **2013**, *53*, 252–258. [[CrossRef](#)]

42. Suárez-García, A.; Granados-López, D.; González-Peña, D.; Díez-Mediavilla, M.; Alonso-Tristán, C. Seasonal characterization of CIE standard sky types above Burgos, northwestern Spain. *Sol. Energy* **2018**, *169*, 24–33. [[CrossRef](#)]
43. Gueymard, C.A.; Ruiz-Arias, J.A. Extensive worldwide validation and climate sensitivity analysis of direct irradiance predictions from 1-min global irradiance. *Sol. Energy* **2016**, *128*, 1–30. [[CrossRef](#)]
44. Littlefair, P.J. A comparison of sky luminance models with measured data from Garston, United Kingdom. *Sol. Energy* **1994**, *53*, 315–322. [[CrossRef](#)]
45. Littlefair, P.J. The luminance distributions of clear and quasi-clear skies. In Proceedings of the CIBSE National Lighting Conference, Cambridge, UK, 27–30 March 1994; pp. 267–283.
46. Kittler, R.; Perez, R.; Darula, S. A new generation of sky standards. In Proceedings of the Eighth European Lighting Conference, Amsterdam, The Netherlands, 11–14 May 1997; pp. 359–373.
47. Proutsos, N.; Liakatas, A.; Alexandris, S. Ratio of photosynthetically active to total incoming radiation above a Mediterranean deciduous oak forest. *Theor. Appl. Climatol.* **2019**, *137*, 2927–2939. [[CrossRef](#)]
48. Yu, X.; Guo, X. Hourly photosynthetically active radiation estimation in Midwestern United States from artificial neural networks and conventional regressions models. *Int. J. Biometeorol.* **2016**, *60*, 1247–1259. [[CrossRef](#)] [[PubMed](#)]
49. Peng, S.; Du, Q.; Lin, A.; Hu, B.; Xiao, K.; Xi, Y. Observation and estimation of photosynthetically active radiation in Lhasa (Tibetan Plateau). *Adv. Space Res.* **2015**, *55*, 1604–1612. [[CrossRef](#)]
50. Spiegel, M.R. *Estadística*, 3rd ed.; McGraw-Hill: Mexico city, Mexico, 2002.

Publisher’s Note: MDPI stays neutral with regard to jurisdictional claims in published maps and institutional affiliations.



© 2020 by the authors. Licensee MDPI, Basel, Switzerland. This article is an open access article distributed under the terms and conditions of the Creative Commons Attribution (CC BY) license (<http://creativecommons.org/licenses/by/4.0/>).

Advances in Space Research

Validation and Calibration of Models to Estimate Photosynthetically Active Radiation Considering Different Time Scales and Sky Conditions

--Manuscript Draft--

Manuscript Number:	AISR-D-22-00024
Article Type:	ES - Earth Sciences
Keywords:	Photosynthetically Active Radiation; Solar irradiance; sky types; Model calibration
Corresponding Author:	Ignacio García Ruiz, Ph.D. Public University of Navarre: Universidad Publica de Navarra Pamplona, Navarra SPAIN
First Author:	Marian de Blas, PhD
Order of Authors:	Marian de Blas, PhD Ignacio García Ruiz, Ph.D. Ana García-Rodríguez José Luis Torres, PhD
Abstract:	<p>Photosynthetically Active Radiation (PAR) is a fundamental parameter for developing plant productivity models. Nevertheless, instrumentation for measuring PAR and to record it is scarce at conventional meteorological stations. Several procedures have therefore been proposed for PAR indirect estimation. In this work, 21 previously published analytical models that correlate PAR with easily available meteorological parameters are collected. Although longer time scales were considered in the original publications, a minute range was applied in this work to calibrate the PAR models. In total, more than 10 million input records were gathered from the SURFRAD station network from a 10-year long time series with data frequencies recorded every 1 minute. After calibration, the models were validated for minute and hourly data, obtaining in all cases low fitting errors. The model for the estimation of PAR should then be selected, solely considering the meteorological variables available at the specific location. When applying the calibrated models to input data classified according to sky conditions (from clear to overcast), the PAR models continued to perform satisfactorily, although the error statistics of some models for overcast skies that establish relative values worsened.</p>
Suggested Reviewers:	Harry D. Kambezidis, PhD Research Director, National Observatory of Athens: Ethnikon Asteroskopeion Athenon harry@noa.gr Jesús Polo, PhD Senior Researcher, CIEMAT: Centro de Investigaciones Energeticas Medioambientales y Tecnologicas jesus.polo@ciemat.es Luis Manuel Navas, PhD Professor, Universidad de Valladolid luismmanuel.navas@uva.es

Validation and Calibration of Models to Estimate Photosynthetically Active Radiation Considering Different Time Scales and Sky Conditions

Marian de Blas^a, Ana García-Rodríguez^b, Ignacio García^{a,*}, José Luis Torres^a

^a*Institute of Smart Cities (ISC), Department of Engineering, Public University of Navarre, Campus Arrosadía, 31006 Pamplona, Spain*

^b*Research Group Solar and Wind Feasibility Technologies (SWIFT), Electromechanical Engineering Department, University of Burgos, 09006 Burgos, Spain*

Abstract

Photosynthetically Active Radiation (*PAR*) is a fundamental parameter for developing plant productivity models. Nevertheless, instrumentation for measuring *PAR* and to record it is scarce at conventional meteorological stations. Several procedures have therefore been proposed for *PAR* indirect estimation. In this work, 21 previously published analytical models that correlate *PAR* with easily available meteorological parameters are collected. Although longer time scales were considered in the original publications, a minute range was applied in this work to calibrate the *PAR* models. In total, more than 10 million input records were gathered from the SURFRAD station network from a 10-year long time series with data frequencies recorded every 1 minute. After calibration, the models were validated for minute and hourly data, obtaining in all cases low fitting errors. The model for the estimation of *PAR* should then be selected, solely considering the meteorological variables available at the specific location. When applying the calibrated models to input data classified according to sky conditions (from clear to overcast), the *PAR* models continued to perform satisfactorily, although the error statistics of some models for overcast skies that establish relative values worsened.

Keywords: Photosynthetically active radiation, solar irradiance, sky types, model calibration

*Corresponding author.

Email address: ignacio.garcia@unavarra.es (Ignacio García)

1 Nomenclature

2	<i>AIC</i>	Akaike Information Criterion
3	<i>BIC</i>	Bayesian Information Criterion
4	<i>MPE</i>	Mean Percentage Error
5	<i>PAR</i>	Photosynthetically Active Radiation, expressed either in irradiance units ($\text{W} \cdot \text{m}^{-2}$)
6		or as photon flux density (PPFD) ($\mu\text{mol} \cdot \text{m}^{-2} \cdot \text{s}^{-1}$)
7	<i>RMSE</i>	Root Mean Squared Error
8	<i>RMSE_R</i>	Relative Root Mean Squared Error
9	<i>RSD</i>	Relative Standard Deviation
10	BSRN	Baseline Surface Radiation Network
11	NIR	Near InfraRed irradiance ($\text{W} \cdot \text{m}^{-2}$)
12	QC	Quality Control
13	E_i	Calculated value of <i>PAR</i> ($\text{W} \cdot \text{m}^{-2}$)
14	E_{avg}	Average of calculated values of <i>PAR</i> ($\text{W} \cdot \text{m}^{-2}$)
15	G	Global solar horizontal irradiance ($\text{W} \cdot \text{m}^{-2}$)
16	G_b	Direct solar horizontal irradiance ($\text{W} \cdot \text{m}^{-2}$)
17	G_d	Diffuse solar horizontal irradiance ($\text{W} \cdot \text{m}^{-2}$)
18	M_i	Measured value of <i>PAR</i> ($\text{W} \cdot \text{m}^{-2}$)
19	M_{avg}	Average of measured values of <i>PAR</i> ($\text{W} \cdot \text{m}^{-2}$)
20	N	Total number of <i>PAR</i> data
21	P_0	Extra-terrestrial Photosynthetically Active Radiation on a horizontal surface ($\text{W} \cdot \text{m}^{-2}$)
22	P_{sc}	Solar constant of Photosynthetically Active Irradiance (preset value $530.8 \text{ W} \cdot \text{m}^{-2}$)
23	R^2	Determination coefficient
24	S_i	Sky Index (Igawa, 2014)
25	T_d	Dew point temperature ($^{\circ}\text{C}$)
26	k_T	Clearness index (global solar irradiance over the corresponding irradiance out of
27		the atmosphere)

28	k_d	Diffuse fraction (diffuse solar horizontal irradiance over global solar irradiance)
29	m	Relative optical air mass
30	w	Precipitable water (cm)
31	Δ	Sky's brightness (Perez et al., 1990)
32	ε	Sky's clearness (Perez et al., 1990)
33	θ_z	Solar zenith angle ($^\circ$)

34 1. Introduction

35 Photosynthetically Active Radiation (*PAR*) incident on the vegetal canopy
36 is one of the basic parameters for the characterization of plant growth behav-
37 ior, as plants use energy from solar radiation, emitted within the 400 and 700
38 nm (wave band) spectral range, to activate photosynthesis that transforms
39 solar into chemical energy.

40 The intensity of *PAR* that plants process is a key parameter to con-
41 struct productivity models and cultivation strategies aimed at optimizing
42 the use of energy. A number of published references considered the *PAR*
43 levels that crops process as an input to model the behavior of mixed plan-
44 tations: coconut/corn (Dauzat and Eroy, 1997) maize/peanut (Awal et al.,
45 2006), wheat/cotton (Zhang et al., 2008), maize/soybean; for analyzing the
46 metabolic behavior of aquatic species (O’Gorman et al., 2012); or the growth
47 and the flowering of some plants (Bredmose and Costes, 2017). Research in
48 the field of plant physiology and ecology has included the value of the in-
49 cident *PAR* as a key variable for modeling the photosynthetic behavior of
50 plants in response to sunlight (Bhattacharya, 2019; Campillo et al., 2012;
51 Jajoo et al., 2014; Ogburn and Edwards, 2010), for selecting photosyntheti-
52 cally efficient cultivars (Peng, 2000), for analyzing the metabolic behavior of
53 aquatic species (O’Gorman et al., 2012) and, in some examples, plant growth
54 and flowering (Bredmose and Costes, 2017).

55 *PAR* can be measured in energetic terms ($\text{W} \cdot \text{m}^2$) or in photobiological
56 units, i.e., in terms of photon flux density ($\mu\text{mol} \cdot \text{m}^{-2} \cdot \text{s}^{-1}$). The Photosyn-
57 thetic Photon Flux Density (PPFD) is the number of photons in the 400-700
58 nm waveband incident on unit surface area in unit time (Foyo-Moreno et al.,

59 [2017](#)). [McCree \(1972\)](#) proposed a widely employed constant ratio of 4.57
60 $\mu\text{mol} \cdot \text{J}^{-1}$ between the PPFD and the incident *PAR* in terms of energy.
61 Actually, there is a monochromatic relationship between these two variables
62 and, therefore, the integrated broadband photon flux cannot be directly ob-
63 tained from the global irradiance in the 400-700 nm waveband ([Ross and](#)
64 [Sulev, 2000](#); [Sun et al., 2017](#)). Notwithstanding, [Akitsu et al. \(2015\)](#) ana-
65 lyzed the dependence of McCree’s ratio on climatic factors and considered
66 the constant value acceptable for most purposes.

67 Existing instruments for measuring *PAR* can be classified into two classes
68 ([Möhtus et al., 2012](#)): *PAR* quantum photovoltaic sensors that are sensitive
69 to photoelectric effects; and *PAR* energy sensors, which mainly include ther-
70 moelectric instruments. In addition, some field instruments of these technolo-
71 gies have been developed for measuring absorbed *PAR* in crops and pastures
72 ([Rahman et al., 2014](#)) and for obtaining the daily light integral in greenhouses
73 ([Torres and Lopez, 2012](#)). Nevertheless, despite the *PAR* value being a key
74 variable in physiological models of plant growth, there are only a limited
75 number of meteorological stations around the world that provide data with
76 reliable measurements of this parameter for research ([Foyo-Moreno et al.,](#)
77 [2017](#)). It is also difficult to maintain measurement accuracy and there is no
78 standard for the quality control of *PAR* measurements ([Mizoguchi et al.,](#)
79 [2010, 2013](#)).

80 More often than not, *PAR* is therefore indirectly estimated from other
81 parameters. The physical relationship between *PAR* and global irradiance
82 (*G*) depends on the absorption and dispersion caused by the atmospheric
83 components such as aerosol, water vapor, ozone, and clouds ([Janjai et al.,](#)

84 2015).

85 Some current *PAR* estimation models include inputs obtained from satel-
86 lite data (Hao et al., 2020; Janjai et al., 2015; Vindel et al., 2018b). Like-
87 wise, radiative transfer models use either satellite or terrestrial observations
88 or both (Akitsu et al., 2015; Li et al., 2015; Tang et al., 2017; Wandji Nyamsi
89 et al., 2015, 2019).

90 In general, *PAR* results from physical models are very good, but the
91 required input and the application of the models can be difficult for first-
92 time users. In contrast, semi-empirical models can correlate *PAR* or the
93 *PAR/G* ratio with other parameters directly measured at weather stations
94 or derived from weather station data (Aguiar et al., 2011; Alados et al.,
95 1996; Foyo-Moreno et al., 2017; Ge et al., 2011; Hu et al., 2007; Janjai et al.,
96 2015; Li et al., 2010; Mizoguchi et al., 2013; Wang et al., 2013; Yu et al.,
97 2015; Vindel et al., 2018a). Various models also use artificial neural network
98 techniques with calculable parameters (Ferrera-Cobos et al., 2020; García-
99 Rodríguez et al., 2021; Jacovides et al., 2015; Wang et al., 2016; Zempila
100 et al., 2016).

101 The models cited above considered a time scale ranging from 10 minutes
102 to monthly *PAR* values. Literature reviews revealed that the fitting quality
103 of the different models varied as a function of meteorological, seasonal, and
104 geographic characteristics of locations. The correlation between *PAR* and
105 the meteorological parameters also differed, depending on the local conditions
106 (García-Rodríguez et al., 2020, 2021; Wang et al., 2016). An exhaustive
107 review of empirical models for *PAR* estimation can be found in Nwokolo
108 and Amadi (2018).

109 In the study by [Li et al. \(2010\)](#), the PAR/G ratio increased under high
110 humidity or cloudy conditions, because water vapor content in the atmo-
111 sphere increases the absorption of radiation in the NIR spectrum, whereas
112 the absorption of radiation is unaffected in the PAR region. [Yu et al. \(2015\)](#)
113 analyzed the influence of parameters on semi-empirical models using experi-
114 mental PAR data from the Surface Radiation Budget Network (SURFRAD)
115 for a daily temporal resolution. They observed a high correlation between
116 daily PAR/G and the clearness index (k_T). This ratio denoted high values
117 for low k_T and vice-versa. Likewise, a negative correlation was obtained be-
118 tween the PAR/G ratio and the cosine of the solar zenith angle ($\cos \theta_z$), dew
119 point temperature (T_d) and k_T values and a positive correlation between that
120 ratio and both the diffuse fraction (k_d) and the sky brightness (Δ) values.
121 They also concluded, unlike other published research, that the dew point
122 value, used to describe atmospheric humidity, had no significant influence on
123 the PAR/G ratio.

124 A physical model was published ([Sun et al., 2017](#)) to estimate PAR from
125 both global and direct radiation in the spectral region between 200 and 700
126 nm. This model was validated using data with a 1-minute temporal resolution
127 that included a part of the experimental PAR data used in the present
128 research.

129 In general, the semi-empirical models reported in the literature yielded
130 accurate results, by means of a simple mathematical expression, when applied
131 under local conditions similar to those considered for calibration. In contrast,
132 the transferability of models to other locations and their local adaptation still
133 needs further discussion ([García-Rodríguez et al., 2021](#)).

134 When the calibration site and the location of interest have comparable
135 atmospheric conditions, it is expected that the atmospheric conditions in
136 both places will cause a similar attenuation of solar radiation in the *PAR*
137 wavelength range. Therefore, the model for *PAR* determination should pro-
138 duce accurate results. Different coefficients in similar equations have been
139 proposed, to take into account the sky conditions (Ferrera-Cobos et al., 2020;
140 Jacovides et al., 2007; Wang et al., 2013; Yu et al., 2015).

141 In this work, 21 models for *PAR* estimation were calibrated and evalu-
142 ated. For this purpose, a 10-year long series of 1-minute resolution data was
143 configured from data recorded at seven weather stations within the SUFRAD
144 network, covering a wide range of climatic conditions in the USA. The main
145 objective of this work is to present models that can be generally applied and
146 that provide accurate *PAR* values using meteorological variables measured
147 at ground stations and considering time intervals between 1 minute and 1
148 hour. An objective that was achieved with a data set of more than 10 mil-
149 lion *PAR* and meteorological measurements that are representative of a large
150 variety of regional and weather conditions.

151 The expected errors in *PAR* estimation when the 21 models under anal-
152 ysis were applied were firstly quantified for all sky conditions together and
153 then considering the prevailing sky conditions. By doing so, users who need
154 to know the *PAR* at a given location are provided with a set of easy-to-
155 implement equations and they can select the most appropriate model, de-
156 pending on the available meteorological input data.

157 This paper is organized into five sections. The meteorological data and its
158 classification in sky types are detailed in Section 2. In Section 3, the *PAR*

159 models and the calibration procedure is described. The calibrated models
160 for the minute-time scale and the statistical analysis of the results when the
161 models were applied to two-time scales (minute and hourly) and to different
162 sky types are presented in Section 4. Finally, the conclusions are detailed in
163 Section 5.

164 2. Weather data

165 We used high quality datasets retrieved from the Surface Radiation Bud-
166 get Network (SURFRAD) FTP Server based in the United States: *PAR*
167 on the horizontal plane, global and diffuse solar irradiance on the horizontal
168 plane, air temperature and relative humidity.

169 Global *PAR* was measured with an LI-COR Quantum sensor within the
170 400 to 700 nm broadband range. *PAR* values are given in $\text{W} \cdot \text{m}^{-2}$. The *G*
171 values were obtained from a Spectrolab SR-75 pyranometer and diffuse irradi-
172 ance was measured on the horizontal plane with an Eppley 8-48 pyranometer.
173 Both pyranometers measure data within the 280-3000 nm broadband range.

174 The seven stations belonging to the SURFRAD network are distributed
175 throughout different climatic areas in the United States, as shown in Figure
176 1. The ground properties of these stations were described in [Wandji Nyamsi
177 et al. \(2019\)](#). Table 1 shows the geographical location and the basic climatic
178 data from the seven weather stations.

179 All the SURFRAD stations never started to take measures at the same
180 time. The earliest radiation measurements were taken in 1995 and the latest,
181 in 2003. Notwithstanding, with the aim of comparing similar series of data for
182 model calibration purposes, we considered a common time range of records

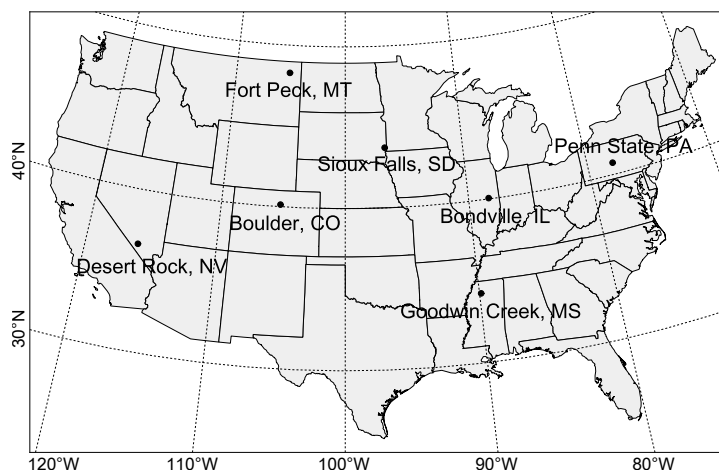


Figure 1. Locations of the seven SURFRAD weather stations.

Table 1. Geographical location and basic climatic data from the seven SURFRAD weather stations.

Station	Code	Latitude (°N)	Longitude (°W)	Elevation (m)	Average temperature (°C)	Average relative humidity (%)	Average G ($W \cdot m^{-2}$)	Average PAR ($W \cdot m^{-2}$)
Bondville, Illinois	BON	40.0519	88.3731	230	11.53	72.65	170.46	73.82
Table Mountain, Boulder, Colorado	TBL	40.1250	105.237	1689	12.25	46.92	193.71	84.29
Desert Rock, Nevada	DRA	36.6237	116.019	1007	18.81	28.04	235.18	104.22
Fort Peck, Montana	FPK	48.3078	105.102	634	5.84	67.24	161.89	72.66
Goodwin Creek, Mississippi	GWN	34.2547	89.8729	98	16.73	71.89	182.14	79.07
Penn. State Univ., Pennsylvania	PSU	40.7201	77.9309	376	10.52	70.01	152.83	65.73
Sioux Falls, South Dakota	SXF	43.734	96.6233	473	7.96	73.13	166.50	74.40

183 between 1/1/2009 and 31/12/2018 at every station, with a temporal resolu-
 184 tion of 1 minute. Irradiance data collected at the stations within the network
 185 had previously passed the Baseline Surface Radiation Network (BSRN) qual-
 186 ity control checks, as explained in [Long and Dutton \(2002\)](#). Unfortunately,
 187 criteria for Quality Control (QC) of PAR are neither covered in the BSRN

188 procedures or in any assessment standards we have consulted in the bibliogra-
189 phy available to us. Therefore, an in-house quality-control method described
190 below was set in accordance with the physical limits of *PAR*. Global *PAR*
191 on the horizontal plane cannot be higher than extraterrestrial *PAR* on the
192 horizontal plane corresponding to the same time. Extraterrestrial *PAR* on
193 the horizontal plane (P_0) is calculated with a correction factor (f_c) applied
194 to the *PAR* solar constant (P_{sc}) that takes into account the eccentricity of
195 the Earth’s orbit and then multiplies the result by the cosine of the solar
196 zenith angle, Equation (1).

$$P_0 = f_c P_{sc} \cos \theta_z. \quad (1)$$

197 [Gueymard \(2018\)](#) obtained a value of $1361.1 \text{ W} \cdot \text{m}^{-2}$ for the solar con-
198 stant or total solar irradiance, but no standardized value for the irradiance
199 in the *PAR* spectral range. The irradiance curve between 400 and 700 nm
200 of the extraterrestrial spectrum proposed by [Gueymard et al. \(2002\)](#) was
201 integrated, in order to estimate this constant, resulting in a value of 530.8
202 $\text{W} \cdot \text{m}^{-2}$. Gueymard’s extraterrestrial spectrum is proposed to determine
203 the reference AM1.5 spectrum specified in standard IEC 60904-3:2019 ([IEC,](#)
204 [2019](#)). Data corresponding to solar elevation angles lower than 5° were dis-
205 carded to avoid the cosine response problems of global irradiance and *PAR*
206 measuring instruments.

207 Table 2 shows the number of available measurements at each station to
208 calibrate and to validate *PAR* estimation models after having passed the QC.
209 Calibration of a model implies using 50% of the data, alternatively chosen,
210 for the model calibration and 50% to validate the resulting expressions. Data

211 are classified into five sky types according to the Sky Index (S_i) proposed
 212 by [Igawa \(2014\)](#) that can be seen in Table 3. This classification analyzes the
 213 influence of a given atmospheric condition, represented by the sky type, on
 214 the behavior of the models to be evaluated.

Table 2. Total data and data classified according to the sky type that have passed the quality control and the solar minimum elevation parameter for each station. Time series includes data from 2009 to 2018.

Station	All sky	Clear	I-Clear	Intermediate	I-Overcast	Overcast
BON	1371257	636401	259743	352698	105381	17034
%	100	46.41	18.94	25.72	7.68	1.24
DRA	1852600	1399386	185258	214100	49715	4141
%	100	75.54	10	11.56	2.68	0.22
FPK	1363076	682583	232362	323409	108049	16673
%	100	50.08	17.05	23.73	7.93	1.22
GWN	1478690	700298	265390	340367	138794	33841
%	100	47.36	17.95	23.02	9.39	2.29
PSU	1310735	490228	216272	348225	200990	55020
%	100	37.4	16.5	26.57	15.33	4.2
SXF	1413606	701128	229540	327663	130533	24742
%	100	49.6	16.24	23.18	9.23	1.75
TBL	1545048	883883	182998	314297	138336	25534
%	100	57.21	11.84	20.34	8.95	1.65
Total	10335012	5493907	1571563	2220759	871798	176985
%	100	53.16	15.21	21.49	8.44	1.71

Table 3. Sky classification according to the Sky Index (Si) proposed by [Igawa \(2014\)](#) and PAR/G mean values and standard deviation obtained for each sky type.

Sky classification	Sky Index (Si)
Clear Sky (Clear)	<0.15
Intermediate Clear Sky (I-Clear)	$0.15 \leq Si < 0.3$
Intermediate Sky (Intermediate)	$0.3 \leq Si < 0.9$
Intermediate Overcast Sky (I-Overcast)	$0.9 \leq Si < 1.15$
Overcast Sky (Overcast)	$Si \geq 1.15$

215 3. Methodology

216 Table 4 shows the mathematical expressions corresponding to the 21 mod-
 217 els considered in this work for estimating PAR .

218 SURFRAD stations register a large number of meteorological variables,
 219 but only those necessary for the application of the models are considered in
 220 this project: global PAR on the horizontal plane, global and diffuse solar
 221 irradiance on the horizontal plane, and air temperature and relative humid-
 222 ity. Various models are used to estimate atmospheric water vapor content
 223 that include as a variable either the dew point, T_d ($^{\circ}\text{C}$) (e.g., M1, M3; M8;
 224 M10), or the precipitable water content, w (cm) (e.g. M11, M13), or the va-
 225 por pressure, e (hPa) (e.g., M18, M19). These parameters are not directly
 226 registered in the stations; hence they are estimated on the basis of either
 227 air temperature or relative humidity. Notice that M21 is a variation of M15
 228 which includes an independent term.

229 Models M1 to M10 for the PAR/G fraction were previously calibrated
 230 by [Yu et al. \(2015\)](#), considering daily values obtained from the SURFRAD

Table 4. Models evaluated for PAR estimation.

Model	Expression	Variables	Reference
M1	$PAR = G(a_1 \ln \varepsilon + b_1 \ln \Delta + c_1 T_d + d_1 \cos^2 \theta_z + f_1)$	$G, \varepsilon, \Delta, T_d, \cos \theta_z$	Alados et al. (1996)
M2	$PAR = G(a_2 \ln \varepsilon + b_2 \ln \Delta + c_2 \cos^2 \theta_z + d_2)$	$G, k_d, \Delta, \cos \theta_z$	Alados et al. (1996)
M3	$PAR = G(a_3 \ln k_T + b_3 T_d + c_3 \cos \theta_z + d_3)$	$G, k_T, T_d, \cos \theta_z$	Alados et al. (1996)
M4	$PAR = G(a_4 \ln k_T b_4 \cos \theta_z + c_4)$	$G, k_T, \cos \theta_z$	Alados et al. (1996)
M5	$PAR = G(a_5 \ln k_T + b_5)$	G, k_T	Wandji Nyamsi et al. (2019)
M6	$PAR = G[a_6 (\ln k_T)^2 + b_6 \ln k_T + c_6]$	G, k_T	Yu et al. (2015)
M7	$PAR = G(a_7 \ln k_d + b_7 \ln \Delta + c_7)$	G, Δ, k_d	Yu et al. (2015)
M8	$PAR = G[a_8 (\ln k_T)^2 + b_8 \ln k_T + c_8 T_d + d_8]$	G, k_T, T_d	Yu et al. (2015)
M9	$PAR = G[a_9 (\ln k_T)^2 + b_9 \ln k_T + c_9 \cos \theta_z + d_9]$	$G, k_T, \cos \theta_z$	Yu et al. (2015)
M10	$PAR = G[a_{10} (\ln k_T)^2 + b_{10} \ln k_T + c_{10} T_d + d_{10} \cos \theta_z + f_{10}]$	$G, k_T, T_d, \cos \theta_z$	Yu et al. (2015)
M11	$PAR = G(a_{11} \ln \varepsilon + b_{11} \ln \Delta + c_{11} \ln w + d_{11} \cos \theta_z + f_{11})$	$G, \varepsilon, \Delta, w, \cos \theta_z$	Hu et al. (2007)
M12	$PAR = G(a_{12} \ln \varepsilon + b_{12} \ln \Delta + c_{12} \cos \theta_z + d_{12})$	$G, \varepsilon, \Delta, \cos \theta_z$	Hu et al. (2007)
M13	$PAR = G(a_{13} \ln k_T + b_{13} w + c_{13} \cos \theta_z + d_{13})$	$G, k_T, w, \cos \theta_z$	Hu et al. (2007)
M14	$PAR = (a_{14} k_T + b_{14} k_T^2 + c_{14} k_T^3 + d_{14}) (\cos \theta_z)^{f_{14}}$	$k_T, \cos \theta_z$	Wang et al. (2013)
M15	$PAR = a_{15} k_T \cos \theta_z$	$k_T, \cos \theta_z$	Foyo-Moreno et al. (2017)
M16	$PAR = a_{16} G + b_{16}$	G	Aguiar et al. (2011)
M17	$PAR = a_{17} G + b_{17} k_T + c_{17}$	G, k_T	Aguiar et al. (2011)
M18	$PAR = a_{18} G + b_{18} k_T + c_{18} \Delta e + d_{18}$	G, k_T, e	Aguiar et al. (2011)
M19	$PAR = G(a_{19} \ln k_T + b_{19} \ln m + c_{19} e + d_{19})$	$G, k_T, m^{(*)}, e$	Mizoguchi et al. (2013)
M20	$PAR = a_{20} G + b_{20} G \cos \theta_z + c_{20} G k_T + d_{20}$	$G, k_T, \cos \theta_z$	Ge et al. (2011)
M21	$PAR = a_{23} k_T \cos \theta_z + b_{23}$	$k_T, \cos \theta_z$	Variation of M15

(*) Relative optical air mass (m) calculated according to [Kasten and Young \(1989\)](#).

231 station network over the period between 2009 and 2010 and for all sites and
232 all sky conditions together. The resulting R^2 values ranged from 0.4599 (M5)
233 to 0.5475 (M10), which are low values for this parameter, and RMSE values
234 (in $\text{MJ} \cdot \text{m}^{-2}$) from 0.02131 (M9) to 0.02326 (M7). It should be noted that
235 [Yu et al. \(2015\)](#) attributed models M5 to M10 to various authors, but on
236 consulting the referenced publications, it was found that the models and
237 the citations could not be cross-referenced. In this work, we have therefore
238 attributed the models whose original reference is uncertain to [Yu et al. \(2015\)](#).

239 We downloaded 10335012 data items (Table 2) from all stations that had
 240 passed the QC to conduct the calibration process described in this work
 241 and to fit the results of models M1 to M21. All the models are fitted for
 242 PAR (in $W \cdot m^{-2}$) and not for the PAR/G fraction, in order to achieve
 243 homogeneity. However, models M1 to M13 and M19 were originally published
 244 considering PAR/G as the dependent variable. A minute time base was used
 245 to adjust the models, because the PAR values obtained with this frequency
 246 were thought to provide users with useful input data for later studies that
 247 might require in-depth analysis. The behavior of the models obtained from
 248 the adjustment considering an hourly basis will also be evaluated, since data
 249 from the input parameters required in the models is often available at this
 250 frequency. Although the models could be tested for larger time bases (daily
 251 PAR values), PAR values of that frequency are not considered to be of
 252 practical interest. In each case, the models that offered the best results were
 253 selected.

254 The following statistics, described by Equations (2) to (6), were used for
 255 the validation of the models:

- 256 • Determination coefficient:

$$R^2 = \frac{\sum_{i=1}^N (E_i - E_{avg})(M_i - M_{avg})}{\left\{ \left[\sum_{i=1}^N (E_i - E_{avg})^2 \right] \left[\sum_{i=1}^N (M_i - M_{avg})^2 \right] \right\}^{0.5}}. \quad (2)$$

- 257 • Root Mean Squared Error:

$$RMSE = \left[\frac{1}{N} \sum_{i=1}^N (E_i - M_i)^2 \right]^{0.5}. \quad (3)$$

- 258 • Relative Root Mean Squared Error:

$$RMSEr(\%) = \frac{100}{M_{avg}} \left[\frac{1}{N} \sum_{i=1}^N (E_i - M_i)^2 \right]^{0.5}. \quad (4)$$

- 259 • Relative Standard Deviation:

$$RSD(\%) = \left[\frac{1}{N} \sum_{i=1}^N \left(\frac{E_i - M_i}{M_i} \right)^2 \right]^{0.5} 100. \quad (5)$$

- 260 • Mean Percentage Error:

$$MPE(\%) = \frac{1}{N} \left(\sum_{i=1}^N \frac{E_i - M_i}{M_i} \right) 100, \quad (6)$$

261 where E_i is the calculated value, E_{avg} is the mean of the calculated
 262 values, M_i is the measured value, M_{avg} is the mean of the measured
 263 values and N is the total number of data items.

264 4. Results and Discussion

265 Table 5 shows the results of the coefficients for models M1 to M21, cali-
 266 brated for all sites and all sky types together.

267 Figure 2a shows the statistical results derived from the fit of the experi-
 268 mental data obtained at minute frequency with the theoretical models. All
 269 the models yielded very satisfactory fitted results, with high values of the co-
 270 efficient of determination R^2 over 0.99 and $RMSE$ values ranging from 8.416
 271 $W \cdot m^{-2}$ in M10 to 10.93 $W \cdot m^{-2}$ in M15. As can be seen, relative deviations
 272 are low, although in some of the models some of the statistics were some-
 273 what higher. Based on these results of the models under study, it cannot be

Table 5. Calibrated models for PAR using 1-minute input data.

Model	Calibrated expression
M1	$PAR = G(-0.0270876\varepsilon - 0.028342 \ln \Delta + 0.000152279T_d - 0.0206671 \cos^2 \theta_z + 0.425525)$
M2	$PAR = G(-0.0280839 \ln \varepsilon - 0.0286075 \ln \Delta - 0.0182345 \cos^2 \theta_z + 0.425987)$
M3	$PAR = G(-0.0278875 \ln k_T + 0.000129279T_d - 0.028706 \cos \theta_z + 0.437906)$
M4	$PAR = G(-0.0295837 \ln k_T - 0.0258378 \cos \theta_z + 0.435928)$
M5	$PAR = G(-0.0350336 \ln k_T + 0.415212)$
M6	$PAR = G[-0.0340535 (\ln k_T)^2 - 0.0757318 \ln k_T + 0.406944]$
M7	$PAR = G(0.0336608 \ln k_d - 0.0349165 \ln \Delta + 0.413051)$
M8	$PAR = [-0.0349876 (\ln k_T)^2 - 0.0774526 \ln k_T - 0.0000716119T_d + 0.406896] (36)$
M9	$PAR = G[-0.0197733 (\ln k_T)^2 - 0.0538075 \ln k_T - 0.02303 \cos \theta_z + 0.428876]$
M10	$PAR = G[-0.0169287 (\ln k_T)^2 - 0.0490527 \ln k_T + 0.0000967929T_d - 0.0255814 \cos \theta_z + 0.431371]$
M11	$PAR = G(-0.0271005 \ln \varepsilon - 0.0284931 \ln \Delta + 0.0022675 \ln w - 0.0297581 \cos \theta_z + 0.435327)$
M12	$PAR = G(-0.028097 \ln \varepsilon - 0.0287232 \ln \Delta - 0.0264467 \cos \theta_z + 0.434845)$
M13	$PAR = G(-0.0281807 \ln k_T + 0.000938004w - 0.0279869 \cos \theta_z + 0.436261)$
M14	$PAR = (481.162k_T + 202.545k_T^2 - 167.836k_T^3 + 16.7594) (\cos \theta_z)^{0.928878}$
M15	$PAR = 574.278k_T \cos \theta_z$
M16	$PAR = 0.413286G + 8.38447$
M17	$PAR = 0.414235G - 1.94159k_T + 9.13333$
M18	$PAR = 0.41312G - 0.0993371k_T + 0.0885944\Delta e + 7.6279$
M19	$PAR = G(-0.0277219 \ln k_T + 0.0176706 \ln m + 0.000155103e + 0.409838)$
M20	$PAR = 0.474298G - 0.0196574G \cos \theta_z - 0.0483035Gk_T + 1.403$
M21	$PAR = 550.309k_T \cos \theta_z + 11.5173$

274 said that there are one or more models that stand out for their good or bad
275 quality. AIC and BIC values have also been used to assess model fit but
276 the results were inconclusive. Only models M15 and M21 showed somewhat
277 higher deviation errors. We therefore recommend that the user selects the
278 model to be used for PAR estimation, depending on the input parameters
279 available, since the quality of the results obtained will be very similar. In
280 this sense, there are 10 models which only require G , since the parameters

281 k_T , $\cos\theta_z$, m or Δ are determined from this value. These models are M4,
 282 M5, M6, M9, M14, M15, M16, M17, M20 and M21. Models M3, M8, M10,
 283 M13, M18 and M19 require G , humidity and temperature records, variables
 284 usually measured at most stations. In models M2, M7 and M12, the diffuse
 285 irradiance (G_d) is required in addition to G , a variable that is not available
 286 at many weather stations. Model M1 demands G , G_d , humidity and temper-
 287 ature values. Model M12 needs direct irradiance (G_b), G and G_d and finally,
 288 inputs for model M11 are G , G_b , G_d , humidity and temperature records.

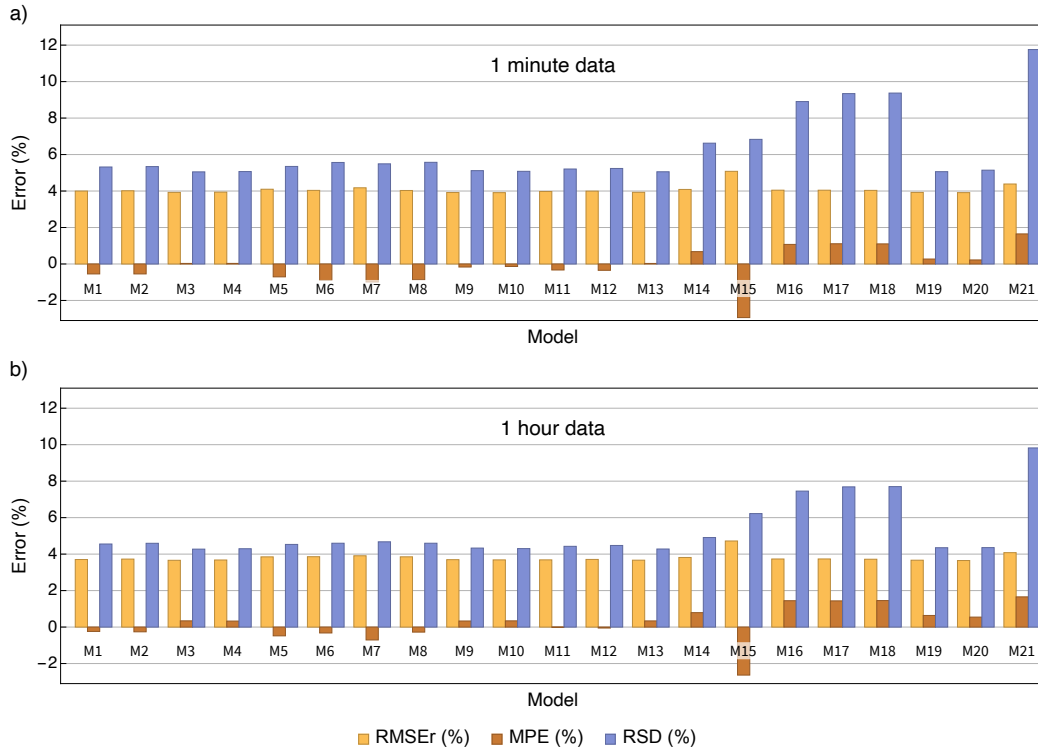


Figure 2. Statistical results of models at 1 minute (a) and 1 hour (b) input data.

289 Figure 2b shows the results of the statistics when the calibrated models

290 listed in Table 5 are applied on hourly input data. The good quality of the
291 fitted results was maintained; no single model stood out due to its better or
292 worse quality. Only the behavior of the M15 and M21 models was somewhat
293 worse, as was the case in the previous minute-time scale calibration.

294 Figure 3 show the fit results of the *PAR* models when the measured data
295 (Table 2) are classified into the five sky types proposed by Igawa (2014). In
296 clear skies, which account for 53.1% of categories, the fitting errors remained
297 small, with slightly improved percentage errors compared to those obtained
298 when analyzing all skies together. The same was observed for intermediate
299 clear skies (15.2% of the situations), in that the M15 and M21 model results
300 had again somewhat worse fitting values, which was also observed for in-
301 termediate skies (21.5% of the cases). Intermediate overcast skies represent
302 8.5% of the total and overcast skies 1.7%. In these last two types of skies,
303 worse *RSD*(%) and *MPE*(%) values can be seen, as well as a wider range
304 of dispersion in the errors obtained for the different models. In clear to in-
305 termediate skies, most models tend to underestimate *PAR* values whereas
306 in intermediate-overcast and overcast skies, the tendency was reverted and
307 *PAR* was overestimated by most models. All models yielded higher R^2 values
308 than 0.99 for the five sky types.

309 5. Conclusions

310 The use of a large time series including data on *PAR*, and both global
311 and diffuse irradiance, as well as other meteorological variables, such as tem-
312 perature and relative humidity, measured in the SURFRAD network of the
313 USA at minute frequency, provides high quality data covering a wide range

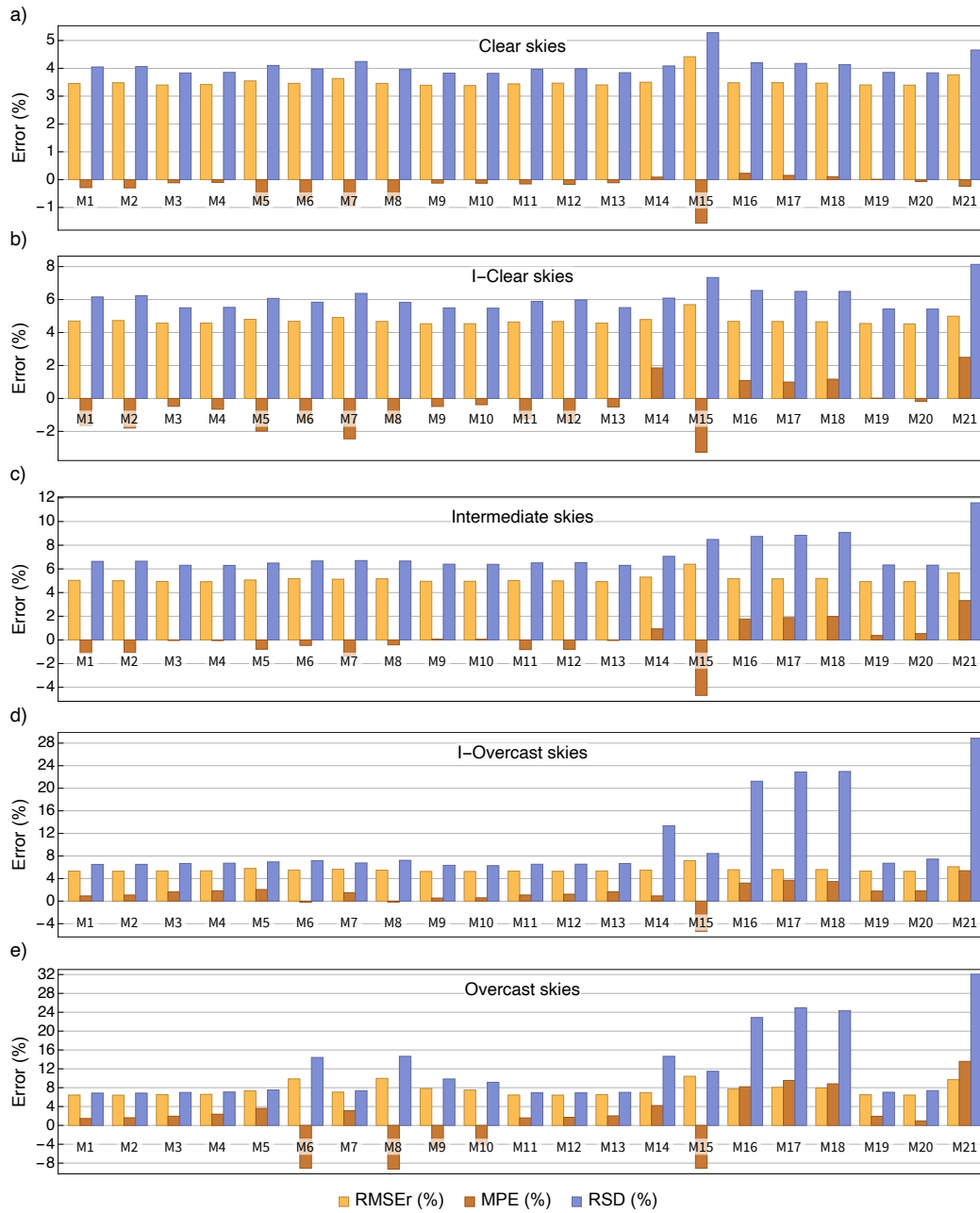


Figure 3. Statistical errors for the five sky types and 1-minute input data.

314 of climatic conditions.

315 The data have been used to calibrate 21 models previously published
316 in the literature, to obtain *PAR* from climatic parameters that are easily
317 measurable at weather stations.

318 If the calibrated models are applied to minute data, in all cases very
319 satisfactory fitting results are achieved, with coefficients of determination
320 above 0.99 and *RMSEr* ranging from 3.9% to 5%. When the same models are
321 applied to hourly data, the quality of the *PAR* results obtained is maintained
322 and the *RMSEr* values varied between 3.6% and 4.7%, the M15 and M21
323 models giving somewhat worse results. Taking account of the statistical
324 indices, therefore, none of the reviewed models stands out from among the
325 others. The selection of the model for the estimation of *PAR* should then
326 be done exclusively considering the meteorological variables available in the
327 specific location.

328 Although the proposed models can potentially be applied to longer time
329 ranges than one hour, it was considered that the practical results of using
330 *PAR* values of higher temporal resolution might worsen the quality.

331 Finally, *PAR* radiation is expected to behave similarly at different lo-
332 cations when a certain sky type is present, so the models' performance for
333 the different sky conditions could be extrapolated to any location. When
334 sky types are taken into account, after classifying skies into five categories
335 ranging from clear to overcast, it was observed that in the overcast skies the
336 error statistics giving relative values worsened in the models where global
337 irradiance was not considered or had been integrated in the linear equation
338 (M15 to M18 and M21). Therefore, in the case of overcast skies, the use of

339 models other than those listed above is recommended.

340 **Funding**

341 The authors gratefully acknowledge the financial support provided by the
342 Spanish Ministry of Science & Innovation under the I+D+i state program
343 “Challenges Research Projects” (Ref. RTI2018-098900-B-I00).

344 **Acknowledgments**

345 We would like to thank those responsible for the SURFRAD networks for
346 making complete and quality weather data freely available to users.

347 **Credit Author Statement**

348 **Marian de Blas:** Investigation, Methodology, Formal Analysis, Original
349 draft preparation; **Ana García-Rodríguez:** Formal Analysis, Validation;
350 Reviewing and Editing; **Ignacio García:** Investigation, Methodology, Soft-
351 ware, Visualization; Writing- Reviewing and Editing; **José Luis Torres:**
352 Conceptualization, Writing- Reviewing and Editing Supervision.

353 **References**

354 Aguiar, L.J.G., Fischer, G.R., Ladle, R.J., Malhado, A.C.M., Justino,
355 F.B., Aguiar, R.G., da Costa, J.M.N., 2011. Modeling the photosyn-
356 thetically active radiation in South West Amazonia under all sky con-
357 ditions. *Theoretical and Applied Climatology* 108, 631–640. doi:[10.1007/
358 s00704-011-0556-z](https://doi.org/10.1007/s00704-011-0556-z).

359 Akitsu, T., Kume, A., Hirose, Y., Ijima, O., Nasahara, K.N., 2015. On
360 the stability of radiometric ratios of photosynthetically active radiation to
361 global solar radiation in Tsukuba, Japan. *Agricultural and Forest Meteo-*
362 *rology* 209, 59–68. doi:[10.1016/j.agrformet.2015.04.026](https://doi.org/10.1016/j.agrformet.2015.04.026).

363 Alados, I., Foyo-Moreno, I., Alados-Arboledas, L., 1996. Photosynthetically
364 active radiation: measurements and modelling. *Agricultural and Forest*
365 *Meteorology* 78, 121–131. doi:[10.1016/0168-1923\(95\)02245-7](https://doi.org/10.1016/0168-1923(95)02245-7).

366 Awal, M., Koshi, H., Ikeda, T., 2006. Radiation interception and use by
367 maize/peanut intercrop canopy. *Agricultural and Forest Meteorology* 139,
368 74–83. doi:[10.1016/j.agrformet.2006.06.001](https://doi.org/10.1016/j.agrformet.2006.06.001).

369 Bhattacharya, A., 2019. Radiation-Use Efficiency Under Differ-
370 ent Climatic Conditions, in: *Changing Climate and Resource*
371 *Use Efficiency in Plants*. Elsevier, pp. 51–109. URL: [https:
372 //linkinghub.elsevier.com/retrieve/pii/B9780128162095000027](https://linkinghub.elsevier.com/retrieve/pii/B9780128162095000027),
373 doi:[10.1016/B978-0-12-816209-5.00002-7](https://doi.org/10.1016/B978-0-12-816209-5.00002-7).

374 Bredmose, N., Costes, E., 2017. Axillary Bud Growth, in: *Reference Mod-*
375 *ule in Life Sciences*. Elsevier. URL: [https://www.sciencedirect.](https://www.sciencedirect.com)

376 com/science/article/pii/B9780128096338050561
377 linkinghub.elsevier.com/retrieve/pii/B9780128096338050561,
378 doi:10.1016/B978-0-12-809633-8.05056-1.

379 Campillo, C., Fortes, R., del Henar Prieto, M., 2012. Solar Radi-
380 ation Effect on Crop Production, in: Solar Radiation. InTech. fig-
381 ure 1. URL: [http://www.intechopen.com/books/solar-radiation/
382 solar-radiation-effect-on-crop-production](http://www.intechopen.com/books/solar-radiation/solar-radiation-effect-on-crop-production), doi:10.5772/34796.

383 Dauzat, J., Eroy, M., 1997. Simulating light regime and intercrop
384 yields in coconut based farming systems, in: Developments in
385 Crop Science. Elsevier. volume 25, pp. 87–98. URL: [https://www.
386 sciencedirect.com/science/article/pii/S0378519X97800116](https://www.sciencedirect.com/science/article/pii/S0378519X97800116)
387 <https://linkinghub.elsevier.com/retrieve/pii/S0378519X97800116>,
388 doi:10.1016/S0378-519X(97)80011-6.

389 Ferrera-Cobos, F., Vindel, J., Valenzuela, R., González, J., 2020. Mod-
390 els for estimating daily photosynthetically active radiation in oceanic and
391 mediterranean climates and their improvement by site adaptation tech-
392 niques. *Advances in Space Research* 65, 1894–1909. doi:10.1016/j.asr.
393 2020.01.018.

394 Foyo-Moreno, I., Alados, I., Alados-Arboledas, L., 2017. A new conventional
395 regression model to estimate hourly photosynthetic photon flux density
396 under all sky conditions. *International Journal of Climatology* doi:10.
397 1002/joc.5063.

398 García-Rodríguez, A., García-Rodríguez, S., Díez-Mediavilla, M., Alonso-

- 399 Tristán, C., 2020. Photosynthetic active radiation, solar irradiance and
400 the cie standard sky classification. *Applied Sciences (Switzerland)* 10, 1–
401 14. doi:[10.3390/app10228007](https://doi.org/10.3390/app10228007).
- 402 García-Rodríguez, A., Granados-López, D., García-Rodríguez, S., Díez-
403 Mediavilla, M., Alonso-Tristán, C., 2021. Agricultural and Forest Me-
404 teorology Modelling Photosynthetic Active Radiation (PAR) through
405 meteorological indices under all sky conditions. *Agricultural and Forest*
406 *Meteorology* 310. doi:[10.1016/j.agrformet.2021.108627](https://doi.org/10.1016/j.agrformet.2021.108627).
- 407 Ge, S., Smith, R.G., Jacovides, C.P., Kramer, M.G., Carruthers, R.I., 2011.
408 Dynamics of photosynthetic photon flux density (PPFD) and estimates
409 in coastal northern California. *Theoretical and Applied Climatology* 105,
410 107–118. doi:[10.1007/s00704-010-0368-6](https://doi.org/10.1007/s00704-010-0368-6).
- 411 Gueymard, C.A., 2018. A reevaluation of the solar constant based on a 42-
412 year total solar irradiance time series and a reconciliation of spaceborne
413 observations. *Solar Energy* 168, 2–9. doi:[10.1016/j.solener.2018.04.](https://doi.org/10.1016/j.solener.2018.04.001)
414 [001](https://doi.org/10.1016/j.solener.2018.04.001).
- 415 Gueymard, C.A., Myers, D., Emery, K., 2002. Proposed reference irradiance
416 spectra for solar energy systems testing. *Solar Energy* 73, 443–467. doi:[10.](https://doi.org/10.1016/S0038-092X(03)00005-7)
417 [1016/S0038-092X\(03\)00005-7](https://doi.org/10.1016/S0038-092X(03)00005-7).
- 418 Hao, D., Asrar, G.R., Zeng, Y., Zhu, Q., Wen, J., Xiao, Q., Chen, M., 2020.
419 DSCOVER/EPIC-derived global hourly and daily downward shortwave and
420 photosynthetically active radiation data at 0.1° x 0.1° resolution. *Earth*
421 *System Science Data* 12, 2209–2221. doi:[10.5194/essd-12-2209-2020](https://doi.org/10.5194/essd-12-2209-2020).

- 422 Hu, B., Wang, Y., Liu, G., 2007. Measurements and estimations of photosyn-
423 thetically active radiation in Beijing. *Atmospheric Research* 85, 361–371.
424 doi:[10.1016/j.atmosres.2007.02.005](https://doi.org/10.1016/j.atmosres.2007.02.005).
- 425 IEC, 2019. IEC 60904-3: 2019. Photovoltaic devices - Part 3: Measurement
426 principles for terrestrial photovoltaic (PV) solar devices with reference
427 spectral irradiance data. Technical Report. International Electrotechni-
428 cal Commission.
- 429 Igawa, N., 2014. Improving the All Sky Model for the luminance and radi-
430 ance distributions of the sky. *Solar Energy* 105, 354–372. doi:[10.1016/j.
431 solener.2014.03.020](https://doi.org/10.1016/j.solener.2014.03.020).
- 432 Jacovides, C., Tymvios, F., Assimakopoulos, V., Kaltsounides, N., 2007.
433 The dependence of global and diffuse PAR radiation components on sky
434 conditions at Athens, Greece. *Agricultural and Forest Meteorology* 143,
435 277–287. doi:[10.1016/j.agrformet.2007.01.004](https://doi.org/10.1016/j.agrformet.2007.01.004).
- 436 Jacovides, C., Tymvios, F., Boland, J., Tsitouri, M., 2015. Artificial Neural
437 Network models for estimating daily solar global UV, PAR and broadband
438 radiant fluxes in an eastern Mediterranean site. *Atmospheric Research*
439 152, 138–145. doi:[10.1016/j.atmosres.2013.11.004](https://doi.org/10.1016/j.atmosres.2013.11.004).
- 440 Jajoo, A., Ladle, R.J., Zivcak, M., Łukasik, I., Goltsev, V., Brestic,
441 M., Oukarroum, A., Dąbrowski, P., Ahmad, P., Samborska, I.A.,
442 Cetner, M.D., Kalaji, H.M., 2014. The Use of Chlorophyll Flu-
443 orescence Kinetics Analysis to Study the Performance of Photo-
444 synthetic Machinery in Plants, in: *Emerging Technologies and*

- 445 Management of Crop Stress Tolerance. Academic Press, pp. 347–
446 384. URL: [https://www.sciencedirect.com/science/article/pii/
447 B9780128008751000156](https://www.sciencedirect.com/science/article/pii/B9780128008751000156), doi:10.1016/b978-0-12-800875-1.00015-6.
- 448 Janjai, S., Wattan, R., Sripradit, A., 2015. Modeling the ratio of photosyn-
449 thetically active radiation to broadband global solar radiation using ground
450 and satellite-based data in the tropics. *Advances in Space Research* 56,
451 2356–2364. doi:10.1016/j.asr.2015.09.020.
- 452 Kasten, F., Young, A.T., 1989. Revised optical air mass tables and approxi-
453 mation formula. *Applied Optics* 28, 4735. doi:10.1364/AO.28.004735.
- 454 Li, L., Xin, X., Zhang, H., Yu, J., Liu, Q., Yu, S., Wen, J., 2015. A method for
455 estimating hourly photosynthetically active radiation (PAR) in China by
456 combining geostationary and polar-orbiting satellite data. *Remote Sensing
457 of Environment* 165, 14–26. doi:[https://doi.org/10.1016/j.rse.2015.
458 03.034](https://doi.org/10.1016/j.rse.2015.03.034).
- 459 Li, R., Zhao, L., Ding, Y., Wang, S., Ji, G., Xiao, Y., Liu, G., Sun, L.,
460 2010. Monthly ratios of PAR to global solar radiation measured at north-
461 ern Tibetan Plateau, China. *Solar Energy* 84, 964–973. doi:10.1016/j.
462 solener.2010.03.005.
- 463 Long, C., Dutton, E., 2002. BSRN Global Network Recommended QC Tests,
464 v2.0, in: Report No 1-3, Baseline Surface Radiation Network.
- 465 McCree, K., 1972. Test of current definitions of photosynthetically active
466 radiation against leaf photosynthesis data. *Agricultural Meteorology* 10,
467 443–453. doi:10.1016/0002-1571(72)90045-3.

- 468 Mizoguchi, Y., Ohtani, Y., Aoshima, T., Hirakata, A., Yuta, S., Takanashi,
469 S., Iwata, H., Nakai, Y., 2010. Comparison of the characteristics of five
470 quantum sensors. *Bulletin of FFPRI* 9, 113–120.
- 471 Mizoguchi, Y., Yasuda, Y., Ohtani, Y., Watanabe, T., Kominami, Y., Ya-
472 manoi, K., 2013. A practical model to estimate photosynthetically active
473 radiation using general meteorological elements in a temperate humid area
474 and comparison among models. *Theoretical and Applied Climatology* 115,
475 583–589. doi:[10.1007/s00704-013-0912-2](https://doi.org/10.1007/s00704-013-0912-2).
- 476 Mõttus, M., Sulev, M., Baret, F., Lopez-Lozano, R., Reinart, A.,
477 2012. Photosynthetically Active Radiation: Measurement photosyn-
478 thesis/photosynthetic(ally) active radiation (PAR) measurement and
479 Modeling photosynthesis/photosynthetic(ally) active radiation (PAR)
480 modeling, in: Meyers, R.A. (Ed.), *Encyclopedia of Sustainability Science*
481 *and Technology*. Springer New York, New York, NY, pp. 7902–7932.
482 URL: https://doi.org/10.1007/978-1-4419-0851-3_{ }451[http:](http://link.springer.com/10.1007/978-1-4419-0851-3_{ }451)
483 [//link.springer.com/10.1007/978-1-4419-0851-3_{ }451](http://link.springer.com/10.1007/978-1-4419-0851-3_{ }451),
484 doi:[10.1007/978-1-4419-0851-3_451](https://doi.org/10.1007/978-1-4419-0851-3_451).
- 485 Nwokolo, S., Amadi, S., 2018. A Global Review of Empirical Models for
486 Estimating Photosynthetically Active Radiation. *Trends in Renewable*
487 *Energy* 4, 236–327. doi:[10.17737/tre.2018.4.2.0079](https://doi.org/10.17737/tre.2018.4.2.0079).
- 488 Ogburn, R.M., Edwards, E.J., 2010. The Ecological Water-Use Strategies
489 of Succulent Plants, in: *Advances in Botanical Research*. Academic
490 Press. volume 55, pp. 179–225. URL: [https://www.sciencedirect.](https://www.sciencedirect.com/science/article/pii/B9780123808684000041)
491 [com/science/article/pii/B9780123808684000041](https://www.sciencedirect.com/science/article/pii/B9780123808684000041)[https://](https://www.sciencedirect.com/science/article/pii/B9780123808684000041)

492 linkinghub.elsevier.com/retrieve/pii/B9780123808684000041,
493 doi:10.1016/B978-0-12-380868-4.00004-1.

494 O’Gorman, E.J., Pichler, D.E., Adams, G., Benstead, J.P., Cohen, H.,
495 Craig, N., Cross, W.F., Demars, B.O., Friberg, N., Gíslason, G.M.,
496 Gudmundsdóttir, R., Hawczak, A., Hood, J.M., Hudson, L.N., Johansson,
497 L., Johansson, M.P., Junker, J.R., Laurila, A., Manson, J.R., Mavromati,
498 E., Nelson, D., Ólafsson, J.S., Perkins, D.M., Petchey, O.L., Plebani,
499 M., Reuman, D.C., Rall, B.C., Stewart, R., Thompson, M.S., Wood-
500 ward, G., 2012. Impacts of Warming on the Structure and Functioning
501 of Aquatic Communities, in: Woodward, G., Jacob, U., O’Gorman,
502 E.J.B.T.A.i.E.R. (Eds.), *Advances in Ecological Research*. Academic
503 Press. volume 47, pp. 81–176. URL: [https://www.sciencedirect.](https://www.sciencedirect.com/science/article/pii/B9780123983152000028)
504 [com/science/article/pii/B9780123983152000028](https://www.sciencedirect.com/science/article/pii/B9780123983152000028)[https://](https://linkinghub.elsevier.com/retrieve/pii/B9780123983152000028)
505 linkinghub.elsevier.com/retrieve/pii/B9780123983152000028,
506 doi:10.1016/B978-0-12-398315-2.00002-8.

507 Peng, S., 2000. Single-leaf and canopy photosynthesis of rice11Citation:
508 Sheehy JE, Mitchell PL, Hardy B, editors. 2000. Redesigning rice photo-
509 synthesis to increase yield. Proceedings of the Workshop on The Quest to
510 Reduce Hunger: Redesigning Rice Photosynthesis, 30 Nov., in: *Studies*
511 *in Plant Science*. Elsevier. volume 7, pp. 213–228. URL: [https://www.](https://www.sciencedirect.com/science/article/pii/S0928342000800178)
512 [sciencedirect.com/science/article/pii/S0928342000800178](https://www.sciencedirect.com/science/article/pii/S0928342000800178)[https:](https://linkinghub.elsevier.com/retrieve/pii/S0928342000800178)
513 [//linkinghub.elsevier.com/retrieve/pii/S0928342000800178](https://linkinghub.elsevier.com/retrieve/pii/S0928342000800178),
514 doi:10.1016/S0928-3420(00)80017-8.

515 Perez, R., Ineichen, P., Seals, R., Michalsky, J.J., Stewart, R., 1990. Modeling

516 daylight availability and irradiance components from direct and global irra-
517 diance. *Solar Energy* 44, 271–289. doi:[10.1016/0038-092X\(90\)90055-H](https://doi.org/10.1016/0038-092X(90)90055-H).

518 Rahman, M.M., Stanley, J.N., Lamb, D.W., Trotter, M.G., 2014. Method-
519 ology for measuring fAPAR in crops using a combination of active op-
520 tical and linear irradiance sensors: a case study in Triticale (X Triti-
521 cosecale Wittmack). *Precision Agriculture* 15, 532–542. doi:[10.1007/
522 s11119-014-9349-6](https://doi.org/10.1007/s11119-014-9349-6).

523 Ross, J., Sulev, M., 2000. Sources of errors in measurements of PAR. *Agricultural and Forest Meteorology* 100, 103–125. doi:[10.1016/S0168-1923\(99\)
524 00144-6](https://doi.org/10.1016/S0168-1923(99)00144-6).

526 Sun, Z., Liang, H., Liu, J., Shi, G., 2017. Estimation of photosynthetically
527 active radiation using solar radiation in the UV–visible spectral band. *Solar
528 Energy* 153, 611–622. doi:[10.1016/j.solener.2017.06.007](https://doi.org/10.1016/j.solener.2017.06.007).

529 Tang, W., Qin, J., Yang, K., Niu, X., Min, M., Liang, S., 2017. An efficient
530 algorithm for calculating photosynthetically active radiation with MODIS
531 products. *Remote Sensing of Environment* 194, 146–154. doi:[10.1016/j.
532 rse.2017.03.028](https://doi.org/10.1016/j.rse.2017.03.028).

533 Torres, A.P., Lopez, R.G., 2012. Measuring Daily Light Integral in a Green-
534 house Commercial Greenhouse Production Purdue extension HO-238-W.
535 URL: www.hort.purdue.edu.

536 Vindel, J., Valenzuela, R., Navarro, A., Zarzalejo, L., 2018a. Methodology for
537 optimizing a photosynthetically active radiation monitoring network from

- 538 satellite-derived estimations: A case study over mainland Spain. *Atmo-*
539 *spheric Research* 212, 227–239. doi:[10.1016/j.atmosres.2018.05.010](https://doi.org/10.1016/j.atmosres.2018.05.010).
- 540 Vindel, J.M., Valenzuela, R.X., Navarro, A.A., Zarzalejo, L.F., Paz-Gallardo,
541 A., Souto, J.A., Méndez-Gómez, R., Cartelle, D., Casares, J.J., 2018b.
542 Modeling photosynthetically active radiation from satellite-derived esti-
543 mations over mainland Spain. *Remote Sensing* 10, 1–13. doi:[10.3390/
544 rs10060849](https://doi.org/10.3390/rs10060849).
- 545 Wandji Nyamsi, W., Blanc, P., Augustine, J.A., Arola, A., Wald, L., 2019. A
546 New Clear-Sky Method for Assessing Photosynthetically Active Radiation
547 at the Surface Level. *Atmosphere* 10, 219. doi:[10.3390/atmos10040219](https://doi.org/10.3390/atmos10040219).
- 548 Wandji Nyamsi, W., Espinar, B., Blanc, P., Wald, L., 2015. Estimating
549 the photosynthetically active radiation under clear skies by means of a
550 new approach. *Advances in Science and Research* 12, 5–10. doi:[10.5194/
551 asr-12-5-2015](https://doi.org/10.5194/asr-12-5-2015).
- 552 Wang, L., Gong, W., Li, C., Lin, A., Hu, B., Ma, Y., 2013. Measure-
553 ment and estimation of photosynthetically active radiation from 1961 to
554 2011 in Central China. *Applied Energy* 111, 1010–1017. doi:[10.1016/j.
555 apenergy.2013.07.001](https://doi.org/10.1016/j.apenergy.2013.07.001).
- 556 Wang, L., Kisi, O., Zounemat-Kermani, M., Hu, B., Gong, W., 2016. Model-
557 ing and comparison of hourly photosynthetically active radiation in differ-
558 ent ecosystems. *Renewable and Sustainable Energy Reviews* 56, 436–453.
559 doi:[10.1016/j.rser.2015.11.068](https://doi.org/10.1016/j.rser.2015.11.068).

- 560 Yu, X., Wu, Z., Jiang, W., Guo, X., 2015. Predicting daily photosyn-
561 thetically active radiation from global solar radiation in the Contigu-
562 ous United States. *Energy Conversion and Management* 89, 71–82.
563 doi:[10.1016/j.enconman.2014.09.038](https://doi.org/10.1016/j.enconman.2014.09.038).
- 564 Zempila, M.M., Taylor, M., Bais, A., Kazadzis, S., 2016. Modeling the
565 relationship between photosynthetically active radiation and global hori-
566 zontal irradiance using singular spectrum analysis. *Journal of Quantitative*
567 *Spectroscopy and Radiative Transfer* 182, 240–263. doi:[10.1016/j.jqsrt.](https://doi.org/10.1016/j.jqsrt.2016.06.003)
568 [2016.06.003](https://doi.org/10.1016/j.jqsrt.2016.06.003).
- 569 Zhang, L., van der Werf, W., Bastiaans, L., Zhang, S., Li, B., Spiertz, J.,
570 2008. Light interception and utilization in relay intercrops of wheat and
571 cotton. *Field Crops Research* 107, 29–42. doi:[10.1016/j.fcr.2007.12.](https://doi.org/10.1016/j.fcr.2007.12.014)
572 [014](https://doi.org/10.1016/j.fcr.2007.12.014).

Declaration of interests

The authors declare that they have no known competing financial interests or personal relationships that could have appeared to influence the work reported in this paper.

The authors declare the following financial interests/personal relationships which may be considered as potential competing interests:

Highlights

Validation and Calibration of Models to Estimate Photosynthetically Active Radiation Considering Different Time Scales and Sky Conditions

Marian de Blas, Ana García-Rodríguez, Ignacio García, José Luis Torres

- *PAR*, a key parameter for productivity models, is rarely measured at weather stations
- 21 *PAR* models calibrated with a 10-year series for minute frequency
- Low errors obtained with calibrated *PAR* models for minute and hourly frequencies
- *PAR* values are calculated considering the prevailing sky conditions performance

Department of Engineering

Campus Arrosadía – Los Olivos Building
31006 Pamplona, Spain
Tel.: +34 948 169689
email: ignacio.garcia@unavarra.es



Pamplona, 03 January 2022

Dear Editor,

I am pleased to submit the paper “Validation and Calibration of Models to Estimate Photosynthetically Active Radiation Considering Different Time Scales and Sky Conditions” for publication in “Advances in Space Research”. The authors consider your journal as the most appropriate for the submission of our manuscript, whose topic is within its scope and stated aims.

A calibration of 21 PAR models using different time scales and data over 10 years has been conducted, including data from 7-ground meteorological stations of proven quality from the SURFRAD network, in the USA. Calibration of the models was for all sky conditions including all data in the database and considering different sky conditions classified in the Igawa Sky index, from overcast to clear skies. After calibration, the models were validated for minute and hourly data, obtaining in all cases low fitting errors. The results suggested that the performance of any model under the different sky conditions could be extrapolated to any location.

The Acknowledgements section of our submission mentions all organizations that have funded our research:

- Spanish Ministry of Science & Innovation under the R&D+i State Program “Challenges Research Projects” (Ref. RTI2018-098900-B-I00).

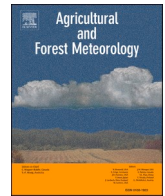
In consultation with my co-authors, we wish to suggest three experts as possible reviewers of this paper. Their names and emails will be included in the submission system.

A native English speaker working as a professional translator has reviewed and edited the manuscript. We hope that its contents will meet the requirements that characterize your prestigious publication in terms of quality and scientific interest.

Yours sincerely,

A handwritten signature in blue ink, enclosed in a blue oval. The signature appears to be 'Ignacio García'.

Ignacio García, on behalf of all authors



Modelling Photosynthetic Active Radiation (PAR) through meteorological indices under all sky conditions

A. García-Rodríguez, D. Granados-López, S. García-Rodríguez, M. Díez-Mediavilla, C. Alonso-Tristán*

Research Group Solar and Wind Feasibility Technologies, SWIFT, Electromechanical Engineering Department, Avda. Cantabria s/n, 09006, Burgos, Spain

ARTICLE INFO

Keywords:

PAR
Modelling
CIE standard sky classification

ABSTRACT

In this study, ten-minute meteorological data-sets recorded at Burgos, Spain, are used to develop models of Photosynthetic Active Radiation (PAR) following two different procedures: multilinear regression and Artificial Neural Networks. Ten Meteorological Indices (MIs) are chosen as inputs to the models: clearness index (k_t), diffuse fraction (k_d), direct fraction (k_b), Perez's clear sky index (ϵ), brightness index (Δ), cloud cover (CC), air temperature (T), pressure (P), solar azimuth cosine ($\cos Z$), and horizontal global irradiation ($RaGH$). The experimental data are clustered according to the sky conditions, following the CIE standard sky classification. A previous feature selection procedure established the most adequate MIs for modelling PAR in clear, partial and overcast sky conditions. $RaGH$ was the common MI used by all models and for all sky conditions. Additional variables were also included: the geometrical parameter, $\cos Z$, and three variables related to the sky conditions, k_t , ϵ , and Δ . Both modelling methods, multilinear regression and ANN, yielded very high determination coefficients (R^2) with very close results in the models for each of the different sky conditions. Slight improvements can be observed in the ANN models. The results underline the equivalence of multilinear regression models and ANN models of PAR following previous feature selection procedures.

1. Introduction

Photosynthetic Active Radiation, PAR, is the region of the solar spectrum between 400 and 700 nm (Alados et al., 2000) used by plants in the photosynthesis process. PAR knowledge can provide key inputs for modelling biomass and forestry production (Aguar et al., 2012; Landsberg and Waring, 1997), plant growth (Liu et al., 2016), natural greenhouse illumination (Alados et al., 1996) and the calculation of the euphotic depth of the oceans (Kirk, 1979), among others. Usually, Photosynthetic Photon Flux Density, Q_p ($\mu\text{mol}\cdot\text{s}^{-1}\cdot\text{m}^{-2}$), is measured and converted into energy units using the McCree's conversion factor ($4.57 \mu\text{mol}\cdot\text{J}^{-1} \pm 3\%$) depending on climatic factors (Akitsu et al., 2015)). Spatial distribution and long-term trends of PAR have been reported in many early studies developed in Europe (Ferrera-Cobos et al., 2020; Jacovides et al., 2003; Jacovides et al., 2007; Leuchner et al., 2011), China (Hu et al., 2018; Hu et al., 2010; Liang and Xia, 2005; Wang et al., 2015), United States (Yu et al., 2015) or Africa (Finch et al., 2004).

Alternative procedures have been developed for calculating PAR, due

to the scarcity of PAR data from direct measurements at ground meteorological stations. These procedures include other meteorological and climatic variables, mainly horizontal solar global irradiation ($RaGH$). Many studies have established the PAR/ $RaGH$ ratio at between 0.45 and 0.50 (Meek et al., 1984; Monteith, 1973; Moon, 1940; Stanhill and Fuchs, 1977; Szeicz, 1974; Tsubo and Walker, 2005), depending on the location, solar elevation or atmospheric aerosols, and water vapor concentrations. Empirical models based on linear regressions have been developed for PAR estimates. Turbidity, cloud cover, atmospheric water and aerosols content, clearness and sky brightness, diffuse fraction, dew point temperature, and solar zenith angle have, among others, been used as data input for multilinear models around the world (Al-Shooshan, 1997; Alados et al., 1996; Bat-Oyun et al., 2012; González and Calbó, 2002; Janjai et al., 2015; Peng et al., 2015; Wang et al., 2016; Yu et al., 2015; Zhang et al., 2000). However, the resulting models are strongly location dependent. Their use at other locations is not immediate, and requires new experimental studies (Al-Shooshan, 1997; Alados and Alados-Arboledas, 1999; Ferrera-Cobos et al., 2020; Nwokolo and Amadi, 2018). Satellite data have also been used for

* Corresponding author.

E-mail address: catristan@ubu.es (C. Alonso-Tristán).

<https://doi.org/10.1016/j.agrformet.2021.108627>

Received 3 May 2021; Received in revised form 16 July 2021; Accepted 21 August 2021

Available online 2 September 2021

0168-1923/© 2021 The Author(s).

Published by Elsevier B.V. This is an open access article under the CC BY-NC-ND license

(<http://creativecommons.org/licenses/by-nc-nd/4.0/>).



Fig. 1. Experimental facility on the roof of the Higher Polytechnic School of Burgos University, Spain.

Table 1
Technical specifications of pyranometers and pyrheliometer.

Model	SR11	DR01	ML-020P
Measurement Range	0 to 3000 (W/m ²)	0 to 4000 (W/m ²)	0–3000 (μmol/s·m ²)
Calibration uncertainty	< 1.8 % (k = 2)	< 1.2 % (k = 2)	< 2 % (k = 2)
Spectral Range	285 to 3000 × 10 ⁻⁹ m	200 to 4000 × 10 ⁻⁹ m	400 to 700 nm
Sensitivity (nominal)	15 × 10 ⁻⁶ V/(W/m ²)	10 × 10 ⁻⁶ V/(W/m ²)	0.15 × 10 ⁻⁶ V/(μmol/s·m ²)
Operating temperature range	-40°C to 80°C	-40°C to 80°C	-10°C to 50°C
Temperature response	<± 2% (-10°C to 40°C)	< ± 1 % (-10°C to 40°C)	±1.1% (-10°C to 50°C)

Table 2
Sky Camera Technical specifications.

Model	SONA201-D
Sensor	CMOS-2.3MP
Vision Angle	<180° (fisheye lens)
Operating temperature	-40°C to 55°C
Image format	RAW

estimating *PAR* (Gao et al., 2011; Janjai and Wattan, 2011; Li et al., 2015; Vindel et al., 2018), although those models need to be validated from ground measured *PAR* data.

Over recent years, machine learning algorithms (ML) have been developed as a useful tool for modelling meteorological and climatic data (Huntingford et al., 2019; Torres et al., 2011). Artificial Neural Networks (ANN) have been used for modelling *PAR*, with different meteorological variables as input. Horizontal global solar irradiance, solar azimuth angle, clearness index and different parameters to take into account the atmospheric water vapor content such as the vapour content, the wet bulb temperature or the dew point temperature, are the most common inputs for developing an ANN for *PAR* estimations (Foyo-Moreno et al., 2017; Jacovides et al., 2015; Yu and Guo, 2016).

The sky conditions have a relatively low influence on the *PAR* /*RaGH* ratio. Escobedo et al. (Escobedo et al., 2009) concluded that the sky conditions had no influence on *PAR* levels within a variation of ± 8%.

This conclusion might appear to contradict the definition of the *PAR* models in relation to sky conditions (Alados et al., 2000; Bosch et al., 2009; Dye, 2004; Serrano and Boscà, 2011). Most studies have determined that the *PAR*/*RaGH* ratio presents the highest values for cloud-covered skies and the lowest for clear skies (Blackburn and Proctor, 1983; García-Rodríguez et al., 2020; Stigter and Musabilha, 1982; Yamashita and Yoshimura, 2018) where the definition of the sky type is based on different criteria in each of the reviewed works (García-Rodríguez et al., 2020).

Independently of the *PAR* modelling procedure, *RaGH* has proven to be sufficient in itself as a factor to obtain accurate *PAR* data (±5% accuracy), with no consideration given to sky conditions (Ferrera-Cobos et al., 2020) using different time intervals (hourly, daily, monthly basis). However, the inclusion of other meteorological variables in the model improved the estimations of *PAR*. The objective of this work is the establishment of *PAR* models based on meteorological variables (or meteorological indices (MIs)) that are easily accessible at ground meteorological facilities. Its main novelties include the influence of sky conditions on the models, paying attention to the CIE standard sky classification (ISO, 2004), and using data collected at ten-minute intervals.

The following MIs are included in the study: clearness index (k_t), diffuse fraction (k_d), direct fraction (k_p), Perez’s clearness sky index (ϵ), brightness index (Δ), cloud cover (CC), air temperature (T), pressure (P), solar azimuth cosine ($\cos Z$), and horizontal global irradiation (*RaGH*). First, a feature selection procedure was applied, to identify related features and remove the irrelevant or less important ones. After the feature selection procedure, two different strategies were used for modelling *PAR*: multilinear regression and ANN. Analysis and comparisons of both models were conducted to study the influence of sky conditions on the accuracy of the model. The experimental data for this study were collected in an experimental campaign that ran from April 2019, to February 2021, in Burgos, Spain.

The paper will be structured as follows: after the Introduction Section, the experimental facility and the measurement campaign as well the quality filters applied to the experimental data will be described in Section 2. This Section will also include the definition and description of the meteorological indices used for modelling *PAR*. The CIE standard sky classification in Burgos, Spain, during the experimental campaign will be introduced in Section 3, as well the statistical analysis of the experimental data. In Section 4, the feature selection algorithm will be described. In Sections 5 and 6, the *PAR* modelling will be introduced using multilinear regression models and ANNs, respectively. Finally, the main results and some conclusions will be advanced in Section 7.

2. Experimental section

The ground meteorological facility where the experimental data used in this study were recorded, is located on the flat roof of the Higher Polytechnic School building (EPS) of Burgos University, Spain (42°21’04” N, 3°41’20” W, 856 m above mean sea level) and it is shown in Fig. 1. A complete description of the meteorological facility can be found in previous papers (García-Rodríguez et al., 2020; Granados-López et al., 2020; Granados-López et al., 2021; Suárez-García et al., 2020).

The following parameters are required for calculation of the ten MIs detailed in this study: solar horizontal global irradiance, *RaGH*; horizontal diffuse irradiance, *RaDH*; beam irradiance, *RaB*; cloud cover, *CC*; *PAR* data; air temperature, *T*; pressure, *P*; and the sky conditions under CIE standard. *RaGH*, *RaDH* and *RaB* were measured using a Hukseflux pyranometers, model SR11, and a Hukseflux pyrheliometer, model DR01, respectively (Hukseflux, Delft, The Netherlands). The beam irradiance sensor was installed on a sun tracker, model Sun-Tracker 3000, from Geónica (Geónica, Madrid, Spain). The diffuse irradiance sensor was protected from direct sunlight by a shadow hat. An ML-020P quantum sensor was used to measure Q_p . Cloud cover, *CC*, was

Table 3
Sky scanner technical specifications.

Model	MS-321LR Sky Scanner
FOV	11°
Luminance	0 to 50 kcd/m ²
Radiance	0 to 300 W/m ²
A/D Convertor	16 bits
Calibration Error	2%

measured by a sky camera model SONA201D (Sieltec Canary Islands, Spain) and the sky luminance and irradiance distribution, needed to establish the CIE standard sky conditions, was determined with a commercial MS-321LR sky scanner manufactured by EKO instruments (EKO Instruments Europe B.V., Den Haag, The Netherlands). Technical specifications of all instruments are shown in Tables 1–3

All meteorological and radiometric data were recorded every five minutes (averages from 30 seconds). Q_p data ($\mu\text{mol}\cdot\text{s}^{-1}\cdot\text{m}^{-2}$) were converted into PAR data ($\text{W}\cdot\text{m}^{-2}$) using McCree’s conversion factor ($4.57 \mu\text{mol}\cdot\text{J}^{-1}$). The sky scanner was adjusted on a monthly basis for taking measurements from sunrise to sunset. It completed a full scan in four minutes and started a new scan every 10 min. The first and last measurements of the day were discarded, as well as measurements higher than $50 \text{ kcd}\cdot\text{m}^{-2}$ and lower than $0.1 \text{ kcd}\cdot\text{m}^{-2}$, following the specifications of the equipment. Only simultaneous data-sets could be used. Experimental data were analyzed and then filtered using conventional quality criteria (Guemard and Ruiz-Arias, 2016). If a data-set failed to pass the quality criteria, then all the simultaneous data-sets were rejected. The original data-set counted 71600 datum, 36% of which were eliminated after the filtering procedure.

Five of the meteorological indices (MIs) used in this study were directly obtained from the experimental measurements: cloud cover (CC), from the sky camera; air temperature and pressure (T , P); horizontal global irradiation ($RaGH$); and PAR, measured by the pyranometers and the quantum sensor, respectively. Solar azimuth cosine ($\cos Z$) was calculated from the geometrical data of the location, using well-known mathematical relationships (Iqbal, 1983). The other MI -clearness index (Iqbal, 1983), k_t , horizontal diffuse fraction (Erbs et al., 1982), k_d ; beam fraction (Suárez-García et al., 2020), k_b ; and Perez’s clearness index, ϵ ; and brightness factor, Δ (Perez et al., 1990) were calculated using Eqs. (1) to ((6):

$$k_t = \frac{RaGH}{B_{sc}\cdot\epsilon_0\cdot\cos Z_s} \tag{1}$$

where, B_{sc} is the extraterrestrial irradiance constant ($1361.1 \text{ W}/\text{m}^2$ (Guemard, 2018)); Z_s is the angle between sky zenith, and sun, and ϵ_0 is the average value of the orbital eccentricity of the Earth, calculated from eq. 2:

$$\epsilon_0 = 1 + 0.033\cdot\cos\left(2\cdot\pi\cdot\frac{d_n}{365}\right) \tag{2}$$

where d_n is the day of the year.

$$k_d = \frac{RaDH}{RaGH} \tag{3}$$

$$k_b = \frac{RaB\cdot\text{sen}\gamma_s}{RaGH} \tag{4}$$

where γ_s is the solar elevation;

$$\epsilon = \frac{\frac{RaDH+RaB}{RaDH} + k\cdot Z_s^3}{1 + k\cdot Z_s^3} \tag{5}$$

where k is 1.04 for Z_s expressed in rad (or $5.56\cdot 10^{-6}$ if Z_s is expressed in degrees); and

$$\Delta = \frac{m\cdot RaDH}{B_{sc}\cdot\epsilon_0} \tag{6}$$

where m is the optical air mass calculated using the Kasten model (Kasten, 1993).

3. CIE standard sky classification in Burgos

Following the analysis, great variability was observed in the experimental data, due to the different environmental and atmospheric conditions during the extensive experimental campaign. In many studies, the CIE standard sky classification for homogeneous skies has been considered an adequate representation of empirical sky conditions (Alshabani, 2011; Li and Cheung, 2006; Li et al., 2008; Torres et al., 2010a; Torres et al., 2010b; Tregenza, 2004). Sky types of the same category have the same well-defined sky luminance pattern. The general formula for defining the relative pattern of luminance for any sky type is a combination of a gradation function, dependent on two parameters,

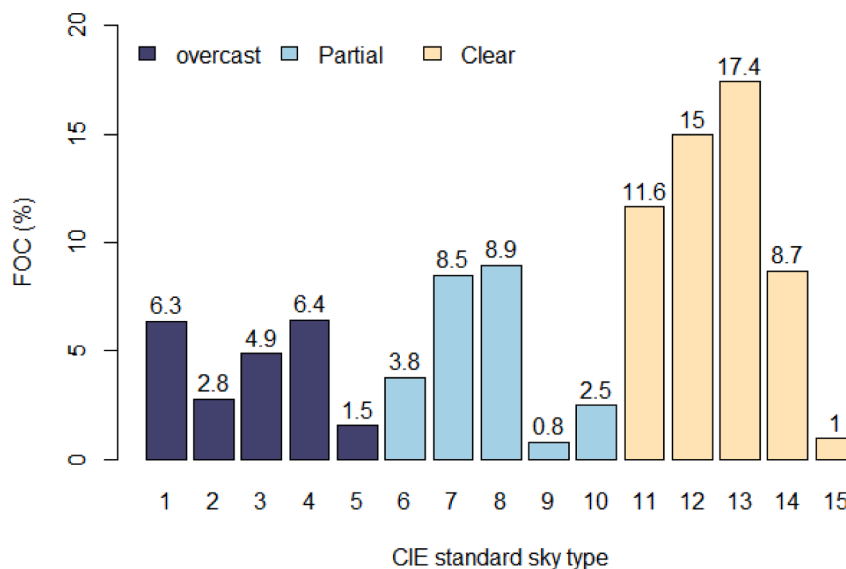


Fig. 2. Frequency of occurrence (FOC, %) of CIE standard sky types in Burgos, Spain, between April 2019 and February 2021.

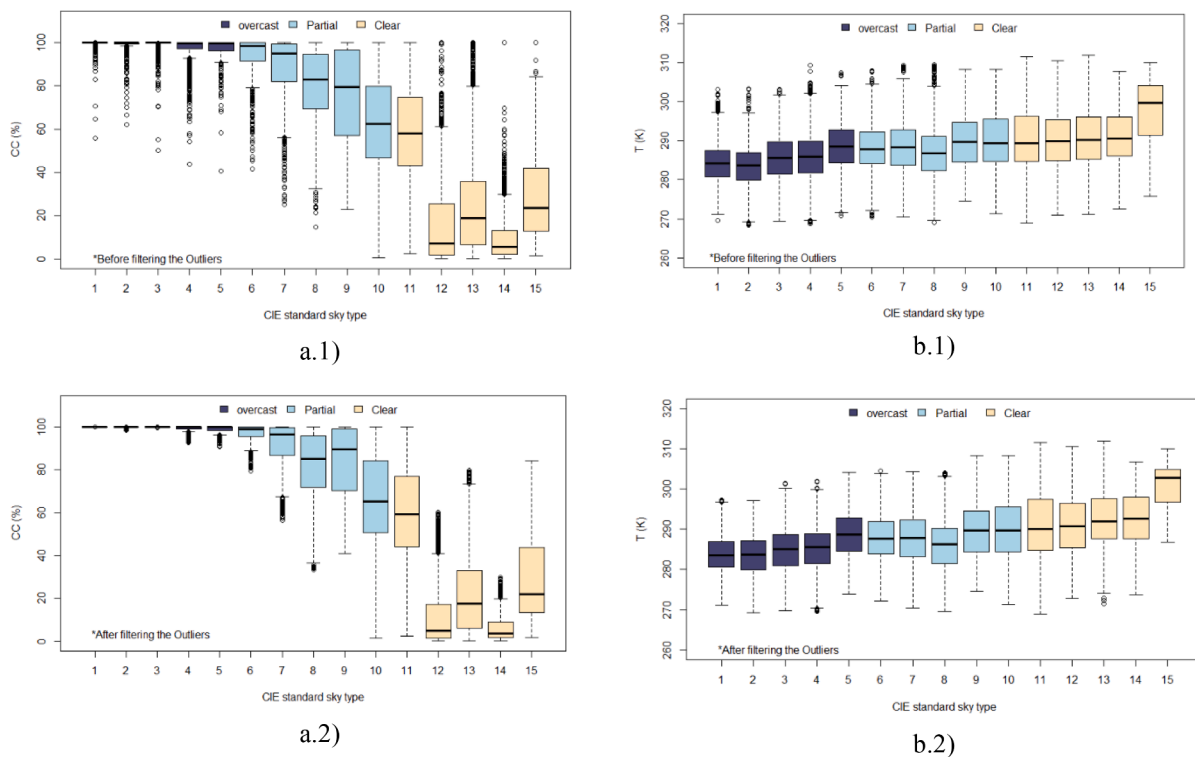


Fig. 3. Statistical analysis of air temperature, T (a), and cloud cover, CC (b), vs. CIE standard sky type: before (1) and after (2) filtering the outliers.

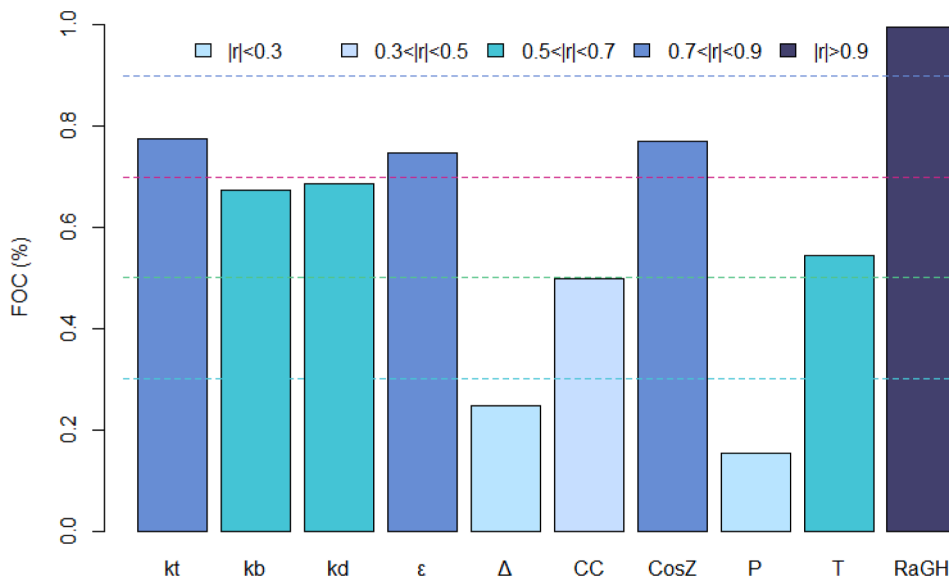


Fig. 4. The Pearson Correlation Coefficient ($r(PAR, MI_i)$) calculated for the 10 MIs used in this study.

Table 4

The Pearson correlation coefficient or Pearson's $r(PAR, MI_i)$ taking into account the sky conditions defined by the CIE standard sky classification (overcast, partial and clear).

	$ r(PAR, MI_i) $				
CIE sky type	[1-0.9]	(0.9-0.7)	(0.7-0.5)	(0.5-0.3)	(0.3,0]
Overcast	RaGH	k_t, Δ	cosZ	k_b, ϵ	P, T
Partial	RaGH	cosZ	k_t, ϵ	k_b, T	CC, P
Clear	RaGH, cosZ	ϵ	k_t	k_b, T	

and the indicatrix function, which considers the scatter of luminance with regard to the direction of sunrays, modelled as a function of three adjustable parameters. The gradation function modifies the luminance value between the horizon and the local zenith, assigning the highest luminance value to the zenith with cloudy skies and in reverse to clear skies. The indicatrix function shows the dispersion in the atmosphere of sunlight. The maximum luminance appears near the solar position, decreasing rapidly with the distance to the sun. Each of the functions takes six different forms and the combination yields 36 sky types from which 15 were selected: five overcast, five partly cloudy, and five clear sky types. Once the sky types are identified, the basic solar irradiance and daylight illuminance on the surfaces of interest can be obtained

Table 5
Multilinear regression models of *PAR*.

Sky conditions	Multilinear regression model	R^2	nRMSE (%)	nMAE (%)	nMBE (%)
Clear skies (MLR1)	$PAR = 0.3806 \cdot RaGH + 0.524 \cdot \varepsilon + 33.247 \cdot \cos Z - 2.646$	0.991	3.93	2.72	$-2 \cdot 10^{-6}$
Partial skies (MLR2)	$PAR = 0.3958 \cdot RaGH + 18.282 \cdot \cos Z - 2.508$	0.976	7.81	5.04	$-2 \cdot 10^{-6}$
Overcast skies (MLR3)	$PAR = 0.4335 \cdot RaGH - 7.726 \cdot k_t - 9.078 \cdot \Delta + 4.065$	0.985	6.62	4.44	$-5 \cdot 10^{-6}$

through simple mathematical expressions (Li et al., 2013). Therefore, the CIE standard sky taxonomy was selected for atmospheric conditions reference. A complete description of the CIE standard sky classification and the procedure to obtain the CIE standard sky classification from the sky scanner measurements can be found in previous works (Granados-López et al., 2021; Suárez-García et al., 2020; Suárez-García et al., 2018). Fig. 2 shows the Frequency Of Occurrence (FOC) of the different CIE standard sky types in Burgos during the experimental campaign, which extended from April, 2019 to February, 2021. As can be seen, in Burgos, the clear sky conditions were prevalent, as sky types 11 to 15 were the most frequent over the period under study. Sky type 13 (Cloudless polluted with a broader solar corona) had the highest FOC (17.4%) followed by sky types 7 (Partly cloudy with a uniform gradation and a brighter circumsolar effect) and 8 (Partly cloudy, rather uniform with a clear solar corona).

Once the reference sky conditions had been established, The MIs included in the study were analyzed from the sky conditions to identify the correlation between the MIs and the CIE standard sky conditions. The box-plot of the MIs, with respect to the CIE standard sky type, gave the following conclusions: air temperature, pressure, and $\cos Z$ were not influenced by the sky type, while CC , k_t , k_d , k_b , ε , and Δ were greatly affected by the sky conditions. A new quality test of the experimental data was introduced, discarding any simultaneous data corresponding to outliers in the box-plots. Fig. 3 shows the results for CC and T , where the influence of the sky type on the MI value is almost negligible in the case of T and very important in the case of CC . The discarded data reached 10%.

4. Feature selection

Feature Selection (FS) is the identification of related features within a set of data and the removal of irrelevant or less important features that contribute little or nothing to the definition of the target variable, so as to achieve models of greater accuracy. FS is one of the core concepts of ML that will impact on the performance of the developed model, improving its precision and reducing its complexity and overfitting as well as its runtime.

In this work, the Pearson criterion was used to analyze the degree of correlation of each of the selected MIs to *PAR*. The Pearson criterion is based on the Pearson correlation coefficient, r . For the case under study, if *PAR* and one selected MI are strongly correlated, the Pearson coefficient is 1 (direct correlation) or -1 (inverse correlation). However, a Pearson coefficient near 0 implies a weak or null correlation. The Thumb rule (Mukaka, 2012) established five r intervals for the correlation: direct ($1 \geq |r(PAR, MI_i)| \geq 0.9$), strong ($0.9 > |r(PAR, MI_i)| \geq 0.7$), moderate ($0.7 > |r(PAR, MI_i)| \geq 0.5$), weak ($0.5 > |r(PAR, MI_i)| \geq 0.3$), and negligible ($|r(PAR, MI_i)| < 0.3$).

Fig. 4 shows the Pearson coefficient, $r(PAR, MI_i)$, calculated for the 10 MIs used in this study, regardless of the sky conditions. A direct correlation was obtained between *PAR* and *RaGH* and a strong correlation between *PAR* and ε , k_t , and $\cos Z$. The r coefficient with the other MIs was moderate, weak or negligible, so, these MIs were discarded as

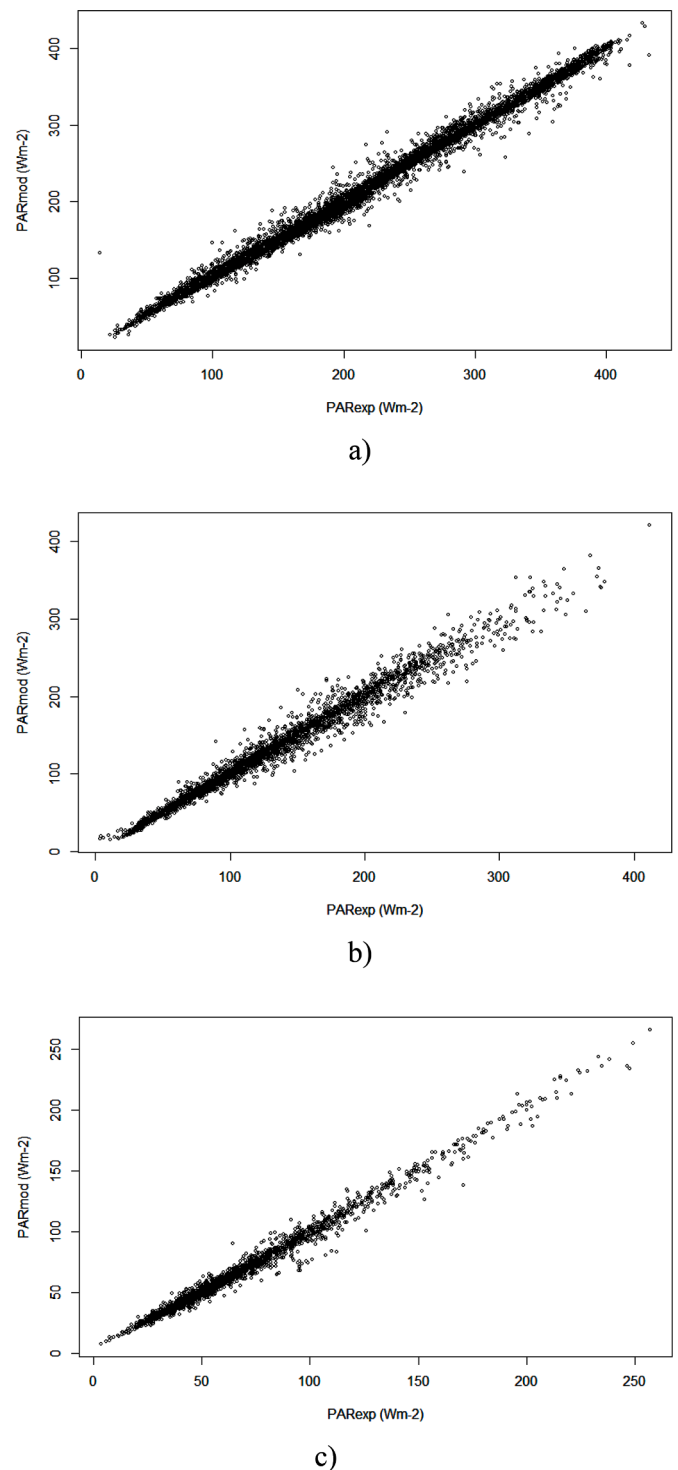


Fig. 5. Correlogram of the multilinear regression model of *PAR*: a) Clear skies; b) Partial skies; c) Overcast skies.

inputs for modelling *PAR*.

As Fig. 4 highlights, *RaGH*, the geometric parameter solar azimuth cosine, $\cos Z$, Perez's clearness index, ε , and the clearness index, k_t , showed the strongest correlation to *PAR* ($|r(PAR, MI_i)| > 0.7$). These results agree with the literature, in that *RaGH* (or alternatively k_t) is the most widely used parameter for modelling *PAR* (Nwokolo and Amadi, 2018). Air pressure, P , the brightness factor, Δ , and cloud cover, CC , presented weak correlations with *PAR*.

The data were clustered, taking into account the CIE standard sky

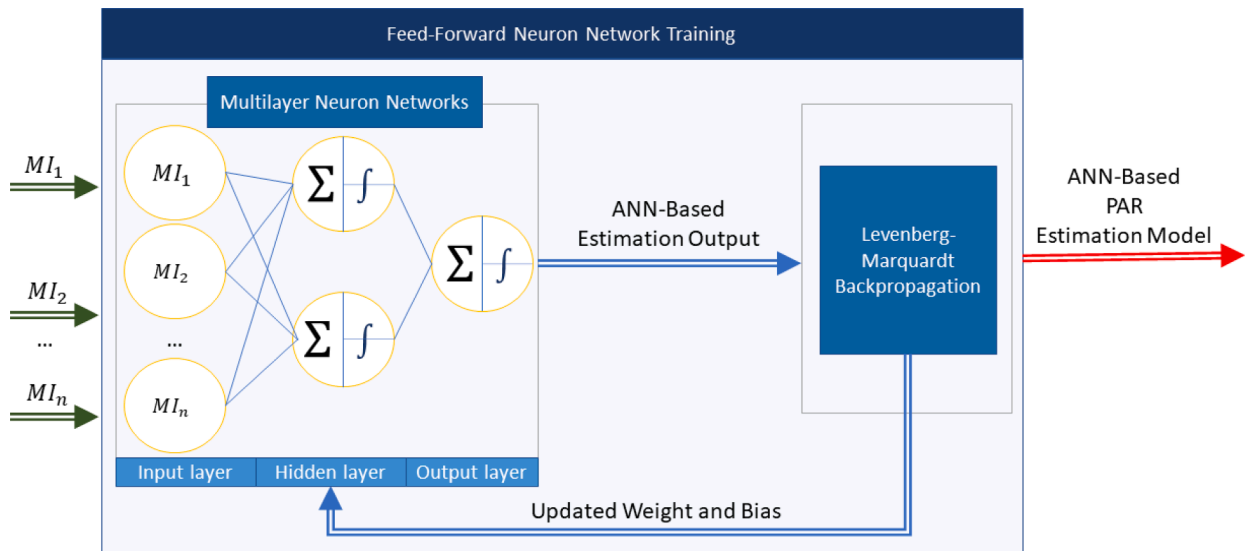


Fig. 6. ANN system architecture using the Levenberg-Marquardt Backpropagation algorithm.

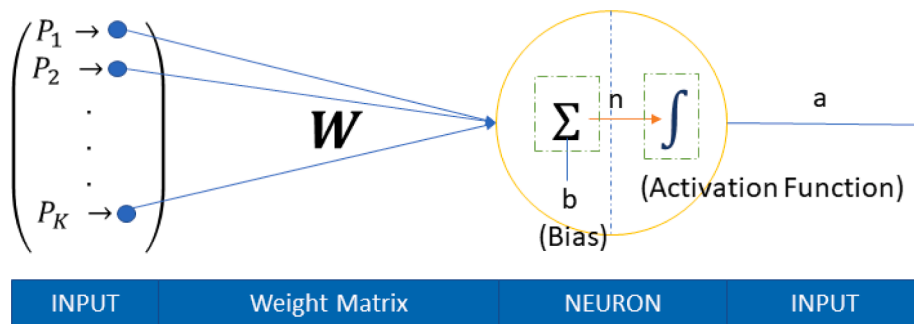


Fig. 7. Scheme of a neuron with k inputs. The weighting matrix and the bias are used for calculating the neuron output through the activation function.

Table 6
Statistical results of the ANN models.

Sky conditions	R^2	$nRMSE$ (%)	$nMAE$ (%)	$nMBE$ (%)
Clear skies (ANN1)	0.992	3.846	2.59	$-2 \cdot 10^{-6}$
Partial skies (ANN2)	0.977	7.795	5.00	$-3 \cdot 10^{-6}$
Overcast skies (ANN3)	0.987	6.466	4.34	$-5 \cdot 10^{-6}$

classification for clear sky (CIE sky types 1 to 5), and partial (CIE sky types 6 to 10) and overcast sky conditions. The Pearson correlation coefficient or Pearson's $r(PAR, MI_i)$ was calculated taking into account the sky classification and the results are shown in Table 4.

RaGH was the MI with the strongest correlation to *PAR*, regardless of sky conditions. *cosZ* only showed a very strong correlation to *PAR* for clear skies. MIs with strong correlations to *PAR* were ϵ for clear skies, *cosZ*, for partial skies, and k_t , and Δ in overcast sky conditions. The brightness factor, Δ , that presented weak correlations to *PAR* when data were not clustered, highlighted its strong correlation in overcast sky conditions. In the following sections, the *PAR* is modelled by following different procedures for each of the CIE standard sky conditions that were developed using the MIs with the Pearson correlation coefficient $|r(PAR, MI_i)| > 0.7$.

5. Multilinear regression models

Three multilinear regression models, one for each sky type, were formulated to estimate *PAR*, based on the previous feature selection

process shown in Table 4. The experimental data-set, taking into account the CIE standard classification, was randomly divided into two groups: the first one, comprising 85% of the data, was used to fit the models. The other group, with the remaining 15% of the data, was used to validate the models. The statistics used for this validation were as follows: the corresponding determination coefficient (R^2), the normalized mean bias error (*nMBE*), the normalized mean absolute error, *nMAE*, and the root mean square error (*nRMSE*). The expressions for these last three statistical terms are:

$$nMBE = \frac{1}{PAR_{exp}} \frac{\sum_{i=1}^n (PAR_{mod} - PAR_{exp})}{n} \times 100 (\%) \quad (7)$$

$$nRMSE = \frac{1}{PAR_{exp}} \sqrt{\frac{\sum_{i=1}^n (PAR_{mod} - PAR_{exp})^2}{n}} \times 100 (\%) \quad (8)$$

$$nMAE = \frac{1}{PAR_{exp}} \frac{\sum_{i=1}^n |PAR_{mod} - PAR_{exp}|}{n} \times 100 (\%) \quad (9)$$

where n is the number of the experimental data used for fitting the models; PAR_{mod} are the modelled values of *PAR*; and PAR_{exp} is the experimental value of *PAR*. As Table 5 shows, the results of fitting the models presented good correlation with the experimental data, given that $R^2 > 0.97$ and *nRMSE* was lower than 8% and *nMAE* lower than 5%. The small and negative values of *nMBE* indicate that the models present a good fit although tend to underestimate *PAR* values. The graph in Fig. 5 shows the multilinear regression models for each of the sky

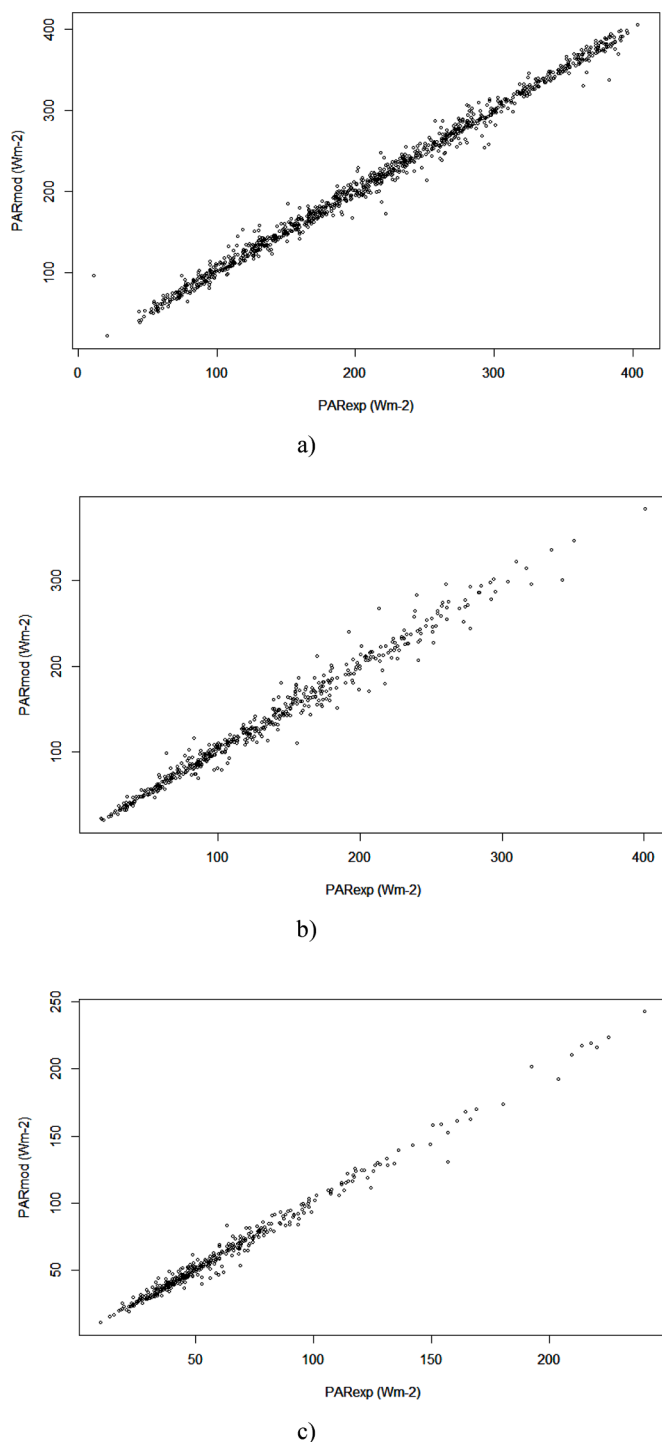


Fig. 8. Correlogram of the ANN model of PAR: a) Clear skies; b) Partial skies; c) Overcast skies.

Table 7
Results of the correlograms of the different models.

Sky conditions	R ²	Slope	Intercept (W·m ⁻²)	Sky conditions	R ²	Slope	Intercept(W·m ⁻²)
Clear skies (MLR1)	0.992	1.0009	-0.6753	Clear skies (ANN1)	0.992	1.0004	-0.5484
Partial skies (MLR2)	0.978	0.9922	0.6845	Partial skies (ANN2)	0.978	0.9924	0.6078
Overcast skies (MLR3)	0.987	0.9990	-0.2836	Overcast skies (ANN3)	0.988	1.0002	-0.3550

conditions.

6. Artificial neural network for modelling PAR

This section proposes an Artificial Neural Network (ANN) trained with the Levenberg-Marquardt Back-Propagation (LMBP) algorithm (Du and Stephanus, 2018) that is used to model PAR for each of the CIE standard sky conditions (clear, partial and overcast skies). ANN training uses an iterative process to assign the correct weight that each neuron must set to each input to obtain the desired output value, PAR data in this case. Including the dependency between the input and output variables is not necessary, because the ANN is training to learn this dependency. ANN works as a ‘black box’ and only the final result is known and not the intermediate processes that are followed. It is therefore not possible to obtain the relationship between the input variables and their relative weight in the final result. Fig. 6 illustrates the system architecture used in this work.

A three-layer configuration has been chosen: the input layer, where the selected MIs for the model were introduced in the system; the hidden layer, or the information processing centers and the output layer, where the result is obtained. Each processing center (neuron) adjusts to the other neurons in an interactive process. The fit of the weights (weighting matrix, W) in each iteration is done using the Levenberg Marquardt algorithm (Lv et al., 2017). Fig. 7 shows the structure of a neuron where the input information is calculated from eq. 10:

$$n = \sum_{j=1}^K W_j P_j + b \tag{10}$$

W_j are the components of the weighting matrix, P_j are the input variables and b is the bias. The neuron generates an output, a, in Fig. 7, through the activation function (f(n)) given, in this work, by Eq. 11:

$$f(n) = \frac{1}{1 + e^{-n}} \tag{11}$$

The input data-set of an ANN is divided into three groups for its training process: a training group (with 70% of data), a validation data-set (15% of data) and a test data-set (15% of data). The training and validation groups have been established by dividing the fitting dataset used in the MLR modelling. The training group is used to determine the weighted matrix and the bias in an iterative process. The training is over when the results of the performance of the resulting model, calculated using the validation set, reach the desired quality. The test data group is used to calculate the performance of the model. The test data-set matched the one used for the test of the multilinear regression models fitted in the previous section.

Three ANNs were developed and tested in this work, one for each sky type, based on the feature selection previously performed and shown in Table 4. The statistic used for the validation of the models were the corresponding determination coefficient (R²), the normalized mean bias error (nMBE), and the normalized root mean square error (nRMSE), previously defined. Table 6 summarizes the statistical results of the ANNs, and Fig. 8 shows a graph of these results.

The slope and intercept (W·m⁻²) of the correlograms shown in Figs. 5 and 8 give a practically perfect fit for all sky conditions, as the results show in Table 7.

7. Conclusions

Two different procedures, multilinear regression and ANNs, have been used to develop *PAR* models using Meteorological Indices (MIs). A previous feature selection procedure has been performed with the Pearson's correlation coefficient that pointed to the most influential variables, so that the irrelevant ones could be discarded. As its main novelty, sky conditions were included in the modelling of *PAR*, using the CIE standard sky classification as the criterion for the definition of clear, partial, and overcast skies. The experimental data-set collected at ten-minute intervals, was extended for twenty-two months. In addition to the traditional quality filters for solar radiation measurements, a second filtering procedure has been applied in statistical terms and according to the clustering of the data following the CIE standard sky classification, which guarantees the quality and homogeneity of the experimental data for each of the established sky conditions.

A feature selection procedure has been applied before the modelling of *PAR*, for selecting the most influential variables and discarding the most redundant ones. In the feature selection procedure, a maximum of three MIs were selected as input for the models. *RaGH* was the common MI used by all models and for all sky conditions. The additional variables were the geometrical parameter, $\cos Z$, and three variables related to the sky conditions, k_t , ϵ , and Δ . These variables have been used in other works for modelling *PAR* (Aguiré et al., 2012; Alados-Arboledas et al., 2000; Alados et al., 1996; López et al., 2001; Wang et al., 2014) with different time intervals and following different strategies, obtaining comparable results to this work.

Both modelling methods, multilinear regression and ANN, have obtained very high determination coefficients (R^2) with very close results in the models for each of the different sky conditions. Slight improvements were observed in the ANN models. The lowest *nRMSE* values were obtained for clear skies models while modelling of partial conditions yielded the highest values. *nMBE* values were practically insignificant in all cases, although its negative value showed that all models tend to underestimate *PAR* values.

Regarding the ANN models of *PAR*, the use of Levenberg-Marquardt Back-Propagation (LMBP) algorithm with three layers (input, hidden layer and output) was the chosen configuration, based on literature data (Ferrera-Cobos et al., 2020) and previous experience.

In this study, the equivalence of multilinear regression models and ANN models of *PAR* following a feature selection procedure has been highlighted. The main advantage of the multilinear regression models is knowledge of the relationship between the variables: in the case of *PAR*, the *RaGH* coefficient indicated that *PAR* value is higher under overcast sky conditions than in partial and clear skies, as previous works have demonstrated (García-Rodríguez et al., 2020). The transferability of the models to other locations and its local adaptation will be discussed in future works.

CRedit authorship contribution statement

A. García-Rodríguez: Investigation, Methodology, Formal analysis, Validation. **D. Granados-López:** Investigation, Methodology, Formal analysis, Validation. **S. García-Rodríguez:** Investigation, Methodology, Software, Visualization. **M. Díez-Mediavilla:** Conceptualization, Supervision, Funding acquisition, Project administration. **C. Alonso-Tristán:** Conceptualization, Supervision, Writing – review & editing, Funding acquisition, Project administration.

Declaration of Competing Interest

The authors declare that they have no known competing financial interests or personal relationships that could have appeared to influence the work reported in this paper.

Acknowledgments

The authors gratefully acknowledge the financial support provided by the Regional Government of Castilla y León, under projects BU021G19 and INVESTUN/19/BU/0004 and the Spanish Ministry of Science & Innovation under the I+D +i state program "Challenges Research Projects" (Ref. RTI2018-098900-B-I00). Diego Granados López expresses his thanks to the Junta de Castilla y León for economic support (PIRTU Program, ORDEN EDU/556/2019).



References

- Aguiré, L.J.G., et al., 2012. Modeling the photosynthetically active radiation in South West Amazonia under all sky conditions. *Theor. Appl. Climatol.* 108 (3-4), 631–640.
- Akitsu, T., Kume, A., Hirose, Y., Ijima, O., Nasahara, K.N., 2015. On the stability of radiometric ratios of photosynthetically active radiation to global solar radiation in Tsukuba. *Japan. Agric. For. Meteorol.* 209-210, 59–68.
- Al-Shooshan, A.A., 1997. Estimation of photosynthetically active radiation under an arid climate. *J. Agric. Eng. Res.* 66 (1), 9–13.
- Alados-Arboledas, L., Olmo, F., Alados, I., Perez, M., 2000. Parametric models to estimate photosynthetically active radiation in Spain. *Agric. For. Meteorol.* 101 (2-3), 187–201.
- Alados, I., Alados-Arboledas, L., 1999. Validation of an empirical model for photosynthetically active radiation. *Int. J. Climatol.* 19 (10), 1145–1152.
- Alados, I., Foyo-Moreno, I., Alados-Arboledas, L., 1996. Photosynthetically active radiation: measurements and modelling. *Agric. For. Meteorol.* 78 (1-2), 121–131.
- Alados, I., Olmo, F.J., Foyo-Moreno, I., Alados-Arboledas, L., 2000. Estimation of photosynthetically active radiation under cloudy conditions. *Agric. For. Meteorol.* 102 (1), 39–50.
- Alshabani, K., 2011. Finding frequency distributions of CIE Standard General Skies from sky illuminance or irradiance. *Light. Res. Technol.* 43 (4), 487–495.
- Bat-Oyun, T., Shinoda, M., Tsubo, M., 2012. Effects of cloud, atmospheric water vapour and dust on photosynthetically active radiation and total solar radiation in a Mongolian grassland. *J. Arid Land* 4 (4), 349–356.
- Blackburn, W.J., Proctor, J.T.A., 1983. Estimating photosynthetically active radiation from measured solar irradiance. *Sol. Energy* 31 (2), 233–234.
- Bosch, J.L., López, G., Battles, F.J., 2009. Global and direct photosynthetically active radiation parameterizations for clear-sky conditions. *Agric. For. Meteorol.* 149 (1), 146–158.
- Du, Y.-C., Stephanus, A., 2018. Levenberg-Marquardt neural network algorithm for degree of arteriovenous fistula stenosis classification using a dual optical photoplethysmography sensor. *Sensors* 18 (7), 2322.
- Dye, D.G., 2004. Spectral composition and quanta-to-energy ratio of diffuse photosynthetically active radiation under diverse cloud conditions. *J. Geophys. Res. Atmos.* 109 (10), D10203, 1–12.
- Erbs, D.G., Klein, S.A., Duffie, J.A., 1982. Estimation of the diffuse radiation fraction for hourly, daily and monthly-average global radiation. *Solar Energy* 28 (4), 293–302.
- Escobedo, J.F., Gomes, E.N., Oliveira, A.P., Soares, J., 2009. Modeling hourly and daily fractions of UV, PAR and NIR to global solar radiation under various sky conditions at Botucatu. *Brazil. Appl. Energy* 86 (3), 299–309.
- Ferrera-Cobos, F., Vindel, J., Valenzuela, R., González, J., 2020. Models for estimating daily photosynthetically active radiation in oceanic and mediterranean climates and their improvement by site adaptation techniques. *Adv. Space Res.* 65 (8), 1894–1909.
- Finch, D., Bailey, W., McArthur, L., Nasitwitwi, M., 2004. Photosynthetically active radiation regimes in a southern African savanna environment. *Agric. For. Meteorol.* 122 (3-4), 229–238.
- Foyo-Moreno, I., Alados, I., Alados-Arboledas, L., 2017. A new conventional regression model to estimate hourly photosynthetic photon flux density under all sky conditions. *Int. J. Climatol.* 37, 1067–1075.
- Gao, Z., Xie, X., Gao, W., Chang, N.B., 2011. Spatial analysis of terrain-impacted photosynthetic active radiation (PAR) using MODIS data. *GISCI. Remote Sens.* 48 (4), 501–521.
- García-Rodríguez, A., García-Rodríguez, S., Díez-Mediavilla, M., Alonso-Tristán, C., 2020. Photosynthetic Active Radiation, Solar Irradiance and the CIE Standard Sky Classification. *Appl. Sci.* 10 (22), 8007.
- González, J.A., Calbó, J., 2002. Modelled and measured ratio of PAR to global radiation under cloudless skies. *Agric. For. Meteorol.* 110 (4), 319–325.
- Granados-López, D., Díez-Mediavilla, M., Dieste-Velasco, M.L., Suárez-García, A., Alonso-Tristán, C., 2020. Evaluation of the vertical sky component without obstructions for daylighting in Burgos, Spain. *Appl. Sci.* 10 (9), 3095.
- Granados-López, D., Suárez-García, A., Díez-Mediavilla, M., Alonso-Tristán, C., 2021. Feature selection for CIE standard sky classification. *Sol. Energy* 218, 95–107.
- Gueymard, C.A., 2018. A reevaluation of the solar constant based on a 42-year total solar irradiance time series and a reconciliation of spaceborne observations. *Sol. Energy* 168, 2–9.
- Gueymard, C.A., Ruiz-Arias, J.A., 2016. Extensive worldwide validation and climate sensitivity analysis of direct irradiance predictions from 1-min global irradiance. *Sol. Energy* 128, 1–30.
- Hu, B., et al., 2018. Trends of photosynthetically active radiation over China from 1961 to 2014. *Int. J. Climatol.* 38 (10), 4007–4024.

- Hu, B., Wang, Y., Liu, G., 2010. Long-term trends in photosynthetically active radiation in Beijing. *Adv. Atmos. Sci.* 27 (6), 1380–1388.
- Huntingford, C., et al., 2019. Machine learning and artificial intelligence to aid climate change research and preparedness. *Environ. Res. Lett.* 14 (12), 124007.
- Iqbal, M., 1983. *An introduction to solar radiation*.
- ISO, 2004. *Spatial Distribution of Daylight-CIE Standard General Sky*. ISO-15469:2004 (E). Geneva, Switzerland.
- Jacovides, C.P., Tymvios, F.S., Asimakopoulos, D.N., Theofilou, K.M., Pashiardes, S., 2003. Global photosynthetically active radiation and its relationship with global solar radiation in the Eastern Mediterranean basin. *Theor. Appl. Climatol.* 74 (3-4), 227–233.
- Jacovides, C.P., Tymvios, F.S., Assimakopoulos, V.D., Kaltsounides, N.A., 2007. The dependence of global and diffuse PAR radiation components on sky conditions at Athens, Greece. *Agric. For. Meteorol.* 143 (3-4), 277–287.
- Jacovides, C.P., Tymvios, F.S., Boland, J., Tsitouri, M., 2015. Artificial neural network models for estimating daily solar global UV, PAR and broadband radiant fluxes in an eastern Mediterranean site. *Atmos. Res.* 152, 138–145.
- Janjai, S., Wattan, R., 2011. Development of a model for the estimation of photosynthetically active radiation from geostationary satellite data in a tropical environment. *Remote Sens. Environ.* 115 (7), 1680–1693.
- Janjai, S., Wattan, R., Sripradit, A., 2015. Modeling the ratio of photosynthetically active radiation to broadband global solar radiation using ground and satellite-based data in the tropics. *Adv. Space Res.* 56 (11), 2356–2364.
- Kasten, F., 1993. Discussion on the relative optical air mass. *Light. Res. Technol.* 25 (3), 129–130.
- Kirk, J.T.O., 1979. Spectral distribution of photosynthetically active radiation in some South-eastern Australian Waters. *Mar. Freshwater Res.* 30 (1), 81–91.
- Landsberg, J.J., Waring, R.H., 1997. A generalised model of forest productivity using simplified concepts of radiation-use efficiency, carbon balance and partitioning. *Forest Ecol. Manag.* 95 (3), 209–228.
- Leuchner, M., Hertel, C., Menzel, A., 2011. Spatial variability of photosynthetically active radiation in European beech and Norway spruce. *Agric. For. Meteorol.* 151 (9), 1226–1232.
- Li, D.H.W., Chau, N.T.C., Wan, K.K.W., 2013. Predicting daylight illuminance and solar irradiance on vertical surfaces based on classified standard skies. *Energy* 53, 252–258.
- Li, D.H.W., Cheung, G.H.W., 2006. Average daylight factor for the 15 CIE standard skies. *Light. Res. Technol.* 38 (2), 137–152.
- Li, D.H.W., Lam, T.N.T., Cheung, K.L. and Tang, H.L., 2008. *An analysis of luminous efficacies under the CIE standard skies*. 33(11): 2357-2365.
- Li, L., et al., 2015. A method for estimating hourly photosynthetically active radiation (PAR) in China by combining geostationary and polar-orbiting satellite data. *Remote Sens. Environ.* 165, 14–26.
- Liang, F., Xia, X.A., 2005. Long-term trends in solar radiation and the associated climatic factors over China for 1961-2000. *Ann. Geophys.* 23 (7), 2425–2432.
- Liu, Z., Wu, C., Xu, S., 2016. Analyzing the potential of different fractions of photosynthetically active radiation (FPARS) to estimate gross primary production. *Int. Geosci. Remote Sens. Symp. (IGARSS)* 4355–4358.
- López, G., Rubio, M.A., Martínez, M., Batlles, F.J., 2001. Estimation of hourly global photosynthetically active radiation using artificial neural network models. *Agric. For. Meteorol.* 107 (4), 279–291.
- Lv, C., et al., 2017. Levenberg–Marquardt backpropagation training of multilayer neural networks for state estimation of a safety-critical cyber-physical system. *IEEE Trans. Industr. Inform.* 14 (8), 3436–3446.
- Meek, D.W., Hatfield, J.L., Howell, T.A., Idso, S.B., Reginato, R.J., 1984. Generalized relationship between photosynthetically active radiation and solar radiation. *J. Agron.* 76 (6), 939–945.
- Monteith, J.L., 1973. *Principles of environmental physics*.
- Moon, P., 1940. Proposed standard solar-radiation curves for engineering use. *J. Franklin Inst.* 230 (5), 583–617.
- Mukaka, M., 2012. Statistics corner: a guide to appropriate use of correlation in medical research. *Malawi Med. J.* 24 (3), 69–71.
- Nwoko, S.C., Amadi, S.O., 2018. A global review of empirical models for estimating photosynthetically active radiation. *Tr. Ren. Energy* 4 (2), 236–327.
- Peng, S., et al., 2015. Observation and estimation of photosynthetically active radiation in Lhasa (Tibetan Plateau). *Adv. Space Res.* 55 (6), 1604–1612.
- Perez, R., Ineichen, P., Seals, R., Michalsky, J., Stewart, R., 1990. Modeling daylight availability and irradiance components from direct and global irradiance. *Sol. Energy* 44 (5), 271–289.
- Serrano, M.A., Boscà, J.V., 2011. Validation of a method to estimate direct normal irradiance of UVA and PAR bands from global horizontal measurements for cloudless sky conditions in Valencia, Spain, by a measurement campaign. *Theor. Appl. Climatol.* 103 (1), 95–101.
- Stanhill, G., Fuchs, M., 1977. The relative flux density of photosynthetically active radiation. *J. Appl. Ecol.* 14 (1), 317–322.
- Stigter, C.J., Musabihla, V.M.M., 1982. The conservative ratio of photosynthetically active to total radiation in the tropics (Dar es Salaam). *J. Appl. Ecol.* 19 (3), 853–858.
- Suárez-García, A., Díez-Mediavilla, M., Granados-López, D., González-Peña, D., Alonso-Tristán, C., 2020. Benchmarking of meteorological indices for sky cloudiness classification. *Sol. Energy* 195, 499–513.
- Suárez-García, A., Granados-López, D., González-Peña, D., Díez-Mediavilla, M., Alonso-Tristán, C., 2018. Seasonal characterization of CIE standard sky types above Burgos, northwestern Spain. *Sol. Energy* 169, 24–33.
- Szeicz, G., 1974. Solar radiation for plant growth. *J. Appl. Ecol.* 11 (2), 617–636.
- Torres, A.F., Walker, W.R., McKee, M., 2011. Forecasting daily potential evapotranspiration using machine learning and limited climatic data. *Agric. Water Manag.* 98 (4), 553–562.
- Torres, J.L., de Blas, M., García, A., Gracia, A., de Francisco, A., 2010a. Sky luminance distribution in Pamplona (Spain) during the summer period. *J. Atmos. Sol.-Terr. Phys.* 72 (5-6), 382–388.
- Torres, J.L., de Blas, M., García, A., Gracia, A., de Francisco, A., 2010b. Sky luminance distribution in the North of Iberian Peninsula during winter. *J. Geophys. Res. Solid Earth* 72 (16), 1147–1154.
- Tregenza, P.R., 2004. Analysing sky luminance scans to obtain frequency distributions of CIE Standard General Skies. *Light. Res. Technol.* 36 (4), 271–279.
- Tsubo, M., Walker, S., 2005. Relationships between photosynthetically active radiation and clearness index at Bloemfontein, South Africa. *Theor. Appl. Climatol.* 80 (1), 17–25.
- Vindel, J.M., et al., 2018. Modeling Photosynthetically active radiation from satellite-derived estimations over Mainland Spain. *Remote Sens.* 10 (6), 849.
- Wang, L., et al., 2015. Modeling and analysis of the spatiotemporal variations of photosynthetically active radiation in China during 1961-2012. *Renew. Sustain. Energy Rev.* 49, 1019–1032.
- Wang, L., Gong, W., Hu, B., Zhu, Z., 2014. Analysis of photosynthetically active radiation in Northwest China from observation and estimation. *Int. J. Biometeorol.* 59 (2), 193–204.
- Wang, L., Kisi, O., Zounemat-Kermani, M., Hu, B., Gong, W., 2016. Modeling and comparison of hourly photosynthetically active radiation in different ecosystems. *Renew. Sustain. Energy Rev.* 56, 436–453.
- Yamashita, M., Yoshimura, M., 2018. Influence of sky conditions on estimation of photosynthetic photon flux density for agricultural ecosystem. *Int. Arch. Photogramm. Remote Sens. Spat. Inf. Sci.* 42, 3.
- Yu, X., Guo, X., 2016. Hourly photosynthetically active radiation estimation in Midwestern United States from artificial neural networks and conventional regressions models. *Int. J. Biometeorol.* 60 (8), 1247–1259.
- Yu, X., Wu, Z., Jiang, W., Guo, X., 2015. Predicting daily photosynthetically active radiation from global solar radiation in the Contiguous United States. *Energy Convers. Manag.* 89, 71–82.
- Zhang, X., Zhang, Y., Zhou, Y., 2000. Measuring and modelling photosynthetically active radiation in Tibet Plateau during April-October. *Agric. For. Meteorol.* 102 (2-3), 207–212.

Article

Extension of PAR Models under Local All-Sky Conditions to Different Climatic Zones

Ana García-Rodríguez , Sol García-Rodríguez, Diego Granados-López, Montserrat Díez-Mediavilla and Cristina Alonso-Tristán * 

Research Group Solar and Wind Feasibility Technologies (SWIFT), Electromechanical Engineering Department, University of Burgos, 09006 Burgos, Spain; agrodriguez@ubu.es (A.G.-R.); solgr@ubu.es (S.G.-R.); dgranados@ubu.es (D.G.-L.); mdmr@ubu.es (M.D.-M.)

* Correspondence: catristan@ubu.es or cristinaalonso.tristan@gmail.com

Abstract: Four models for predicting Photosynthetically Active Radiation (PAR) were obtained through MultiLinear Regression (MLR) and an Artificial Neural Network (ANN) based on 10 meteorological indices previously selected from a feature selection algorithm. One model was developed for all sky conditions and the other three for clear, partial, and overcast skies, using a sky classification based on the clearness index (k_t). The experimental data were recorded in Burgos (Spain) at ten-minute intervals over 23 months between 2019 and 2021. Fits above 0.97 and Root Mean Square Error (RMSE) values below 7.5% were observed. The models developed for clear and overcast sky conditions yielded better results. Application of the models to the seven experimental ground stations that constitute the Surface Radiation Budget Network (SURFRAD) located in different Köppen climatic zones of the USA yielded fitted values higher than 0.98 and RMSE values less than 11% in all cases regardless of the sky type.



Citation: García-Rodríguez, A.; García-Rodríguez, S.; Granados-López, D.; Díez-Mediavilla, M.; Alonso-Tristán, C. Extension of PAR Models under Local All-Sky Conditions to Different Climatic Zones. *Appl. Sci.* **2022**, *12*, 2372. <https://doi.org/10.3390/app12052372>

Academic Editors: Harry D. Kambezidis and Basil Psiloglou

Received: 12 January 2022
Accepted: 22 February 2022
Published: 24 February 2022

Publisher's Note: MDPI stays neutral with regard to jurisdictional claims in published maps and institutional affiliations.



Copyright: © 2022 by the authors. Licensee MDPI, Basel, Switzerland. This article is an open access article distributed under the terms and conditions of the Creative Commons Attribution (CC BY) license (<https://creativecommons.org/licenses/by/4.0/>).

Keywords: photosynthetically active radiation; k_t sky classification; ANN; multilinear regression models

1. Introduction

Photosynthetically Active Radiation (PAR) is a key factor for photosynthesis, vegetation growth, and climate change. The importance of its measurement and modelling is widely recognized [1–3], as PAR has a major influence on plant canopy growth, agricultural yields, and other environmental variables. Measurement of the PAR band is needed for sky-modelling of biomass growth and forestry production [3–6] and in natural greenhouse illumination [7]. Moreover, PAR affects the relationship between atmospheric systems and plants, so much so that its availability is a regulatory factor in the natural carbon cycle and in CO₂, water, and energy exchanges within the atmosphere [8].

Within the solar radiation spectrum, PAR is the portion with a wavelength between 400 and 700 nm [9]. Unfortunately, PAR sensors are not commonly found at ground meteorological stations [10]. It is therefore usually measured on the basis of other meteorological parameters and variables. The relationship between two different variables and PAR has been analyzed in different works, obtaining mathematical models of greater or lesser accuracy. Many of these models described in the literature for modelling PAR are based on linear regressions of global horizontal radiation [3,11,12], optical air mass [1], and the clearness index [13]. Other authors modelled PAR by simultaneously taking several variables into account: solar radiation, solar zenith angle, columnar perceptible water vapour, and aerosol optical depth [14]. Wang et al. [13] estimated PAR with the clearness index, day length, and zenith angle. Ferrera-Cobos et al. [15] used Global Horizontal Irradiance (R_{aGH}), Global extraterrestrial irradiance (G_0), atmospheric Temperature (T), and Relative Humidity (RH) as input variables for their models. These relationships have been analysed in most studies as a function of sky conditions [16] to estimate PAR for clear skies where the most important

variable is the solar zenith angle. The brightness index indicates whether the model is used in the presence of clouds. In several studies, *PAR* has been treated as a variable that depends on the location where it is measured or estimated [17]. As regards measurement temporality, the ratio of *PAR* and insolation in both tropical and arctic regions has been observed to remain fairly constant on different days and over longer time scales, regardless of cloud cover, atmospheric composition, surface type, season, and day length [18].

Ferrera-Cobos et al. [15] modeled *PAR* in oceanic and Mediterranean climates, testing 22 (11 multi-linear regression and 11 artificial neural network) models, using *RaGH*, G_0 , T , and RH as their input variables. They concluded that areas with different climatic conditions needed different models. The Mediterranean climatic models showed better fits, and the models for oceanic climates needed some corrections depending on their geographical location, as the higher humidity of an oceanic climate, due to higher levels of atmospheric water vapour, means more radiation in the infrared spectrum, increasing the *PAR* to G_0 ratio. Although the combination of using geostationary and polar-orbiting satellites is an optimal solution for estimating *PAR*, a network of *PAR* sensors is necessary for better validation [18]. Sudhakar et al. proposed a *PAR* estimation model for India at six latitudes between 9° to 34° , based on hourly and monthly averages of daily global radiation and a power regression model that accounted for different solar angles, cloud cover, and climatic conditions, which they linked to *RaGH* [3].

Several researchers have used data from different satellites, supplied from CM-SAF, to develop their *PAR* models, although field data had to be used for validation in each study [12,15]—a need that Vindel et al. [19] considered when presenting methodology to determine optimal locations for *PAR* measurement stations. This methodology is based on a clustering process applied to the k_t , *PAR*, calculated by dividing the *PAR* at the Earth's surface by the part of the spectrum corresponding to the *PAR* band at the top of the atmosphere (39.8% of the total).

In recent years, machine learning techniques have been used to develop algorithms for estimating *PAR*. The most decisive variable for *PAR* estimation was *RaGH* when comparing MLR and ANN models, regardless of climate [15]. Even when ANN models were run, their results clearly worsened without *RaGH*. In this sense, Jacovides [20] used the *sunshine fraction* (nN), T , *RaGH*, G_0 , and RH as input variables for the ANN models. They found that sunshine duration plays an important role in obtaining acceptable model predictions and that the model that best predicted *PAR* values combined sunshine duration and *RaGH*.

Lopez et al. [10] presented a model using *PAR* data collected at radiometric stations using a neural network. They estimated *PAR* with *RaGH* as the only measured variable. A second ANN model based on sunshine duration measurements was shown to be an acceptable alternative for calculating *PAR*. In contrast, Pankaew et al. [21] developed an ANN model for estimating hourly *PAR* data using seven atmospheric parameters (cosine of solar zenith angle, cloud index, precipitable water content, and aerosol optical depth) as the input collected from satellite data. They concluded that *PAR* estimation with an ANN model presented a good fit with a root mean square difference of 10.2%. Qin et al. [2] tested eight artificial intelligence models, among which the BackPropagation neural network model yielded the highest accuracy. Wang et al. [22] proposed three improved ANN models: MLP, Generalized Regression Neural Network (GRNN), and Radial Basis Neural Network (RBNN) for *PAR* estimation, from long-term hourly observations of *RaGH* and meteorological variables (air temperature, relative humidity, dew point temperature, water vapour pressure, air pressure). They found that different meteorological parameters influenced *PAR* estimation in accordance with each particular (agricultural land, soil, forest, bay, prairie, desert, and lake) ecosystem.

Yu et al. [23] studied the relationship between hourly *PAR* and *RaGH* from data collected over three years at the Bondville, IL, and Sioux Falls, SD, ground weather stations (United States). From these data, they determined the temporal variability of the *PAR* fraction and its dependence on different sky conditions (defined by the clearness index (k_t)). Furthermore, the results in terms of the normalized Root Mean Square Error ($nRMSE$), the

(R^2) coefficient of determination, the Mean Percentage Error (MPE), and Relative Standard Error (RSE) from the ANN-based models were compared with the same results from four existing conventional regression models. The authors found that the ANN model could accurately predict hourly *PAR*, especially under cloudy and clear sky conditions.

In general, as the literature review has highlighted, research on the modelling of different components of solar radiation has focused on obtaining models at specific locations, which can rarely be applied directly to other locations and usually requires local recalibration to achieve adequate results. In this study, our aim is to extend locally obtained models for *PAR* estimations as a function of the sky type to other locations. The sky conditions were determined from the clearness index (k_t). Three different *PAR* models, one for each sky type (clear, overcast, and partial), were developed from experimental data collected over ten-minute intervals at Burgos, Spain. The meteorological indices had previously been selected as the model inputs. Multi-Linear Regression (MLR) and ANN were the two modelling procedures. Both models were applied to experimental *PAR* data from all seven ground stations that form the SURFRAD network, corresponding to various Köppen–Geiger climate classification types [24].

The structure of this paper is as follows: after the Introduction Section, the databases, including the meteorological measurement stations, are described in Section 2. This section also includes the definition and description of the meteorological indices used for modelling *PAR*. In Section 3, the feature selection algorithm is described and *PAR* modelling is introduced using MLR and ANN models. In Section 4, the adjustment of the models obtained in Burgos for their application to the seven SURFRAD meteorological stations located in the United States is described. Finally, the main results and conclusions are presented in Section 5.

2. Description of the Experimental Data

Figure 1 shows the location of the weather station in Burgos, Spain (42°21'04" N, 3°41'20" W, 856 metres Above Mean Sea Level) (AMSL) where the data were collected for this study. The prevailing climate in Burgos, both oceanic and Mediterranean, is classified as Csb in the Köppen climate classification system. This weather station, described in previous work [25], is situated on the flat roof of a building at the University of Burgos, with no external obstructions or reflections from other surfaces. In addition, data were collected from all seven stations within the Surface Radiation Budget Network (SURFRAD), dependent on the National Oceanic and Atmospheric Administration (NOAA): Bondville station, Sioux Falls station, Boulder station, Desert Rock station, Fort Peck station, Goodwin Creek Station, and Penn State station. Figure 2 shows the location of the weather station in Burgos and the location of the seven SURFRAD weather stations.

In Burgos, *RaGH* and Diffuse Horizontal Irradiation (*RaDH*) were measured in $W \cdot m^{-2}$ using a Hukseflux pyranometer, model SR11, and a Hukseflux pyrliometer, model DR01, respectively. *PAR* was measured from Photosynthetic Photon Flux Density, Q_p ($\mu mol \cdot s^{-1} \cdot m^{-2}$), data and was then converted into *PAR* data ($W \cdot m^{-2}$) using McCree's conversion factor ($4.57 \mu mol \cdot J^{-1}$) [26] using a EKO quantum sensor, model ML-020P. All meteorological and radiometric data were recorded every ten minutes (averages from 30 s). The experimental campaign took place from April 2019 to February 2021. Experimental data were analyzed and then filtered using conventional quality criteria [27]. If a dataset failed to pass the quality criteria, then all simultaneous datasets were rejected. The original dataset counted 71,600 datums (ten-minute datasets), 36% of which were eliminated after the filtering procedure. In the USA, *PAR*, global, and diffuse irradiance values are given in $W \cdot m^{-2}$. The *PAR* values were measured employing a LI-COR Quantum sensor, while the *RaGH* values were measured using a pyranometer Spectrolab SR-75, and *RaDH* was measured with an Eppley, Model 8–48 pyranometer. The experimental campaign spanned 10 years, from January 2009 to December 2018 at each station, with a temporal resolution of 1 min, moving to ten-minute values by calculating the average of the values within that interval.

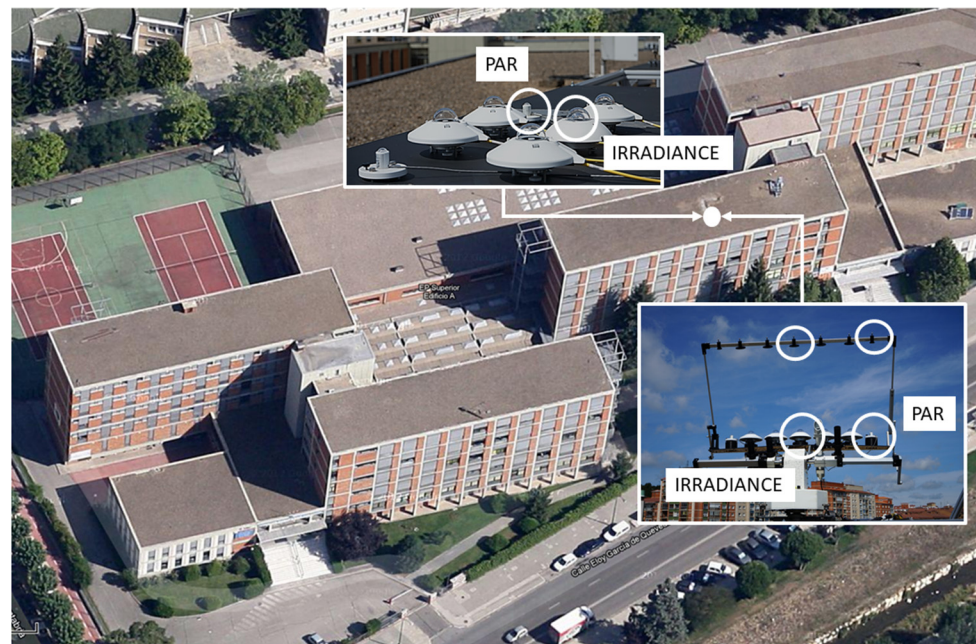


Figure 1. Experimental facility on the roof of the Higher Polytechnic School of.

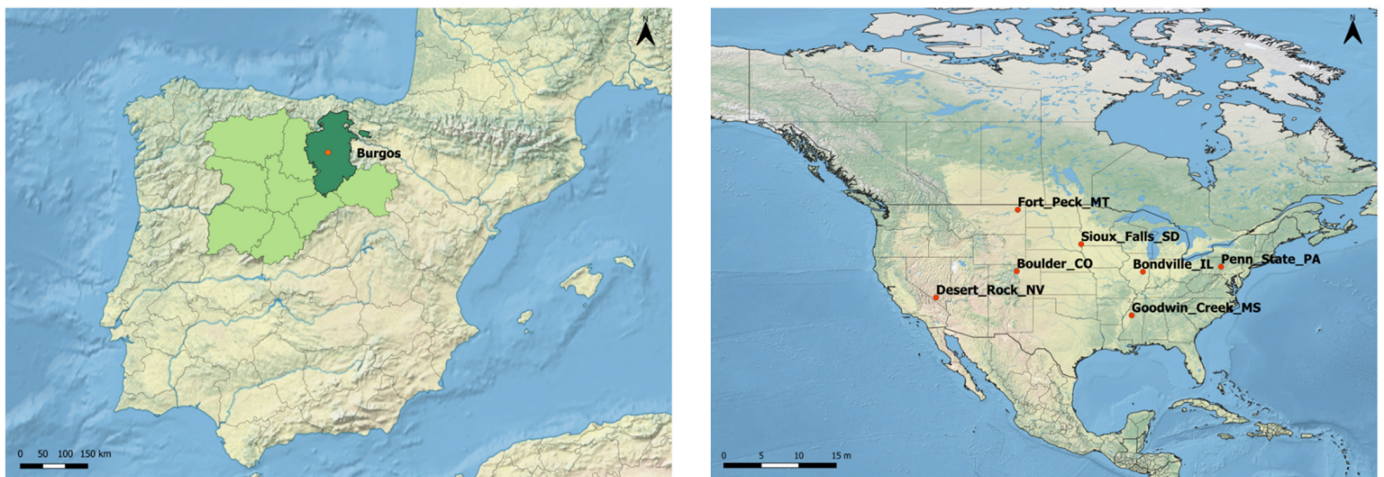


Figure 2. Location of the weather stations (Burgos and USA).

Burgos University, Spain. The Q_p , $RaGH$, and $RaDH$ sensors are shown in the detailed pictures.

Each Meteorological Index (MI) shown in Table 1 was determined at the single Spanish station and the seven meteorological stations in the USA. The following meteorological indices were directly obtained from the experimental measurements: T , P , $RaGH$, and PAR , obtained from Q_p , which were measured with pyranometers and a quantum sensor, respectively. The solar azimuth cosine ($\cos Z$) was calculated from the geometrical data of the location, using well-established mathematical relationships [28]. Finally, the dew point temperature (T_d) was calculated from the vapour water pressure [29] and RH . The other indices, k_f [28], the horizontal diffuse fraction, k_d [30], and Perez's clearness index, ϵ , and Perez's brightness factor, Δ [31], were calculated using equations described elsewhere [32].

Table 1. Meteorological indices (MIs) measured in Burgos.

MI	MI	Expression	Ref.
$RaGH$	Global Horizontal Irradiance	recorded	
k_d	Horizontal diffuse fraction	$k_d = \frac{RaDH}{RaGH}$	[30]
Q_p	Photosynthetic photon flux density	recorded	
PAR	Photosynthetically active radiation	$PAR = Q_p / 4.57 \mu\text{mol}\cdot\text{J}^{-1}$	[26]
k_t	Clearness index	$k_t = \frac{RaGH}{B_{sc}\cdot\epsilon_0\cdot\cos Z_s}$	[28]
T	Air temperature	recorded	
P	Pressure	recorded	
T_d	Dew point temperature	$T_d = \frac{35.859\cdot\log P_v - 21.48496}{\log P_v - 10.2858}$	[29]
$\cos Z$	Solar azimuth cosine	$\cos Z = \sin\delta\cdot\sin\phi + \cos\delta\cdot\cos\phi\cdot\cos\omega$	[28]
ϵ	Perez’s clearness index	$\epsilon = \frac{\frac{RaDH+RaB}{RaDH} + k\cdot Z_s^3}{1+k\cdot Z_s^3}$	[31]
Δ	Perez’s Brightness factor	$\Delta = \frac{m\cdot RaDH}{B_{sc}\cdot\epsilon_0\cdot\cos Z_s}$	[31]

$\epsilon_0 = 1 + 0.033\cdot\cos[2\cdot\pi\cdot d_n/365]$ is the average value of the orbital eccentricity of the Earth. d_n is the day of the year. B_{sc} is the extraterrestrial irradiance constant ($1361.1 \text{ W}\cdot\text{m}^{-2}$ [33]). $k = 1.04$ (or 5.56×10^{-6} if Z_s is expressed in degrees). Z_s is the angle between the sky zenith and sun. δ, ϕ, ω are the respective declination, hour angle, and geographic latitude of the specific location.

3. Methodology

The dataset was distributed into three categories of sky conditions based on the clearness index, k_t , [28] and the values adapted by Suarez-García [34] considering clear [0.65, 1), partial (0.35, 0.65), and overcast ($0 < 0.35$] skies. Figure 3 shows the Frequency Of Occurrence (FOC) of the different sky types in Burgos during the experimental campaign, which extended from April 2019 to February 2021. As can be seen, in Burgos, the clear sky conditions were prevalent except from November to January, when cloudy sky conditions occur more frequently.

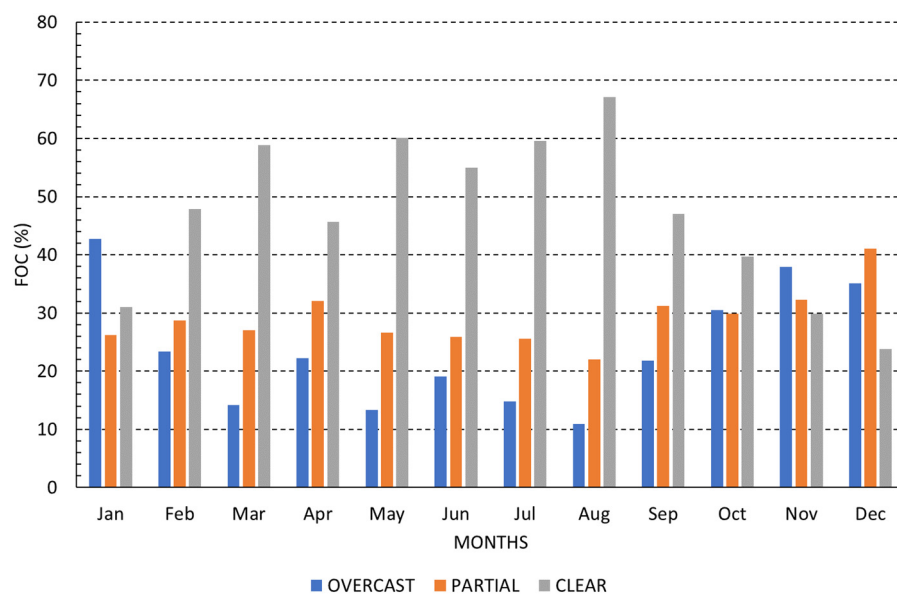


Figure 3. Monthly Frequency Of Occurrence (FOC, %) of clear, partial, and cloudy sky conditions based on the clearness index, k_t , in Burgos, Spain, between April 2019 and February 2021.

3.1. Feature Selection

The meteorological indices with the greatest influence on the *PAR* estimation models were selected to improve the precision and reduce the complexity of obtaining the models in Burgos, regardless of whether all sky types that can appear in Burgos were considered or whether the data were classified into clear, partial, and overcast skies. The first step determines the relationship of the different MIs to the *PAR*. The Pearson criterion, based on the Pearson correlation coefficient (*r*), was used to determine the influence or weight that each of index has on the *PAR* component. The criteria are as follows: if *r* is close to 0, the corresponding MI has a very weak relationship with *PAR*, whereas if it is close to 1, or -1 , the relationship is very strong. The Thumb rule [35] established five *r* intervals for the correlation: direct ($1 \geq |r(PAR, MI_i)| \geq 0.9$), strong ($0.9 > |r(PAR, MI_i)| \geq 0.7$), moderate ($0.7 > |r(PAR, MI_i)| \geq 0.5$), weak ($0.5 > |r(PAR, MI_i)| \geq 0.3$), and negligible ($|r(PAR, MI_i)| < 0.3$). Table 2 shows the different intervals of Pearson’s coefficients for the different MIs according to the classification of skies over Burgos with the *k_t* sky classification (clear, partial, and overcast).

Table 2. Pearson’s *r* (*PAR*, *MI_i*) based on the sky conditions according to the *k_t* sky classification (clear, partial, and overcast).

<i>k_t</i> Sky Type	$ r(PAR, MI_i) $				
	[1–0.9]	(0.9–0.7]	(0.7–0.5]	(0.5–0.3]	(0.3,0]
All sky conditions	<i>RaGH</i>	<i>cosZ</i> , <i>k_t</i>	<i>k_d</i> , ϵ	<i>T</i>	Δ , <i>P</i> , <i>T_d</i>
Clear	<i>RaGH</i> , <i>cosZ</i>		<i>k_t</i> , ϵ	<i>T</i>	<i>k_d</i> , Δ , <i>P</i> , <i>T_d</i>
Partial	<i>RaGH</i> , <i>cosZ</i>			<i>T</i>	<i>k_t</i> , <i>k_d</i> , Δ , ϵ , <i>P</i> , <i>T_d</i>
Overcast	<i>RaGH</i>	<i>cosZ</i>	<i>k_t</i> , Δ		<i>k_d</i> , ϵ , <i>P</i> , <i>T</i> , <i>T_d</i>

From the results shown in Table 2, it can be observed that *RaGH* is the MI that has a very strong and direct influence on *PAR* for all types of skies, coinciding with the results obtained by Ferrera-Cobos et al. [15]. Likewise, for all-sky types, *cosZ* and *k_t* also have a strong relationship, and *k_d* and ϵ have a moderate relationship with *PAR*. In the case of analyzing clear skies, there is a direct and strong relation with *RaGH* and a moderate relation with *k_t*, *cosZ*, and ϵ . For partial skies, there is also a direct and strong relation, in addition to *RaGH*, with *cosZ*. For overcast skies, there is also a direct and strong relation with *cosZ* and a moderate relation with *k_t*, and Δ . The rest of the indices (*T*, *k_d*, *P*, *T_d*) presented a weak or negligible relation with *PAR*, so these MIs were discarded as inputs for modelling *PAR*. These results agree with the literature, insofar as *RaGH* and *cosZ* are two of the variables with the strongest influence on *PAR* measurements [17,36].

3.2. Multilinear Regression Models

Once the meteorological indices with high influence on the *PAR* component were determined, taking into account all the sky types and the three sky types (clear, partial, and overcast), four MLR models were developed with which to estimate *PAR*: one MLR model for all sky types and one for each sky type. The indices selected with Pearson’s correlation coefficient (*r*) were taken as input variables in all models.

The working method to obtain the MLR models was as follows: the experimental dataset was divided into two groups. The first group contained 85% of the data and was used to fit the models. The other group, with the remaining 15% of the data, was used to validate the models using the conventional statistics corresponding to the coefficient of determination (*R*²), the normalized Mean Bias Error (*nMBE*), and the normalized Root Mean Square Error (*nRMSE*), calculated from Equations (1) and (2):

$$nMBE = \frac{1}{PAR_{exp}} \frac{\sum_{i=1}^n (PAR_{mod} - PAR_{exp})}{n} \times 100 (\%) \tag{1}$$

$$nRMSE = \frac{1}{PAR_{exp}} \sqrt{\frac{\sum_{i=1}^n (PAR_{mod} - PAR_{exp})^2}{n}} \times 100 \text{ (\%)} \tag{2}$$

where n represents the amount of experimental data used for fitting the models; PAR_{exp} is the experimental value of PAR , and PAR_{mod} is the modelled PAR value. Table 3 shows the mathematical expressions of the four regression models and the fit of each one with their mean square error. As Table 3 shows, the model fitting results presented good correlations with the experimental data, given $R^2 > 0.97$ and $nRMSE$ lower than 8%. The small and negative values of $nMBE$ indicated that the models presented a good fit although they tended to underestimate the PAR values. It can be seen that the model for clear skies showed the highest accuracy with an R^2 of 0.99 and had the lowest errors, for $nRMSE$ and for $nMBE$.

Table 3. Multilinear regression models of PAR .

Sky Conditions	Multilinear Regression Model	R^2	$nRMSE$ (%)	$nMBE$ (%)
All skies (MLR1)	$PAR = 12.12 + 0.40 \cdot RaGH + 15.74 \cdot \cos Z - 11.44 \cdot kt - 10.64 \cdot kd - 0.47 \cdot \epsilon$	0.994	4.37	-2.74×10^{-13}
Clear skies (MLR2)	$PAR = -18.12 + 0.33 \cdot RaGH + 83.15 \cdot \cos Z + 24.19 \cdot kt + 0.71 \cdot \epsilon$	0.990	3.27	-1.45×10^{-14}
Partial skies (MLR3)	$PAR = -1.81 + 0.40 \cdot RaGH + 13.75 \cdot \cos Z$	0.977	6.80	-5.32×10^{-13}
Overcast skies (MLR4)	$PAR = -0.03 + 0.42 \cdot RaGH + 6.88 \cdot \cos Z + 1.58 \cdot kt - 6.12 \cdot \Delta$	0.978	7.33	1.87×10^{-13}

3.3. Artificial Neural Network Model

Another PAR estimation method used an ANN trained with the Levenberg–Marquardt Back-Propagation (LMBP) algorithm [37]. In this case, a 3-layer configuration was chosen: the input layer, with each MI for each model, the hidden layer with the information processing centres (neurons), and the output layer, with the results. The explanation of the iterative process and the fitting are explained elsewhere [32].

For this purpose, four networks were developed and tested in this work, one for all skies and another three for each sky type, based on each selected MI with its previously determined Pearson’s correlation coefficient shown in Table 2. The R^2 , the $nMBE$, and the $nRMSE$ statistics, previously defined above, were used for the validation of the models. Table 4 summarizes the statistical results of each ANN. It can be seen that a very good fit was obtained for each ANN with an $R^2 > 0.97$ and $nRMSE < 8\%$.

Table 4. Statistical results of the ANN models.

Sky Conditions	R^2	$nRMSE$ (%)	$nMBE$ (%)
All skies (ANN1)	0.994	4.22	2.84×10^{-3}
Clear skies (ANN2)	0.992	3.01	-4.68×10^{-2}
Partial skies (ANN3)	0.977	6.80	4.06×10^{-3}
Overcast skies (ANN4)	0.978	7.28	-3.50×10^{-2}

A check was performed with 15% of the values not used in the generation of the models to validate the results of both the MLR and ANN models, which confirmed the good fit of the models for all sky types, both for the regressions and the neural networks. The results, presented below in Table 5, show the MLR results on the left and ANN results on the right.

As can be seen from the data in the table, both “data treatment” methods are optimal, as the R^2 is greater than 0.97 and the errors are less than 7%. The best-fitting model in both cases is the one applied to clear skies with fit values of 0.99 and mean square errors of less than 3%.

Table 5. Validation of MLR and ANN models.

Sky Conditions	R^2	$nRMSE$ (%)	$nMBE$ (%)	Sky Conditions	R^2	$nRMSE$ (%)	$nMBE$ (%)
All skies (MLR1)	0.994	4.48	-5.20×10^{-3}	All skies (ANN1)	0.994	4.35	-4.00×10^{-3}
Clear skies (MLR2)	0.992	3.00	1.21×10^{-1}	Clear skies (ANN2)	0.993	2.782	4.89×10^{-2}
Partial skies (MLR3)	0.978	6.72	-6.02×10^{-2}	Partial skies (ANN3)	0.978	6.71	-5.26×10^{-2}
Overcast skies (MLR4)	0.982	6.63	-4.84×10^{-2}	Overcast skies (ANN4)	0.982	6.59	-5.10×10^{-1}

4. Extension of the Models to Other Locations

The final objective of this work was to verify whether the models obtained with the experimental values obtained in Burgos (Spain) were valid for other climatic zones, for which purpose all seven SURFRAD stations in the USA were selected and the multilinear regression and neural network models were applied with the coefficients obtained for Burgos to check their fit.

The seven American stations are at the geographical locations shown in Table 6. The type of climate at each station was also included in this table, according to the Köppen climatic classification [38]: hot desert climate (Bwh); hot-summer humid continental climate (Dfa); warm-summer humid continental climate (Dfb); humid subtropical climate (Cfa); cold semi-arid climate (BSk).

Table 6. Geographical data of SURFRAD weather stations.

	Latitude (°N)	Latitude (°W)	Altitude (m.a.s.l.)	Climate
Bondville, Illinois	40.05192	88.37309	230	Dfa
Table Mountain, Boulder, Colorado	40.12498	105.2368	1689	Bsk
Desert Rock, Nevada	36.62373	116.01947	1007	Bwh
Fort Peck, Montana	48.30783	105.1017	634	Bsk
Goodwin Creek, Mississippi	34.2547	89.8729	6	Cfa
Penn State, Univ. Pennsylvania	40.72012	77.93085	376	Dfb
Sioux Falls, South Dakota	43.73403	96.62328	473	Dfa

(m.a.s.l.: meters above sea level).

The models based on the data collected at Burgos were applied to the seven American meteorological stations and compared with their own primary data. For this purpose, the R^2 coefficient and the $nRSME$ and $nMBE$ errors were obtained for all stations, both with the MLR and the ANN models for all sky types and for each particular sky type, as shown in Table 7.

Observing Table 7, it can be seen that the fit values were also very good with an R^2 greater than 0.99 for all stations and both the MLR and ANN models. The $nRMSE$ was always less than 7%, and all $nMBE$ values showed that all the models overestimated the PAR values, albeit with minimally higher values. The station with the lowest $nRMSE$ and the best fit was Penn State, for both the MLR and ANN results.

If the results for clear skies are analyzed (Table 8), it can be observed that the fit was also very good with an R^2 higher than 0.98 (although slightly lower than the study carried out for all types of sky conditions). In this case, the $nRMSE$ was lower, and at no station did it exceed 6%.

When the study was centred upon partial skies (Table 9), the R^2 values were greater than 0.99 and the errors were less than 9.5%. Finally, when the study was performed with overcast skies (Table 10), the R^2 value was greater than 0.98 and the errors with MLR were less than 8%. In this case, the $nRMSE$ at the Desert Rock station where the climate is hot and arid was slightly higher than the rest (11.07%) in the ANN study.

If the results are analysed by climatic zones, it can be seen that there were hardly any differences in the fit (R^2); all values were higher than 0.98 regardless of the sky type analysed. Figures 4 and 5 show the $nRMSE$ values for the four sky categories (all-sky type, clear, partial, and overcast) at all stations, for the MLR and the ANN models. When analysing the results for all sky types, the highest error occurred in the cold semi-arid zone (Bsk) (far from the climatic zone for which the regression and ANN models were obtained) and the lowest RMSE in continental zones with greater similarity to the climatic zone in which the models were obtained in Burgos. For clear skies in both the MLR and ANN models, the errors were slightly lower at all stations; the lowest RMSE was also obtained in continental climate zones (Dfb and Dfa) and the highest error in desert zones (Bwh).

Table 7. Model fit values for MLR models (left) and for ANN models (right) for all-sky types.

USA Stations	MLR			ANN		
	R^2	$nRMSE$ (%)	$nMBE$ (%)	R^2	$nRMSE$ (%)	$nMBE$ (%)
Bondville, Illinois	0.994	4.62	1.89	0.994	4.90	2.54
Table Mountain, Boulder, Colorado	0.996	4.93	3.48	0.996	5.48	4.18
Desert Rock, Nevada	0.997	6.10	5.36	0.997	6.75	6.04
Fort Peck, Montana	0.994	6.46	4.94	0.994	6.87	5.45
Goodwin Creek, Mississippi	0.995	4.66	2.48	0.995	5.15	3.33
Penn State, Univ. Pennsylvania	0.995	4.35	1.34	0.995	4.62	2.07
Sioux Falls, South Dakota	0.995	6.34	5.00	0.995	6.84	5.59

Table 8. Model fit values for MLR (left) and ANN (right) models under clear sky conditions.

USA Stations	MLR			ANN		
	R^2	$nRMSE$ (%)	$nMBE$ (%)	R^2	$nRMSE$ (%)	$nMBE$ (%)
Bondville, Illinois	0.985	4.05	1.61	0.985	4.13	1.28
Table Mountain, Boulder, Colorado	0.993	4.50	3.30	0.992	4.67	3.13
Desert Rock, Nevada	0.994	5.50	4.87	0.994	5.77	4.77
Fort Peck, Montana	0.988	5.41	4.16	0.987	5.31	3.74
Goodwin Creek, Mississippi	0.985	4.25	2.37	0.984	4.46	2.06
Penn State, Univ. Pennsylvania	0.987	3.77	1.20	0.986	4.02	0.95
Sioux Falls, South Dakota	0.991	5.44	4.49	0.990	5.36	4.03

Table 9. Model fit values for MLR (left) and ANN (right) under partial sky conditions.

USA Stations	MLR			ANN		
	R^2	$nRMSE$ (%)	$nMBE$ (%)	R^2	$nRMSE$ (%)	$nMBE$ (%)
Bondville, Illinois	0.990	5.66	3.15	0.990	5.67	3.19
Table Mountain, Boulder, Colorado	0.994	6.21	4.67	0.994	6.24	4.72
Desert Rock, Nevada	0.996	9.29	8.23	0.996	9.33	8.31
Fort Peck, Montana	0.991	8.06	6.51	0.991	8.08	6.56
Goodwin Creek, Mississippi	0.992	5.87	4.00	0.992	5.90	4.04
Penn State, Univ. Pennsylvania	0.991	5.00	2.27	0.991	5.00	2.30
Sioux Falls, South Dakota	0.992	7.62	6.22	0.992	7.64	6.26

Table 10. Model fit values for MLR (left) and ANN (right) under overcast sky conditions.

USA Stations	MLR			ANN		
	R^2	$nRMSE$ (%)	$nMBE$ (%)	R^2	$nRMSE$ (%)	$nMBE$ (%)
Bondville, Illinois	0.984	6.29	−0.23	0.984	7.13	3.32
Table Mountain, Boulder, Colorado	0.992	4.60	0.70	0.992	6.23	4.18
Desert Rock, Nevada	0.993	7.91	5.81	0.993	11.07	9.40
Fort Peck, Montana	0.989	6.11	2.61	0.988	8.48	6.37
Goodwin Creek, Mississippi	0.987	5.75	0.19	0.986	6.82	3.48
Penn State, Univ. Pennsylvania	0.987	6.11	−1.67	0.987	6.15	1.91
Sioux Falls, South Dakota	0.989	6.07	1.88	0.988	8.14	5.54

The errors at all stations were somewhat higher for overcast skies ranging from 4.6 to 11.07, although the ANN model still yielded the highest RMSE for the hot desert zone (Bwh). The overcast skies can present very different conditions depending on parameters such as the degree of cloud cover, its thickness, and the presence of aerosols, which have a great influence on the phenomena of absorption and dispersion of solar radiation.

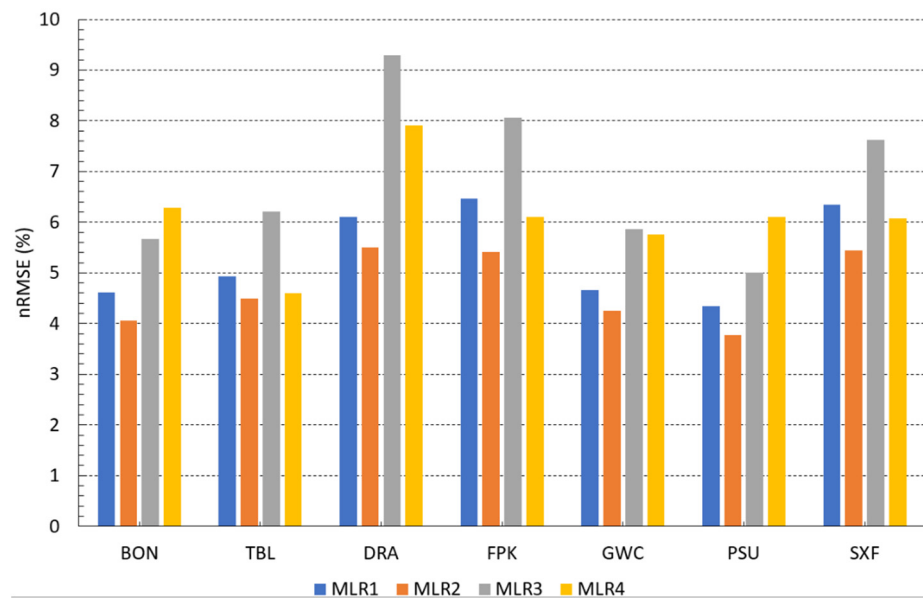


Figure 4. nRMSE (MLR) values (%) for all sky type categories at the SURFRAD stations.

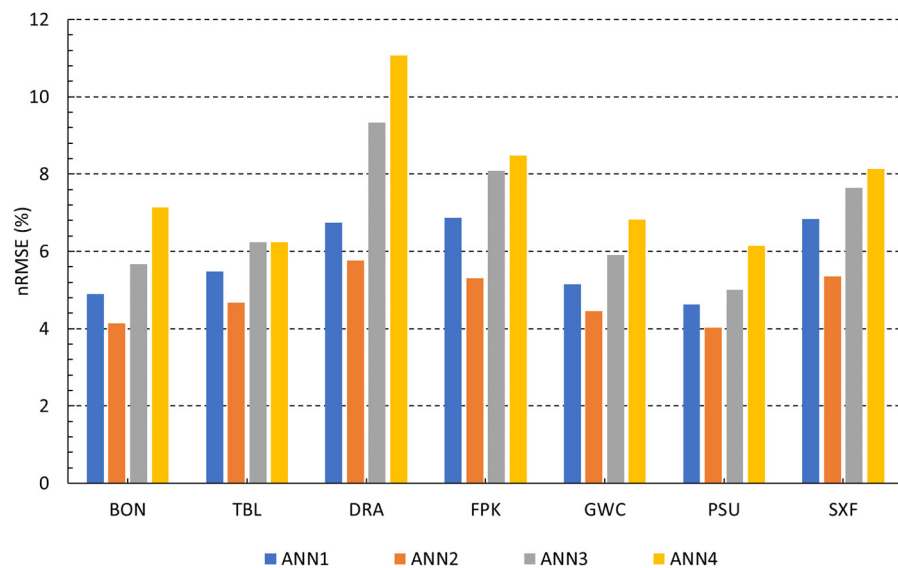


Figure 5. nRMSE (ANN) values (%) for all sky type categories at the SURFRAD stations.

5. Conclusions

A set of MLR and ANN models were obtained to model *PAR* from a set of meteorological indices in Burgos. It was determined that the most influential variable when modelling *PAR*, both when analysing all-sky types and for each particular type (clear, partial, and overcast skies) was *RaGH*. For clear and partial skies, *cosZ* also had a very strong influence, while this same MI also had a strong relationship with *PAR* for all-sky types and for overcast skies. The MI k_t had a strong relationship with *PAR* for all-sky types, while the relationship was moderate for clear, partial, and overcast skies. Perez’s clearness index, ϵ , showed a moderate relationship with *PAR* for all-skies and clear skies, and Δ was the MI with a moderate relationship for overcast skies.

Four *PAR* estimation models were obtained with MLR models that yielded an $R^2 > 0.97$, reaching an $R^2 > 0.99$ in the cases of all-skies types and clear skies; the mean square errors were lower than 8%, although this error was 3.27% for clear skies. The statistical coefficients of the ANN model were also very well adjusted because the R^2 value was in all cases

greater than 0.97 and the $nRMSE$ was also less than 8%. In this case, the model fitted clear skies better than any other, obtaining an $R^2 > 0.99$ and an $nRMSE$ of 3.01%.

These models obtained in Burgos were directly applied to seven SURFRAD stations in the USA to verify their utility, obtaining a very good fit for all of them for all sky conditions, with both MLR and ANN models, as the R^2 values were greater than 0.98 and the mean square errors were less than 11%. It is worth noting that clear skies were the sky type condition where the $nRMSEs$ were the lowest, between 3 and 5%. Models for overcast sky conditions presented worse results, mainly due to the variability of the phenomena of absorption and dispersion of solar radiation that can appear under cloudy sky conditions and that cannot be characterized by a single parameter such as k_t . It was also noteworthy that the models showed a worse fit at Desert Rock station under all sky conditions, each with an $nRMSE$ at around 9–10% for partial and overcast skies. There were no significant differences when the data were studied by climatic zones, which in all cases showed a good fit with an R^2 higher than 0.98, a lower $nRMSE$ in continental zones (Dfa and Dfb), and higher errors in semi-arid and desert zones (Bsk and Bwh).

Both the MLR and ANN models that were used to estimate PAR on the basis of experimental data collected at Burgos may be used in other locations independently of the climatology, insofar as they yielded very good statistical coefficients across the seven meteorological stations representative of very different climates within the United States. They also fitted well for different climates, although in the case of a hot arid climate, the models presented the largest quadratic errors for each type of sky.

Author Contributions: Conceptualization, M.D.-M. and C.A.-T.; methodology, A.G.-R. and S.G.-R.; software, D.G.-L.; validation, D.G.-L., A.G.-R., M.D.-M.; formal analysis, A.G.-R. and S.G.-R.; investigation, A.G.-R. and S.G.-R.; original draft preparation, M.D.-M.; writing—review and editing, C.A.-T.; visualization, A.G.-R. and S.G.-R.; supervision, M.D.-M. and C.A.-T.; project administration, M.D.-M.; funding acquisition, C.A.-T. All authors have read and agreed to the published version of the manuscript.

Funding: This research was funded by the Spanish Ministry of Science and Innovation, grant number RTI2018-098900-B-I00, and Consejería de Empleo e Industria, Junta de Castilla y León, grant number INVESTUN/19/BU-0004.

Data Availability Statement: Not applicable.

Acknowledgments: We would like to thank the SURFRAD network for placing complete and quality weather data in the public domain. Diego Granados López gratefully acknowledges economic support from the Junta de Castilla-León (ORDEN EDU/556/2019).

Conflicts of Interest: The authors declare no conflict of interest.

Abbreviation

Acronyms

ANN	Artificial Neural Network
MPE	Mean Percentage Error
MI	Meteorological Index
MLR	MultiLinear Regression
m.a.s.l.	meters above sea level
NOAA	National Oceanic and Atmospheric Administration
$nRMSE$	Normalized Root Mean Square Error
$nMBE$	Normalized Mean Bias Error
RSE	Relative Standard Error
SURFRAD	Surface Radiation Budget Network

Meteorological variables

$\cos Z$	Solar azimuth cosine ($^\circ$)
Δ	Perez's brightness factor (dim)
ϵ	Perez's clearness index (dim)
$RaGH$	Global Horizontal Irradiance ($W \cdot m^{-2}$)

$RaDH$	Diffuse Horizontal Irradiance ($W \cdot m^{-2}$)
RaB	Beam Irradiance ($W \cdot m^{-2}$)
k_d	Horizontal diffuse fraction (dim)
k_t	Clearness Index (dim)
P	Atmospheric Pressure (kPa)
PAR	Photosynthetically Active Radiation ($W \cdot m^{-2}$)
Q_p	Photosynthetic photon flux density ($\mu mol \cdot s^{-1} \cdot m^{-2}$)
r	Pearson correlation coefficient (dim)
RH	Relative Humidity (%)
T	Atmospheric Temperature ($^{\circ}C$)
T_d	Dew point temperature ($^{\circ}C$)




References

- Hu, B.; Yu, Y.; Liu, Z.; Wang, Y. Analysis of Photosynthetically Active Radiation and Applied Parameterization Model for Estimating of PAR in the North China Plain. *J. Atmos. Chem.* **2016**, *73*, 345–362. [\[CrossRef\]](#)
- Qin, W.; Wang, L.; Zhang, M.; Niu, Z.; Luo, M.; Lin, A.; Hu, B. First Effort at Constructing a High-Density Photosynthetically Active Radiation Dataset during 1961–2014 in China. *J. Clim.* **2019**, *32*, 2761–2780. [\[CrossRef\]](#)
- Sudhakar, K.; Srivastava, T.; Satpathy, G.; Premalatha, M. Modelling and Estimation of Photosynthetically Active Incident Radiation Based on Global Irradiance in Indian Latitudes. *Int. J. Energy Environ. Eng.* **2013**, *4*, 21. [\[CrossRef\]](#)
- Aguiar, L.J.G.; Fischer, G.R.; Ladle, R.J.; Malhado, A.C.M.; Justino, F.B.; Aguiar, R.G.; da Costa, J.M.N. Modeling the Photosynthetically Active Radiation in South West Amazonia under All Sky Conditions. *Theor. Appl. Climatol.* **2012**, *108*, 631–640. [\[CrossRef\]](#)
- Landsberg, J.J.; Waring, R.H. A Generalised Model of Forest Productivity Using Simplified Concepts of Radiation-Use Efficiency, Carbon Balance and Partitioning. *For. Ecol. Manag.* **1997**, *95*, 209–228. [\[CrossRef\]](#)
- Rubio, M.A.; López, G.; Tovar, J.; Pozo, D.; Batlles, F.J. The Use of Satellite Measurements to Estimate Photosynthetically Active Radiation. *Phys. Chem. Earth* **2005**, *30*, 159–164. [\[CrossRef\]](#)
- Alados, I.; Foyo-Moreno, I.; Alados-Arboledas, L. Photosynthetically Active Radiation: Measurements and Modelling. *Agric. For. Meteorol.* **1996**, *78*, 121–131. [\[CrossRef\]](#)
- Deo, R.C.; Downs, N.J.; Adamowski, J.F.; Parisi, A.V. Adaptive Neuro-Fuzzy Inference System Integrated with Solar Zenith Angle for Forecasting Sub-Tropical Photosynthetically Active Radiation. *Food Energy Secur.* **2019**, *8*, e00151. [\[CrossRef\]](#)
- Alados-Arboledas, L.; Olmo, F.J.; Alados, I.; Pérez, M. Parametric Models to Estimate Photosynthetically Active Radiation in Spain. *Agric. For. Meteorol.* **2000**, *101*, 187–201. [\[CrossRef\]](#)
- López, G.; Rubio, M.; Martínez, M.; Batlles, F. Estimation of Hourly Global Solar Radiation Using Artificial Neural Network. *Agric. For. Meteorol.* **2001**, *107*, 279–291. [\[CrossRef\]](#)
- Majnooni-heris, A. Estimating Photosynthetically Active Radiation (PAR) Using Air Temperature and Sunshine Durations. *J. Biodivers. Environ. Sci.* **2014**, *5*, 371–377.
- Vindel, J.M.; Valenzuela, R.X.; Navarro, A.A.; Zarzalejo, L.F.; Paz-Gallardo, A.; Souto, J.A.; Méndez-Gómez, R.; Cartelle, D.; Casares, J.J. Modeling Photosynthetically Active Radiation from Satellite-Derived Estimations over Mainland Spain. *Remote Sens.* **2018**, *10*, 849. [\[CrossRef\]](#)
- Wang, L.; Gong, W.; Li, C.; Lin, A.; Hu, B.; Ma, Y. Measurement and Estimation of Photosynthetically Active Radiation from 1961 to 2011 in Central China. *Appl. Energy* **2013**, *111*, 1010–1017. [\[CrossRef\]](#)
- Zempila, M.M.; Taylor, M.; Bais, A.; Kazadzis, S. Modeling the Relationship between Photosynthetically Active Radiation and Global Horizontal Irradiance Using Singular Spectrum Analysis. *J. Quant. Spectrosc. Radiat. Transf.* **2016**, *182*, 240–263. [\[CrossRef\]](#)
- Ferrera-Cobos, F.; Vindel, J.M.; Valenzuela, R.X.; González, J.A. Models for Estimating Daily Photosynthetically Active Radiation in Oceanic and Mediterranean Climates and Their Improvement by Site Adaptation Techniques. *Adv. Space Res.* **2020**, *65*, 1894–1909. [\[CrossRef\]](#)
- Möttus, M.; Ross, J.; Sulev, M. Experimental Study of Ratio of PAR to Direct Integral Solar Radiation under Cloudless Conditions. *Agric. For. Meteorol.* **2001**, *109*, 161–170. [\[CrossRef\]](#)
- Nwokolo, S.; Amadi, S.O. A Global Review of Empirical Models for Estimating Photosynthetically Active Radiation. *Trends Renew. Energy* **2018**, *4*, 236–327. [\[CrossRef\]](#)
- Frouin, R.; Pinker, R.T. Estimating Photosynthetically Active Radiation (PAR) at the Earth's Surface from Satellite Observations. *Remote Sens. Environ.* **1995**, *51*, 98–107. [\[CrossRef\]](#)
- Vindel, J.M.; Valenzuela, R.X.; Navarro, A.A.; Zarzalejo, L.F. Methodology for Optimizing a Photosynthetically Active Radiation Monitoring Network from Satellite-Derived Estimations: A Case Study over Mainland Spain. *Atmos. Res.* **2018**, *212*, 227–239. [\[CrossRef\]](#)
- Jacovides, C.P.; Tymvios, F.S.; Boland, J.; Tsitouri, M. Artificial Neural Network Models for Estimating Daily Solar Global UV, PAR and Broadband Radiant Fluxes in an Eastern Mediterranean Site. *Atmos. Res.* **2015**, *152*, 138–145. [\[CrossRef\]](#)
- Pankaew, P.; Pattarapanitchai, S.; Buntoung, S.; Wattan, R.; Masiri, I.; Sripradit, A.; Janjai, S. Estimating Photosynthetically Active Radiation Using an Artificial Neural Network. In Proceedings of the 2014 International Conference and Utility Exhibition on Green Energy for Sustainable Development (ICUE), Pattaya, Thailand, 19–21 March 2014.

22. Wang, L.; Kisi, O.; Zounemat-Kermani, M.; Hu, B.; Gong, W. Modeling and Comparison of Hourly Photosynthetically Active Radiation in Different Ecosystems. *Renew. Sustain. Energy Rev.* **2016**, *56*, 436–453. [[CrossRef](#)]
23. Yu, X.; Guo, X. Hourly Photosynthetically Active Radiation Estimation in Midwestern United States from Artificial Neural Networks and Conventional Regressions Models. *Int. J. Biometeorol.* **2016**, *60*, 1247–1259. [[CrossRef](#)] [[PubMed](#)]
24. Peel, M.; Finlayson, B.; McMahon, T. Updated World Map of the Köppen-Geiger Climate Classification. *Hydrol. Earth Syst. Sci.* **2007**, *11*, 1633–1644. [[CrossRef](#)]
25. García-Rodríguez, A.; García-Rodríguez, S.; Díez-Mediavilla, M.; Alonso-Tristán, C. Photosynthetic Active Radiation, Solar Irradiance and the Cie Standard Sky Classification. *Appl. Sci.* **2020**, *10*, 8007. [[CrossRef](#)]
26. Akitsu, T.; Kume, A.; Hirose, Y.; Ijima, O.; Nasahara, K. On the Stability of Radiometric Ratios of Photosynthetically Active Radiation to Global Solar Radiation in Tsukuba, Japan. *Agric. For. Meteorol.* **2015**, *209–210*, 59–68. [[CrossRef](#)]
27. Gueymard, C.A.; Ruiz-Arias, J.A. Extensive Worldwide Validation and Climate Sensitivity Analysis of Direct Irradiance Predictions from 1-Min Global Irradiance. *Sol. Energy* **2016**, *128*, 1–30. [[CrossRef](#)]
28. Iqbal, M. *An Introduction to Solar Radiation*; Academic Press: New York, NY, USA, 1983.
29. Heating, Refrigerating American Society of y Air Conditing Engineers. American Society of Heating, Refrigerating y Air conditioning Engineers. In *ASHRAE Handbook*; Ashrae: Atlanta, GA, USA, 2015; ISBN 9781936504459.
30. Erbs, D.G.; Klein, S.A.; Duffie, J.A. Estimation of the Diffuse Radiation Fraction for Hourly, Daily and Monthly-Average Global Radiation. *Sol. Energy* **1982**, *28*, 293–302. [[CrossRef](#)]
31. Perez, R.; Ineichen, P.; Seals, R.; Michalsky, J.; Stewart, R. Modeling Daylight Availability and Irradiance Components from Direct and Global Irradiance. *Sol. Energy* **1990**, *44*, 271–289. [[CrossRef](#)]
32. García-Rodríguez, A.; Granados-López, D.; García-Rodríguez, S.; Díez-Mediavilla, M.; Alonso-Tristán, C. Modelling Photosynthetic Active Radiation (PAR) through Meteorological Indices under All Sky Conditions. *Agric. For. Meteorol.* **2021**, *310*, 108627. [[CrossRef](#)]
33. Gueymard, C.A. A Reevaluation of the Solar Constant Based on a 42-Year Total Solar Irradiance Time Series and a Reconciliation of Spaceborne Observations. *Sol. Energy* **2018**, *168*, 2–9. [[CrossRef](#)]
34. Suárez-garcía, A.; Granados-lópez, D.; González-peña, D.; Alonso-tristán, C. Benchmarking of Meteorological Indices for Sky Cloudiness Classification. *Sol. Energy* **2020**, *195*, 499–513. [[CrossRef](#)]
35. Mukaka, M.M. Statistics Corner: A Guide to Appropriate Use of Correlation Coefficient in Medical Research. *Malawi Med. J.* **2012**, *24*, 69–71. [[PubMed](#)]
36. Foyo-Moreno, I.; Alados, I.; Alados-Arboledas, L. A New Conventional Regression Model to Estimate Hourly Photosynthetic Photon Flux Density under All Sky Conditions. *Int. J. Climatol.* **2017**, *37*, 1067–1075. [[CrossRef](#)]
37. Du, Y.C.; Stephanus, A. Levenberg-Marquardt Neural Network Algorithm for Degree of Arteriovenous Fistula Stenosis Classification Using a Dual Optical Photoplethysmography Sensor. *Sensors* **2018**, *18*, 2322. [[CrossRef](#)] [[PubMed](#)]
38. Kottek, M.; Grieser, J.; Beck, C.; Rudolf, B.; Rubel, F. World Map of the Köppen-Geiger Climate Classification Updated. *Meteorol. Z.* **2006**, *15*, 259–263. [[CrossRef](#)]

Article

A Multicriteria Evaluation of Sustainable Riparian Revegetation with Local Fruit Trees around a Reservoir of a Hydroelectric Power Plant in Central Brazil

José Roberto Ribas ^{1,*}, Jorge Santos Ribas ², Andrés Suárez García ³, Elena Arce Fariña ⁴, David González Peña ⁵ and Ana García Rodríguez ⁵

¹ Department of Industrial Engineering, Universidade Federal do Rio de Janeiro, Rio de Janeiro 21941-485, Brazil

² Agricultural and Livestock Defense Agency of the State of Paraná, Cabral 80035-050, Brazil; jribas@adapar.pr.gov.br

³ University Defense Center, Spanish Naval School, 36920 Marín, Spain; asuarez@tud.uvigo.es

⁴ Research Group Cybernetics Science and Technology (CTC), Department of Industrial Engineering, University of A Coruña, 15405 Ferrol, Spain; elena.arce@udc.es

⁵ Research Group Solar and Wind Feasibility Technologies (SWIFT), Electromechanical Engineering Department, Universidad de Burgos, 09006 Burgos, Spain; davidgp@ubu.es (D.G.P.); agrodriguez@ubu.es (A.G.R.)

* Correspondence: ribas@poli.ufrj.br



Citation: Ribas, J.R.; Ribas, J.S.; García, A.S.; Fariña, E.A.; Peña, D.G.; Rodríguez, A.G. A Multicriteria Evaluation of Sustainable Riparian Revegetation with Local Fruit Trees around a Reservoir of a Hydroelectric Power Plant in Central Brazil. *Sustainability* **2021**, *13*, 7849. <https://doi.org/10.3390/su13147849>

Academic Editor: Brian Deal

Received: 4 June 2021

Accepted: 9 July 2021

Published: 14 July 2021

Publisher's Note: MDPI stays neutral with regard to jurisdictional claims in published maps and institutional affiliations.



Copyright: © 2021 by the authors. Licensee MDPI, Basel, Switzerland. This article is an open access article distributed under the terms and conditions of the Creative Commons Attribution (CC BY) license (<https://creativecommons.org/licenses/by/4.0/>).

Abstract: The construction of hydropower plants often requires the flooding of large land areas, causing considerable alterations in the natural environment. In the region surrounding the reservoir of the Corumbá IV hydroelectric plant, located in the Cerrado region of Central Brazil, two types of soil predominate, classified as Dystroferic Red Latosol and Dystroferic Haplic Cambisol. The plant owners have to restore the degraded biome after the flooding of the margins caused by the filling of the reservoir. An experiment was carried out with fifteen native species, selected for having ideal phytosociological properties. Nine of them showed a survivability considered satisfactory in a planting situation, with a view to large-scale planting. Assuming that the planting of native fruit trees can be a quick solution to the attraction and preservation of wildlife, it would therefore provide sustainable riparian revegetation around the reservoir. We adopted the SIMOS technique to rank the criteria based on four morphological features and a Fuzzy AHP model to rank the contributions of the nine fruit tree species to the sustainable restoration of part of the riparian vegetation cover around the reservoir. In practical terms, we concluded that the soil types did not have any influence on tree survival after two years of growth, but the native trees' morphological features varied among the species. These findings simplify the large-scale planting of seedlings that must be carried out by the operator in the riparian forest around the reservoir.

Keywords: revegetation; power plant reservoir; SIMOS; Fuzzy AHP; Brazilian Cerrado

1. Introduction

A hydropower plant provides clean and renewable energy, controls floods, and offers the most efficient and flexible means of storing large amounts of energy, with instant response to changes in electricity demand [1,2]. On the other hand, it modifies rivers and their ecosystems by fragmenting channels, changing river flows, and transforming watersheds. Perverse effects provoked by artificial reservoirs can be seen through the increase in the riverine population, water pollution by untreated sewage, deforestation, and water withdrawals for irrigation and municipal water supply [3–8]. The outcome is the disintegration of aquatic and terrestrial ecosystems. Among many upstream impacts, the water impoundment destroys the vegetation in and around the reservoir area, causes habitat fragmentation, and blocks the natural flow of nutrients [9]. Moreover, the flooding

and transformed regime during all stages of the project increase the concentration of pollutants and remove habitats for terrestrial wildlife [10]. Reforestation by planting trees in cleared sites bordering a reservoir, where the existing vegetation is in most cases restricted to pasture, is an important means to restore tree cover, although it is not a straightforward process [11]. The sustainability of reforestation projects [12–14], competition for land with farming and livestock grazing [15,16], and biodiversity [17] may affect the ability to attract wildlife and improve environmental quality.

After forest conversion to human land uses, there are four different modes of reforestation: (a) spontaneous natural regeneration, (b) assisted natural regeneration, (c) agroforestry, and (d) commercial tree planting [18]. Previous research on native seedlings for restoration of degraded environments was carried out in different contexts, mainly because of the wide diversity of biomes affected by the various stages of degradation worldwide. Among other issues, researchers have studied the growth, yield, and economic viability of different tree species [19–21], the influence of pedological factors [22,23], climatic factors [24], and the impact of biotic factors on water resources and other water-related issues [25,26], as well as the search for sustainable solutions to social and economic demands [27]. Seedlings of native species have been recommended because of their better resistance against local pests and adaptability to the climate and pedological conditions of the region [28–30]. Grossnickle and MacDonald [31] identified the attributes that are used to assess the quality of seedlings and how this is used in forest restoration programs; Bojórquez-Tapia et al. [32] used an integrated approach with GIS and MCDA to identify main land degradation drivers in a study area, and Holl and Brancalion [33] recommended community involvement and an adequate time scale for maintenance and monitoring to achieve the potential benefits of increasing tree cover.

Research aimed at the conservation and sustainability of nature using multiple criteria decision analysis (MCDA) has been classified into forest management and restoration; conservation prioritization and planning; protected area planning and management; and mapping of biodiversity according to wilderness and naturalness [34]. Regarding forest management and restoration, Martin et al. [35] assessed economic-environmental tradeoffs related to restoration strategies; Forsyth et al. [36] considered alternative water catchments; Harrison and Qureshi [37] calculated the preference weights of environmental, social, and economic objectives in ranking riparian revegetation options; and Aguirre-Salado et al. [38] adopted the Universal Soil Loss Equation and MCDA to identify physically degraded sites in need of feasible ecosystem restoration.

The Brazilian Cerrado is a tropical savanna biome consisting of different types of vegetation and physiognomies: (a) *cerradão*, an almost closed woodland with crown cover of 50% to 90%, made up of tall trees, typically found in most riparian forest formations along the banks of medium and large rivers; (b) *cerrado sensu strictu*, with more than 30% crown cover, having formations of shrubs and 3–8 m tall trees with twisted branches; (c) *campo sujo* (“dirty field”), with scattered shrubs and small trees and a large proportion of grasslands; and (d) *campo limpo* (“clean field”), consisting only of dry grasslands, without shrubs or trees [39]. The soil and climate characteristics of the Brazilian Cerrado biome are peculiar, marked by a high variety of soils and rainfall seasonality, with extremes. The wet season is concentrated between October and March, with annual average rainfall of 800 to 2000 mm. During the dry season, July and August have almost no rain and the relative air humidity reaches 10%. The temperature ranges from 18 °C to 28 °C. The climate is classified as Aw, or Equatorial Savannah, according to the Köppen system, with dry winter [40].

The Brazilian Forest Code determines that some areas, because of their importance to preserving the environment and water resources, are considered areas of permanent preservation, such as areas adjacent to rivers or natural or artificial reservoirs, springs, hill-tops, and hillside properties with inclinations steeper than 45°. Artificial water reservoirs for energy generation or water supply must have permanent preservation areas located 100 m wide along their banks, measured from the limit determined by the maximum

water level in the reservoir. Suppression of vegetation in these areas can only occur in cases of public need or social interest, provided it is previously authorized by the proper environmental agencies. This measure created a riparian line of native trees along both borders of the majority of the Brazilian Cerrado rivers, but part of the remaining area was deforested. This biome is the second most important agricultural biome in Brazil, covering almost 200 million hectares. Half of this area has been replaced by cropland and pasture [41]. The biodiversity of the Brazilian Cerrado is high, with about 7000 species of plants, 199 species of mammals, and 837 species of birds, among others. The substitution of forest by crops is increasingly threatening this biodiversity [42]. To mitigate this problem when infrastructure projects such as hydropower plants are built, reforestation projects are required to mitigate the impacts on ecosystems. However, approximately 200–300 species per hectare are replaced by only a few species that show fast growth and high survival rate, such as eucalyptus, with negative consequences to the local fauna, endangering animal species [43]. In the study reported here, we analyzed the contribution of nine species of fruit trees of native to the Brazilian Cerrado biome in terms of their morphological features for revegetation around the reservoir of a hydroelectric plant, aiming at large-scale planting to restore the local biome.

2. Materials and Methods

The reservoir area of the Corumbá IV power plant, located in the Central region of Brazil, is delimited by the border between a permanent preservation area and the neighboring properties. It was formed by the impoundment of the Corumbá River, which flooded an extensive native riparian forest area and required rerouting the main highway in the area. The water partially or totally flooded the bordering properties. It forced some rural inhabitants to move to urban areas and transformed the surrounding landscape of the municipalities directly affected by the reservoir, among them Abadiânia and Alexânia (Figure 1). The municipality is the local administrative unit in Brazil. It is akin to a county, except that government is by a single mayor and municipal council. Municipalities range from lightly populated rural ones with one or two small towns to heavily populated urban ones that are part of greater metropolitan regions. During the construction period of the Corumbá IV power plant reservoir, illegal charcoal makers and cattle breeders extracted the vegetation in the region, eliminating virtually all its wildlife. The riparian forest disappeared and most of the vegetation remaining around the reservoir's borders was pasture, mainly consisting of *Brachiaria* sp. grass. Moreover, different forms of illegal fishing combined with wastewater discharge have decimated the fish population [44].

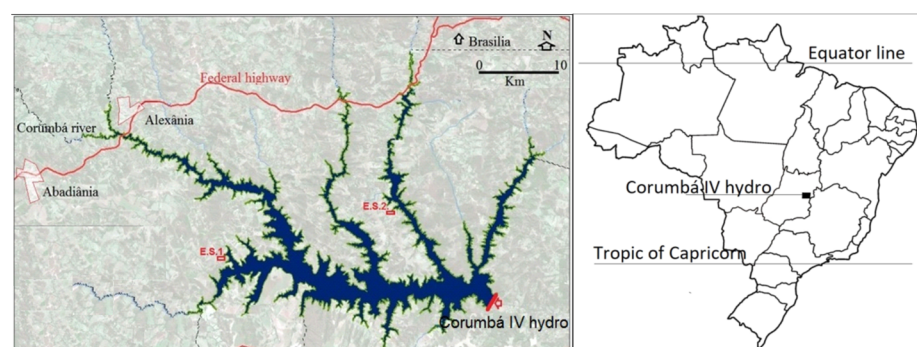


Figure 1. Corumbá IV reservoir (Brazil).

The state of Goiás, where the reservoir is located, is characterized by public policies strongly oriented to agricultural production and livestock breeding. The inexistence of soil conservation techniques and the removal of gallery forests have contributed to the disappearance of entire species native to the Brazilian Cerrado. The few initiatives to restore the forests have been limited to the planting of high-performance exotic trees. Reforestation with exotic tree species in Brazil is mainly with species of Eucalyptus and

Pinus, widely used in South America [45–47]. Although they have fair resistance against environmental threats, insects, and microorganisms and provide satisfactory forest yield, they do not add value to ecosystems, mainly because they upset the balance between flora and fauna, favorably biased to the exotic trees [48]. First developed in Queensland, Australia [49], the framework species method involves the planting of indigenous trees that attract wild animals, which in turn are responsible for seed dispersion and germination, rapidly reestablishing the forest structure and revitalizing the ecosystem [20].

The experimental sites are identified as ES-1 and ES-2 (Figure 1), both located on the margins of the reservoir of the Corumbá IV hydroelectric power plant, located in central Brazil. They were in an advanced state of degradation caused by native tree deforestation, partial reforestation with exotic species like Eucalyptus, livestock grazing, and reservoir pollution due to indiscriminate discharge of untreated wastewater. The heterogeneity of soil between these sites was the primary factor for their choice among several location alternatives. The predominant types of soil in the study area are Dystroferic Red Latosol and Dystroferic Haplic Cambisol. Table 1 shows the granulometric and chemical compositions for the soils of the two experimental sites. The soil samples were analyzed for pH (0.01 M CaCl₂; 1:5 soil: solution), Al, Mg, K, P, Fe, and C according to procedures recommended by Silva [50]. The Ca²⁺, Mg²⁺ and Al³⁺ were extracted using 1 mol L⁻¹ KCl solution (Al³⁺ by tritration with 0.2 mol L⁻¹ NaOH; Ca²⁺ and Mg²⁺ by atomic absorbium spectrophotometry); and available K, P, and Fe were extracted with Mehlich-I. Concentration of K⁺ was determined by flame spectrophotometry, P was determined by calorimetry using an UV-Vis spectrometer, and Fe was determined by atomic absorbium spectrophotometry. The (H + Al) was extracted by calcium acetate pH 7.0 and determined by titration with 0.2 mol L⁻¹ NaOH. Organic carbon was determined by Walkley-Black (Na₂Cr₂O₇ + H₂SO₄). Sum of base (SOB = Ca + Mg + K) and CEC pH 7.0 (CEC pH 7.0 = Ca + Mg + K + (H + Al)) were also determined. Organic matter was calculated considering the C content of 58%. Four samples were extracted, and the averages of the compositions were calculated for ES-1 and ES-2 sites. The granulometric composition is the determining factor for their differentiation, as they have relatively higher proportions of sand and silt, respectively. These soils are acidic with a pH approximately equal to 5 and have a low level of nutrients such as phosphorus, calcium, and sodium. The soil organic carbon (SOC), a critical indicator of soil health because it reflects the level of soil functionality associated with soil structure, hydraulic properties, and microbial activity, has a composition level considered medium, in both types of soils [51]. The sum of bases (SB) of the soil represents the sum of the exchangeable cation contents (SB = Ca²⁺ + Mg²⁺ + K⁺), except for H⁺ and Al³⁺. Base saturation (V%) is an excellent indicator of the general conditions of soil fertility, being used even as a complement in soil nomenclature. Both soils at ES-1 and ES-2 sites are considered dystrophic, or poorly fertile, as they present V% less than 50%, in this case 20% and 18%, respectively. A low V% index means that there are small amounts of cations, such as Ca²⁺, Mg²⁺, and K⁺, saturating the negative charges of the colloids and that most of them are being neutralized by H⁺ and Al³⁺. These dystrophic soils are poor in Ca²⁺, Mg²⁺, and K⁺ and have a very high exchangeable aluminum content, with aluminum saturation (Al sat%) above 50%. They have also a high content of iron and aluminum, which cause clogging of particles and a reduction in soil permeability. High levels of iron prevent the fixation of phosphorus in the particles, whose content is poor in these soils, hindering root absorption and the energy source of adenosine triphosphate (ATP), essential for photosynthesis, cell division, and growth. Excess aluminum, in turn, hinders the regular absorption of water and nutrients by the deeper roots, causing superficial rooting and limiting the growth of trees [39]. The aluminum saturation of 61% and 62% for ES-1 and ES-2, respectively, confirms the high toxicity of both soils.

The accessibility of the sites and the commitment of the farmer to performing daily inspection were taken into consideration as well [52]. Experimental site ES-1 has a total area of 9379 m², which includes the firebreak perimeter and the access road. Its geographic coordinates for one vertex are S: 16°16'51.6" and WO: 48°29'7.8", and for the opposite

vertex are S: 16°16'55.0" and WO: 48°29'4.4". The soil classification is Dystrorubic Red Latosol, here called Latosol, rich in iron, with a clayey structure [53]. Experimental site ES-2 has a total area of 9655 m², with firebreak and access road. Its geographic coordinates for one vertex are south: 16°12'55.7" and west: 48°18'22.2", and for the opposite vertex are S: 16°13'1.4" and WO: 48°18'20.2". The soil classification is Dystrorubic Hapli Cambisol, here briefly called by Cambisol, with a light sandy loam structure [53].

Table 1. Soil granulometric and chemical composition.

	Granulometric Composition			pH	Chemical Composition (cmolc/dm ³ = mE/100 mL)				
	Clay (%)	Sand (%)	Silt (%)		SOB **	V%	CEC	SOC ***	SOM ****
ES-1	31.3	47.5	21.2	5.0	1.07	20	5.30	11.1	19.1
ES-2	29.4	60.0	10.6	4.8	0.90	18	5.14	13.1	22.4

	Chemical Composition (cmolc/dm ³ = mE/100 mL)							
	P *	Ca	Mg	K	Na	Fe *	Al	Al sat %
ES-1	1.1	0.4	0.4	0.18	0.02	299	1.7	61
ES-2	0.7	0.4	0.2	0.20	0.02	241	1.5	62

* Measured in mg/dm³ = ppm; ** SOB: sum of bases; *** SOC: soil organic carbon in g/kg; **** SOM: soil organic matter in g/kg; V%: base saturation in percentage; P is P₂O₅ and Fe is Fe₂O₃.

2.1. Sampling Procedure

A phytosociological analysis considering the possible adaptation to the two types of soil initially identified 15 native fruit tree species as being viable [54]. All these fruits are juicy and sweet and make up part of the basic diet of many native species of birds and mammals. The protection of the two experimental sites against animal and human invasions was achieved with fences of barbed wire supported by autoclaved eucalyptus stakes erected along their perimeters. In order to evaluate the plants' ability to survive in the presence of *Brachiaria* sp., the grass was not removed, and the seedlings were planted in holes spaced three meters apart [55]. Finally, three organic elements were added: fertilizer made from chicken excrement, a compound of aquatic macrophytes applied on the crown of the plants, and a pesticide against ants. The fertilizer is plentiful and available without charge from local poultry farms and the aquatic macrophytes were harvested directly from the reservoir. A total of 1942 seedlings of the 15 species were planted in a randomized block design in the experimental sites ES-1 and ES-2, but since six species were excluded from the study, the remaining number of seedlings planted was reduced to 1248. However, two years after the seedlings were planted, six species were unable to adapt to the aggressive conditions of the soil and competition with *Brachiaria* sp. grass, having an average survival rate of only 8.6%, significantly different from the remaining group of nine species, with an average survival rate of 56% (p -value < 0.001). The nine species selected for the present study are listed in Table 2. The binomial name and the Brazilian common name of the six species not considered in the present study are: *Cheilochlinium cognatum* (Bacupari da Mata), *Anacardium humile* St.Hilaire (Cajuí), *Eugenia dysenterica* (Cagaita), *Brosimum gaudichaudii* Tréc (Mama Cadela), *Hancornia speciosa* Gomes (Mangaba) and *Caryocar brasiliense* Cambess (Pequi).

The first measurements were carried out two years after planting. The researchers responsible for site inspection, measurement, and reporting were a forest engineer, an agriculture technician, and one of the authors. The inspections were performed in sunny and dry weather. The dry season from May to September is particularly severe in Central Brazil. On the other hand, the wet season in the summer receives almost 50 times more than the average precipitation [56]. Although the planting in both experimental sites was done in the beginning of the wet season, the hot weather and intense rainstorms influenced the survival capacity of some species. Moreover, the presence of *Brachiaria* sp. grass covering the entire experimental sites posed additional challenges to the seedlings. This exotic African grass was introduced by farmers in the Brazilian Cerrado for pasture. Due to its high dispersion capacity for vegetative seedling reproduction, fast reproductive cycle, high photosynthesis

efficiency for nutrient usage, fast growth, resistance against livestock trampling, and fire tolerance, this grass has been a successful invader of natural ecosystems [57]. The competition between native plants and exotic grasses for soil nutrition resources changes the vegetation morphology. It also reduces the quantity and changes the composition of nutrients available for plant consumption, increasing plant vulnerability [58,59].

Table 2. Native fruit trees used in the experiment.

Abbreviation Identification	Binomial Name	Brazilian Common Name
PgS	<i>Psidium guineense</i> Swartz	Araçá Vermelho
SsAG	<i>Sterculia striata</i> A.St.-Hill & Gaudin	Chichá
IAW	<i>Ingá Alba</i> (Sw) Willd	Ingá
HsMH	<i>Hymenaea stigonocarpa</i> Mart. ex Hayne	Jatobá do Cerrado
GaLL	<i>Genipa americana</i> L.	Jenipapo
TsAR	<i>Talisia esculenta</i> (A.St.-Hill.) Radlk	Pitomba
AcLE	<i>Acrocomia aculeata</i> (Jacq.) Lodd. Ex Mart.	Macaúba
Byr	<i>Byrsonima verbascifolia</i> (L.) L.C.Rich	Murici
AaAR	<i>Alibertia edulis</i> (L.C.Rich) A.Riche ex DC.	Marmelada de Bezerro

2.2. Data Analysis

For the problem analyzed here, the comparison of the four morphological features—trees' percentage of survivors (SUR), average diameter at breast height (DBH), average total height (HEI), and average number of leaves per branch (LEA)—by means of the fuzzy analytic hierarchy process (FAHP) allowed the assignment of weights to them. Then, the comparison of the species measurements for each criterium resulted in the species performance metrics as shown in Figure 2. The analytic hierarchy process (AHP) is a MCDA method based on priority theory whose main characteristic is the decomposition of a problem into two elements, the criteria, and the alternatives. The criteria are compared to each other in terms of their relative importance to achieve a certain result and then the alternatives are compared to each other according to their performance in relation to each of the criteria. The main limitation of this method is that it is not able to reproduce inaccuracy and uncertainty [60,61]. Fuzzy AHP allows including a measure of inaccuracy in any step of the analysis. This measure is represented by α -cuts delimitating a fuzzy membership function (FMF), which defines a range over a set of possible values for the fuzzy variables. Thus, inaccuracy is incorporated into the assessment procedure, allowing a more coherent approach to the real world, thus influencing the conclusion. Chang [62] proposed a method for synthesizing the model solution and tested the respective algorithm to solve hierarchy problems associated with fuzzy logic.

The SIMOS elicitation method [63] was used to obtain comparison scores of the degree of importance between the criteria. An expert received four cards containing identification of the four criteria and twelve blank cards. He was asked to place the cards containing the criteria identifications in descending order of importance. Each blank card inserted between two criteria indicated the degree of importance of that criterion over the next one. The greater the number of blank cards, the greater the degree of importance, with the absence of cards meaning that the criteria are equally important. The cards with the criteria occupy a certain position, which divided by the total number of cards results in the normalized weight by the SIMOS procedure. To convert these weights into scores according to the Saaty procedure, the change to base eight plus one was used [64]. In this study, the cards' order represented the importance of the criteria that influence the survival of the species in the long run.

To apply the fuzzy AHP technique for the ranking of the tree species, we used the base eight plus one method, referring to the tree with the best performance. The result of the numerator or denominator, depending on the direction, must be rounded to the nearest integer. Therefore, the variable scores of relative survival rates are converted to the Saaty

scale. The advantage of this approach is that it meets the format requirement of the input data established by Saaty and Vargas [65] and the resulting matrix is transitive.

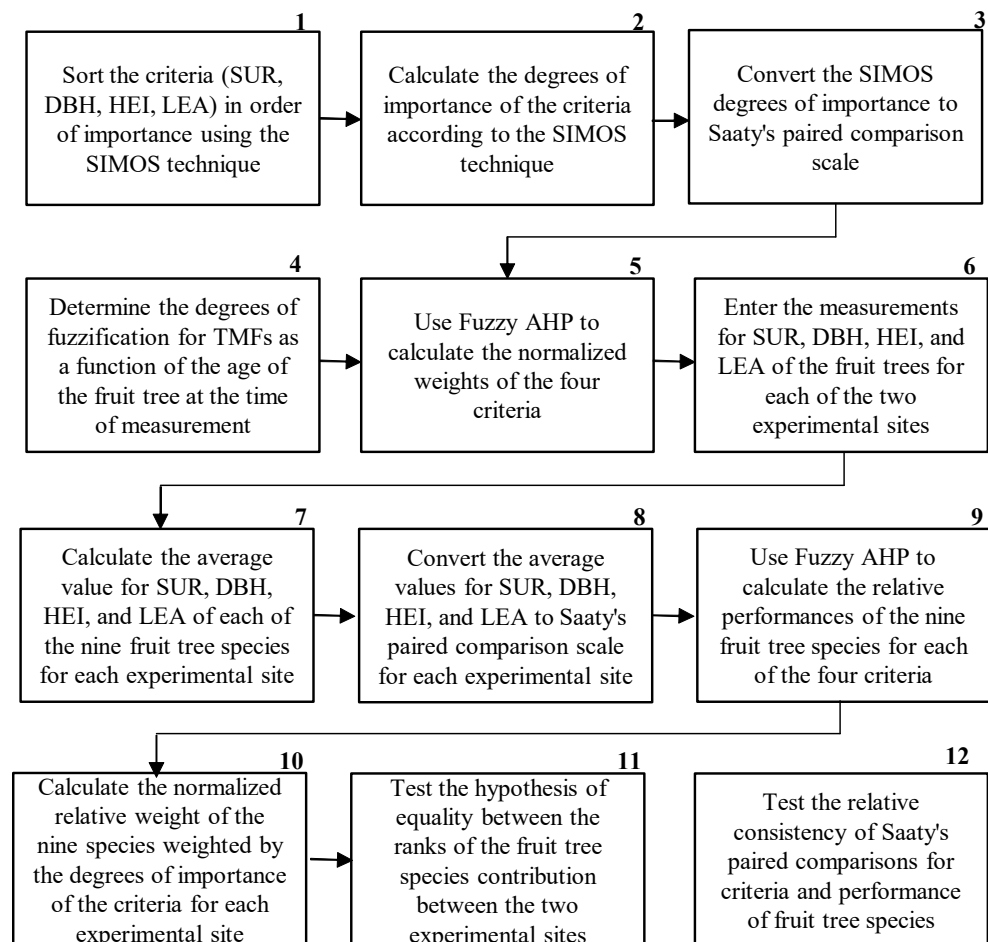


Figure 2. Flowchart of the proposed method.

3. Results

Two years after planting, the nine native trees' capacity to survive and their average traits measured—DBH, total height, and number of leaves—varied, as shown in Figure 3. Since these morphological features provide the best estimate of seedling performance after planting [66–68], we specified them as the criteria of the MCDA model to estimate the contributions of species to the sustainable restoration of the biome through new vegetation cover with fruit trees around the reservoir.

The assignment of scores aims to obtain the values of the criteria and the average values of measurements of seedling species so they can be processed by the FAHP algorithm. For this to be possible, we first converted the comparison among criteria values to a 4×4 matrix and the performance of the average values of measurements to a 9×9 matrix compatible with the Saaty scale [65], and then fuzzified them.

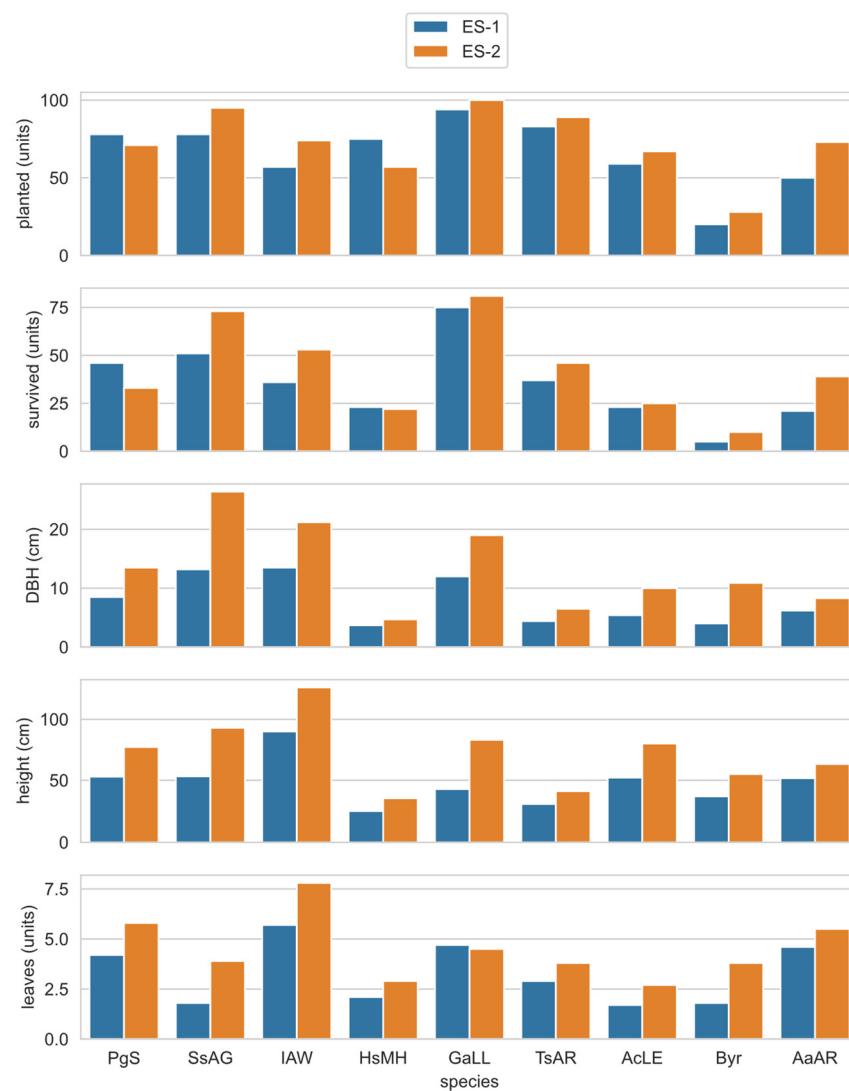
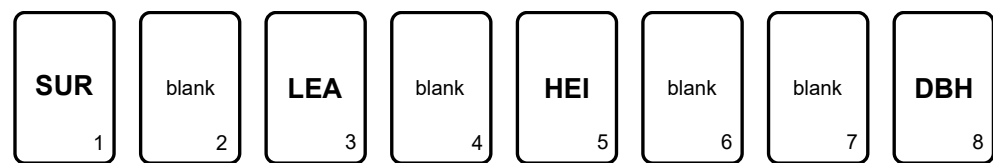


Figure 3. Measurements of seedlings planted after two years for each site.

3.1. Relative Importance among Criteria

The specialist chosen to give an opinion on the degree of relative importance among the four criteria is an agricultural engineer with 40 years of experience in the area of agricultural sciences. (The aim of identifying the fruit trees that would present the best performance for the revegetation of the surroundings of the reservoir led us to omit some representative variables for the environment, such as the stem CO₂ efflux, which contributes to the ecosystem respiration and carbon sequestration [63,69]). Using the SIMOS approach, he ordered the cards according to Figure 4. If a blank card was inserted between two criteria, it means that a displacement occurred in one position in the order of importance. The greater the number of blank cards between two criteria, the larger this displacement is, where just one blank card means “slightly more important”, two blank cards mean “more important”, and three blank cards means “much more important”. The absence of a blank card between two criteria indicates a tie. The position value divided by the sum of criteria positions results in a basic or normalized score. Although the blank card occupies a position, no score is assigned to it since it is not a criterion.



SUR, SURvivors; LEA, LEAves; HEI, HEIght; DBH, Diameter at Breast Height.

Figure 4. Relative comparison between criteria according to the SIMOS technique.

Thus, for any species, the percentage of survivors (SUR) was slightly more important than the average number of leaves per branch (LEA); which in turn was slightly more important than average total height (HEI); this being more important than average DBH. The expert gave the following explanation: “Two years after planting, the plants continue to seek stability in the formation of the regenerative forest (attempt to survive) in an abundant climate in the sun, with rains from October to April and drought from May to September. The soil continues to have *Brachiaria* sp. grass, which was introduced throughout the Cerrado. The percentage of surviving plants in relation to those planted after this period is the most important criterion, as it identifies the ability of these native plants to adapt to the two predominant types of soil surrounding the reservoir, which is highly representative throughout the entire length of the Biome. Very close in degree of importance is the average number of leaves of each species, because the leaves absorb intense local solar radiation through photosynthesis transform thermal energy into chemical energy, producing sugar, starch, and cellulose, which are essential for plant growth. The average height of each species is slightly less important than both of the previous criteria, but high values are essential for the plant to be able to compete favorably with *Brachiaria* sp. and the other species that make up the experiment, competing for space to access solar radiation. The DBH is the least important among these criteria, but significant values denote greater capacity of the wood in the transport of mineral salts and water collected from the soil by the roots.” To obtain the matrix of paired comparisons shown in Table 2, we used base eight plus one according to the approach proposed by Ribas and Silva Rocha [64]. On the Saaty scale, whose domain ranges from 1/9 to 9, when comparing two elements, the unit value means equality, so to measure the comparative distance between such elements, it is necessary to subtract them and add one. On this same scale, the reverse situation is represented by the reciprocal of the value, so if the value 2 means that element A is slightly more important than B, the value 1/2 will mean that element B is slightly less important than A. In this way, reorganizing the matrix’s differences between the four criteria in the new base will produce the input data organized in accordance with the Saaty pairwise comparison matrix, providing values suitable for calculating weights by the FAHP method. The advantage of this approach is that the resulting matrix of Table 3 is transitive.

Table 3. Matrix of paired comparisons among criteria.

	SUR	LEA	HEI	DBH
SUR	1	2	3	5
LEA	1/2	1	2	4
HEI	1/3	1/2	1	3
DBH	1/5	1/4	1/3	1

3.2. Comparison of Fruit Tree Species Relative to Each Other

To change the scale for a given species, it is necessary to multiply the species measure by eight and then divide it by the highest survival rate among all species. The result must be added to one and rounded to the nearest integer number. The matrix of paired comparisons was constructed in the same way as for the criteria of the previous step. Again, the resulting matrix was compatible with the Saaty scale and could be used as input for the FAHP method. For example, Table 4 shows the matrix of paired comparisons of seedlings

planted at the ES-1 site in relation to the survival criterion (SUR), being similar to the other criteria and the ES-2 site.

Table 4. ES-1 survival (SUR) rates converted to the Saaty pairwise comparison matrix.

	PGs	SsAG	IAW	HsMH	GaLL	TsAR	AcLE	BgT	AeAR
PGs	1	1/2	1	4	1/3	3	3	4	3
SsAG	2	1	2	5	1/2	4	4	5	4
IAW	1	1/2	1	4	1/3	3	3	4	3
HsMH	1/4	1/5	1/4	1	1/6	1/2	1/2	1	1/2
GaLL	3	2	3	6	1	5	5	6	5
TsAR	1/3	1/4	1/3	2	1/5	1	1	2	1
AcLE	1/3	1/4	1/3	2	1/5	1	1	2	1
BgT	1/4	1/5	1/4	1	1/6	1/2	1/2	1	1/2
AeAR	1/3	1/4	1/3	2	1/5	1	1	2	1

For the matrix of paired comparisons between criteria and for the performance matrices of the seedling species in relation to each of the criteria in both sites, the fuzzy values were calculated upward and downward by a triangular membership function. The criterion for establishing the fuzzification degree (δ), was based on the number of years elapsed between measuring the survival rate and planting the seedlings, equal to 3.0 for one to three years, 2.0 for four to five years, and 1.5 for a period greater than five years. Since the measurement at both sites took place two years after planting, the value set for δ was equal to 3.0.

In the next step, the values of the synthetic extensions were calculated according to the FAHP method and used to calculate the possibilities of dominance in the pairwise comparison among the nine species. The resulting entries in the paired comparison matrix and the δ value of 3.0 were input data for the FAHP, whose normalized degrees of importance for the four criteria are shown in Table 5.

Table 5. Normalized degrees of importance for morphological features.

SUR	LEA	HEI	DBH
0.285	0.270	0.248	0.197

3.3. Calculation of Performance of the Fruit Tree Survival Rates at Both Sites

Considering the convexity of the fuzzy set, the Min operator [70] was used to obtain the degrees of possibility. The performances obtained for the nine species relative to the four criteria were normalized to find their estimated contribution to revegetation, as shown in Figure 5 for the sites ES-1 and ES-2, respectively.

3.4. Consistency Analysis of the Pairwise Comparison Matrix

Inconsistency between the scores of the pairwise comparison matrix in Table 4 occurs when the procedure of changing the scale, rounding, and reorganizing the survival rates according to the Saaty table is not efficient, failing to guarantee the transitivity of the matrix of paired comparisons. To ensure that both matrices are transitive, Saaty proposed the calculation of the consistency index [71]. The consistency ratio (CR) is found by comparing the consistency index (CI) of the matrix of pairwise comparisons against the consistency index of a random-like matrix (RI), where RI is the random index table value according to the number of species. The optimal value for the criteria to be evaluated as consistent would be $CR \leq 0.1$ [71]. For four criteria, the RI value is 0.8816 and for nine species, the RI value is 1.45. We checked the consistency of the survival rates converted to the Saaty pairwise comparison matrices. The results shown in Table 6 demonstrate that criteria ES-1 and ES-2 scores had CR values below 0.1, so all matrices were consistent and transitive.

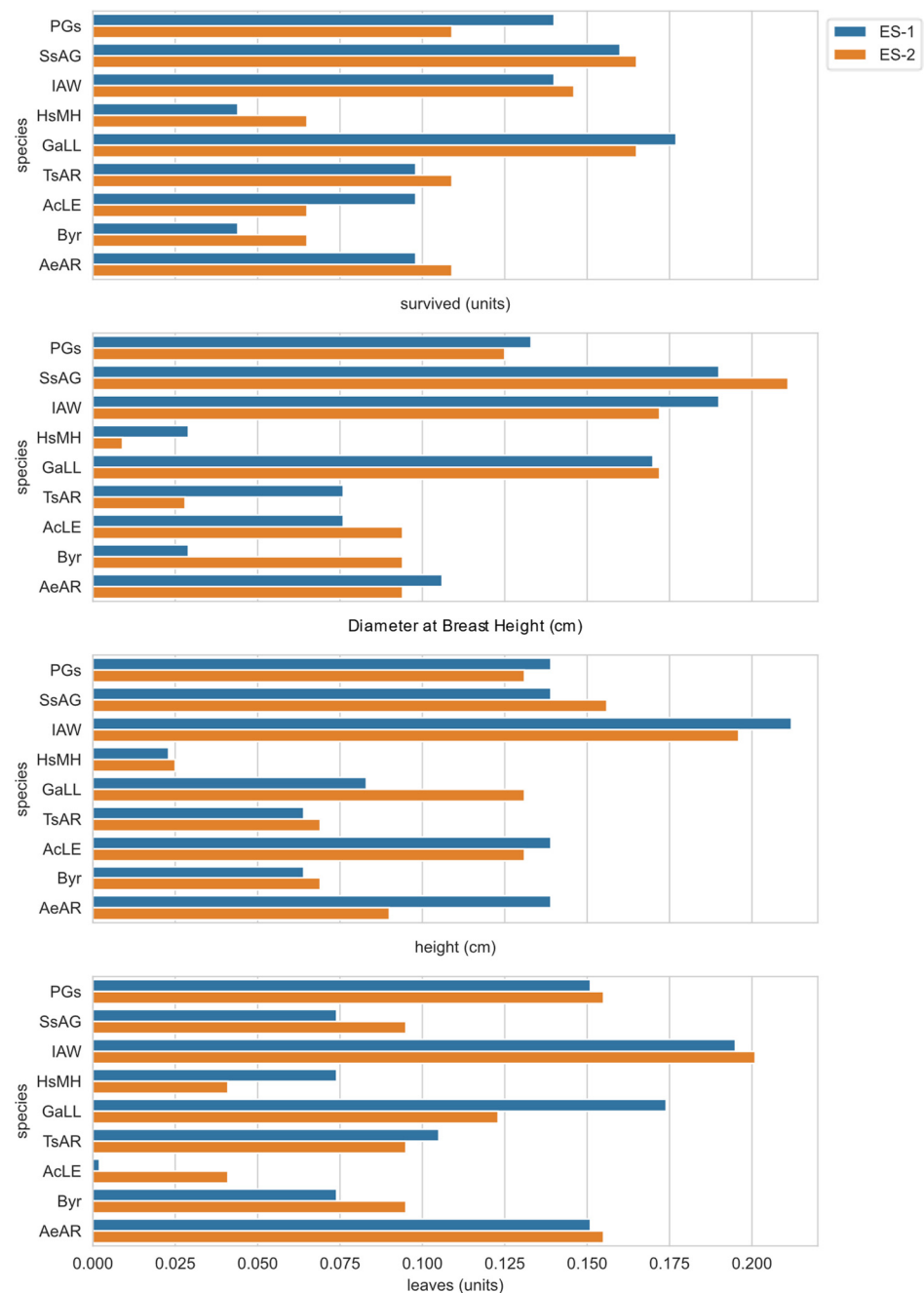


Figure 5. Species performance for each of the criteria.

Table 6. Consistency of the Saaty pairwise comparison matrices for ES-1 and ES-2.

Criteria	ES-1				ES-2				
	SUR	LEA	HEI	DBH	SUR	LEA	HEI	DBH	
CI	0.017	0.019	0.025	0.019	0.031	0.012	0.017	0.023	0.031
CR	0.019	0.013	0.017	0.013	0.021	0.008	0.012	0.016	0.022

4. Discussion

The intensity of solar radiation and rainfall are climatological factors that affect the survival of the seedlings. The dry season from May to September is particularly severe in the state of Goias. The average monthly precipitation in July is only 1.7 mm, with a standard deviation of 3.5 mm. On the other hand, the wet season in the summer receives 47 times

higher average precipitation, 882.6 mm. Although the planting in both experimental sites was done in the month of October, the hot weather with an average monthly temperature ranging from 30 °C to 32 °C and intense rainstorms influenced the survival capacity of some species.

As shown in Table 7, five species can be responsible for three-fourths of the revegetation of the reservoir margins if the results of this experiment are confirmed in large-scale planting. The production of Ingá (IAW), Chichá (SaAG), Jenipapo (GaLL), Araçá Vermelho (PgS), and Marmelada de Bezerro (AaAR) would not only serve for sustainable restoration of the biome, but also in some cases could produce an economic gain for the riverside population, since many of them are employed in the food industry.

The Pearson correlation value between the two columns of Table 7 of 0.9634 and the *p*-value close to zero demonstrated that the relative contributions of the nine species to the two types of soil had no significant differences. The same conclusion occurred with the Spearman rank correlations of the relative positions of the species, being equal to 0.90, with a *p*-value near zero. The vegetation and soil are intimately related, while the former protects the soil surface against water and wind erosion, induces the transfer of nutrients to the soil and provide surface soil enhancement [72], the latter is essential for the establishment of plant communities [73]. Because the proportion of surviving trees two years after planting was approximately equal between the two sites (53% for ES-1 and 58% for ES-2), we can state that the ability of the fruit trees to survive did not depend on the type of soil (between Latosol and Cambisol, the two predominant soils around the reservoir). Vegetation and soil are so closely related that it is hard to identify cause-and-effect relationships. For instance, vegetation can protect soil surface against erosion and influence the transfer of nutrients to the soil solution, especially iron and aluminum, adding organic components to the soil. The Latosol of ES-1 is highly weathered and has low natural fertility and a limited reserve of nutrients. It tends to have good physical but poor chemical properties relative to plant growth. The good physical properties are mainly due to high aggregate stability. Strong aggregate stability allows water and air to move through the soil readily and permits roots to penetrate with little resistance. The Cambisol of ES-2, on the other hand, is characterized by low natural fertility and high aluminum saturation. It has a high content of gravel and cobblestone [74]. The biome of ES-1 and ES-2 is classified according to its vegetation and physiognomies as “dirty field” and riverine forest. The latter aspect is ubiquitous throughout the Brazilian Cerrado biome, where nearly all water bodies are fringed by forests. This forest network is determined by the year-round high soil moisture, which despite the long dry season in the region, provides a suitable habitat for a large number of typical moist forest species. Soil moisture is one factor affecting plant performance, mostly restricted to soils that are well drained throughout the year, commonly causing pronounced physiognomic and floristic changes in the case of seasonally waterlogged grasslands. Where inter-fluvial lands are bordered by veredas (marshy grasslands), it is common to observe a decline in mean tree height and increased density of woody plants toward the land margin, where a distinct community of native tree species that are more resistant to soil saturation occurs. Another factor is the aluminum in the soil. The levels of this element are high in the dystrophic Brazilian Cerrado soils, making them extremely toxic to most cultivated plants. However, most native species are aluminum-tolerant, as would be expected. The tolerant species include a number of diverse unrelated families that accumulate aluminum in their tissues, particularly in leaves, but also in roots [39]. The roots of the trees, in turn, help to preserve the stability of the slopes on the banks of the reservoir, through hydro-mechanical reinforcement within the rooted zone. The combination of forest species with shrubs and grasses creates a dense mesh that prevents the formation of erosion and siltation along the reservoir [75,76] (Supplementary Materials).

Table 7. Weights of species contributions to the revegetation of sites.

Species	ES-1		ES-2	
PGs	0.141	3rd	0.1302	4th
SsAG	0.137	4th	0.1531	2nd
IAW	0.183	1st	0.1785	1st
HsMH	0.044	9th	0.0377	9th
GaLL	0.152	2nd	0.1465	3rd
TsAR	0.087	6th	0.0796	8th
AcLE	0.078	7th	0.0807	6th
Byr	0.054	8th	0.0799	7th
AeAR	0.124	5th	0.1139	5th

5. Conclusions

Two effects were specified as factors in the proposed model: (1) two experimental sites containing two different types of predominant soil; and (2) 1248 seedlings of nine fruit tree species, randomly dispersed in these two sites, measured by applying four criteria. The model also considered the combined effect involving the criterion weights and the species performance relative to the criteria.

The large-scale agricultural expansion in the state of Goiás, stimulated by growing global food demand, has increased deforestation in areas with high potential for production of beef and soybeans. Another factor is paper demand, causing the expansion of planted forests. Currently, only a small part of the original biome remains, most of it located in protected areas such as along riverbanks and in headwater areas. The filling of the Corumbá IV reservoir inundated pasture and cropland and partially flooded riparian forest areas. The occurrence of the exotic invasive grass *Brachiaria* sp. in nearly the entire region, the hot temperature and generally dry weather, the concentration of aluminum in the soil, and the widespread presence of livestock are some of the technical difficulties found in the Brazilian Cerrado in Goiás to reforestation with native trees. The natural regeneration of the environment is seriously affected by the presence of *Brachiaria* sp. Due to its aggressiveness and high competitiveness for solar radiation and soil nutrients, whenever an area is converted with this exotic grass for cattle grazing, it is difficult to revert to its original condition with native vegetation. Therefore, its presence in ES-1 and ES-2 sites is one of the main causes of the high mortality rate observed in most seedlings [77,78]. Urban expansion, spread of croplands, commercial tree plantation with *Eucalyptus* and *Pinus*, and higher cost of seedlings and maintenance of native trees are additional issues deterring municipal authorities and farmers from sustainable reforestation practices. The planting of native fruit trees scattered in large groves can contribute to the vegetative cycle (flowering, fruiting, ripening), offering wildlife habitats and wildlife corridors, thus increasing biodiversity by enabling aquatic and riparian animals to move along river systems, gradually reintegrating the fragmented landscapes. This action also acts as an erosion buffer and provides shaded areas for leisure activities by riverine communities.

This study showed that the contribution of tree species is independent of the two most common soil types. These findings simplify the decision for extensive plantation around reservoirs with seedlings of native tree species having better survivability. Regardless of biome, instead of replanting riparian forests with exotic trees, Brazilian hydropower companies should use seedlings of native fruit trees, thus providing a short-term solution for wildlife habitat and promoting faster local environmental recovery as a whole.

Supplementary Materials: The following are available online at <https://www.mdpi.com/article/10.3390/su13147849/s1>.

Author Contributions: Conceptualization, methodology, investigation, formal analysis, and original draft preparation, J.R.R. and J.S.R.; data curation, visualization, review and editing, A.S.G. and E.A.F.; project administration and funding acquisition, D.G.P. and A.G.R. All authors have read and agreed to the published version of the manuscript.

Funding: This research was funded by Corumbá Concessões S/A, grant number PD-2262-1204/2012, Spanish Ministry of Science and Innovation, grant number RTI2018-098900-B-I00, and the Regional Government of Castilla y León under the “Health and Safety Program” (INVESTUN/19/BU/0004).

Institutional Review Board Statement: Not applicable.

Informed Consent Statement: Not applicable.

Data Availability Statement: Ribas, J.R.; Ribas, J.S.; Data Analysis of the Evaluation of Sustainable Riparian Revegetation with Local Fruit Trees around a Reservoir of a Hydroelectric Power Plant in Central Brazil. *Mendeley Data*, V1, doi:10.17632/h36pb9v55v.1.

Acknowledgments: The authors thank the Corumbá Concessões S/A and the Defense University Center at the Spanish Naval Academy (CUD-ENM) for all the support provided for this research.

Conflicts of Interest: The authors declare no conflict of interest.

References

- Egré, D.; Milewski, J.C. The diversity of hydropower projects. *Energy Policy* **2002**, *30*, 1225–1230. [\[CrossRef\]](#)
- Zhang, L.; Chai, J.; Zhu, J.; Zhao, Z. Dynamic simulation and assessment of the ecological benefits of hydropower as an alternative energy for thermal power under ecological civilization construction: A case study of Fujian, China. *Energy Sci. Eng.* **2020**, *8*, 2426–2442. [\[CrossRef\]](#)
- World Commission on Dams (WCD). *Dams and Development: A New Framework for Decision-Making: The Report of the World Commission on Dams*; Earthscan: London, UK, 2001.
- Van Looy, K.; Tormos, T.; Souchon, Y. Disentangling dam impacts in river networks. *Ecol. Ind.* **2014**, *37*, 10–20. [\[CrossRef\]](#)
- Tealdi, S.; Camporeale, C.; Ridolfi, L. Modeling the impact of river damming on riparian vegetation. *J. Hydrol.* **2011**, *396*, 302–312. [\[CrossRef\]](#)
- De Faria, F.A.; Davis, A.; Severini, E.; Jaramillo, P. The local socio-economic impacts of large hydropower plant development in a developing country. *Energy Econ.* **2017**, *67*, 533–544. [\[CrossRef\]](#)
- Zeľeňáková, M.; Fijko, R.; Diaconu, D.C.; Remeňáková, I. Environmental impact of small hydro power plant—A case study. *Environments* **2018**, *5*, 12. [\[CrossRef\]](#)
- Botelho, A.; Ferreira, P.; Lima, F.; Pinto, L.M.C.; Sousa, S. Assessment of the environmental impacts associated with hydropower. *Renew. Sustain. Energy Rev.* **2017**, *70*, 896–904. [\[CrossRef\]](#)
- Zarfl, C.; Berlekamp, J.; He, F.; Jähnig, S.C.; Darwall, W.; Tockner, K. Future large hydropower dams impact global freshwater megafauna. *Sci. Rep.* **2019**, *9*, 1–10. [\[CrossRef\]](#)
- Moran, E.F.; Lopez, M.C.; Moore, N.; Muller, N.; Hyndman, D.W. Sustainable hydropower in the 21st century. *Proc. Natl. Acad. Sci. USA* **2018**, *115*, 11891–11898. [\[CrossRef\]](#)
- Le, H.D.; Smith, C.; Herbohn, J. What drives the success of reforestation projects in tropical developing countries? The case of the Philippines. *Glob. Environ. Chang.* **2014**, *24*, 334–348. [\[CrossRef\]](#)
- Reed, M.S.; Stringer, L.; Dougill, A.; Perkins, J.; Athlipheng, J.; Mulale, K.; Favretto, N. Reorienting land degradation towards sustainable land management: Linking sustainable livelihoods with ecosystem services in rangeland systems. *J. Environ. Manag.* **2015**, *151*, 472–485. [\[CrossRef\]](#)
- Chazdon, R.L.; Cullen, L., Jr.; Padua, S.M.; Padua, C.V. People, primates and predators in the Pontal: From endangered species conservation to forest and landscape restoration in Brazil’s Atlantic Forest. *R. Soc. Open Sci.* **2020**, *7*, 200939. [\[CrossRef\]](#)
- Buchanan, S.W.; Baskerville, M.; Oelbermann, M.; Gordon, A.M.; Thevathasan, N.V.; Isaac, M.E. Plant diversity and agroecosystem function in riparian agroforests: Providing ecosystem services and land-use transition. *Sustainability* **2020**, *12*, 568. [\[CrossRef\]](#)
- Meyfroidt, P. Environmental cognitions, land change and social-ecological feedbacks: Local case studies of forest transition in Vietnam. *Hum. Ecol.* **2013**, *41*, 367–392. [\[CrossRef\]](#)
- Lambin, E.F.; Meyfroidt, P. Global land use change, economic globalization, and the looming land scarcity. *Proc. Natl. Acad. Sci. USA* **2011**, *108*, 3465–3472. [\[CrossRef\]](#)
- Kemppinen, K.M.; Collins, P.M.; Hole, D.G.; Wolf, C.; Ripple, W.J.; Gerber, L.R. Global reforestation and biodiversity conservation. *Conserv. Biol.* **2020**, *34*, 1221–1228. [\[CrossRef\]](#)
- Chazdon, R.L. Making tropical succession and landscape reforestation successful. *J. Sustain. For.* **2013**, *32*, 649–658. [\[CrossRef\]](#)
- Calvo-Alvarado, J.C.; Arias, D.; Richter, D. Early growth performance of native and introduced fast growing tree species in wet to sub-humid climates of the Southern region of Costa Rica. *For. Ecol. Manag.* **2007**, *242*, 227–235. [\[CrossRef\]](#)
- Le, H.D.; Smith, C.; Herbohn, J.; Harrison, S. More than just trees: Assessing reforestation success in tropical developing countries. *J. Rural Stud.* **2012**, *28*, 5–19. [\[CrossRef\]](#)
- Silva, R.R.; Oliveira, D.R.; da Rocha, G.P.; Vieira, D.L. Direct seeding of Brazilian savanna trees: Effects of plant cover and fertilization on seedling establishment and growth. *Restor. Ecol.* **2015**, *23*, 393–401. [\[CrossRef\]](#)
- Miina, J.; Saksa, T. Predicting regeneration establishment in Norway spruce plantations using a multivariate multilevel model. *New For.* **2006**, *32*, 265–283. [\[CrossRef\]](#)

23. Budke, J.C.; Jarenkow, J.A.; de Oliveira-Filho, A.T. Relationships between tree component structure, topography and soils of a riverside forest, Rio Botucaraí, Southern Brazil. *Plant Ecol.* **2007**, *189*, 187–200. [[CrossRef](#)]
24. Vargas-Rodriguez, Y.L.; Vázquez-García, J.A.; Williamson, G.B. Environmental correlates of tree and seedling–sapling distributions in a Mexican tropical dry forest. *Plant Ecol.* **2005**, *180*, 117–134. [[CrossRef](#)]
25. van Dijk, A.I.; Keenan, R.J. Planted forests and water in perspective. *For. Ecol. Manag.* **2007**, *251*, 1–9. [[CrossRef](#)]
26. Valdecantos, A.; Fuentes, D.; Smanis, A.; Llovet, J.; Morcillo, L.; Bautista, S. Effectiveness of low-cost planting techniques for improving water availability to *Olea Europaea* seedlings in degraded drylands. *Restor. Ecol.* **2014**, *22*, 327–335. [[CrossRef](#)]
27. Piotto, D.; Craven, D.; Montagnini, F.; Alice, F. Silvicultural and economic aspects of pure and mixed native tree species plantations on degraded pasturelands in humid Costa Rica. *New For.* **2010**, *39*, 369–385. [[CrossRef](#)]
28. Engel, V.L.; Parrotta, J.A. An evaluation of direct seeding for reforestation of degraded lands in central Sao Paulo state, Brazil. *For. Ecol. Manag.* **2001**, *152*, 169–181. [[CrossRef](#)]
29. Lamb, S.E.; Jørstad-Stein, E.C.; Hauer, K.; Becker, C. Development of a common outcome data set for fall injury prevention trials: The Prevention of Falls Network Europe consensus. *J. Am. Geriatr. Soc.* **2005**, *53*, 1618–1622. [[CrossRef](#)] [[PubMed](#)]
30. Dodd, M.B.; Power, I.L. Direct seeding of indigenous tree and shrub species into New Zealand hill country pasture. *Ecol. Manag. Restor.* **2007**, *8*, 49–55. [[CrossRef](#)]
31. Grossnickle, S.C.; MacDonald, J.E. Seedling quality: History, application, and plant attributes. *Forests* **2018**, *9*, 283. [[CrossRef](#)]
32. Bojórquez-Tapia, L.A.; Cruz-Bello, G.M.; Luna-González, L. Connotative land degradation mapping: A knowledge-based approach to land degradation assessment. *Environ. Model. Softw.* **2013**, *40*, 51–64. [[CrossRef](#)]
33. Holl, K.D.; Brancalion, P.H. Tree planting is not a simple solution. *Science* **2020**, *368*, 580–581. [[CrossRef](#)] [[PubMed](#)]
34. Esmail, B.A.; Geneletti, D. Multi-criteria decision analysis for nature conservation: A review of 20 years of applications. *Methods Ecol. Evol.* **2018**, *9*, 42–53. [[CrossRef](#)]
35. Martin, D.M.; Hermoso, V.; Pantus, F.; Olley, J.; Linke, S.; Poff, N.L. A proposed framework to systematically design and objectively evaluate non-dominated restoration tradeoffs for watershed planning and management. *Ecol. Econ.* **2016**, *127*, 146–155. [[CrossRef](#)]
36. Forsyth, G.; Le Maitre, D.C.; O’Farrell, P.J.; Van Wilgen, B. The prioritisation of invasive alien plant control projects using a multi-criteria decision model informed by stakeholder input and spatial data. *J. Environ. Manag.* **2012**, *103*, 51–57. [[CrossRef](#)] [[PubMed](#)]
37. Qureshi, M.E.; Harrison, S.R. Application of the analytic hierarchy process to riparian revegetation policy options. *Small-Scale For. Econ. Manag. Policy* **2003**, *2*, 441–458. [[CrossRef](#)]
38. Aguirre-Salado, C.A.; Miranda-Aragón, L.; Pompa-García, M.; Reyes-Hernández, H.; Soubervielle-Montalvo, C.; Flores-Cano, J.A.; Méndez-Cortés, H. Improving identification of areas for ecological restoration for conservation by integrating USLE and MCDA in a GIS-environment: A pilot study in a priority region Northern Mexico. *ISPRS Int. J. Geo Inf.* **2017**, *6*, 262. [[CrossRef](#)]
39. Oliveira-Filho, A.T.; Ratter, J.A. *Vegetation Physiognomies and Woody Flora of the Cerrado Biome*; Oliveira, P., Marquis, R., Eds.; Columbia University Press: New York, NY, USA, 2002; Volume 13, p. 91.
40. Kottek, M.; Grieser, J.; Beck, C.; Rudolf, B.; Rubel, F. World map of the Köppen-Geiger climate classification updated. *Meteorol. Z.* **2006**, *15*, 259–263. [[CrossRef](#)]
41. Carvalho, F.M.; Júnior, P.D.M.; Ferreira, L.G. The Cerrado into-pieces: Habitat fragmentation as a function of landscape use in the savannas of central Brazil. *Biol. Conserv.* **2009**, *142*, 1392–1403. [[CrossRef](#)]
42. Klink, C.A.; Machado, R.B. Conservation of the Brazilian cerrado. *Conserv. Biol.* **2005**, *19*, 707–713. [[CrossRef](#)]
43. Martinelli, L.A.; Naylor, R.; Vitousek, P.M.; Moutinho, P. Agriculture in Brazil: Impacts, costs, and opportunities for a sustainable future. *Curr. Opin. Environ. Sustain.* **2010**, *2*, 431–438. [[CrossRef](#)]
44. Ribas, J.R. An assessment of conflicting intentions in the use of multipurpose water reservoirs. *Water Resour. Manag.* **2014**, *28*, 3989–4000. [[CrossRef](#)]
45. Paulucio, V.d.O.; Silva, C.F.d.; Martins, M.A.; Pereira, M.G.; Schiavo, J.A.; Rodrigues, L.A. Reforestation of a degraded area with *Eucalyptus* and *Sesbania*: Microbial activity and chemical soil properties. *Rev. Brasil. Ciência Solo* **2017**, *41*, 41. [[CrossRef](#)]
46. De Carvalho, J.C.B.; Espíndola, C.R.; Alves, M.C.; Figueiredo, G.C.; Dechen, S.C.F. Recovery of an oxisol degraded by the construction of a hydroelectric power plant. *Rev. Brasil. Ciência Solo* **2015**, *39*, 1776–1785. [[CrossRef](#)]
47. Brockerhoff, E.G.; Jactel, H.; Parrotta, J.A.; Ferraz, S.F. Role of eucalypt and other planted forests in biodiversity conservation and the provision of biodiversity-related ecosystem services. *For. Ecol. Manag.* **2013**, *301*, 43–50. [[CrossRef](#)]
48. Carriere, R.; Lohmann, L. *Pulping the South: Industrial Tree Plantations and the World Paper Economy*; Zed Books: London, UK, 1996.
49. Tucker, N.I.; Murphy, T.M. The effects of ecological rehabilitation on vegetation recruitment: Some observations from the Wet Tropics of North Queensland. *For. Ecol. Manag.* **1997**, *99*, 133–152. [[CrossRef](#)]
50. Da Silva, F.C. *Manual de Análises Químicas de Solos, Plantas e Fertilizantes (Handbook of Chemical Analysis of Soils, Plants and Fertilizers)*; Embrapa Informação Tecnológica: Rio de Janeiro, Brazil; Embrapa Solos Brasília: Brasília, Brazil, 2009.
51. Hou, D.; Bolan, N.S.; Tsang, D.C.; Kirkham, M.B.; O’Connor, D. Sustainable soil use and management: An interdisciplinary and systematic approach. *Sci. Total Environ.* **2020**, *729*, 138961. [[CrossRef](#)] [[PubMed](#)]
52. Schuren, S.; Snelder, D. *Tree Growing on Farms in Northeast Luzon (The Philippines): Smallholders’ Motivations and Other Determinants for Adopting Agroforestry Systems*; Snelder, D., Lasco, R., Eds.; Springer: New York, NY, USA, 2008; p. 75.

53. Dos Santos, H.; Jacomine-Klinger, P.; Dos Anjos, L.; De Oliveira, V.; Lumbreras, J.F.; Coelho, M.; De Almeida, J.; de Araújo Filho, J.; De Oliveira, J.; Cunha, T. *Sistema Brasileiro de Classificação de Solos*; Embrapa: Brasília, Brazil, 2018.
54. Silva, D.; Silva, J.; Junqueira, N.; Andrade, L. *Frutas do Cerrado*; Embrapa: Planaltina, Brazil, 2001.
55. Bullock, J.M. *Gaps in Seedling Colonization*; Fenner, M., Ed.; CAB International: Wallingford, UK, 2000; Volume 2, p. 375.
56. INPE. *Sistema de Organização Nacional de Dados Ambientais*; Instituto Nacional de Pesquisas Espaciais: Natal, Brazil, 2021.
57. Levine, J.M.; Vila, M.; Antonio, C.M.D.; Dukes, J.S.; Grigulis, K.; Lavorel, S. Mechanisms underlying the impacts of exotic plant invasions. *Proc. R. Soc. Lond. Ser. B Biol. Sci.* **2003**, *270*, 775–781.
58. Da Silva, D.M.; Batalha, M.A. Defense syndromes against herbivory in a cerrado plant community. *Plant Ecol.* **2011**, *212*, 181–193. [[CrossRef](#)]
59. Celis, G.; Jose, S. Restoring abandoned pasture land with native tree species in Costa Rica: Effects of exotic grass competition and light. *For. Ecol. Manag.* **2011**, *261*, 1598–1604. [[CrossRef](#)]
60. Büyüközkan, G.; Ruan, D. Evaluation of software development projects using a fuzzy multi-criteria decision approach. *Math. Comput. Simul.* **2008**, *77*, 464–475. [[CrossRef](#)]
61. Chand, P.; Thakkar, J.J.; Ghosh, K.K. Analysis of supply chain complexity drivers for Indian mining equipment manufacturing companies combining SAP-LAP and AHP. *Resour. Policy* **2018**, *59*, 389–410. [[CrossRef](#)]
62. Chang, D. Applications of the extent analysis method on fuzzy AHP. *Eur. J. Oper. Res.* **1996**, *95*, 649–655. [[CrossRef](#)]
63. Pictet, J.; Bollinger, D. The silent negotiation or how to elicit collective information for group MCDA without excessive discussion. *J. Multi-Criteria Decis. Anal.* **2005**, *13*, 199–211. [[CrossRef](#)]
64. Ribas, J.R.; Rocha, M.d.S. A decision support system for prioritizing investments in an energy efficiency program in favelas in the city of Rio de Janeiro. *J. Multi Criteria Decis. Anal.* **2015**, *22*, 89–99. [[CrossRef](#)]
65. Saaty, T.L.; Vargas, L.G. *How to Make a Decision*; Springer: New York, NY, USA, 2012; p. 1.
66. Bazzaz, F.; Ackerly, D.; Reekie, E. *Reproductive Allocation in Plants*; Fenner, M., Ed.; CAB International: Wallingford, UK, 2000; Volume 2, p. 30.
67. Pons, T. *Seed Responses to Light*; Fenner, M., Ed.; CAB International: Wallingford, UK, 2000; Volume 2, p. 237.
68. Mexal, J.G.; Landis, T.D. Target Seedling Concepts: Height and Diameter. 1990. Available online: <https://agris.fao.org/agris-search/search.do?recordID=US9143647> (accessed on 4 June 2014).
69. Rodríguez-Calcerrada, J.; Martin-StPaul, N.K.; Lempereur, M.; Ourcival, J.M.; del Rey, M.d.C.; Joffre, R.; Rambal, S. Stem CO₂ efflux and its contribution to ecosystem CO₂ efflux decrease with drought in a Mediterranean forest stand. *Agric. For. Meteorol.* **2014**, *195*, 61–72. [[CrossRef](#)]
70. Klir, G.J.; Yuan, B. Fuzzy sets and fuzzy logic: Theory and applications. *Possibility Theory Vs. Probab.Theory* **1996**, *32*, 207–208.
71. Saaty, T. *Optimization in Integers and Related Problems Extreme*; McGraw-Hill: New York, NY, USA, 1970.
72. Ellis, M.; Mathews, E. Needs and trends in building and HVAC system design tools. *Build. Environ.* **2002**, *37*, 461–470. [[CrossRef](#)]
73. Ruggiero, P.G.C.; Batalha, M.A.; Pivello, V.R.; Meirelles, S.T. Soil-vegetation relationships in cerrado (Brazilian savanna) and semideciduous forest, Southeastern Brazil. *Plant Ecol.* **2002**, *160*, 1–16. [[CrossRef](#)]
74. Motta, P.; Curi, N.; Franzmeier, D. *Relation of Soils and Geomorphic Surfaces in the Brazilian Cerrado*; Oliveira, P., Marquis, R., Eds.; Columbia University Press: New York, NY, USA, 2002; Volume 13, p. 13.
75. Stokes, A.; Norris, J.E.; Van Beek, L.; Bogaard, T.; Cammeraat, E.; Mickovski, S.B.; Jenner, A.; Di Iorio, A.; Fourcaud, T. *How Vegetation Reinforces Soil on Slopes*; Springer: New York, NY, USA, 2008; p. 65.
76. Capobianco, V.; Robinson, K.; Kalsnes, B.; Ekeheien, C.; Høydal, Ø. Hydro-mechanical effects of several riparian vegetation combinations on the streambank stability—A benchmark case in southeastern Norway. *Sustainability* **2021**, *13*, 4046. [[CrossRef](#)]
77. Fagundes, N.C.A.; Braga, L.D.L.; Silva, W.A.; Coutinho, C.A.; Neves, W.V.; De Souza, R.A.; Veloso, M.D.D.M.; Nunes, Y.R.F. Survival of saplings in recovery of riparian vegetation of pandeiros river (MG). *Floresta Ambient.* **2018**, *25*, 25. [[CrossRef](#)]
78. Rossi, J.; Celini, L.; Mora, P.; Mathieu, J.; Lapied, E.; Nahmani, J.; Ponge, J.; Lavelle, P. Decreasing fallow duration in tropical slash-and-burn agriculture alters soil macroinvertebrate diversity: A case study in southern French Guiana. *Agric. Ecosyst. Environ.* **2010**, *135*, 148–154. [[CrossRef](#)]